DATA-DRIVEN SYSTEM IDENTIFICATION OF STRONGLY NONLINEAR MODAL INTERACTIONS AND MODEL UPDATING OF NONLINEAR DYNAMICAL SYSTEMS

BY

KEEGAN JAMES MOORE

DISSERTATION

Submitted in partial fulfillment of the requirements
for the degree of Doctor of Philosophy in Mechanical Engineering
in the Graduate College of the
University of Illinois at Urbana-Champaign, 2018

Urbana, Illinois

Doctoral Committee:

Professor Alexander F. Vakakis, Chair and Director of Research
Professor Lawrence A. Bergman, Co-Director of Research
Adjunct Research Professor D. Michael McFarland
Assistant Professor Sameh H. Tawfick
Assistant Professor Kathryn H. Matlack

Abstract

Experimental measurements are fundamental for the calibration and validation of computational models. When a model fails to reproduce measurements, engineers must identify and incorporate the unmodeled and/or uncertain dynamics to reconcile theoretical prediction and experimental observation. While linear identification tools are well-established, practicing engineers face significant barriers when identifying and constructing reduced-order models of the dynamics of nonlinear dynamical systems; the reason is that, typically, nonlinearities introduce new dynamical phenomena that have no counterparts in linear settings. This dissertation focuses on a recently developed, data-driven nonlinear system identification and reduced-order modeling methodology that enables one to detect, characterize and model system nonlinearity using existing computational models and experimental data. This task necessitates the synergistic implementation of diverse theoretical, computational and experimental techniques such as multiple-scale and averaging approximations, resonance capture analyses, empirical mode decomposition, wavelet and Hilbert transforms, and experimental modal analysis.

The first portion of this dissertation concerns the development of an advanced signal decomposition procedure, termed wavelet-bounded empirical mode decomposition, and considers applications to the detection of strongly nonlinear modal interactions that populate the dynamics of a cantilever beam with local stiffness nonlinearity and that of a linear oscillator coupled to a vibro-impact nonlinear energy sink (i.e., a strongly nonlinear broadband absorber). The second portion examines the physical underpinnings of the proposed methodology for detecting (even strongly) nonlinear interactions in the form of internal resonances in the measured time series caused by nonlinear modal energy exchanges. Using as an example the dynamics of a cantilever beam supported by a local smooth nonlinearity, the theoretical predictions are validated by experimental measurements and post-processing analysis. The third portion focuses on the identification of a nonlinear energy sink connected to a model airplane wing; the respective theoretical and computational models are updated to accurately capture the nonlinear effects, as indicated by comparison with the measured data. The final portion considers the global effects induced by local lightweight nonlinear attachments by examining the dynamics of a model airplane with a nonlinear stores installed on each wing. The stores

are found to induce significant changes in the global dynamics of the plane even though they are local attachments, including strongly nonlinear energy exchanges facilitated by internal resonances between the modes of the plane.

To Cassandra M. Zelch

Acknowledgments

At the start of my Ph.D., I informed my advisors, Professors Alexander F. Vakakis and Lawrence A. Bergman, that my undergraduate experience was uninspiring and that I sought significant challenge throughout my graduate studies. They assured me that I would have no trouble finding that challenge. Now, nearing the end of my graduate education, I am pleased to write that their promise has been sufficiently fulfilled. This dissertation would not have been possible without their support, guidance and encouragement throughout my research. Our weekly meetings provided precisely enough freedom for me to explore my own ideas while preventing me from drifting too far off our chosen path. I am truly indebted to them for all they have taught me, and I can only hope to emulate them as an advisor to my own students.

I want to extend my gratitude to Professor D. Michael McFarland, who often provided critical insight and guidance throughout my career at Illinois. I would like to thank the remaining members of my committee: Professors Sameh H. Tawfick and Kathryn H. Matlack, who both aided in the evaluation of this dissertation and offered essential advice during my search for a faculty position. I am grateful for the aid provided by Professor Melih Eriten and Mehmet Kurt in the beginning of my Ph.D., which helped jumpstart the research presented in this dissertation, as well as for their continued involvement in our weekly research meetings.

I am most grateful and fortunate to have a received a National Science Foundation Graduate Research Fellowship, which supported me throughout the majority of my research and opened the doors to many different opportunities that might have remained closed otherwise. I would also like to acknowledge the support I received from the Department of Mechanical Science and Engineering at Illinois through various assistantships and fellowships.

I would like to acknowledge my various colleagues and lab-mates: Antoine Blanchard, Jonathan Bunyan, Sandra Chiacchiari, Hasan Hakim, Chris Herrera, Jiheng Jing, Yang Liu, Alireza Mojahed, Josef Sabuda, Qifan Zhang, Yijing Zhang and Zhen Zhang. I am proud to call Alireza Mojahed one of my close friends; I have thoroughly enjoyed our conversations and the opportunity to learn about Persian culture. I look forward to our future collaborations. I must also thank David C. Lang for always offering an interesting perspective on life and scholarship, and for our active discussions regarding many different video games,

music and anime, which often provided a needed escape from reality. I am grateful for my friendship with Allen T. Mathis, which has proven fruitful on both academic and non-academic fronts. I enjoyed our frank discussions regarding the state of the mechanical joints community and individual research topics, and I am excited for any future collaborations we might embark on. I would like to extend my gratitude to my parents, Stephen G. Moore and Jaqueline M. Moore, and my sister, Caitlin J. Moore, for their support and love during this endeavor.

Most importantly, I must extend my eternal gratitude to my soul mate, Cassandra M. Zelch. Her love has always been an important escape from reality, while also giving me the strength and motivation to pursue it wholeheartedly. Truly, without her love and support, none of my endeavors throughout graduate school would have proved successful. This dissertation is dedicated to her.

Table of Contents

List of Tables

List of Figures

Chapter 1

Introduction

1.1 Motivation

Experimental measurements are fundamental for the calibration and validation of computational models. In the vibration industry, such testing is so crucial that approximately $2 billion is spent per year on vibration testing in the US alone [Sakion, 2014]. However, analysts are often ill-equipped to identify and interpret nonlinearity and, as a result, important dynamics is lost during model calibration. This loss translates into three major costs: first, when a computational model used for design fails to accurately predict operating response due to missing dynamics, the chance of product failure in the field is significantly increased. Second, missing dynamics often forces engineers to over-design systems to account for uncertain operating conditions, leading to increased costs in terms of materials, larger product weight and lost opportunities to take advantage of the nonlinearity. The third major cost comes in the form of missed opportunities for structural health monitoring, which feeds back into the cost of product failure. The total monetary consequence of missing dynamics (the sum of the three costs) comes out to be approximately $1 trillion per year [Casadei and Broda, 2008, Sakion, 2014, Brake, 2018].

With such a significant cost associated with missing nonlinear dynamics, why are practicing engineers not conversant with nonlinearity? The answer is that nonlinearity introduces dynamic phenomena that have no counterparts in linear dynamics; however, the toolboxes of practicing engineers are dominated by linear theories and methods. Furthermore, practicing engineers can be classified with respect to nonlinearity into three groups: first, there are those that are unaware of nonlinearities in their systems and the accompanying consequences or benefits. Engineers in this group typically view nonlinear effects as noise and apply techniques such as averaging to remove them from the data, but doing so removes important physics and makes the data meaningless. The second group are aware of nonlinearity in their systems, but are uninformed of the potential gains or dangers. As example of this group comes from the ground vibration testing of the Airbus A400M [Ahlquist et al., 2011]. In this study, the engineers recognized the effects of nonlinearity in the measured data, but nonetheless fitted a linear model to the data. The third group are engineers who are

aware of nonlinearity and the potential dangers, but are ill-equipped to identify and model it accurately in a timely fashion. An example of this group comes from the modal testing of the Cassini spacecraft [Carney et al., 1997]. In their experiments, the longitudinal mode of the Huygens probe was found to decrease in frequency with increasing excitation amplitude. Engineers were aware that 15% reduction in frequency would lead to accelerations in the probe exceeding 50% of the design specifications, resulting from the coupling of the mode to the driving force of the stage-two rocket. After a four-month investigation, the source of the nonlinearity was determined, but only a significantly reduced model could be created. Consequently, the engineers were forced to retest the spacecraft at higher loads to validate the model, and, ultimately, a linear finite element model was tuned using the measured response. As can be seen, the output of any of these groups is a linear model that has been calibrated using nonlinear or (worse) linearized data.

As such, there is a current need for nonlinear system identification (NSI) and model updating tools that are both broadly applicable and widely accessible. These methods should sidestep the steep analytical, computational and experimental costs incurred by traditional NSI methods by relying on existing modeling and testing methodologies. To meet this need, this dissertation introduces a data-driven NSI methodology that augments, instead of replacing, industry-standard procedures for modeling and testing while providing accurate and physically meaningful insight into the physics governing nonlinear dynamical systems.

1.2 Literature Review of Nonlinear System Identification (NSI)

System identification concerns the development of mathematical models using the measured output of a system to a given input. For the identification of linear vibrating systems, experimental modal analysis in its various incarnations has gained widespread acceptance throughout academia and industry. By assuming linearity and stationarity, experimental modal analysis assesses the dynamic content of a measured signal using Fourier-transforms (FTs). Experimental modal analysis has been well documented by Ramsey [1975, 1976], Silva [1999] and Ewins [2000], and other methods for linear system identification and modal analysis are described by Ibrahim [1973, 1977, 1999], Ibrahim and Mikulcik [1977], Halvorsen and Brown [1977], Juang and Pappa [1985], Leuridan et al. [1985], Ljung [1987], Söderström and Stoica [1988], Allemang and Brown [1998] and Allemang and Phillips [2004]. In practice, many systems exhibit significant nonlinear and nonstationary behavior due to multi-physical interactions [Brandon, 1998] and, in these cases, FT-based methods cannot properly isolate and extract the nonlinearity from the measured response. As such, FT-based procedures often lead inexperienced analysts to misinterpret internal resonances as natural frequencies or to confuse the effects of nonlinearity with that of noise such that the analyst ends up purging physically

meaningful information from the data. Consequently, there is a need for an effective system identification, reduced-order modeling and model updating methodology for characterizing strongly nonlinear and nonstationary dynamical phenomena. Furthermore, such a methodology must build upon existing linear system identification and experimental measurement techniques such that it is both broadly applicable and widely accessible.

Current and previous methods for nonlinear system identification (NSI) are reviewed by Kerschen et al. [2006], Worden and Tomlinson [2010] and Noël and Kerschen [2017]. Typical nonparametric NSI methods include the proper orthogonal decomposition (POD) [Feeny and Kappagantu, 1998, Kerschen et al., 2005, Azeez and Vakakis, 2001, Bellizzi and Sampaio, 2006, Allison et al., 2008, Herrera et al., 2017], smooth orthogonal decomposition Chelidze and Zhou [2006], Volterra theory [Li and Billings, 2011], Kalman filter [Mariani and Ghisi, 2007], Bayesian approaches [Worden and Hensman, 2012, Worden and Manson, 2012, Worden and Becker, 2012, Tiboaca et al., 2014, Baldacchino et al., 2016] and machine learning [Worden and Green, 2017]. With regard to methods for nonlinear parameter estimation, of note are the restoring force method [Masri and Caughey, 1979], NARMAX (Nonlinear AutoRegressive Moving Average models with eXogeneous inputs) methods [Leontaritis and Billings, 1985, Billings, 2013], harmonic balance method [Lyashevskiy et al., 1995, Lyashevskiy and Chen, 1997, Thothadri et al., 2003, Thothadri and Moon, 2005], methods based on Hilbert transform [Feldman, 2011], subspace identification [Lacy and Bernstein, 2005, Noël and Kerschen, 2013] and others. The neural network approach is another popular parametric methodology for system identification and damage-detection. Several noteworthy works related to this approach are due to [Liang et al., 2001, Masri et al., 2000].

Proper orthogonal decomposition is a popular nonparametric methodology for system identification. Ma et al. [2000] employed POD to compute nonlinear normal modes (NNMs) of a system of coupled beams, Georgiou [2005] used it to study the nonlinear modes of a system of coupled rods, and Galvanetto et al. [2008] employed it to detect structural damage. Using POD, Cusumano and Bai [1993] and Cusumano et al. [1994] studied the chaotic vibrations of a 10-degree-of-freedom (DOF) impact oscillator and a flexible-beam impact oscillator, respectively. Moreover, Ritto et al. [2011] applied POD to perform model reduction of a vibro-impact (VI) rod, and Azeez and Vakakis [2001] used it to extract dominant coherent structures of a VI beam from experimental time-series data and used those structures to derive low-dimensional reduced-order models (ROMs) through a Galerkin reconstruction process. Clement et al. [2014] proposed the sliding window proper orthogonal decomposition, which combines POD and the continuous Gabor transform to extract the linear and nonlinear normal modes of weakly damped multi-DOF (MDOF) mechanical systems.

Note that these techniques are only applicable to specific classes of dynamical systems; in addition,

some functional form is assumed for modeling the system nonlinearity. Recently, a new NSI technique with promise of broad applicability was presented, employing empirical mode decomposition (EMD) [Huang et al., 1998], under the assumption that the measured time series can be decomposed in terms of a finite number of harmonic components in the form of fast, nearly monochromatic, oscillations that are modulated by slow-varying amplitudes [Lee et al., 2009b, Vakakis et al., 2011]. Lee et al. [2005] and Lee et al. [2009a] applied this NSI method to study the interactions between a lightly damped, linear oscillator and a smoothly nonlinear attachment and a vibro-impact attachment, respectively. The same NSI procedure was applied by Kurt et al. [2012] and Kurt et al. [2014b] to a cantilever beam with vibro-impacts and with a grounded cubic spring, respectively, and found that the strong nonlinearity gives rise to strongly nonlinear beat phenomena, caused by IR interactions of the nonlinear normal modes of the system. The procedure was further adapted by Kurt et al. [2017] to estimate the model nonlinearity and identify parameters using global dynamics as depicted in wavelet frequency-energy plots [Vakakis et al., 2008].

1.3 Literature Review of Reduced-order Modeling and Model Updating

Model updating concerns the correction of computational models to improve their prediction of experimental measurements by processing and integrating dynamic response data from test structures [Mottershead and Friswell, 1993]. The importance of model updating first emerged during the 1990s with the rise of accessible personal computing and the spread of the finite element (FE) method [Friswell and Mottershead, 1995]. Reviews of existing linear FE model updating techniques are given by Mottershead and Friswell [1993], Friswell and Mottershead [1995], Hemez and Doebling [2001] and Datta [2002]. Of the methods discussed in these works, sensitivity-based updating methods have seen large success and have been applied to damage assessment and structural health monitoring by Link et al. [1996], Brownjohn et al. [2001], Teughels et al. [2002], Zárate and Caicedo [2008], Mottershead et al. [2011]. However, these methods are limited by assumptions of linearity and stationarity and, as such, cannot be applied to nonlinear systems and data.

To handle nonlinearity, researchers have turned to data-driven modeling approaches wherein a mathematical model is extracted directly from experimental measurements without prior knowledge of the functional form of that model. Recent attempts to incorporate data-driven modeling methods into model updating include [Jaishi and Ren, 2005, Zimmerman and Lynch, 2006, Weng et al., 2009, Derkevorkian et al., 2014, Pokale and Gupta, 2014]. Kerschen and Golinval [2004] proposed using POD and auto-associative neural networks as a data-driven model updating procedure for nonlinear vibrating structures. Similarly,

Derkevorkian et al. [2014] developed a reduced-order modeling and model updating procedure that employed trained neural networks and relatively large-scale data sets to soil-foundation-superstructure interactions. Using a particle filtering algorithm and Bayesian principles, Pokale and Gupta [2014] were able to detect damage in vibrating beams by estimating changes in damping and flexural rigidity. Kalaycıoğlu and Özgüven [2014] demonstrated that the use of structural modification methods for data-driven modeling and updating can be applied so long as the modifications remain local; that is, the nonlinearities do not affect the global dynamics of the structure. Canbaloğlu and Özgüven [2016] proposed the pseudo-receptance difference method that focuses on extracting linear frequency-response functions from experimental measurements of nonlinear systems that do not exhibit linear behavior at low amplitude excitations. Wang et al. [2018a] proposed a nonlinear model updating procedure for localized nonlinearities by computing a semi-analytical output residual using response data measured under harmonic excitation.

Reduced-order models are often constructed to simplify the analysis of complicated, nonlinear structures. The reduction can occur in the simplification of the physics governing the system (e.g., modeling the transverse deflection of a thin beam as a spring with polynomial-type nonlinearity) or in a reduction of the number of DOFs in a computational model through condensation procedures. The former is normally employed to reduce the analysis necessary to study a system whereas the latter concerns the reduction of large FE models such that they are computationally tractable or such that the reduced coordinates correspond to sensing locations. Methods for the computation of ROMs have mostly been developed for linear models, but these methods tend to focus on applications in individual fields. For example, methods from structural dynamics and control [Craig, 2000, Bai, 2002, Gugercin and Antoulas, 2004, Klerk et al., 2008] and numerical mathematics [Freund, 2003]. Kerschen et al. [2006] present a review of reduced-order modeling methods for nonlinear systems.

Nataraj and Nelson [1989] applied the component mode synthesis method [Hurty, 1965, Benfield and Hruda, 1971] to investigate the periodic solutions of rotor dynamic systems with nonlinear supports and Kisa et al. [1998] used it to study the dynamics of cracked beams under impulsive excitations. Additionally, Apiwattanalunggarn et al. [2005] extended the component-mode synthesis method to nonlinear systems by employing nonlinear normal modes (NNMs) and applied the procedure to study the dynamics of systems with localized nonlinearities. Proper orthogonal decomposition is a popular method for the construction of ROMs for both linear and nonlinear systems Kerschen et al. [2005]. Ritto et al. [2011] applied POD to perform model reduction a VI rod, and Azeez and Vakakis [2001] used it to extract dominant coherent structures of a VI beam from experimental time-series data and used those structures to derive low-dimensional reduced-order models (ROMs) through a Galerkin-based reconstruction process.

Other approaches for creating ROMs of nonlinear dynamical systems include: Krysl et al. [2001] employed a Ritz-based approximation technique for computing ROMs of nonlinear FE models of dynamical structures. Segalman [2007] employed a Galerkin approximation procedure in which the conventional functions are augmented with a set of discontinuous ones to compute ROMs of nonlinear dynamical systems with local nonlinearities. Saito and Epureanu [2011] proposed the use of bi-linear normal modes, which use two sets of normal modes and special boundary conditions to capture the spatial structures that appear in the dynamics, and applied the procedure to localized piecewise-linear oscillators. Zucca and Epureanu [2014] extended the approach to structures with intermittent friction contacts. Using the harmonic balance method and the modal expansion technique, Mohammadali and Ahmadian [2014] formulated an exact condensation method that converts equations of motion (EOMs) into a set of nonlinear algebraic equations that are considerably small. [Gonçalves et al., 2016] combined the perturbation analysis with the Galerkin method to compute ROMs for the nonlinear dynamic analysis of shells and plates. Rutzmoser and Rixen [2017] developed a reduced-order modeling procedure based on snapshot generation and subspace projection techniques and applied it to the analysis of a nonlinear rubber boot. Jain and Tiso [2018] developed a similar procedure where the ROM is created by projecting the governing EOMs onto a modal basis and then lifting that basis and corresponding transient modal analysis to a quadratic manifold. Haller and Ponsioen [2017] proposed an exact model reduction technique through the means of a slow-fast decomposition where the dynamics is reduced to a slow manifold in terms of soft DOFs.

1.4 Proposed Methodology and Background Information

Before describing the method sequentially, we start by framing the class of systems to which it is applicable and the accompanying assumptions. In theory, the method applies to any system that can be naturally described by time-scales and a characteristic time-varying energy quantity, and possesses an underlying linear structure that permits the formulation of the Rayleigh quotient (RQ) operator. Thus, the method may be applicable to a broad class of systems in many fields; however, in this work, we focus on mechanical structures undergoing linear and nonlinear vibrations, where the modal characteristics of the structure (frequencies and periodic motions) and mechanical energy serve as the time-scales and characteristic time-varying quantity, respectively. Under this framework, we make the following assumptions:

1. At some energy value, the response of the system is linear, can be accurately measured using standard sensor equipment and signal processing methods, and the RQ operator can be formulated.

2. The sensors are well-placed and sufficiently capture the response of the system.

3. The number of sensors exceeds the number of modes of the underlying linear structure, in the frequency range of interest, by at least a factor of two.

4. The total number of DOFs in the structure far exceeds the number of modes of the underlying linear structure, in the frequency range of interest. Preferably, the structure is continuous leading to an infinity of DOFs, and the number of modes of interest is finite.

5. A FE model, or other suitable linear model, is available and sufficiently reproduces the response of the system to low energy inputs. This may be achieved using linear updating techniques [Friswell and Mottershead, 1995].

6. The boundary conditions are well-approximated in the linear model and accounted for in the RQ formulation.

7. Each sensor corresponds to a DOF in the linear model, but the total number of DOFs in the model can exceed the number of sensors.

8. The displacement response of the system, measured at varying excitation levels, is available a priori for each DOF included in the linear model. Displacement responses can be obtained from acceleration measurements through numerical integration, variational methods [Moreu and Spencer, 2015], or Kalman filtering [Kalman, 1960].

9. The analyst is familiar with the modal characteristics of the underlying linear system (especially since an updated linear modal is assumed to be available) and can determine the likely ratios at which IRs can occur.

10. The damping of the system is small enough such that the frequency change of an NNM is less than 10% within one-half cycle of the fundamental harmonic.

11. The nonlinearity is localized, and the response at the location of nonlinearity is measured by at least one sensor. The nonlinearity can be localized by using techniques such as that in [Wang et al., 2018b].

The first of these describes the fundamental assumption underlying the method, which allows the formulation of the RQ operator. No assumption is made concerning the energy levels where the linear response manifests. In this work, we use the underlying linear structure that manifests at low energy values to formulate the RQ operator. The third and fourth assumptions correspond to the basic requirements of sensor placement and signal processing for vibration measurements of mechanical structures. Assumptions five through seven indicate that this method requires an updated, linear model that accurately captures the

underlying linear dynamics of the system. The eighth assumption stems from the fact that the proposed method is data-driven and cannot function without existing data. The ninth assumption reflects the fact that the proposed method does not substitute for intimate knowledge of the modal characteristics of the underlying linear system. Rather, the proposed method relies on such knowledge. The tenth assumption places a restriction on the amount of damping that is permissible for the proposed method to be successful and is based on our experience thus far. The last assumption reflects the fact that the method is developed for and applied to systems with local nonlinearities, and that it has not been applied to structures with global nonlinearities.

With these assumptions in hand, we now describe the essential steps required for the method and conclude the section with a discussion of some optional steps. For given transient displacement response data, measured or simulated at sufficient locations, and a corresponding linear model, the proposed method is summarized by the following steps:

1. For n measurement coordinates, extract n proper orthogonal modes (POMs) using singular value decomposition from windowed segments of a single time record.

2. Using the POMs, compute the estimated RQs for the NNMs within the frequency range of interest, and plot these as functions of energy or time.

3. Characterize the nonlinearity and identify the modal interactions present in the measured response using the RQ frequency-energy plot (FEP).

4. Compute the characteristic displacement as defined for the system, and plot the RQ estimates as functions of that characteristic displacement to form the RQ frequency-displacement plot (FDP).

5. Based on the previous characterization, propose a model for the nonlinearity and derive the frequency-displacement relationship.

6. Identify the unknown parameters explicitly or using an optimization routine.

While the number of POMs extracted is equal to the number of DOFs in the linear model, only the POMs that correspond to the number of NNMs in the frequency range of interest are considered. We stress that the primary purpose of the method, at least in this work, is to serve as a data-driven method for detecting the presence of nonlinearity and the accompanying strongly nonlinear modal interactions, as well as a means for nonlinear system identification in the presence of strongly nonlinear attachments. As such, the method does not substitute for knowledge of the modal characteristics of the structure. Other techniques, such as wavelets and wavelet-bounded EMD [Moore et al., 2018b,c], are necessary to gain an in-depth understanding of the

modal interactions. However, the relative simplicity of the proposed method and its use of time-domain data and linear FE models, which are both readily available to practicing engineers, enable its use without incurring the steep costs associated with traditional nonlinear methods.

As such, it is beneficial to provide definitions of some of the strongly nonlinear dynamical phenomena that will be encountered throughout this dissertation are. First, the phenomenon of internal resonance describes a strongly nonlinear energy exchange between two structural modes resulting from coupling of the modes (even if they are broadly spaced in the frequency spectrum) and giving rise to nonlinear beat phenomena [Manevich and Manevitch, 2005]. Internal resonance arises when the frequencies of two modes are rationally related (allowing the modes to couple directly or through higher harmonics), which has no counterpart in linear theory. Indeed, in the linear beat phenomenon (which occurs when two modes are closely spaced in the frequency spectrum) the apparent energy exchanges occur between physical coordinates whereas the actual modes do not exchange energy at all. Mode conversion is an accompanying feature of IRs and is defined as the transformation of one mode into the other. Consequently, the resulting response can be either time-periodic (if the ratio of frequencies of the modes is rational) or quasi-periodic (if the ratio of the frequencies of the modes is irrational) [Kerschen et al., 2008]. Moreover, IRs have been shown to result in energy localization as in targeted energy transfer applications [Vakakis et al., 1996, 2008], to significantly alter stress distributions leading to component failure [Ehrhardt et al., 2017], and to trigger bifurcations in the dynamics that change the stability of NNMs [Attar et al., 2017].

Second, the concept of resonance capture is defined, in this dissertation at least, as the phenomenon wherein the frequency of a local strongly nonlinear attachment tunes and locks onto the frequency of a mode or modes of the base structure (comparable definitions can be found in [Arnold, 1988, Quinn et al., 1995, Vakakis et al., 2004, Quinn, 2006, Kerschen et al., 2007]).This locking (also known as phase locking) results in a direct (and irreversible in the presence of damping) transfer of energy from the base mode into the local nonlinear attachment. These resonance captures arise from the ability of the attachment to vary its frequency based on the energy present in the system. In the presence of damping and impulsive forcing, the resonance captures evolve along a resonance manifold [Quinn, 2006] for a short period of time and are termed transient resonance captures (TRCs). For harmonic forcing or for systems without damping the resonance captures remain on these manifolds for all time and are termed sustained resonance captures (SRCs).

1.5 Organization

The organization of this dissertation is as follows: Chapter 2 introduces the basic elements of the data-driven nonlinear system identification and model updating methodology proposed in this dissertation. As such, a sufficient understanding of each of these tools and concepts is vital for their synergistic implementation in the proposed methodology.

Chapter 3 introduces the wavelet-bounded empirical mode decomposition (WBEMD) method for nonlinear time-series analysis and presents three applications. First, the method is applied to a two component signal to study the effects of parameters and to compare WBEMD with other EMD-based methods. The second application concerns the study of the dynamics of a cantilever beam with strong stiffness nonlinearity and the accompanying IRs, frequency transitions and periodic solutions. The final application explores the role that higher harmonics play in TRCs that occur in the dynamics of an oscillator with a vibro-impact attachment.

Chapter 4 examines the use of the proposed methodology for detecting strongly nonlinear modal interactions directly from measured time-series data and considers two applications. First, a theoretical study is performed using a cantilever beam with a strong grounding stiffness nonlinearity. Following the theoretical study, an experimental study of a comparable cantilever beam is examined and used to verify the results of the theoretical study. Wavelet-bounded empirical mode decomposition is used extensively in both cases to examine the IRs that occur in the response of each system.

Chapter 5 presents the proposed data-driven nonlinear system identification and model updating methodology and considers four applications. First, the methodology is applied to a computational study of a cantilevered airplane wing with a strongly nonlinear local attachment connected to the wing tip. The second application concerns the experimental verification of the computational study and demonstrates the applicability of the methodology to real data (that incorporates noise and uncertainty).

Chapter 6 investigates the global effects induced by lightweight, local nonlinear attachments on the dynamics of a model airplane. First, a computational study of the response of a model airplane with strongly nonlinear stores is presented, and the proposed methodology is applied to examine the changes to the global dynamics created by the stores. Finally, an experimental study is performed on a comparable model airplane with comparable nonlinear stores, and the measured response is used to investigate the global effects.

Chapter 2

Elements of Proposed Data-driven NSI and Model Updating Methodology

The proposed methodology synergistically combines three established theoretical concepts with five well-known computational methods. The theoretical concepts are, namely, (i) the nonlinear normal mode theory and their representation in frequency-energy plots, which provide the means to study the frequency-energy dependence exhibited by strongly nonlinear dynamical systems as well as the resulting bifurcations and modal interactions; (ii) the averaging theorem and resonant dynamics, which provide the theoretical foundation for the relation between rationally related modal frequencies and nonlinear resonance; and (iii) slow-flow dynamics, which provides the means of analytically and computationally verifying the existence of and classifying nonlinear resonances (including IRs and TRCs) that are present in the measured time-series. The computational methods are, namely, (i) the proper orthogonal decomposition, which is a system identification and order-reduction methodology that provides an orthogonal basis of modes – the proper orthogonal modes (POMs) – which coincide with the principal axes of inertia of the "cloud of measured data in space and time and, hence, are optimal in that sense; (ii) the Rayleigh quotient (RQ) which provides a computational estimate of the fundamental natural frequency of a linear vibrating system based on an assumed trial function for the fundamental normal mode; (iii) Guyan reduction which is a static condensation method that can be applied to reduce the number of DOFs in a discretized model; (iv) the wavelet and Hilbert transforms, which provide time-frequency and analytic representations of a real-valued signal, respectively; and (v) the empirical mode decomposition (EMD) which is a computational method for decomposing oscillatory signals into a finite basis of nearly orthogonal, monochromatic intrinsic mode functions (IMFs), each possessing a characteristic time scale of the co-existing slow and fast processes occurring in the measured dynamics. In the following exposition, each of these methods and concepts is described in detail.

2.1 Nonlinear Normal Modes (NNMs) and Frequency-energy Plots (FEPs)

In the study of linear vibrations, no other method or theory is as celebrated as the theory of linear normal modes. Linear normal modes (LNMs) provide a unique physical interpretation of the dynamics governing a linear system that is both easy to understand and mathematically useful. Specifically, LNMs form an orthogonal basis that can be used to decouple the equations of motion, such that a set of independent equations, each governing a single LNM, are obtained. This linear independence gives rise to several important properties:

1. Invariance: energy induced in one LNM cannot be shared or exchanged with any other LNM. Consequently, if only one LNM is excited, then all other LNMs remain quiescent for all time.

2. Modal superposition: free and forced responses can be expressed as linear combinations of individual LNM motions.

3. Uniqueness: for given forcing and initial conditions, each LNM admits a single solution that is unique and exists. Furthermore, the number of LNMs that govern the motion of the system is equal to the number of degrees-of-freedom (DOF) in that system.

Despite the usefulness and simplicity of LNMs, linearity is rarely encountered in real-life systems and applications. Indeed, linearity is considered to be the exception whereas nonlinearity is the norm. Moreover, any attempt to apply linear analysis to a nonlinear system results, at best, in a suboptimal design. At worst, important dynamical phenomena is missed during the design phase, which then manifests during operation and can lead to critical system failure. Such failures can result in significant costs and may lead to injuries or fatalities. Thus, there is a need for a framework that builds upon the theory of LNMs, but is suitable for the study of nonlinear systems.

In this context, the theory of nonlinear normal modes (NNMs) provides a strong theoretical and mathematical foundation for analyzing a wide array of nonlinear dynamical phenomena, while remaining conceptually similar to LNMs. The simplest definition, proposed by Rosenberg [1960, 1962, 1966], of a NNM is a vibration in unison of the system (i.e., synchronous oscillations). For the purposes of this work, this definition is a bit too restrictive as will be seen in the coming discussion. Instead, a NNM is defined to be a time-periodic (not necessarily synchronous) oscillation of a nonlinear dynamical system [Vakakis et al., 2008]. Note that this definition does not require the physical response of the system to be time-periodic, only that each NNM governing that response is time-periodic. Thus, this definition persists even during IRs

where the resulting motion may be either time-periodic or quasi-periodic (cf. Section 1.4). Although NNMs are conceptually similar to LNMs, they possess fundamental properties that have no linear counterparts. Some of these properties are:

1. Frequency-energy dependence: NNMs intrinsically depend on the mechanical energy present in the system; this dependence directly prevents the separation of time and space that is typically employed in linear analysis. The associated periodic solutions (i.e., the nonlinear counterparts of linear mode shapes) also depend on energy [Vakakis et al., 2008].

2. Modal interactions (internal resonance): when certain resonance conditions are met (cf. Section 2.7), NNMs become coupled and engage in nonlinear energy exchanges leading to nonlinear beat phenomena [Kurt et al., 2014b]. When weak damping is present, energy is irreversibly transferred from the lower to higher NNMs. Additionally, during resonance, mode conversion occurs where the periodic solution of the lower NNM converts to that of the higher NNM.

3. Mode bifurcations and stability: bifurcations in the dynamics can result in changes to the stability of the NNM. As such, a stable NNM can suddenly become unstable resulting in the creation of additional stable NNMs. This leads to the existence of more NNMs than there are DOFs in the system and also to the response of a nonlinear system being non-unique [Kerschen et al., 2009].

The proper graphical depiction of NNMs is essential for using them to assess and understand the dynamics of a nonlinear system. To meet this requirement, this dissertation employs the frequency-energy plot (FEP) [Vakakis et al., 2008], where the frequency of each NNM is plotted as a function of the total system energy. A useful feature of the FEP is that a system with weak damping can be studied using the FEP of the corresponding undamped and unforced (Hamiltonian) system because weak damping is a parasitic effect and does not significantly alter the dynamics [Vakakis et al., 2008]. However, the presence of weak damping introduces extreme dependence on initial and forcing conditions into the dynamics, such that small variations in initial or forcing conditions can lead to significantly different transitions in the dynamics (i.e., hopping between branches of NNMs). An FEP is constructed by computing the periodic solutions (or orbits) of the Hamiltonian system for varying initial conditions and can only be done analytically for systems with few DOFs [Kurt et al., 2014a]. However, advanced computational tools that can handle systems with many DOFs have been developed including methods based on continuation (specifically, the algorithm termed NNMcont developed by Peeters et al. [2009]) and harmonic balance methods formed by Detroux et al. [2014].

As a demonstration of the power of as FEP, consider the 2-DOF system depicted in Fig. 2.1, which has

the equations of motion

$$\begin{aligned} m_1\ddot{x}_1 + k_1 x_1 + k_2(x_1 - x_2) = 0, \\ m_2\ddot{x}_2 + k_3 x_2 + k_2(x_2 - x_1) + k_{nl} x_2^3 = 0, \end{aligned} \tag{2.1}$$

with system parameters $m_1 = m_2 = 1$ kg, $k_1 = 1$ N/m, $k_2 = 1$ N/m, $k_3 = 2$ N/m, and $k_{nl} = 1$ N/m^3. The FEP corresponding to this system is depicted in Fig. 2.2, which was computed using NNMcont [Peeters et al., 2009]. Each NNM is represented by a single curve in the FEP, which are called the backbone branches. The branches are labeled S11± since they correspond to in-phase (+ sign) and out-of-phase (- sign) synchronous oscillations of the two masses. The Smn± notation denotes a time-periodic motion of the system given in Eq. 2.1 with n being the number of half-waves in x_1, m being the number of half-waves in x_2, both in a half-period of the response, and (±) denotes the in-phase or out-of-phase character of the oscillations. Note that, for low energies, the frequencies of the in-phase and out-of-phase NNMs are almost constant and correspond to the natural frequencies of the underlying linear system.

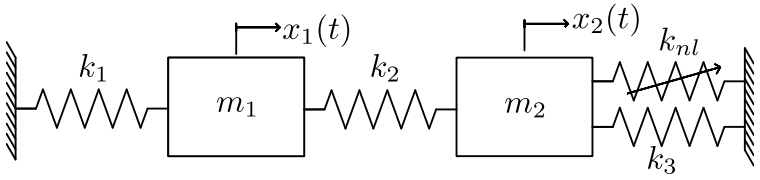

Figure 2.1: 2-DOF system consisting of two linear oscillators with the second oscillator nonlinearly coupled to ground by a nonlinear cubic spring.

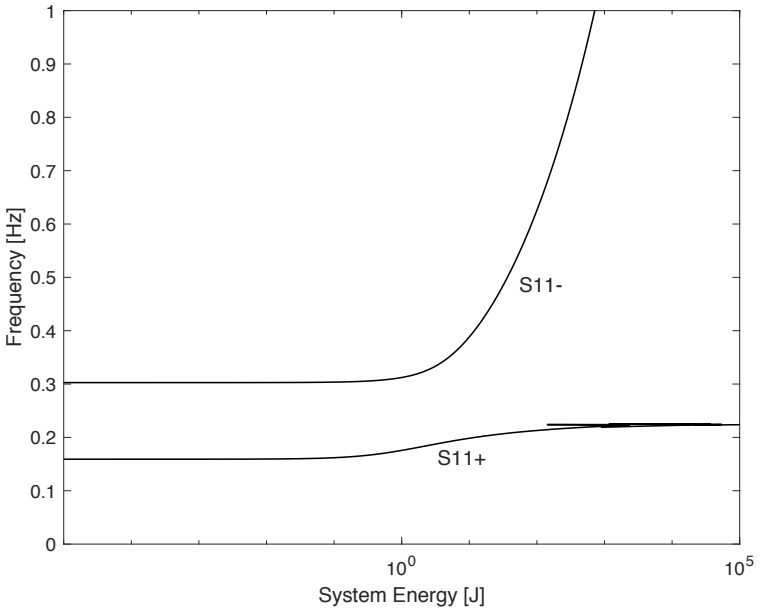

Figure 2.2: Frequency-energy plot of the system depicted in Fig. 2.1.

2.2 Proper Orthogonal Decomposition

The proper orthogonal decomposition (POD) [Kosambi, 1943, Karhunen, 1947, Lévy and Loéve, 1948, Pugachev, 1953, Obukhov, 1954, Holmes et al., 1996, Feeny and Kappagantu, 1998, Kerschen et al., 2005], also known as Karhunen-Loéve decomposition or principle component analysis, is a statistical procedure that reduces a large set of interdependent variables to a smaller set of uncorrelated variables by finding an orthonormal basis that represents the data in a least-squares sense. One major benefit of POD is that it is fully data-driven; that is, it is entirely independent of the process that generates the data and, as such, can be applied to data sets where insufficient a priori knowledge prevents the selection of an appropriate basis prior to decomposition.

In this work, we consider the formulation of POD described by Kerschen et al. [2005], which in turn is based on Chapter 3 of [Holmes et al., 1996]. Consider a random field $\theta(x,t)$ on a domain D. This random field can be decomposed into a time-varying component, $\Theta(x,t)$, and a mean, $\mu(x)$, such that

$$\theta(x,t) = \mu(x) + \Theta(x,t). \tag{2.2}$$

At time t_k, the system admits a snapshot $\Theta^k(x) = \Theta(x,t_k)$. For a given ensemble of snapshots, the objective of POD is the extraction of a basis function, $\psi(x)$, that maximizes the ensemble average of the inner product between $\Theta^k(x)$ and $\psi(x)$, such that

$$\text{Maximize} \left\langle \left| \int_D \Theta^k(x)\psi(x)\,\mathrm{d}x \right|^2 \right\rangle \text{with} \|\psi(x)\| = 1, \tag{2.3}$$

where $\langle\cdot\rangle$ denotes the averaging operation, $\|\cdot\|$ designates the L^2-norm, $|\cdot|$ refers to the modulus, and the constraint, $\|\psi(x)\| = 1$, forces the basis to be unique and guarantees that it contains the greatest energy content among all possible basis functions. The added constraint can be taken into account by the use of a Lagrange multiplier to form the functional

$$J\left[\psi(x)\right] = \left\langle \left| \int_D \Theta^k(x)\psi(x)\,\mathrm{d}x \right|^2 \right\rangle - \lambda\left(\|\psi(x)\| - 1\right), \tag{2.4}$$

which is maximized when its derivative is set to zero. Holmes et al. [1996] showed that this condition reduces to the integral eigenvalue problem

$$\int_D \left\langle \Theta^k(x)\Theta^k(x')\right\rangle \psi(x')\,\mathrm{d}x' = \lambda\psi(x), \tag{2.5}$$

where $\left\langle \Theta^k(x)\Theta^k(x')\right\rangle$ is the averaged auto-correlation function.

Thus, the solution to 2.3 is a infinite set of orthogonal eigenfunctions, $\psi_i(x)$, called the proper orthogonal modes (POMs) with corresponding eigenvalues $\lambda_i \geq 0$, which are termed the proper orthogonal values (POVs). The POVs are representative of the relative energy content contained in the corresponding POMs, such that the energy ratio, ε_i, contained in a certain POM, $\psi_i(x)$, as compared to the total energy in the system is

$$\varepsilon_i = \frac{\lambda_i}{\sum_{j=1}^{\infty} \lambda_j}. \tag{2.6}$$

Furthermore, the POMs may be used as a basis for the decomposition of the field $\Theta(x,t)$

$$\Theta(x,t) = \sum_{i=1}^{\infty} a_i(t)\psi_i(x), \tag{2.7}$$

where the coefficients $a_i(t)$ are uncorrelated, such that

$$\langle a_i(t), a_j(t)\rangle = \lambda_i \delta_{ij}, \tag{2.8}$$

and δ_{ij} is the Kronecker delta defined by

$$\delta_{ij} = \begin{cases} 1 & i = j, \\ 0 & i \neq j. \end{cases} \tag{2.9}$$

The coefficients, $a_i(t)$, are equivalent to the inner product of $\Theta(x,t)$ and $\psi_i(x)$; that is,

$$a_i(t) = \int_D \Theta(x,t)\psi_i(x)\,\mathrm{d}x. \tag{2.10}$$

In practice, data is often discretized in both space and time, and can be arranged into a response matrix

$$\mathbf{X} = [\mathbf{x}_1, \ldots, \mathbf{x}_n] = \begin{bmatrix} x_{11} & \ldots & x_{1n} \\ \vdots & \ddots & \vdots \\ x_{m1} & \ldots & x_{mn} \end{bmatrix}. \tag{2.11}$$

Since the data is likely non-zero mean, the averaged auto-correlation function cannot be used in the computation of the POMs. Instead, it is replaced by the covariance matrix $\Sigma = E\left[(\mathbf{x}-\mu)(\mathbf{x}-\mu)^{\intercal}\right]$, where $E[\cdot]$ denotes the expected value. The set of snapshots is assumed to be large enough that the sample covariance

matrix, Σ_s, can be used to estimate the ensemble covariance matrix, but small enough that the process remains stationary within the time window defined by the snapshots. The sample covariance matrix is defined as

$$\Sigma_s = \frac{1}{n}\begin{bmatrix} \sum_{j=1}^{n}\left(x_{1j} - \frac{1}{n}\sum_{k-1}^{n} x_{1k}\right)^2 & \cdots & \sum_{j=1}^{n}\left(x_{1j} - \frac{1}{n}\sum_{k-1}^{n} x_{1k}\right)\left(x_{mj} - \frac{1}{n}\sum_{k-1}^{n} x_{mk}\right) \\ \vdots & \ddots & \vdots \\ \sum_{j=1}^{n}\left(x_{mj} - \frac{1}{n}\sum_{k-1}^{n} x_{1k}\right)\left(x_{mj} - \frac{1}{n}\sum_{k-1}^{n} x_{mk}\right) & \cdots & \sum_{j=1}^{n}\left(x_{1j} - \frac{1}{n}\sum_{k-1}^{n} x_{1k}\right)^2 \end{bmatrix} \tag{2.12}$$

The POMs and POVs are, therefore, computed as the eigensolution of the sample covariance matrix. Note that, if the number of measurement points is greater than the number of snapshots (i.e., $n > m$), then the method of snapshots [Sirovich, 1987] should be used to compute the sample covariance matrix. In this work, all cases studied will involve data sets where the number of snapshots is much greater than the number of measurement points and, thus, the method of snapshots will not be presented. The reader is referred to [Fakir, 1998] for further information regarding the use of the method of snapshots when applied to dynamical systems.

For discrete systems, the singular value decomposition (SVD) is equivalent to POD [Kerschen et al., 2005] and, thus, SVD can be used to compute the POMs and POVs directly from the response matrix $\mathbf{X}$. By applying SVD, the response matrix $\mathbf{X}$ of dimensions $m \times n$ is factored as

$$\mathbf{X} = \mathbf{U}\mathbf{S}\mathbf{V}^{\intercal}, \tag{2.13}$$

where $\mathbf{U}$ is an $m \times m$ orthonormal matrix containing the left singular vectors, $\mathbf{S}$ is an $m \times n$ pseudo-diagonal and positive semi-definite matrix containing the singular values, and $\mathbf{V}$ is an $n \times n$ orthonormal matrix composed of the right singular vectors. The left singular vectors, which are equivalent to the POMs, and the POVs are computed as the eigenvectors and eigenvalues of the matrix $\mathbf{X}\mathbf{X}^{\intercal}$ respectively. The singular values are equal to the POVs squared and divided by the number of samples m. The right singular vectors, $\mathbf{V}$, contain the time modulation of the corresponding POMs, normalized by the singular values, and are computed as the eigenvectors of the matrix $\mathbf{X}^T\mathbf{X}$. The use of SVD for computation is especially beneficial as its properties ensure that the oriented energy measured in the direction of the kth singular vector is equal to the kth singular value squared. Thus, the POMs are optimal concerning energy content in a least-squares sense and capture more energy per mode than any other set of basis functions.

The main drawback of POD is its dependence on the specific measured response of the dynamical

system, such that if the initial or forcing conditions change so do the results of POD. It follows that if important dynamics of a system are not captured within the time window considered, the POMs will also fail to include these effects. The POMs, which are sensitive to excitations and initial conditions, represent spatial substructures that correspond to the highest variance in the signals, but they are not guaranteed to correspond physically to any dynamically meaningful behavior. Thus, it is not possible to provide a general physical interpretation of the computed orthogonal basis of POMs. However, when applied to a linear dynamical system, the obtained orthonormal basis has been proven to be optimal, such that the time series can be accurately reconstructed using a minimum number of mutually orthogonal modes; moreover, in the limit of infinite measurement points the POMs for linear, discrete, classically damped systems with mass matrices that are proportional to the identity matrix converge to the linear normal modes of vibration [Feeny and Kappagantu, 1998]. Further discussion, including how a POM can be considered the best linear representation of a nonlinear normal mode, can be found in [Kerschen et al., 2005].

2.3 Rayleigh Quotient

The Rayleigh quotient (RQ) provides an estimate of the natural frequency of the fundamental mode of vibration of a linear system using a suitable trial vector or function. The RQ can be used to estimate the frequency of higher modes as long as the trial vector or function is mass-orthogonal to the trial vectors or functions used to estimate the lower modes. The finite element (FE) method will be used extensively throughout this dissertation to discretize continuous systems and, as such, only the discrete formulation of the RQ, based on the discussion in [Meirovitch, 2010], is presented here. The reader is referred to Section 5.8 of [Meirovitch, 1986]. Consider the discretized equations of motion of an undamped, unforced n-DOF system written in matrix form

$$\mathbf{M}\ddot{\mathbf{x}} + \mathbf{K}\mathbf{x} = \mathbf{0}, \tag{2.14}$$

where $\mathbf{M}$ and $\mathbf{K}$ are real symmetric mass and stiffness matrices, respectively. The accompanying eigenvalue problem is

$$\mathbf{K}\mathbf{u}_r = \omega_r^2 \mathbf{M}\mathbf{u}_r, r = 1, \ldots, n. \tag{2.15}$$

Pre-multiplying both sides by $\mathbf{u}_r^\intercal$ and dividing by $\mathbf{u}_r^\intercal \mathbf{M}\mathbf{u}_r$ results in

$$\omega_r^2 = \frac{\mathbf{u}_r^\intercal K \mathbf{u}_r}{\mathbf{u}_r^\intercal M \mathbf{u}_r}, r = 1, \ldots, n, \tag{2.16}$$

which enables the computation of the natural frequencies ω_r provided that the accompanying modal vectors $\mathbf{u}_r$ are known a priori ($r = 1, \ldots, n$). In practice, where the precise modal vectors are seldom known (if they even exist to begin with), the RQ can be used to estimate a natural frequency provided that a suitable trial vector, v, is selected. In this case, the RQ becomes a

$$R(\mathbf{v}) = \frac{\mathbf{v}^\intercal \mathbf{K} \mathbf{v}}{\mathbf{v}^\intercal \mathbf{M} \mathbf{v}}. \tag{2.17}$$

The success of the RQ lends itself to the fact that it is relatively insensitive to the trial vector and has a minimum value equal to the fundamental eigenvalue of the linear mass and stiffness matrices. In this dissertation, the POMs computed from the response of translational DOFs are used as the trial vectors. The POMs, which are mutually orthogonal, but not mass-orthogonal are used independently to estimate the frequency of their respective modes; the frequencies are computed as

$$f_i = \frac{1}{2\pi} \sqrt{R(\mathbf{v}_i)}. \tag{2.18}$$

As previously mentioned, the POMs converge to the normal modes of classically damped, linear systems with identity mass matrices or mass matrices that are proportional to the identity matrix. In this case, the POMs are mass-orthogonal and can be used to compute the exact natural frequencies. For systems with mass matrices that are not proportional to the identity matrix, the POMs are not mass-orthogonal and no rigorous justification for their use as trial vectors can be given. In this dissertation, the use of the FE method results in mass matrices that are sparse, but not diagonal and certainly not proportional to the identity matrix. Furthermore, Guyan reduction [Guyan, 1965] (cf. Section 2.4) is applied to condense out rotational DOFs in all systems studied, and the resulting mass matrices are dense with few, if any, zero entries. Consequently, the procedure is ad hoc, and there is no guarantee that the estimated frequencies will correspond to the natural frequencies of the nonlinear systems under study. Nevertheless, it will be shown that the RQ-based procedure will lead to physically meaningful results, indicating that the computed POMs represent linear approximations of the nonlinear periodic solutions governing the systems considered in this dissertation.

2.4 Guyan Reduction

To calculate the RQ using the POMs, the mass and stiffness matrices of the considered systems were first reduced using Guyan reduction [Guyan, 1965] such that the rotational DOFs of the systems were condensed

out from further computational consideration. The objective of the reduction was to reduce the model to a set of observable DOFs, and the use of Guyan reduction is permissible for the systems considered because the effects of the rotary inertia terms are small. In general, a component mode synthesis method, such as Craig-Bampton reduction [Bampton and Craig, 1968], should be used for systems that possess rotary inertia terms that have large effects on the response. As shown later, the resulting frequency estimates computed using the reduced matrices and POMs provide valuable qualitative and quantitative information, as well as significant physical insight into the strongly nonlinear dynamics of the systems considered in this dissertation. Guyan reduction begins with considering the static system of the form

$$\begin{bmatrix} \mathbf{K}_{mm} & \mathbf{K}_{ms} \\ \mathbf{K}_{sm} & \mathbf{K}_{ss} \end{bmatrix} \begin{Bmatrix} \mathbf{x}_m \\ \mathbf{x}_s \end{Bmatrix} = \begin{Bmatrix} \mathbf{F}_m \\ \mathbf{0} \end{Bmatrix}, \tag{2.19}$$

where the subscripts m and s refer to the master and slave DOFs, respectively. Here the slave DOFs are condensed out by the reduction. Note that in Eq. 2.19 there are no forces applied to the slave DOFs (i.e., DOFs with forces applied cannot be condensed out using Guyan reduction). The slave DOFs are related to the master DOFs through

$$\mathbf{x}_s = -\mathbf{K}_{ss}^{-1}\mathbf{K}_{sm}\mathbf{x}_m. \tag{2.20}$$

A coordinate transformation is then performed such that

$$\begin{Bmatrix} \mathbf{x}_m \\ \mathbf{x}_s \end{Bmatrix} = \begin{bmatrix} \mathbf{I} \\ -\mathbf{K}_{ss}^{-1}\mathbf{K}_{sm} \end{bmatrix} \mathbf{x}_m = \mathbf{T}_m\mathbf{x}_m, \tag{2.21}$$

where $\mathbf{T}$ is the transformation matrix. The mass, damping and stiffness matrices are then reduced through

$$\begin{aligned} \mathbf{M}_m &= \mathbf{T}_m^{\intercal}\mathbf{M}\mathbf{T}_m, \\ \mathbf{D}_m &= \mathbf{T}_m^{\intercal}\mathbf{D}\mathbf{T}_m, \\ \mathbf{K}_m &= \mathbf{T}_m^{\intercal}\mathbf{K}\mathbf{T}_m, \end{aligned} \tag{2.22}$$

which lead to the reduced equations of motion

$$\mathbf{M}_m\ddot{\mathbf{x}}_m + \mathbf{D}_m\dot{\mathbf{x}}_m + \mathbf{K}_m\mathbf{x}_m = \mathbf{F}_m. \tag{2.23}$$

2.5 Wavelet and Hilbert Transforms

The first integral transform that will be used extensively in this work is the wavelet transform (WT), which provides a time-frequency representation of a signal and is exceedingly useful for studying signals that can be characterized as aperiodic, noisy, intermittent, transient, or nonstationary. For such signals, the WT can reveal physically important information that is lost when the same signal is studied using Fourier analysis, including fast Fourier transforms (FFTs). Mathematically, the WT is the convolution of a wavelet function and the signal, and is defined for a continuous signal as

$$Z(\omega, t) = w(\omega) \int_{-\infty}^{\infty} z(\tau) \psi^* \left(\frac{\tau - t}{a} \right) \mathrm{d}\tau, \tag{2.24}$$

where $w(\omega)$ is a weighting function and $\cdot^*$ denotes the complex conjugate. Typically, the weighting function is chosen to be $w(\omega) = 1/\sqrt{\omega}$, in which case the wavelet function is described as normalized and is written more compactly as

$$\psi_{\omega,t}(\tau) = \frac{1}{\sqrt{\omega}} \psi \left(\frac{\tau - t}{\omega} \right). \tag{2.25}$$

Thus, the continuous WT (CWT) is defined to be

$$Z(\omega, t) = \mathrm{WT} \left\{ z(\tau) \right\} = \int_{-\infty}^{\infty} z(\tau) \psi^*_{\omega,t}(\tau) \, \mathrm{d}\tau, \tag{2.26}$$

In this work, the Morlet wavelet [Grossmann and Morlet, 1984] will be used exclusively as the wavelet function and is defined as

$$\psi(\tau) = \frac{1}{\pi^{1/4}} \exp \left[j \omega_0 \tau \right] \exp \left[-\frac{\tau^2}{2} \right], \tag{2.27}$$

and in translated and dilated form is

$$\psi_{\omega,t}(\tau) = \frac{1}{\pi^{1/4}} \exp \left[j \omega_0 \left(\frac{\tau - t}{\omega} \right) \right] \exp \left[-\frac{1}{2} \left(\frac{\tau - t}{\omega} \right)^2 \right], \tag{2.28}$$

where ω_0 is the central frequency, and $j = \sqrt{-1}$. An example of the Morlet wavelet with $\omega_0 = 2\pi$ is presented in Fig. 2.3.

Due to the convolution theorem, the CWT can also be expressed in the form of an inverse Fourier transform [Addison, 2002]

$$Z(\omega, t) = \int_{-\infty}^{\infty} \hat{z}(\lambda) \hat{\psi}^*_{\omega,t}(\omega\lambda) e^{j\lambda t} \, \mathrm{d}\lambda, \tag{2.29}$$

where $\hat{z}(\lambda)$ and $\hat{\psi}_{\omega,t}(\lambda)$ are the Fourier transforms of the signal and wavelet function. The benefit of this

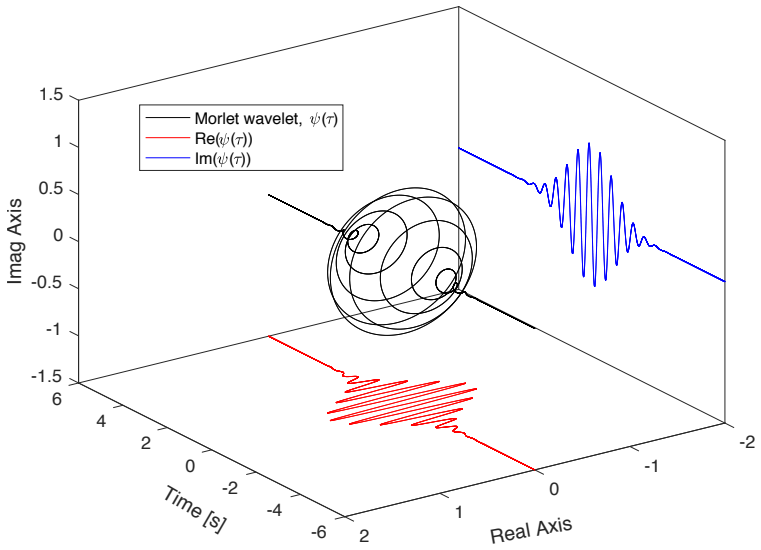

Figure 2.3: The Morlet wavelet with projections onto the real and imaginary planes for $\omega_0 = 2\pi$.

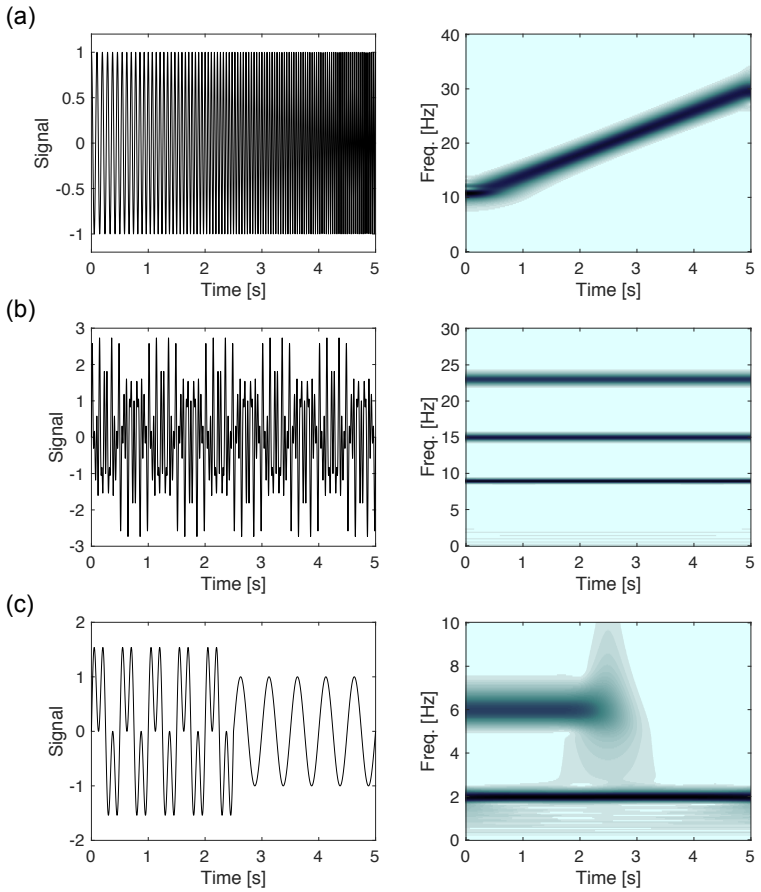

Figure 2.4: Time series and wavelet spectrum of (a) a chirp signal, (b) a signal composed of three sinusoids and (c) a signal composed of two sinusoids for the first half and only one sinusoid for the second half.

representation comes in the practical implementation of the CWT. Indeed, in practice data is often discrete, and the CWT needs to be discretized before it can be applied to such data. Note that the discretized CWT is fundamentally different than the discrete wavelet transform (DWT), and the reader is referred to the discussion in Chapter 3 of [Addison, 2002] for more information regarding the DWT. The benefit of the above representation comes from the fact that $\hat{\psi}_{\omega,t}(\lambda)$ is often known analytically (indeed, it is for the Morlet wavelet), $\hat{z}(\lambda)$ can be computed using the FFT algorithm, and the CWT can then be computed using the inverse FFT of the product above. This procedure is used throughout this work and some examples of its application are presented in Fig. 2.4.

The second integral transform that is essential to this work is the Hilbert transform (HT), which is named after famed mathematician David Hilbert, who introduced it to solve a special case of integral equations in the area of mathematical physics [Korpel, 1982]. The HT of the signal $z(t)$ is defined as

$$\mathrm{HT}\left\{z(t)\right\} = \frac{1}{\pi}\mathrm{p.v.}\int_{-\infty}^{\infty}\frac{z(\tau)}{t-\tau}\,\mathrm{d}\tau, \tag{2.30}$$

where p.v. represents the Cauchy principal value. Physically, the HT acts as a linear filter that shifts the phase of the signal by $\pi/2$ without affecting its amplitude. Thus, if $z(t)$ is real-valued, then so is $\mathrm{HT}\left\{z(t)\right\}$. The double application of the HT returns the original signal with opposite sign (equivalent to shifting the phase by π), and applying the HT four times returns the original signal.

The main benefit of the HT is that it can be used to construct signals that can be decomposed into a polar representation. Specifically, a complex signal is called analytic if its imaginary part is the Hilbert transform of its real part. The analytic signal, $z^{\dagger}(t)$ is defined as

$$z^{\dagger}(t) = z(t) + j\mathrm{HT}\left\{z(t)\right\} \tag{2.31}$$

. The major benefit of constructing an analytic signal is that it can be expressed in polar coordinates such that

$$z^{\dagger}(t) = A(t)e^{j\theta(t)}, \tag{2.32}$$

where $A(t) \equiv \left|z^{\dagger}(t)\right|$ and $\theta(t) \equiv \arg\left[z^{\dagger}(t)\right]$. Additionally, the instantaneous frequency of the signal can be computed as

$$\omega(t) = \frac{\mathrm{d}}{\mathrm{d}t}\theta(t). \tag{2.33}$$

In practice, the HT must be applied to discrete signals and the discrete HT may be used; however, most application utilize FFTs and IFFTs for the computation of the HT. The use of FFTs and IFFTs introduces

high-frequency oscillations into both the phase and amplitude, and low-pass filtering must be applied to the output to remove these. An example of the HT applied to a real valued function to create an analytic function is presented in Fig 2.5 along with the polar decomposition.

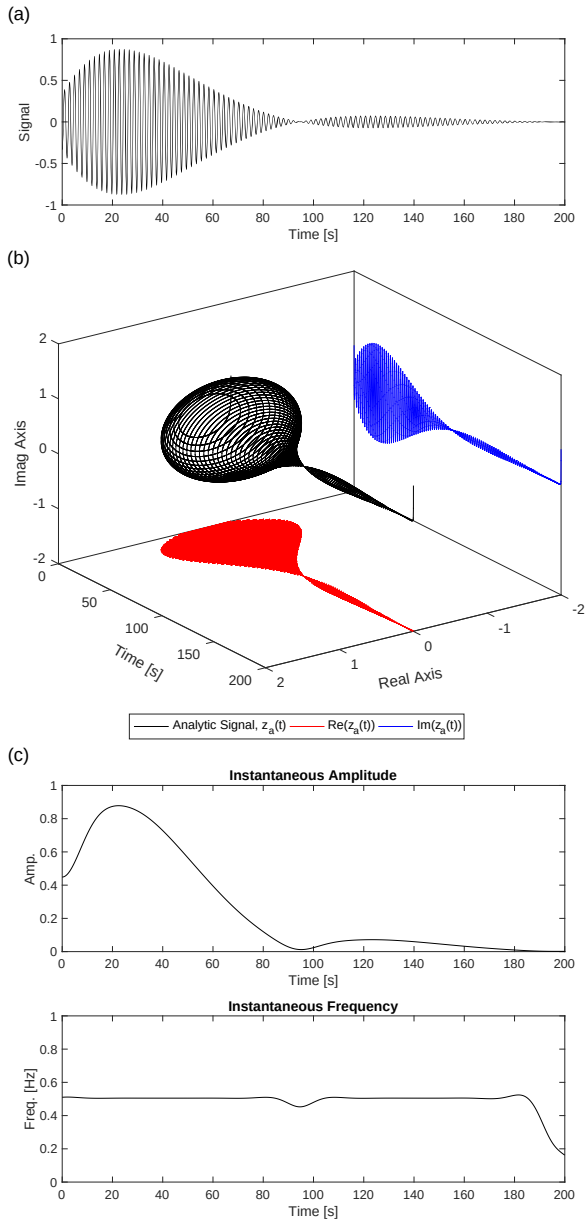

Figure 2.5: (a) Composite signal. (b) Analytic signal created using Eq. 2.31 with projections onto real and imaginary planes. (c) Instantaneous amplitude and frequency of the analytic signal presented in (b).

2.6 Empirical Mode Decomposition (EMD) and Ensemble EMD (EEMD)

The empirical mode decomposition (EMD) proposed by Huang et al. [1998] is a powerful method for decomposing oscillatory signals into a finite basis of nearly orthogonal, monochromatic intrinsic mode functions (IMFs) each possessing a characteristic time scale. EMD is highly suitable for application to nonlinear and nonstationary processes where linear decomposition methods fail to capture the complex nonlinear dynamics. EMD decomposes an oscillatory signal, $u(t)$, with a sifting algorithm consisting of the following steps:

1. Determine all extrema of $u(t)$.
2. Compute two envelopes, $e_{\min}(t)$ and $e_{\max}(t)$, by spline interpolating the minima and maxima of the signal.
3. Compute the average curve between the two envelopes, $R(t) = \left(e_{\max}(t) + e_{\min}(t)\right)/2$.
4. Extract the remainder signal, $c(t) = u(t) - R(t)$.
5. Apply steps 1 through 4 iteratively to $c(t)$ until the maximum value of $R(t)$ is less than a prescribed tolerance, τ.

Upon satisfying 5, $c(t) \equiv c_1(t)$ is regarded as the first IMF and possesses the highest characteristic frequency. A second IMF can be extracted by applying the algorithm to the difference $z_1(t) = u(t) - c_1(t)$. By applying the algorithm recursively, $u(t)$ can be sequentially decomposed into nearly orthogonal IMFs that satisfy

$$u(t) = \sum_{i=1}^{N} c_i(t) + R_{N+1}(t), \max\left(R_{N+1}(t)\right) < \tau. \tag{2.34}$$

The objective of EMD, from an applications viewpoint, is to extract IMFs that are physically and mathematically representative of the original time series. Although the mathematical and physical significance of IMFs have been studied in detail [Sharpley and Vatchev, 2005, Vatchev and Sharpley, 2008, Lee et al., 2009b], applying EMD often results in more IMFs than the number of characteristic time scales actually present (i.e., the method yields spurious, non-physically meaningful IMFs), and care must be taken to select only the physically meaningful IMFs from the extracted ones [Huang et al., 1998, 1999, 2003]. Other tools, such as the WT [Addison, 2002], provide great insight into the characteristic frequencies and their temporal behavior. These tools should be applied to identify the characteristic frequencies before applying EMD.

In addition to spurious IMFs, EMD suffers from a lack of a theoretical foundation; orthogonality between IMFs; uniqueness in the decomposition [Vakakis et al., 2011]; and mode mixing where EMD results in multi-

frequency IMFs. Huang et al. [1999] first described mode mixing as a result of intermittency, defined as the emergence and/or disappearance of a component. A solution is proposed by Huang et al. [1999] by limiting the scale over which a component may pass by changing the choice in extrema for the envelopes. Wu and Huang [2009] proposed another solution, called ensemble EMD (EEMD), which is based on the understanding of EMD as a dyadic filter bank as presented by Flandrin et al. [2004]. EEMD aims to solve the problem of mode mixing by extracting a set of trial IMFs from the original signal plus some finite white noise. The ensemble mean of the trial IMFs is then computed such that the white noise is averaged out and only the IMFs remain.

While these solutions alleviate some of the difficulties, they do not address the problem of mode mixing in application to signals with closely-spaced components as reported by Rilling et al. [2003]. Specifically, their results showed that EMD leads to mode mixing for signals containing two sinusoids which satisfy $0.5 < f_2/f_1 < 2$. Based on these results, Senroy and Suryanarayanan [2007, 2007] proposed the frequency heterodyne as a solution to mode mixing. Frequency heterodyne shifts modes to lower but separate octaves by summing the original signal with its HT [Feldman, 2011], multiplying by a carrier signal with frequency greater than the highest frequency in the signal and then taking the real part. Applying EMD to the shifted signal leads to well-separated IMFs, which, in turn, can be translated back to their original frequencies thus repeating the heterodyne process with the complex conjugate of the carrier signal. While frequency heterodyne is successful when applied to two-component signals, its use becomes limited in signals with more than two components. As the number of components increases, separating them into different octaves becomes increasingly harder and can even result in stronger mode mixing.

A method applicable to signals possessing many modes, proposed by Deering and Kaiser [2005], applied EMD to the sum and difference of $u(t)$ and a masking signal $s(t)$ to extract two intermediate IMFs. The final IMF is then obtained by averaging the two intermediate IMFs. By incorporating $s(t)$ into $x(t)$ EMD is essentially fooled into mixing the correct component with the masking signal. Two mixed IMFs are recovered; however, the masking signal can be completely removed by averaging the two IMFs, resulting in a well-separated IMF. Additionally, since the masking signal depends on the component being extracted, this approach can be applied to a signal with an arbitrary number of components. While this solution addresses both intermittency and closely-spaced modes, there is no general strategy or selection criterion for choosing the appropriate masking signal.

Even without a general criterion, Kurt et al. [2012, 2014b] and Chen et al. [2014] achieved accurate decompositions by manually optimizing each masking signal. Specifically, they proposed the step-by-step EMD approach where the IMFs are extracted one at a time using masking signals and mirror imaging [Lee

et al., 2009b]. To apply step-by-step EMD, the analyst selects the functional form of the masking signal, provides an initial guess for the parameters, applies EMD incorporating the masking signals, and extracts two IMFs. The quality of the decomposition is then evaluated by comparing the time-frequency content of the IMFs using the WT. If the decomposition is successful, then the IMF will contain the highest frequency component while the residual will contain all other components. However, if the decomposition fails, then the analyst must choose new values for the masking signal and repeat the process. After repeating this process numerous times, the analyst obtains an IMF corresponding to the highest component in the original time series and a residual containing all other components. The analyst must then apply the same procedure to the residual to extract the next component, and so on until all components have been decomposed into corresponding IMFs. Although Kurt et al. [2014b] demonstrated the strength and success of step-by-step EMD, the method depends greatly on the skill of the analyst, patience, and available time, which ultimately restricts its usability. Nevertheless, step-by-step EMD represents a significant milestone in the development of EMD-based methods and serves as the starting point for the method developed in Chapter 3.

2.7 The Averaging Theorem and Resonant Dynamics

The averaging theorem and resulting averaging methods, originally due to [Krylov and Bogoliubov, 1934], are celebrated techniques in the area of perturbation theory, and numerous versions have been developed. This work considers the version described in Chapter 4 in [Guckenheimer and Holmes, 1983], which in turn is based on [Hale, 1969], as well as the discussion of Chapter 8 in [Sanders et al., 2007]. Consider the dynamical system

$$\dot{\mathbf{x}} = \varepsilon \mathbf{f}(\mathbf{x}, t, \varepsilon); \mathbf{x} \in U \subseteq \mathbb{R}^n, 0 \leq \varepsilon \leq 1, \tag{2.35}$$

where $\mathbf{f} : \mathbb{R}^n \times \mathbb{R} \times \mathbb{R}^+ \to \mathbb{R}^n$ is $C^p, p \geq 2$, bounded on bounded sets, and of period $T > 0$ in t. The associated autonomous averaged system is defined as

$$\dot{\mathbf{y}} = \varepsilon \frac{1}{T} \int_0^T \mathbf{f}(\mathbf{y}, t, 0)\, \mathrm{d}t \equiv \varepsilon \bar{\mathbf{f}}(\mathbf{y}). \tag{2.36}$$

The averaging theorem states that there exists a C^p change of coordinates $\mathbf{x} = \mathbf{y} = \varepsilon \mathbf{w}(\mathbf{y}, t, \varepsilon)$ under which Eq. 2.35 becomes

$$\dot{\mathbf{y}} = \varepsilon \bar{\mathbf{f}}(\mathbf{y}) + \varepsilon^2 \mathbf{f}_1(\mathbf{y}, t, \varepsilon), \tag{2.37}$$

where $\mathbf{f}_1$ is of period T in t.

In practice, the averaging theorem is applied to partition the dynamics into fast and slow-varying com-

ponents. This is done by averaging out the fast dynamics (which evolve with time t) leaving only the slow dynamics (which evolve with time εt). For details regarding the actual procedures, the reader is referred to [Hale, 1969, Guckenheimer and Holmes, 1983, Sanders et al., 2007]. Often the dynamics can be studied in terms of amplitudes and phases; in which case averaging is performed over the angles. In this case, the dynamical system in 2.35 is expressed as

$$\begin{bmatrix} \dot{\mathbf{r}} \\ \dot{\theta} \end{bmatrix} = \begin{bmatrix} 0 \\ \Omega^0(\mathbf{r}) \end{bmatrix} + \varepsilon \begin{bmatrix} \mathbf{f}^1(\mathbf{r}, \theta, \varepsilon) \\ \Omega^1(\mathbf{r}, \theta, \varepsilon) \end{bmatrix}, \tag{2.38}$$

with initial conditions $\mathbf{r}(0) = \mathbf{r}_0$ and $\theta(0) = \theta_0$ and where $\mathbf{r} \in \mathbb{R}^n, \theta \in \mathbb{T}^m$, and ε is a small parameter. Here $\mathbb{T}^m$ is the m-torus such that $\theta \in \mathbb{R}^m$ and $\mathbf{f}^1(\mathbf{r}, \theta, \varepsilon)$ and $\Omega^1(\mathbf{r})$ are 2-π periodic in each component of θ. For the case that $m = 0$, there exists only one possibility for resonance and that is when $\omega^0(\mathbf{r}_0) = 0$, which occurs on isolated resonance manifolds. Away from these manifolds, one can average over the single angle θ. However, near these manifolds one cannot average over θ and, instead, must apply perturbation methods to study the dynamics. For the case of $m > 1$, such as in any multi-degree-of-freedom (MDOF) vibrating system, things are much more complicated and no complete theory exists [Sanders et al., 2007]. The reason is that the types of resonances that may occur depend on $\mathbf{r}$, and the set of $\mathbf{r}$ for which $\Omega^0(\mathbf{r})$ is resonant is dense. Thus, the remainder of the discussion regarding the averaging theorem will focus on the case where $m = 2$, which will serve the purpose of introducing the relevant parameters for studying resonance in MDOF vibrating systems.

The following discussion is based on Section 8.5 of [Sanders et al., 2007] and begins with the dynamical system

$$\begin{bmatrix} \dot{\mathbf{r}} \\ \dot{\theta} \end{bmatrix} = \begin{bmatrix} 0 \\ \Omega^0(\mathbf{r}) \end{bmatrix} + \varepsilon \begin{bmatrix} \mathbf{R}^1(\mathbf{r}, \theta) \\ 0 \end{bmatrix}, x \in \mathbb{R}^n, \theta \in \mathbb{T}^2, \tag{2.39}$$

where $\mathbf{R}^1(\mathbf{r}, \theta) : \mathbb{R}^n \times \mathbb{T}^m \to \mathbb{R}^n$. Expanding the right-hand side of the equation for $\mathbf{r}$ into a complex Fourier series

$$\dot{\mathbf{r}} = \varepsilon \sum_{k,l=-\infty}^{\infty} \mathbf{C}^1_{k,l}(\mathbf{r}) e^{j(k\theta_1 + l\theta_2)}. \tag{2.40}$$

From this equation, it can be seen that resonance arises when

$$k\Omega^0_1(\mathbf{r}) + l\Omega^0_2(\mathbf{r}) = 0, k, l \in \mathbb{Z}. \tag{2.41}$$

Outside of resonance, averaging leads to

$$\dot{\mathbf{y}} = \varepsilon \mathbf{C}_{00}^{1}(\mathbf{y}). \tag{2.42}$$

However, in the part of $\mathbb{R}^n$ where resonances occur (i.e., when Eq. 2.41 is satisfied), then it is natural to introduce two linearly independent combination angles for θ_1 and θ_2. If one of those combinations is chosen to be $\Phi_{k:l} = k\theta_1 + l\theta_2$, then the equation governing $\Phi_{k:l}$ is slowly varying in a neighborhood where 2.41 is satisfied. Since $\Phi_{k:l}$ is a slow angle, the dynamics cannot be averaged over it. Thus, the averaging theorem fails as a result of the resonance in the dynamics. Conversely, if one can find slow angles present in the dynamics, then one can demonstrate the existence of nonlinear resonance in that dynamics. Furthermore, note that although these concepts were developed for systems with weak nonlinearity (i.e., $\varepsilon \ll 1$), the consequence of resonance introducing slowly varying angles into the dynamics holds true for the case of strong nonlinearity (i.e., for ε of $O(1)$) [Vakakis et al., 2008].

2.8 Slow-flow Dynamics

The *slow-flow* model of a dynamical system concerns the evolution of slow variables that serve to modulate the fast oscillations in the dynamics. This model is related to the method of averaging and other perturbation approaches, but is valid for strongly nonlinear systems. Consider the strongly nonlinear dynamical system

$$\dot{\mathbf{X}} = \mathbf{f}(\mathbf{X}, t), \mathbf{X} = \{\mathbf{x}, \dot{\mathbf{x}}\}^{\intercal} \in \mathbb{R}^{2n}, t \in \mathbb{R}, \tag{2.43}$$

where $\mathbf{f} : \mathbb{R}^{2n} \times \mathbb{R} \to \mathbb{R}^{2n}$ is $C^p, p \geq 2$, bounded on bounded sets, and periodic in t. The slow-flow model is constructed by assuming the dynamics possesses N distinct components at characteristic frequencies $\omega_1, \ldots, \omega_N$, respectively, and expressing the response of each DOF as a summation of independent components

$$x_i(t) = x_i^{(1)}(t) + \cdots + x_i^{(N)}(t), i = 1, \ldots, n, \tag{2.44}$$

where $x_i^{(m)}(t)$ denotes the response of the ith coordinate associated with the frequency ω_m. The characteristic frequencies are termed the *fast frequencies* and are ordered $\omega_1 < \cdots < \omega_N$. We proceed by defining a new complex variable for each component of 2.44,

$$\psi_i^{(m)}(t) = \dot{x_i^{(m)}}(t) + j\omega_m x_i^{(m)}(t), m = 1, \ldots, N, i = 1, \ldots, n. \tag{2.45}$$

This new complex variable can be partitioned into a slowly varying, complex amplitude, $\varphi_i^{(m)}(t)$ that modulates a fast oscillation, $e^{j\omega_m t}$, such that

$$\psi_i^{(m)}(t) = \underbrace{\varphi_i^{(m)}(t)}_{\text{Slow component}} \underbrace{e^{j\omega_m t}}_{\text{Fast component}}, m = 1, \ldots, N, i = 1, \ldots, n. \tag{2.46}$$

This partition is, of course, by no means unique nor universal; however, it allows us to study separately the slow dynamics from the fast dynamics. We proceed by substituting Eqs. 2.44 and 2.46 into Eq. 2.43 and perform N averages over the fast frequencies. This yields

$$\dot{\varphi}_i = \mathbf{F}_i(\varphi_1, \ldots, \varphi_n), \varphi_i = \left\{\varphi_i^{(1)}, \ldots, \varphi_i^{(m)}\right\} \in \mathbb{C}^n, i = 1, \ldots, n. \tag{2.47}$$

The slow-flow equations in 2.47 govern the slow modulations of the N harmonic components of each coordinate of the response. If the fast frequencies of the system are dependent on time or $\mathbf{x}$, then the above partitioning cannot be performed quite as easily. Nevertheless, the concepts developed from this partitioning hold true even for systems where the fast frequencies depend on time or amplitude.

In practice, one typically possesses measured response data without knowing the exact mathematical equations governing that response. As such, one cannot apply the previously discussed procedure to derive the equations governing the slow-flow dynamics. Instead, one must empirically extract the slow-flow dynamics from the measured response data. To this end, recall that the objective of EMD is to extract, from the measured response, a set of nearly orthogonal IMFs that are individually representative of a single characteristic time scale contained in the signal, such that the signal, $x_i(t)$, can be written as

$$x_i(t) = \sum_{k=1}^{N} c_k(t) + R_{N+1}(t), \tag{2.48}$$

where $c_k(t)$ is the kth IMF and $R_{N+1}(t)$ is the remainder signal. Provided that we neglect the remainder signal, the empirical slow-flow can be constructed in a similar manner as was done previously with the exact system [Lee et al., 2009b]. First, the IMFs are complexified using the Hilbert transform, such that

$$\hat{\psi}_i^{(m)}(t) \equiv c_i^{(m)}(t) + j\text{HT}\left\{c_i^{(m)}(t)\right\}, \tag{2.49}$$

This leads to an estimate of the instantaneous amplitude of the mth IMF at the ith coordinate

$$\hat{A}_i^{(m)}(t) = \sqrt{\left(c_i^{(m)}(t)\right)^2 + \left(\text{HT}\left\{c_i^{(m)}(t)\right\}\right)^2}. \tag{2.50}$$

and an estimate of the corresponding instantaneous phase

$$\hat{\theta}_i^{(m)}(t) = \arctan\left(\frac{\mathrm{HT}\left\{c_i^{(m)}(t)\right\}}{c_i^{(m)}(t)}\right). \tag{2.51}$$

The instantaneous frequency of the IMF is then estimated as

$$\hat{\omega}_i^{(m)}(t) = \frac{\mathrm{d}}{\mathrm{d}t}\hat{\theta}_i^{(m)}(t). \tag{2.52}$$

This allows us to form a polar representation of the complexified IMF as

$$\hat{\psi}_i^{(m)}(t) \equiv \hat{A}_i^{(m)}(t)e^{j\hat{\theta}_i^{(m)}(t)}, \tag{2.53}$$

which can be partitioned into slow and fast components provided that a suitable and constant fast frequency, ω_m, can be defined. This partition is written as

$$\hat{\psi}_i^{(m)}(t) \equiv \underbrace{\hat{A}_i^{(m)}(t)e^{j\left[\hat{\theta}_i^{(m)}(t)-\omega_m t\right]}}_{\text{Slow component}} \underbrace{e^{j\omega_m t}}_{\text{Fast component}}, \tag{2.54}$$

which is in the same form as Eq. 2.46 and provides a physical interpretation of the IMFs in terms of slow-flow dynamics [Lee et al., 2009b]. Furthermore, this representation provides a direct path to studying resonances contained in measured response data.

Recall that for systems with two angles (i.e., two fast frequencies, each with their own slow frequencies), the resonance condition can be written as

$$k\Omega_1 + l\Omega_2 = 0, k, l \in \mathbb{Z}, \tag{2.55}$$

which only holds if $k < 0, l > 0$ or $k > 0, l < 0$. For given values of k and l, the case where $k > 0, l < 0$ corresponds to the same type of resonance as the case where $k < 0, l > 0$. As such, we reduce the number of resonance possibilities by defining the resonance condition to be

$$k\Omega_1 - l\Omega_2 = 0, k, l \in \mathbb{Z}^+, \tag{2.56}$$

which leads to the special phase variable

$$\Phi_{k:l} = k\theta_1 - l\theta_2. \tag{2.57}$$

Similarly, using the instantaneous phases of the IMFs, we define the phase variable

$$\hat{\Phi}_{k:l} = k\hat{\theta}_p^{(r)}(t) - l\hat{\theta}_q^{(s)}(t), k, l \in \mathbb{Z}^+. \tag{2.58}$$

Note that we can define this phase variable for any combination of r and s and p and q; however, the number of combinations that must be investigated may be significantly reduced through basic knowledge of the frequency content contained in the measured response (which can be gained through wavelet analysis as described in Section 2.5). In a nonlinear vibrations context, the case where $r \neq s$ and $p = q$ implies an internal resonance between the rth and sth NNMs, which, in the presence of damping, results in an irreversible energy transfer from the lower to higher NNM. The case where $r = s$ and $p \neq q$ implies a resonance capture between the pth and qth coordinates such that the rth NNM facilitates energy exchanges between these coordinates. The case where $r \neq s$ and $p \neq q$ implies a resonance where energy transfers occur between the rth NNM at the pth coordinate to the sth NNM at the qth coordinate.

Chapter 3

Wavelet-bounded Empirical Mode Decomposition (WBEMD)

3.1 Introduction

As mentioned in Section 2.6, step-by-step EMD developed by Kurt et al. [2012] represents a significant milestone in the use of EMD-based techniques for studying the response of strongly nonlinear, vibrating systems. Although rather successful [Kurt et al., 2012, 2014a, Chen et al., 2014], step-by-step EMD incurs a few major drawbacks. First, it depends on a trial-and-error process where the analyst must manually optimize the masking signal such that the extracted IMF is representative of its characteristic time-scale. Second, the assessment of the success of the decomposition is qualitative, relying on the analyst's interpretation of the WT spectrum of the IMF with no quantitative measure incorporated. Third, a successful decomposition may not be optimal, in the sense that the contributions of the corresponding characteristic time-scale and all other time-scales are not maximized and minimized, respectively. Indeed, the contributions of the corresponding and all other time-scales may be large and small, respectively, but this does not mean that they are maximized and minimized, respectively.

To address these shortcomings, we developed the wavelet-bounded EMD (WBEMD), which is a closed-loop, optimization-based solution to the issue of mode mixing. In short, the WBEMD procedure automates the step-by-step EMD procedure by introducing a quantitative measure for the success of the decomposition and by using that measure to drive an optimization of the masking signal parameters. This chapter focuses on derivation and definition of the WBEMD algorithm and its application to several signals with closely-spaced components. The next section introduces the maximum wavelet transform which is used to assess the distribution of a signal in the frequency domain. Section 3.3 describes the derivation of the wavelet-bounding optimization problem as well as the WBEMD algorithm. The fourth section presents three applications of WBEMD and comparisons with EMD and EEMD: first, a two-component signal is used to quantify the strength of WBEMD over EMD and EEMD and to measure the effect of each parameter defined in the

wavelet-bounding optimization problem; second, the impulsively forced, transient response of a cantilever beam with strong, grounding stiffness nonlinearity is considered, and WBEMD is used to reconstruct the corresponding FEP and solutions; and, third, WBEMD is applied to the response of a 2-DOF system with vibro-impacts, and the resulting IMFs are used to investigate the contributions of the higher harmonics and higher resonance captures. The chapter ends with a discussion of possible applications of WBEMD outside of nonlinear vibrations and some concluding remarks.

3.2 The Maximum Wavelet Transform

One of the best ways to assess the success of an EMD-based decomposition is by probing the frequency content of the IMFs. The IMFs are likely to contain remnants of other components in the frequency representation; however, if these remnants have negligible amplitudes compared to the primary (dominant) component, then their presence is inconsequential. Therefore, we define a well-separated IMF as one that has a clear, distinct peak in the frequency domain at the corresponding characteristic frequency, and decays to negligible amplitude at all other characteristic frequencies. Thus, a poorly separated IMF will have peaks at multiple characteristic frequencies. To apply this criterion, we require a transform that results in a smooth distribution in the frequency domain while capturing the dominant nonlinear and nonstationary effects. This renders the fast Fourier transform (FFT) unusable since FFTs often result in jagged representations with numerous peaks around a single component. Instead, we utilize the wavelet transform (WT) [Addison, 2002], which is repeated from Section 2.5,

$$Z(\omega,t) = \mathrm{WT}\left\{z(\tau)\right\} = \int_{-\infty}^{\infty} z(\tau)\psi^{*}_{\omega,t}(\tau)d\tau, \tag{3.1}$$

where $\psi_{\omega,t}(\tau)$ is the mother wavelet function and * denotes the complex conjugate. The Morlet wavelet is used as the mother wavelet function and is defined as

$$\psi_{\omega,t}(\tau) = \frac{1}{\pi^{1/4}}\exp\left[j\omega(\tau-t)\right]\exp\left[-\frac{1}{2}\left(\frac{\omega\left(\tau-t\right)}{\omega_0}\right)^2\right], \tag{3.2}$$

where ω_0 is the central frequency, and $j=\sqrt{-1}$.

Consider that, based on the previous definition, a well-separated IMF must possess a single non-negligible frequency component in the time range of interest. Thus, if an IMF contains multiple non-negligible components, such as the IMF in Fig. 3.1(a) , then the time periods at which those components participate are irrelevant. What matters is that multiple components (with non-negligible amplitude) exist at all. As

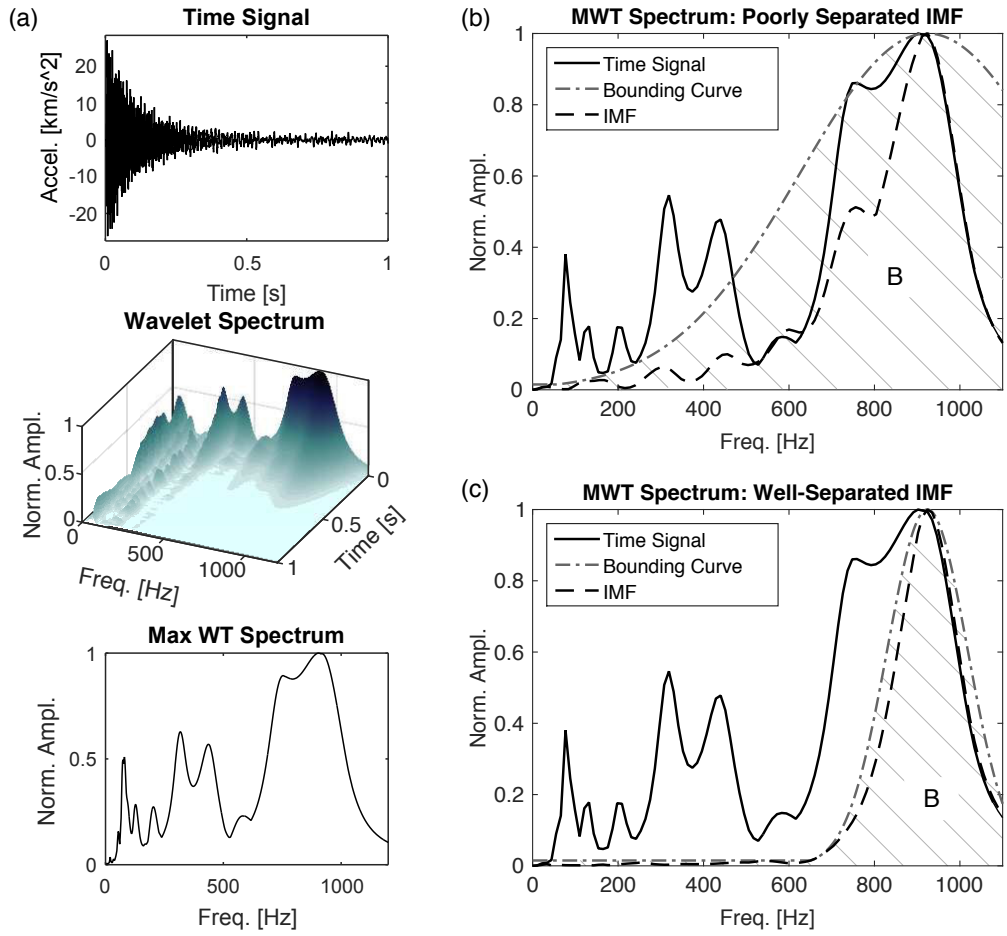

Figure 3.1: (a) The MWT process showing the original time signal, the corresponding wavelet spectrum, and the maximum wavelet transform (MWT) spectrum; (b) MWT spectrum of a poorly separated IMF (c) Maximum wavelet spectrum of a well-separated IMF.

such, only the maximum amplitude at a particular frequency in the WT is relevant for checking the success of the decomposition. Using this information, we remove the time dependence from the WT by taking its maximum over time and define the maximum wavelet transform (MWT) to be

$$\tilde{Z}(\omega) = \text{MWT}\left\{z(t)\right\} \equiv \max_{t}\left[\int_{-\infty}^{\infty} z(\tau)\psi^{*}_{\omega,t}(\tau)d\tau\right]. \tag{3.3}$$

The result of the MWT is a smooth, two-dimensional curve that reveals the distribution of the signal in the frequency domain, as depicted in Fig. 3.1(a). In addition to simplicity, the MWT provides the benefit that if a component has negligible amplitude in the MWT spectrum, then the component has negligible amplitude for all times. Thus, a well-separated IMF (see Fig. 3.1(c)) will result in an MWT spectrum with a single peak at the corresponding characteristic frequency that decays (nearly) monotonically to negligible

amplitude at all other characteristic frequencies. A poorly separated IMF (Fig. 3.1(b)) results in a MWT spectrum with peaks (of comparable amplitudes) at multiple characteristic frequencies.

To measure the quality of an IMF, we start by creating a function, $b(\omega)$, which is well-separated and serves as a bounding function for the IMF in the MWT domain; that is,

$$\forall\omega : b(\omega) \geq \tilde{C}_i(\omega), \tag{3.4}$$

where $\tilde{C}_i(\omega)$ is the MWT of $c_i(t)$. Since $b(\omega)$ is required to have one peak and to vary monotonically from that peak, its width must vary based on the distribution of the IMF in the MWT domain. It follows that the area under the bounding curve B, is relatively large for a poorly separated IMF and relatively small for a well-separated IMF. Thus, by minimizing B for a particular IMF, the isolation of the IMF around the corresponding characteristic frequency is maximized. This minimization procedure is described as wavelet-bounding the IMF, and it serves as the basis for the proposed method, termed wavelet-bounded EMD (WBEMD), which is presented in the next section.

3.3 Wavelet-bounding and WBEMD

Consider the time signal $u(t)$ with characteristic frequencies $\omega_1 > \cdots > \omega_N$, which are identified from the MWT, $\tilde{U}(\omega)$, by the analyst, and suppose that we are trying to extract the ith component from the measured time series,

$$zi(t) = u(t) - \sum_{q=1}^{i=1} c_q(t). \tag{3.5}$$

From here, the frequency ratio ω_i/ω_{i+1} is computed, and based on this value one of the following two procedures is applied. Rilling et al. [2003] found that EMD fails to extract well-separated IMFs for frequency ratios $0.5 < \omega_i/\omega_{i+1} > 2$. Hence, if two neighboring harmonic components are well-separated so that $\omega_i/\omega_{i+1} > 2$ then we compute a masking signal for these components as,

$$s(t) = \max\left[z_i(t)\right]\sin(\omega_i t) \tag{3.6}$$

which is included to prevent mode-mixing due to intermittency. By applying a masking signal with frequency ω_i and amplitude equal to $\max\left[z_i(t)\right]$ we ensure that EMD extracts an IMF that captures the corresponding component at the frequency ω_i. It follows that at times when the mode does not participate it is replaced by the masking signal, which is later removed by averaging. The result is an IMF possessing a single component

that also captures the intermittency of the corresponding mode.

For the case when two neighboring components are closely spaced, i.e., when $\omega_i/\omega_{i+1} \leq 2$ we compute the masking signal as

$$s(t) = \max\left[z_i(t)\right](\alpha \sin(\beta\omega_i t)), \tag{3.7}$$

where α and β are the free parameters used in the optimization. Next, we select initial guesses for α and β, extract the IMF, $c_i(t)$ and compute its MWT, $\tilde{C}_i(\omega)$. Then, we fit a bounding function around the transformed IMF and compute the area under this curve, which indicates the quality of the decomposition. In general, we found that most components resemble a Gaussian function in the MWT spectrum. Thus, we chose a Gaussian function for the bounding function in the form,

$$b(\omega) = \eta\tilde{Z}(\omega_i)\exp\left[-\phi\left(\frac{\omega-\omega_i}{\omega_i-\omega_{i+1}}^2\right)\right], 1 \leq \eta \leq 1.2, \tag{3.8}$$

where $\tilde{Z}_i(\omega_i)$ is the MWT of $z_i(t)$, η and ϕ scale the amplitude and the width of the function, respectively. Additionally, we require that,

$$b(\omega) \geq \varepsilon\tilde{Z}_i(\omega_i), \varepsilon < 1, \tag{3.9}$$

where ε provides a lower tolerance for the bounding function and controls the permissible error in the extracted IMF; its choice is a matter of practical convenience and is application-dependent (we chose $\varepsilon = 0.05$ in this work). As such, the bounding function is a pseudo-Gaussian function with a maximum and minimum amplitude of $\eta\tilde{Z}_i(\omega_i)$ and $\varepsilon f\tilde{Z}_i(\omega_i)$ respectively. If the MWT of an IMF is flat, or otherwise non-Gaussian, around its peak and then the width of the bounding function will be increased drastically to encompass the IMF. Consequently, a well-separated IMF may be rejected or, worse, a poorly-separated IMF may be chosen by the algorithm. This issue is avoided by setting $\eta > 1$ such that the width of the bounding function can be reduced without intersecting the IMF. However, selecting too large of a value for η may also negatively affect the decomposition, and we recommend that η be chosen such that $1 \leq \eta \leq 1.5$ (we selected $\eta = 1.1$ for this work). The parameter ϕ is computed such that the condition $\forall\omega : b(\omega) \geq \tilde{C}_i(\omega)$ is satisfied. Thus, the amplitude of the bounding function is determined entirely by the MWT of the original time series, $\tilde{Z}_i(\omega)$, and its width is determined solely by the MWT of the trial IMF, $\tilde{C}_i(t)$.

Once the bounding function is determined, its area, B, can be used to quantitatively assess the separation of the IMF, and we wish to use this as a cost function for optimizing the parameters α and β such that the extracted IMF is well-separated. Since the smallest possible value of B corresponds to an IMF with zero amplitude at ω_i, we impose the additional constraint that $\max\left[\tilde{C}_i(\omega_i)\right] \geq \gamma\tilde{Z}_i(\omega_i)$, such that γ controls the

minimum allowable amplitude in the IMF at ω_i (we chose $\gamma = 0.85$). Additionally, we can help guide the optimization to better IMFs by introducing the additional constraint $\max\left[\tilde{C}_i(\omega)\right] \leq \delta\tilde{Z}_i(\omega), \omega] \in [0, \omega_{i+1}]$, such that δ controls the maximum allowable amplitude in the IMF away from ω_i (we chose $\delta = 0.15$). The constrained optimization problem can be stated as,

$$\begin{aligned}
\min \quad & B = 2\int_0^{\omega_i} b(\omega)d\omega = 2\eta\tilde{Z}_i(\omega_i)\int_0^{\omega_i} \exp\left[-\phi\left(\tfrac{\omega-\omega_i}{\omega_i-\omega_{i+1}}\right)\right]^2, \\
\text{s.t.} \quad & \max\left[\tilde{C}_i(\omega_i\right] \geq \gamma\tilde{Z}_i(\omega), \\
& \max\left[\tilde{C}_i(\omega\right] \leq \delta\tilde{Z}_i(\omega), \omega \in [0, \omega_{i+1}], \\
& b(\omega) \geq \varepsilon\tilde{Z}_i(\omega_i), \varepsilon < 1, \\
& \forall\omega : b(\omega) \geq \tilde{C}_i(\omega)
\end{aligned} \tag{3.10}$$

The lower limit is set to zero such that the area under the bounding function evaluated at negative frequencies does not contribute to B. Due to the symmetry in the bounding function, the integral is computed up to ω_i and then multiplied by two to get the total area (this is equivalent to integrating from 0 to $2\omega_i$).

Thus far, the method has been described in the continuous domain; however, the numerical approach does not vary greatly. The numerical approach employs the following differences: the WT is computed using the FFT and the inverse FFT, as described in Section 2.5, and the area under the bounding function is computed using a trapezoidal method. Alternatively, the area under the bounding function can be calculated using tabulated values of the error function and interpolation. In this dissertation, we used the trapezoidal method and the patternsearch function in MATLAB®, which directly searches for a global minimum, to perform the minimization of B with $\alpha = 1$ and $\beta = 1$ as initial guesses. Once B is minimized and a well-separated IMF has been extracted, the remainder signal is computed as,

$$z_{i+1}(t) = z_i(t) - c_i(t). \tag{3.11}$$

We then apply the algorithm to $z_{i+1}(t)$ to extract additional IMFs. In this method, we use the EMD code developed for MATLAB® by Rilling et al. [2003] and Flandrin and Rilling [2007]. In Fig. 3.2, we present a flow chart detailing each step in the WBEMD algorithm, as outlined in the previous discussion. In the next sections, we provide three examples of applications of WBEMD: the first for an artificial two-component signal, the second for the response of a cantilever beam with a strong local nonlinearity, and the third to the response of a linear oscillator coupled to a vibro-impact nonlinear energy sink (NES).

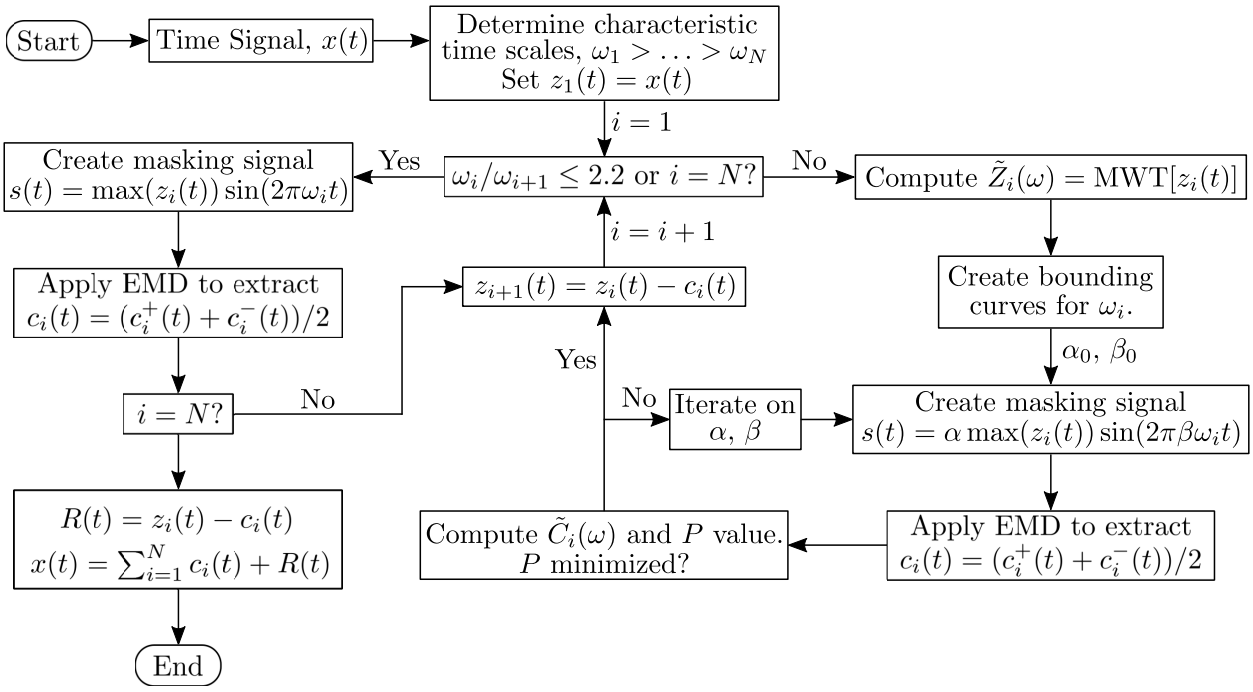

Figure 3.2: Flow chart detailing the WBEMD procedure.

3.4 Applications and Comparisons with EMD and EEMD

3.4.1 Signal with Two Closely-spaced Components

As the first application of WBEMD, we consider the stationary, artificial two-component signal,

$$y(t) = \underbrace{A\sin(2\pi k f_1 t)}_{y_1(t)} + \underbrace{\sin(2\pi f_1 t)}_{y_2(t)} \tag{3.12}$$

where $f_1 = 750$ Hz, $1.05 \leq k \leq 2.2$ and $0.1 \leq A \leq 2$. we vary both the amplitude and frequency ratios to study how these quantities affect the quality of the empirical mode decomposition. Hence, for each value of A and k, we construct the signal $y(t)$, and for comparison purposes we extract six IMFs: Two IMFs using EMD, two using EEMD, and two using WBEMD. Since the original components are known exactly, we can accurately assess the quality of the decompositions by computing the Pearson correlation coefficient (PCC) between the IMFs and the corresponding exact components, $y_1(t)$ and $y_2(t)$. The PCC provides a measure of the linear relationship between two data sets and takes values $-1 \leq$PCC≤ 1, where a value of 0 indicates no relationship (poor correlation) and a value of ± 1 indicates a perfect linear relationship (strong correlation).

In Fig. 3.3, we present the PCC values for the IMFs extracted using (a) EMD, (b) EEMD, and (c) WBEMD. In these plots, light and heavy shaded tiles correspond to strong and weak correlation, respectively.

The most striking feature of these plots is the large, dark bands visible in the lower half of both plots of Fig. 3.3(a). These regions reveal amplitude and frequency ratios where EMD fails to accurately extract the components. Interestingly enough, we find that the performance of EMD relies more on the amplitude ratio than on the frequency ratio, and EMD even performs poorly for frequency ratios greater than two for low enough amplitude ratios. Looking now at the EEMD results, we find that the results for the first IMF mirror those found using EMD except that the shading is lighter, which indicates an improvement over EMD. A new band at large amplitude ratios appears in the results for the second IMF, but the bands seen in the EMD results are mostly eliminated. Overall, EEMD improves upon EMD; however, the presence of the dark bands indicates that it does not entirely resolve the issue of mode mixing. In contrast, no such bands appear in the plots of Fig. 3.3(c), indicating that applying WBEMD results in IMFs that accurately reproduce the original components. The poorest decomposition obtained from the application of WBEMD occurs at an amplitude ratio of 0.1 and a frequency ratio of 1.05, which represents a substantial improvement over EMD and EEMD.

We now seek to study the robustness of WBEMD by applying the same procedure as described above, except that we fix $A = 1$ and vary the parameters $\gamma, \delta, \varepsilon$ and η instead. The parameters $\gamma, \delta, \varepsilon$ and η represent the minimum allowable amplitude at ω_i, the maximum allowable amplitude at ω_{i+1}, the permissible error in the IMF and the maximum amplitude of the bounding function, respectively, and they have nominal values of 0.85, 0.25, 0.05 and 1.1, respectively. To study the effect of each parameter on the decomposition, we fix all other parameters to their nominal values and vary the remaining parameter and the frequency ratio, k. Figure 3.4 presents the PCC values for varying each of the constraint parameters, where the color scale goes from 0.7 to 1. Based on these plots, we find the following optimal ranges: $0.8 \leq \gamma \leq 0.95$, $0 \leq \delta \leq 01.5$, $0 \leq \varepsilon \leq 0.15$, and $1 \leq \eta \leq 1.2$. Note that all of the nominal values selected previously are within the optimal ranges and, moreover, that these results demonstrate the robustness of WBEMD to adjustments in the constraint parameters.

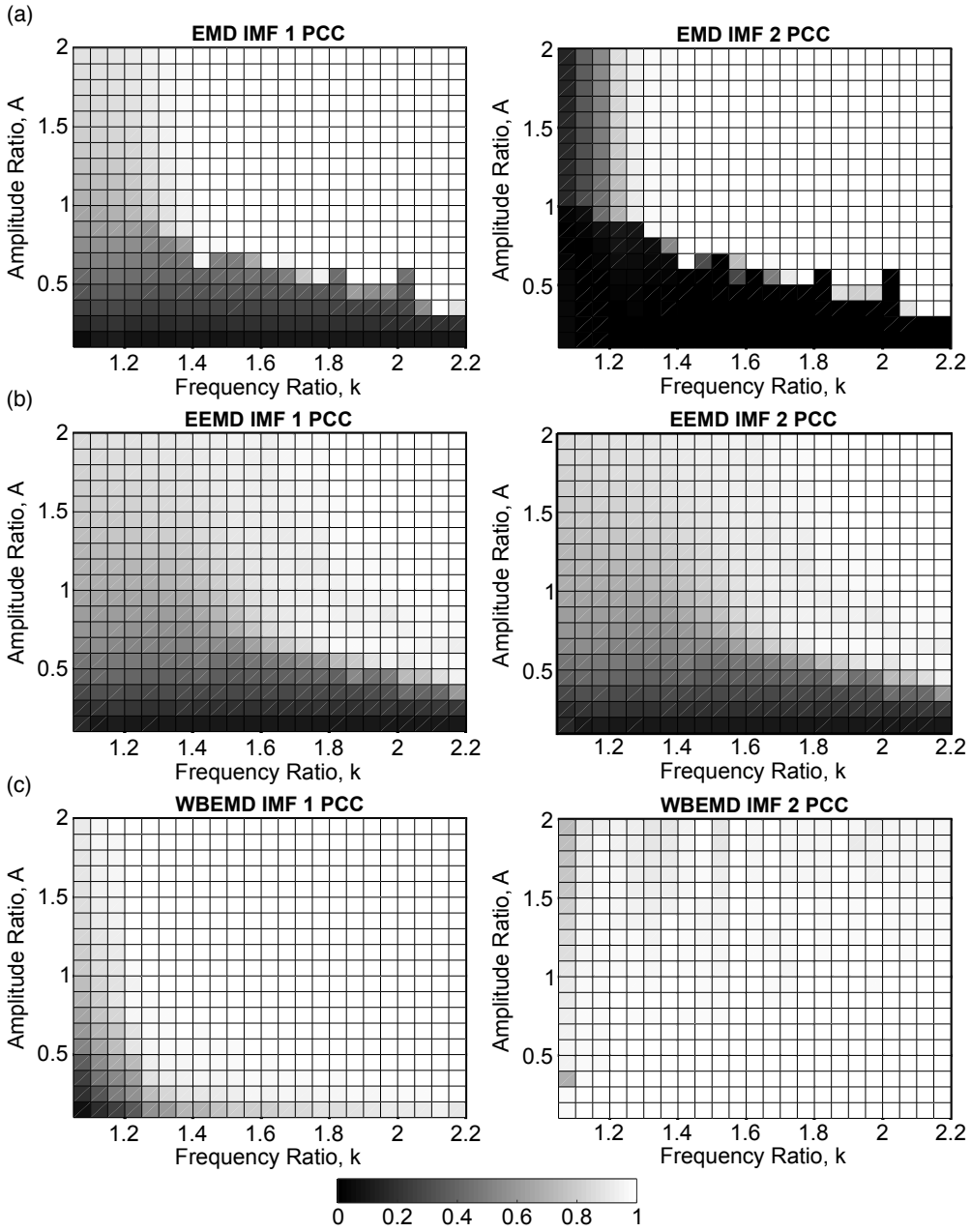

Figure 3.3: The PCC between the components $y_1(t)$ and $y_2(t)$ and the IMFs extracted using (a) EMD, (b) EEMD and (c) WBEMD.

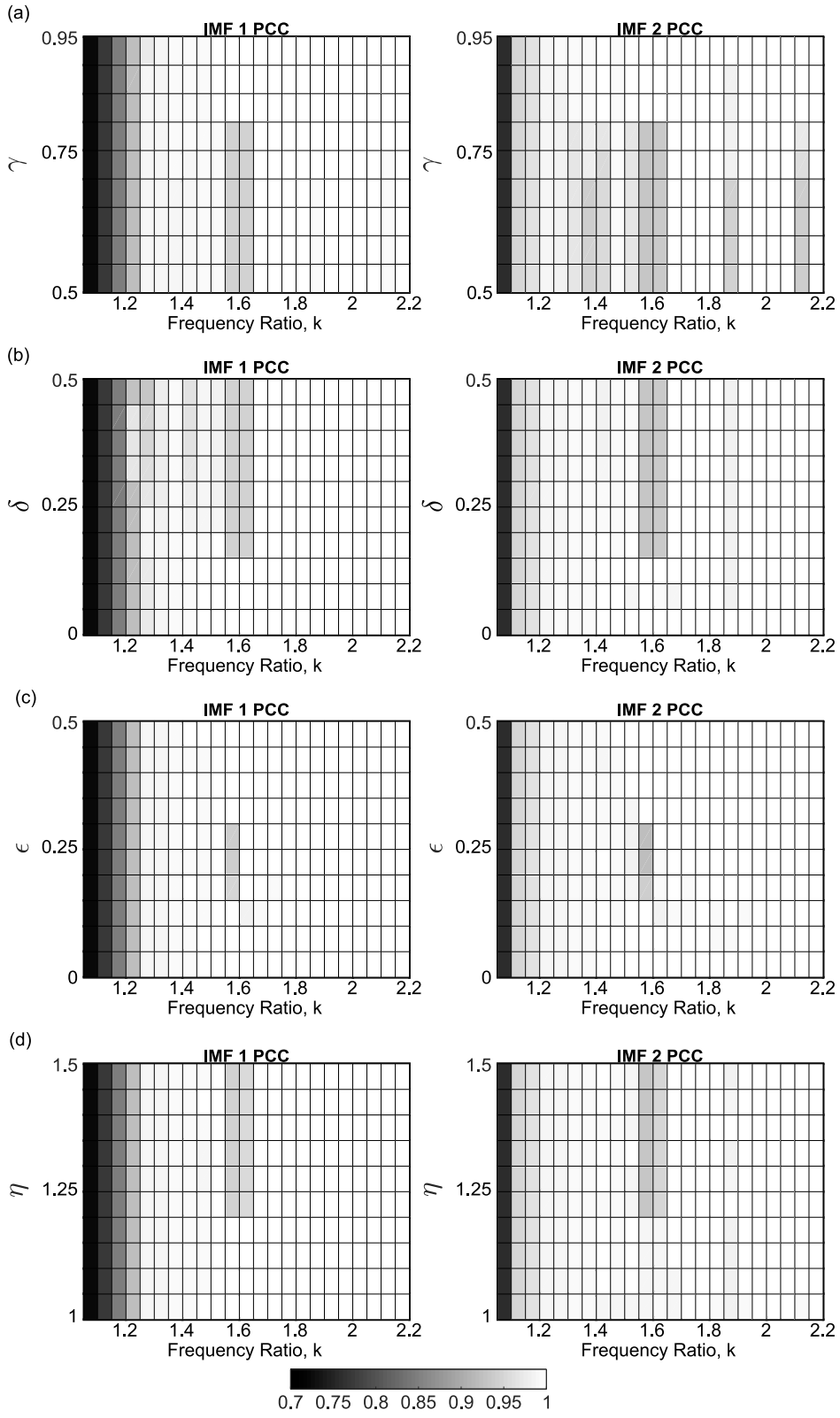

Figure 3.4: The PCC between $y_1(t)$ and $y_2(t)$ and the IMFs extracted using WBEMD for varying frequency ratio, and varying (a) the minimum allowable IMF amplitude, (b) the maximum allowable amplitude away from the characteristic frequency, (c) the permissible error in the IMF, and (d) the maximum amplitude of the bounding function.

3.4.2 Cantilever Beam with Smooth Stiffness Nonlinearity

3.4.2.1 System Configuration

The beam is composed of steel, and it is uniform and homogeneous, with length of 1.3113 m, width of 0.0446 m, thickness of 0.0080 m, elastic modulus of 200×10^9 Pa, and density of 7850 kg/m^3. A schematic representation of the beam is presented in Fig. 3.5. An essentially nonlinear (nonlinearizable) spring with a stiffness of 10^8 N/m^3 and a pure cubic force-displacement law (depicted in Fig. 3.7) is attached transversely at the free end of the beam to ground. The beam was represented by a finite element (FE) model consisting of 10 Euler-Bernoulli beam elements. An impulsive load, in the form of a half-sine with a 1 ms period and maximum amplitude of 3000 N (depicted in Fig. 3.6, is applied to the free end. The equations of motion for the beam are written as

$$\mathbf{M}\ddot{\mathbf{x}} + \mathbf{D}\dot{\mathbf{x}} + \mathbf{K}\mathbf{x} + \mathbf{f}(\mathbf{x}) = \mathbf{F}(t), \tag{3.13}$$

where $\mathbf{M}, \mathbf{D}, \mathbf{K}$ are the mass, damping, and stiffness matrices representing the cantilever beam, respectively, $\mathbf{x}$ is the vector of displacements and rotations (i.e., $\mathbf{x} = [x_1, \theta_1, \ldots, x_{10}, \theta_{10}]^\intercal$), $\mathbf{f}(\mathbf{x})$ is a vector containing the nonlinear spring term (i.e., $\mathbf{f}(\mathbf{x}) = \left[0, 0, \ldots, k_{nl}x_{10}^3, 0\right]^\intercal$), and $\mathbf{F}(t)$ is a vector containing the applied impulsive force (i.e., $\mathbf{F}(t) = [0, 0, \ldots, F(t), 0]^\intercal$).

The beam is assumed to be classically damped [Caughey and O'Kelly, 1965] and the damping matrix is computed using modal damping using the damping ratios presented in Table 3.1 for the first ten modes, which are taken from experimental studies of the modeled beam in [Kurt et al., 2012, Mane et al., 2011]. For NNMs eleven and higher, the damping ratios were assumed to be 0.001 such that these modes do not contribute significantly to the response. Using the mass-orthonormalized mode shape matrix, $\Phi = [\boldsymbol{\varphi}_1 \boldsymbol{\varphi}_2 \ldots \boldsymbol{\varphi}_{20}]$, and

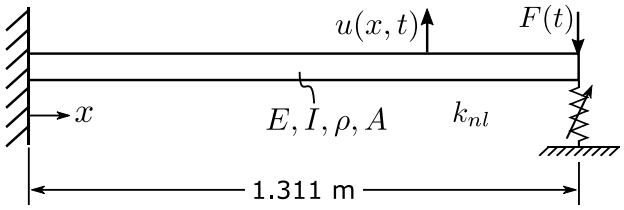

Figure 3.5: Schematic representation of the beam with strong, local stiffness nonlinearity.

natural frequencies $\omega_1, \ldots, \omega_{20}$ (with units of rad/s), the damping matrix is computed as

$$\mathbf{D} = \mathbf{M}\Phi \begin{bmatrix} \zeta_1\omega_1 & & \\ & \ddots & \\ & & \zeta_{20}\omega_{20} \end{bmatrix} \Phi^{\intercal}\mathbf{M}. \tag{3.14}$$

Finally, the applied force is defined as

$$F(t) = 3000 \sin\left(\frac{\pi}{0.001}t\right)\left(H(t) - H(t - 0.001)\right), \tag{3.15}$$

where $H(t)$ is the Heaviside function and is defined as

$$H(t) = \begin{cases} 0 & t < 0, \\ 1/2 & t = 0, \\ 1 & t > 0. \end{cases} \tag{3.16}$$

The transient response of the beam is simulated for 30 seconds by placing the equations of motion into state-space form and numerically integrating using ode45 in MATLAB®.

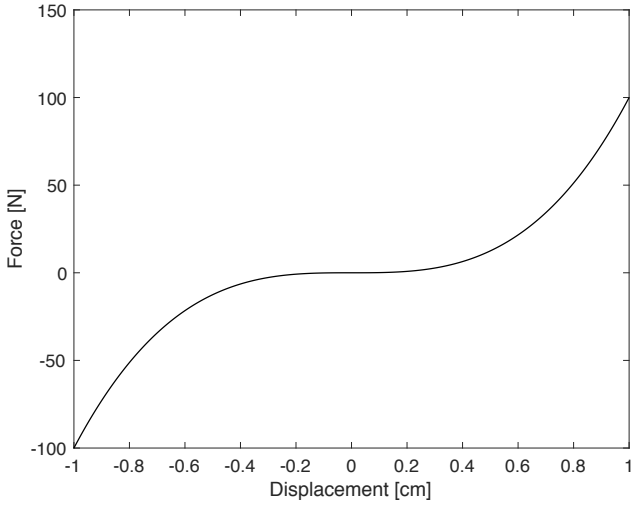

Figure 3.6: Force-displacement law governing the nonlinear spring attached to the free end of the beam.

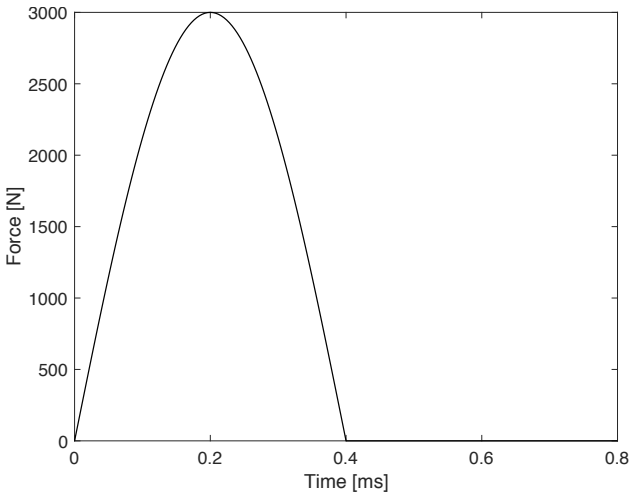

Figure 3.7: Profile of the impulsive load applied to the free end of the beam.

Table 3.1: Frequencies and viscous damping ratios for the leading 10 NNMs.

NNM #	**Frequency [Hz]**	**Damping Ratio**
1	3.794	0.0071
2	23.78	0.0011
3	66.60	0.0014
4	130.6	0.0029
5	216.2	0.0068
6	323.9	0.0013
7	454.5	0.0073
8	608.9	0.0018
9	787.3	0.0023
10	978.7	0.0015

3.4.2.2 Response and Decomposition

The transient displacement response of the free end of the beam, together with the corresponding WT and MWT spectra, are depicted in Fig. 3.8. The WT spectrum reveals that all modes except the first decay and die out before the simulation ends. We find that the first and second modes dramatically shift in frequency as the amplitude decays, which reflects the energy dependence of the transient nonlinear dynamics. Interestingly, the MWT reveals that the first component greatly increases in amplitude when it reaches 8.4 Hz. To further explore these results, we apply EMD, EEMD, and WBEMD to the displacement response in Fig. 3.8 and present the four IMFs extracted in Figs. 3.9 and 3.10 . The indexes of orthogonality [Huang et al., 1998] are 0.0164, 0.0134, and 0.0039 for the IMFs extracted using EMD, EEMD, and WBEMD, respectively. Since applying WBEMD extracts well-separated IMFs, we proceed with our analysis using

only the WBEMD IMFs. Moreover, to avoid confusion we switch the ordering of the IMFs, such that the first IMF corresponds to the first frequency component.

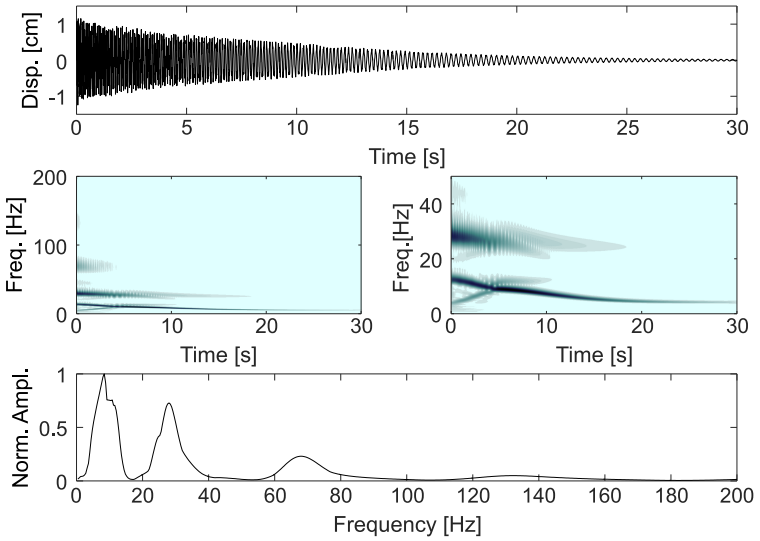

Figure 3.8: Displacement measurement of the free end, corresponding WT and normalized MWT spectra for the cantilever beam with cubic spring at the free end.

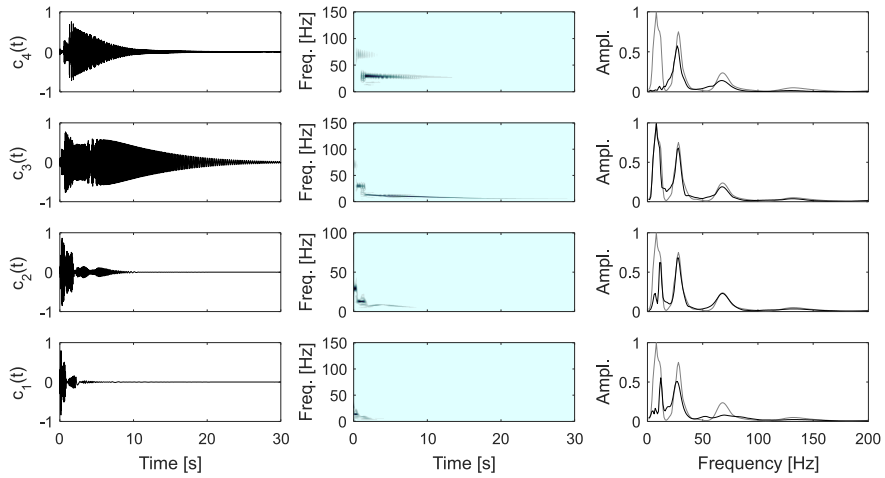

Figure 3.9: Time series, WT spectrum, and normalized MWT spectrum for IMFs separated using EMD. The normalized MWT of the original time series and the IMF are presented as the gray and black lines, respectively.

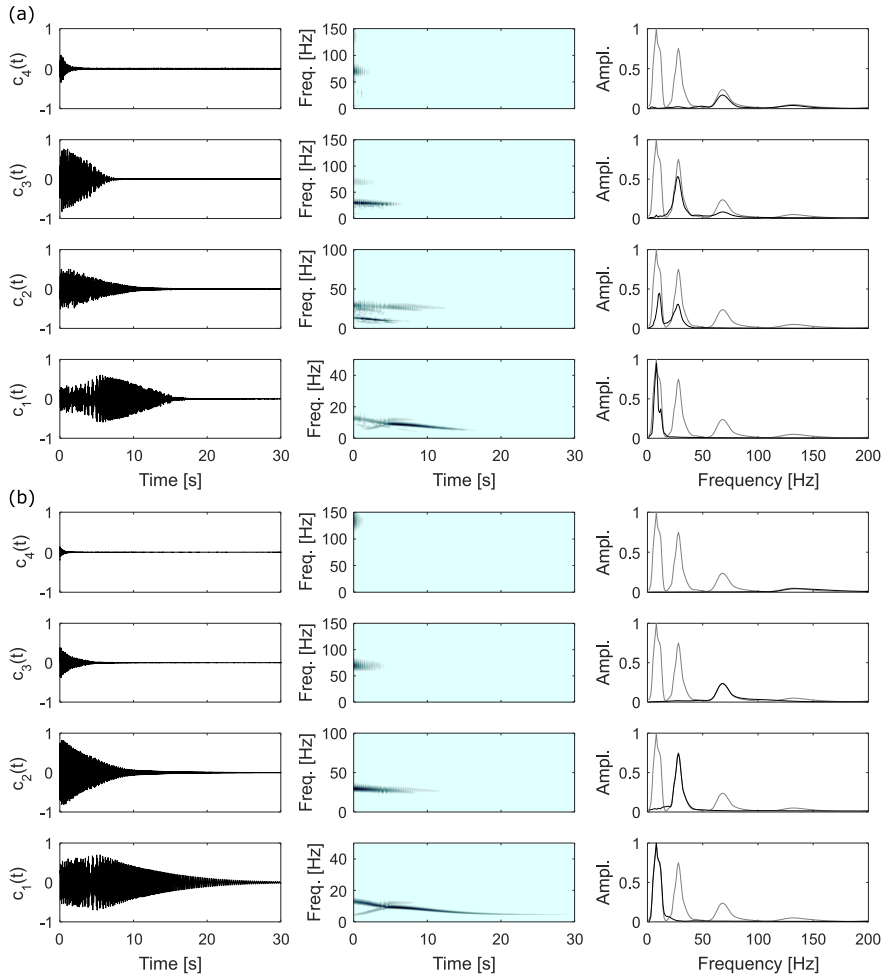

Figure 3.10: Time series, WT spectrum, and the normalized MWT spectrum for IMFs separated using (a) EEMD and (b) WBEMD. The normalized MWT of the original time series and the IMF are presented as the gray and black lines, respectively.

3.4.2.3 FEP Reconstruction and Nonlinear Resonance

To understand the physical significance of the IMFs, we shift our focus to nonlinear normal modes (NNMs); we define an NNM to be a time-periodic oscillation of a nonlinear dynamical system [Vakakis et al., 2008]. A key distinction between NNMs and classical normal modes is that NNMs are strongly dependent on the total energy in the system. Specifically, as energy changes, both the natural frequencies and mode shapes change. In the current system, the cubic spring produces a stiffening effect such that, as energy increases, the natural frequencies increase and the mode shapes change from those of a cantilever beam to those of a fixed-pinned beam. Whereas NNMs provide a global understanding of the nonlinear dynamics, the IMFs provide a local understanding of the transient dynamics because they are representative of, but not entirely equivalent to, the NNMs for the specific forcing and initial conditions applied in the simulation. However,

by probing the dynamics over varying energy ranges and extracting sets of IMFs, we gain a sense of the global dynamics.

The proper graphical depiction is key to using NNMs and IMFs to assess the dynamics. To this end, we employ the frequency-energy plot (FEP) [Vakakis et al., 2008], where the frequency of each NNM is plotted as a function of the total system energy. A useful feature of the FEP, as discussed in Section 2.1, is that systems with weak damping can be studied using the FEP of the corresponding undamped and unforced (Hamiltonian) systems because weak damping is a parasitic effect and does not significantly alter the dynamics [Vakakis et al., 2008]. Since the system is weakly damped, we will use the Hamiltonian FEP to probe the physical significance of the IMFs. The Hamiltonian FEP for the first NNM is computed using the numerical continuation code NNMcont [Peeters et al., 2009], which solves for time-periodic solutions to the equations of motion. The resulting curve, called the backbone branch, is presented as the solid black line in Fig. 3.11. In general, the backbone branch shows a smooth transition from low frequency to high frequency; however, the most interesting features are the subharmonic tongues that emanate from the curve. These features correspond to bifurcations in the NNM that result in internal resonances (IR) (which have no linear counterparts), where energy is transferred from the first NNM to higher NNMs [Vakakis et al., 2008]. Such bifurcations are generic in nonlinear dynamical systems and are not limited to the first and higher NNMs. In fact, the bifurcations and resulting internal resonances occur whenever the frequency of a higher NNM is an integer multiple of the frequency of a lower NNM. An understanding of these features proves invaluable as we examine the IMFs and provide insight into the nonlinear physics governing the response.

With the backbone branch computed, we proceed by constructing the transient, damped FEP by plotting the WT of the response in Fig. 3.8 as a function of frequency and total energy of the system to create a wavelet FEP. The wavelet FEP for the first NNM is depicted in the background of Fig. 3.11 in grayscale, where darker (lighter) shades correspond to strong (weak) participation. Since the wavelet FEP relies directly on the original time series, it provides the most accurate depiction of the relationship between the NNMs and the total system energy. As such, for an IMF to be an accurate representation of a NNM, it must correctly trace the path of the wavelet FEP. To plot the IMFs on the FEP, we first compute the instantaneous frequency for the IMF using the relation,

$$\hat{f}_i(t) = \frac{1}{2\pi}\frac{d}{dt}\left[\frac{\mathrm{HT}\left\{c_i(t)\right\}}{c_i(t)}\right], i = 1, 2, \tag{3.17}$$

where HT is the Hilbert transform [Feldman, 2011]. In practice, the discrete Hilbert transform is used, which introduces high-frequency oscillations into the output; these are removed by applying a low-pass filter

with a 1 Hz cut-off frequency such that the filtered instantaneous frequencies do not oscillate. The IMFs are depicted on the FEP by plotting the instantaneous frequencies as functions of the total system energy computed using the displacement and velocity time series data at each location. If a model of the system is not available, then the total system energy can be estimated from the IMFs using the procedure described in [Vakakis et al., 2011].

Inspecting Fig. 3.11, we find that the WBEMD FEP follows the wavelet FEP, indicating that the IMFs are indeed representative of the first and second NNMs. Starting at high energy and focusing on the first NNM, the first feature we find resembles a subharmonic tongue on the backbone branch. However, this feature is not actually a tongue and is not related to an NNM bifurcation. Instead, this tongue-like feature results from the rapid dissipation of energy that occurs over the first 0.5 seconds and corresponds to the transient response and higher NNMs. Additionally, the IMF FEP is shifted away from the backbone branch, but since the wavelet FEP is also shifted from the backbone branch this result is physical and not an error in the IMF. Instead, the response follows an impulsive orbit [Kerschen et al., 2008], which is one of a countable infinity of possible periodic or quasi-periodic orbits that the transient response can follow. The deviation from the backbone is due solely to the impulsive nature of the applied forcing, and if the system were given initial conditions on the backbone instead, the NNM would follow the backbone branch.

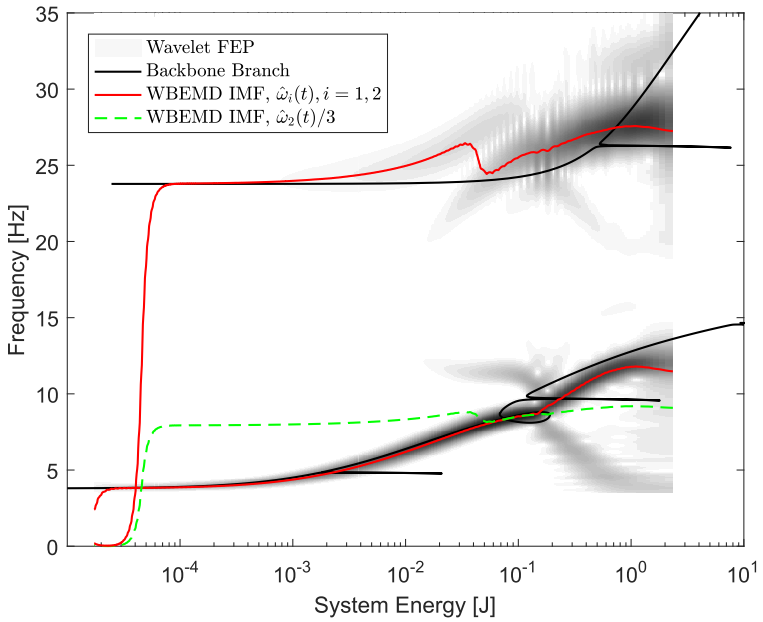

Figure 3.11: Frequency-energy plot for the first two NNMs depicting the backbone branch, the instantaneous frequency of the IMF found using WBEMD, and the wavelet FEP of the displacement response.

The response follows the impulsive orbit until it is captured by the tongue, which corresponds to a 3:1 IR

between the first and second NNMs. To confirm this, we plot $\hat{f}_2(t)/3$ as the dashed green line, which proves that the frequency of the second NNM is three times that of the first NNM on the tongue. This result does not prove that the two NNMs are engaged in an IR, and to conclusively prove this we investigate further by plotting the first two IMFs from 3 seconds to 8 seconds in Fig. 3.12(a). These plots reveal that the two IMFs are engaged in nonlinear beating [Kurt et al., 2014b], which provides physical evidence supporting the hypothesis that the first and second NNM are engaged in an IR. Mathematically, an IR in the dynamics is associated with non-time-like behavior of a certain slow phase of the problem, which leads to the failure of the averaging theorem with respect to that slow phase [Vakakis et al., 2008]. For the current problem, we compute the instantaneous phase of each IMF using the expression,

$$\hat{\theta}_i(t) = \arctan\left(\frac{\mathrm{HT}\left\{c_i(t)\right\}}{c_i(t)}\right), i = 1, 2. \tag{3.18}$$

In [Vakakis et al., 2008], the slow phase is obtained by subtracting the fast phase, $f_i t$ from $\hat{\theta}_i(t)$; however, due to the damping in our system the fast frequency, f_i, is time dependent, which complicates the extraction of the slow phase. Instead, the phase variable for this system is defined to be,

$$\Phi_{3:1} = 3\hat{\theta}_1(t) - \hat{\theta}_2(t), \dot{\Phi}_{3:1} = 3\dot{\hat{\theta}}_1(t) - \dot{\hat{\theta}}_2(t), \tag{3.19}$$

and recognize that the slow phases are only fully separated when the fast phases are related by a 3:1 ratio. This limitation is acceptable because our objective is to prove that an IR occurs when the first NNM is captured on the FEP. Following [Vakakis et al., 2008], we plot the phase difference trajectory; i.e., we plot $\dot{\Phi}_{3:1}$ against $\Phi_{3:1}$ in Fig. 3.12(b). Based on the FEP and the IMFs, we zoom into the phase trajectory for $3 \leq t \leq 8$ and find not only that the phase trajectory is small, but also that it exhibits non-time-like behavior. This result mathematically proves that the first NNM enters into a 3:1 IR with the second NNM, allowing energy to transfer from the first NNM into the second NNM. Immediately after the NNMs escape the IR, the first NNM follows the backbone almost exactly whereas the second NNM suddenly spikes up in frequency, which is due to the additional energy that the second NNM has absorbed from the first NNM.

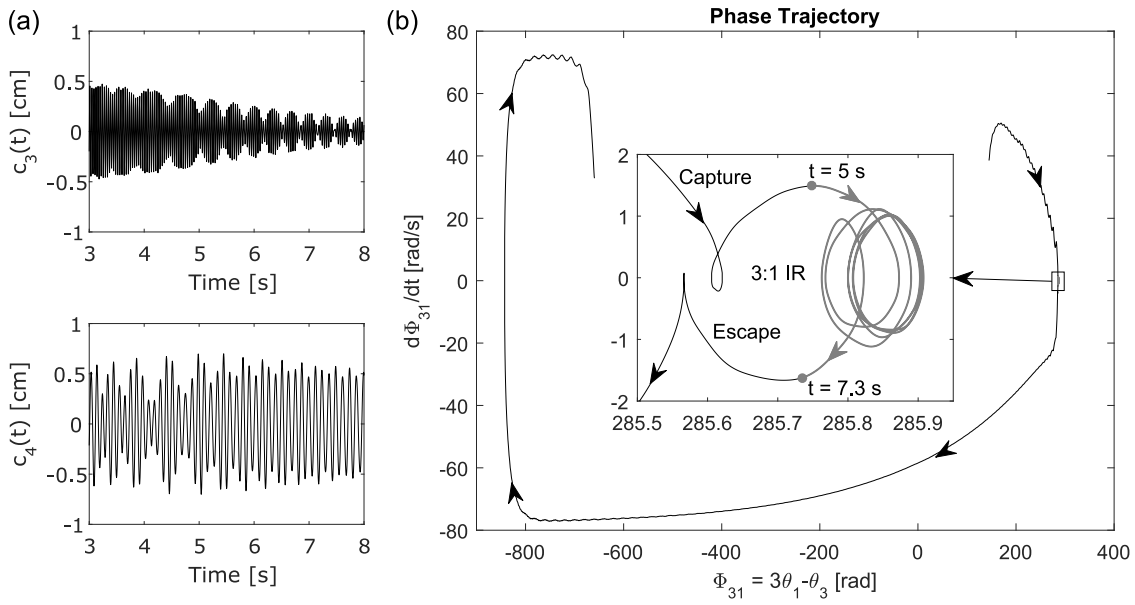

Figure 3.12: (a) WBEMD IMFs corresponding to first and second NNMs zoomed in to show the nonlinear beat phenomena, (b) phase trajectory plot depicting the transient resonance capture between the first and second NNMs.

3.4.2.4 Spatio-temporal IMFs and Reconstruction of Periodic Solutions

As a final investigation of the IMFs, we seek to explain why the amplitude of the first IMF increases to a maximum and then decays to near zero amplitude. As previously mentioned, this system behaves like a cantilever beam at low energies and as a fixed-pinned beam at high energies. This means that as energy increases the amplitude of the free end becomes smaller and smaller relative to the displacement elsewhere, until the restoring force becomes so large that the free end no longer moves and transforms into a node for all periodic solutions. Since we solved directly for the periodic solutions, we can use the Hamiltonian system to study how the solutions change with respect to energy. However, the NNMs (cf. Fig. 3.11) initially follow an impulsive orbit before being captured by the backbone branch, and there is no guarantee that the periodic solutions along the impulsive orbit will correspond to those on the backbone branch. Instead, we apply WBEMD to the displacement response simulated at each DOF and extract a set of spatio-temporal IMFs, where each spatio-temporal IMF corresponds to the response of an NNM in both space and time. Using the spatio-temporal IMFs, we obtain the periodic solution by first computing the instantaneous amplitude at each DOF using

$$\hat{A}_i(t, x_m) = \sqrt{\left(c_i^m(t)\right)^2 + \left(\mathrm{HT}\left\{c_i^m(t)\right\}\right)^2}, \tag{3.20}$$

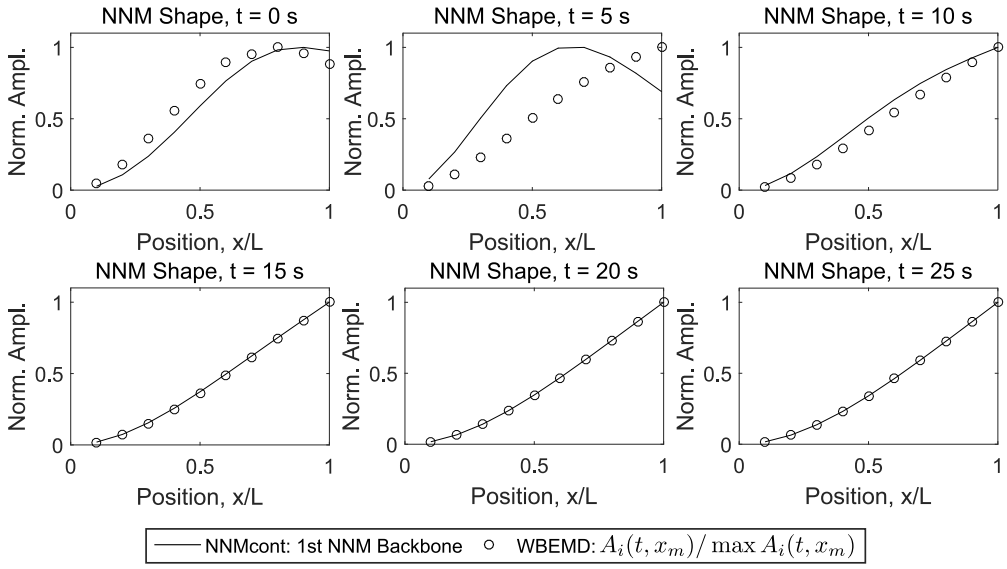

Figure 3.13: Periodic solutions taken from the backbone branch of the first NNM and computed using the instantaneous amplitudes of the IMFs extracted at each DOF.

where $\hat{A}_i(t, x_m)$ is the discrete set of instantaneous amplitudes at the positions $x_m, m = 1, 2, \ldots, N$. A spatially continuous amplitude can be obtained using spline approximations that satisfy the appropriate boundary conditions.

Since our objective is to study how the periodic solution changes with energy, the values of a specific amplitude at any given time are not important; what is important is where the maximum amplitude occurs spatially at any given time. The underlying assumption is that an NNM represents a synchronous, periodic solution; that is, a periodic solution where all DOFs reach their maximum values or pass through zero, at the same time. The periodic solutions are synchronous except when the NNM is engaged in an IR with another NNM. When this occurs, the synchronous, periodic solutions corresponding to each NNM combine and form an asynchronous, periodic solution [Chen et al., 2014] with non-trivial phase differences between coordinate responses. This is particularly important as we have just proven that the first and second NNMs are engaged in a 3:1 IR. However, the proof of the 3:1 IR is only possible if the IMFs are well-separated and physically representative of the individual NNMs during the IR. We proceed by spatially normalizing the instantaneous amplitude at each time instant and obtain the synchronous periodic solution, and plot snapshots of the first periodic solution at 5-second intervals (black circles in Fig. 3.13). We match the frequencies of the IMF and the backbone branch for each snapshot, and plot the corresponding periodic solutions as solid, black lines in Fig. 3.13. The time, frequency, and energy values for the snapshots are presented in Table 3.2.

Starting with the first snapshot, we find that the periodic solution constructed using the spatio-temporal

Table 3.2: Time, frequency, and energy values associated with the snapshots presented in Fig. 3.13.

Time[s]	**Frequency [Hz]**	**IMF Energy [J]**	**Backbone Energy [J]**
0	11.78	4.971	0.414
5	8.70	0.134	0.118
10	6.95	0.019	0.017
15	5.02	2.92×10^{-3}	2.29×10^{-3}
20	4.12	4.98×10^{-4}	3.82×10^{-4}
25	3.86	9.24×10^{-5}	6.12×10^{-5}

IMFs (hereafter referred to as the IMF periodic solution) closely resembles the periodic solution taken from the backbone branch (hereafter referred to as the backbone periodic solution). Interestingly, we find that the anti-node is neither at the free end (cantilever beam mode) nor near the midpoint of the beam (fixed-pinned beam mode) and is, instead, located at the 8th DOF. Looking at the second snapshot, we find that the IMF periodic solution does not match the backbone periodic solution; however, one recalls that at $t = 5$ seconds the first and second NNMs are engaged in an IR. Thus, the mismatch occurs because NNMcont computes the mixed, nonsynchronous, periodic solution whereas the IMF captures the synchronous contribution of only the first NNM. More important, we find that the anti-node has changed from being located at the 8th DOF to the 10th DOF (the free end), which implies that the anti-node is nonstationary and, in fact, shifts from the 8th DOF to the 10th DOF during the first 5 seconds of the response. As the anti-node approaches the free end, the response at the free end, correspondingly, grows larger and larger until it becomes the anti-node and remains as such for the rest of the response. This is exactly the physical mechanism governing the increase in amplitude observed during the first 5 seconds in the first IMF depicted in Fig. 3.11 and is unrelated to the 3:1 IR. Looking at the remaining snapshots, we find that the IMF periodic solution almost exactly matches the backbone periodic solution of the first NNM and that as energy decreases both shapes converge to the first bending mode of a cantilever beam.

These results demonstrate the power of WBEMD for extracting well-separated IMFs, which provide significant insight into the nonlinear physics governing the response of dynamical systems with smooth, local nonlinearities. Hence, WBEMD proves to be a valuable tool for gaining deep understanding of, and interpreting the transient responses of strongly nonlinear dynamical systems including nonlinear modal interactions caused by IRs.

3.4.3 Oscillator with Vibro-impact Nonlinear Energy Sink (NES)

3.4.3.1 System Configuration

We study the dynamics of the single-degree-of-freedom LO with a VI NES (Fig. 3.14) studied by Lee et al. [2009a]. Whereas Lee et al. [2009a] studied the system with viscous damping, we study the system without viscous damping, where the only dissipation is through inelastic VIs. The nondimensionalized equations of motion are

$$\mu\ddot{u}_1 + \sigma\left(u_1 - u_2\right) = 0, \qquad \ddot{u}_2 + u_2 + \sigma\left(u_2 - u_1\right) = 0 \tag{3.21}$$

where u_1 and u_2 are the displacements of the NES and LO, respectively, and the dots represent differentiation with respect to the nondimensional temporal variable ξ. We note that the normalized clearance is set to unity in both directions, such that impacts occur when $|u_1 - u_2| = 1$. The impacts are handled directly through velocity relations rather than using an approximate model such as those used in Mane et al. [2011] and Herrera et al. [2017]. The velocities after impact (denoted by superscripts '+') are computed from the velocities before impact (denoted by superscripts '-') by the relations

$$\dot{u}_1^+ = \frac{\left(\mu - \rho\right)\dot{u}_1^- + \left(1 - \rho\right)\dot{u}_2^-}{1 + \mu}, \qquad \dot{u}_2^+ = \frac{\mu\left(1 + \rho\right)\dot{u}_1^- + \left(1 - \mu\rho\right)\dot{u}_2^-}{1 + \mu} \tag{3.22}$$

where ρ is the coefficient of restitution. The equations of motion, Eqs. 3.21, are integrated using ode15s in MATLAB® until $|u_1 - u_2| = 1$ is satisfied. At this point, the integration is halted, and the solver computes the precise time of impact, such that the total energy (including that dissipated by the VIs) is conserved before and after the impact, which ensures that the simulations are physically accurate [Nucera et al., 2007, Karayannis et al., 2008, Lee et al., 2009a]. After computing the time of impact, the integration is restarted using the displacements at the time of impact and the velocities computed using (10) as the new initial conditions. Using this procedure, the transient response of the system was simulated for a dimensionless time of 2500 for $\sigma = 0.2, \mu = 0.1, \rho = 0.8$ with the initial conditions $u_1(0) = \dot{u}_1(0) = u_2(0) = 0$ and $\dot{u}_2(0) = 5$.

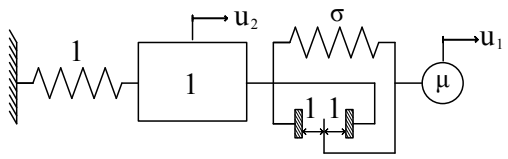

Figure 3.14: System configuration: SDOF linear oscillator coupled to a VI NES.

3.4.3.2 System Response and Analysis

As was shown by Lee et al. [2009a], the dynamics of this system can be partitioned into two regimes: *a linear regime and a strongly nonlinear regime corresponding to energy values where VIs cannot and can occur, respectively.* This partitioning is similar to that of the dynamics of systems with smooth nonlinearities [Moore et al., 2018a, Herrera et al., 2017]; however, in the systems with smooth nonlinearities, the transition between regimes cannot be precisely determined. Rather, the transition occurs over a finite energy range, and the ranges are different for each mode governing the response of the system. In contrast, the division between regimes for the current system occurs at a specific energy value and is the same for all modes. This critical energy value is precisely $e_c = \sigma/2$ or $e_c = 0.1$ for the current system, and corresponds to the minimum system energy necessary for a single VI to occur in the response. In the presence of viscous damping, the two regimes are connected uni-directionally such that, if the system begins in the linear regime, the dynamics can never enter the nonlinear regime without an external source of energy. If the system begins in or enters into the nonlinear regime, then the dynamics naturally decays (due to the VIs and viscous damping) to the point that after some time a final VI occurs, and the system enters the linear regime. In the absence of viscous damping, the VIs become the sole source of dissipation, and once the final VI occurs, the system becomes Hamiltonian. However, the closer the system energy is to the critical energy value, the rarer and less energetic the VIs become, which leads to increasingly less energy being dissipated by the VIs and, consequently, the system only asymptotically approaches the critical energy value.

Thus, without viscous damping, the critical energy value transforms into an impassable barrier that completely divides the two regimes and can only be passed by external input into the system. Moreover, it is possible for a stable limit cycle, which has been shown to exist for systems with elastic impacts [Kryzhevich, 2007], to exist for this system at energies above the critical energy value, but no effort will be made to rigorously prove such in this work. Although viscous damping alters the transition between the two regimes, the presence of weak viscous damping does not alter the dynamics in each regime [Lee et al., 2009a]. Thus, by neglecting viscous damping, the effect of the inelastic VIs on the dynamics can be studied in isolation. The initial conditions chosen in this work place the system energy two orders of magnitude above the critical energy value (the initial energy is 15 normalized units and the critical energy value is 0.1) and allows us to study some of the complicated dynamics and transitions that occur in the nonlinear regime.

To this end, we present the simulated displacement and velocity responses in Figs. 3.15(a) and 3.15(b), respectively, for the LO and the NES. Based on these plots, we divide the response into stages: **stage A:** $0 \leq \xi \leq 340$, **stage B:** $340 \leq \xi \leq 940$, **stage C:** $940 \leq \xi \leq 1420$, and **stage D:** $1420 \leq \xi \leq 2500$. In the first half of stage A, we find that the NES displacement and velocity contain a period of variable

peak amplitude followed by a rapid decay in amplitude. In contrast, the LO exhibits smoothly decaying responses with no irregularities. The latter half of stage A shows that the displacement responses of LO and NES are regular and decay smoothly. The velocity response of the LO also smoothly decays whereas the velocity response of the NES maintains a near-constant amplitude, which results from the irreversible energy transfers from the LO to the NES that occur with each VI. The A-B transition results in an immediate drop and a corresponding increase in the amplitude of the velocity and displacement of the NES, respectively. In stage B, we find that the NES maintains a constant amplitude velocity and that the LO continues to decay smoothly. Just as in stage A, this behavior is the result of the irreversible energy transfer from the LO to the NES incurred by the VIs. In contrast to stage A, the displacement responses of the LO and NES approach near-constant amplitudes, which appears to indicate a drastically reduced dissipation rate. In stage C, the velocity of the NES is irregular and chaotic with a nonzero mean. An interesting observation is that much of the response up to stage C is regular and predictable, even though it occurs at larger energies than in stage C. Even though the response of the NES is irregular, the response of the LO remains regular and smoothly decays. Thus, the chaotic motion appears to be localized to the NES. Stage D marks the end of the chaotic motion and the system settles into a steady, regular motion.

Figure 3.15(c) presents the instantaneous system energy (kinetic plus potential energy) and the total instantaneous energy dissipated by the VIs as percentages of the initial total energy. Stage A is characterized by a significant loss in energy such that by the time of the A-B transition the system has lost over 75% of its initial energy. Stage B is characterized by a decrease in the rate of dissipation such that the system energy almost reaches a constant value. Just as the system energy appears to reach a constant value, the dynamics transitions into stage C, and the irregular and chaotic motion result in increased dissipation. Finally, stage D reveals a period where the system appears to reach a constant energy value (with the actual dissipation being less than 0.5% of the initial energy), which reflects the regular and sustained motion achieved in this stage. Figure 3.16 presents the phase portraits for the relative motion between the LO and the NES for each stage, which reveal the different attractors governing each stage. For further discussion regarding the global dynamics of this system, we refer the reader to [Lee et al., 2009a], where the global dynamics is studied using Poincaré sections, nonlinear normal modes and frequency-energy plots.

For the rest of this work, we define a higher-order TRC to be one where energy is irreversibly transferred from a lower harmonic to a higher harmonic. Furthermore, we classify them as either even or odd TRCs, where even and odd refer to TRCs that occur between the first harmonic of the LO and the even and odd harmonics of the NES, respectively. This distinction does not consider the ratio between the components and, as such, a 3:1 TRC between the first harmonic of the LO and the second harmonic of the NES would be

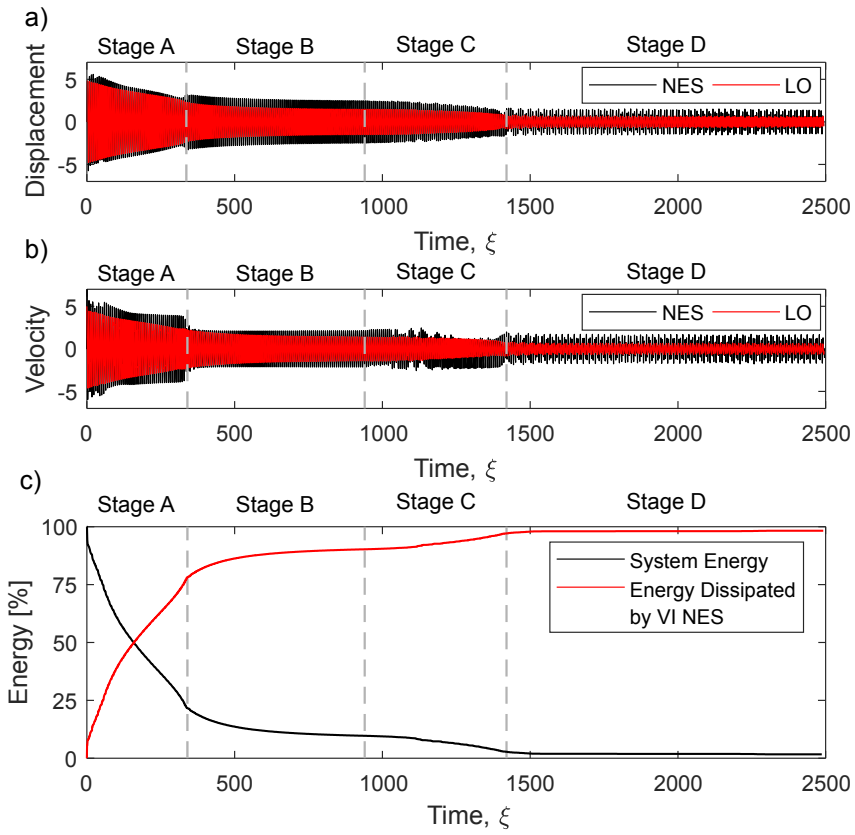

Figure 3.15: (a) Displacement time series and (b) velocity time series for the NES and LO. (c) Instantaneous system energy (kinetic plus potential energy) and the total instantaneous energy dissipated by the VIs presented as percentages of the initial energy.

regarded as an even TRC. Additionally, a 1:1 TRC between two components of the same order, i.e., 1:1 TRC between the second harmonics of both the LO and NES, is classified as a lower order TRC. The classification presented here is by no means unique or universal; however, it will prove beneficial in the coming discussion.

In Fig. 3.17, we present the displacement responses of the LO and NES, and the corresponding WT and MWT spectra. We note that the WT spectra have been scaled such that the darkest and lightest shades correspond to amplitudes of 5 and 0, respectively. From the WT spectra, we find that the LO displacement is dominated by the first component, with the second component weakly participating in stages C and D. In contrast, the NES response, as depicted in its WT spectrum, contains up to six different components throughout the response, with the first component being the only one that persists throughout the response. The first half of stage A contains all six components whereas the second half contains only the odd components. It can be seen that the even harmonics exit the response approximately halfway through stage A, leaving only the odd harmonics for the remainder of the stage. We hypothesize that the loss of

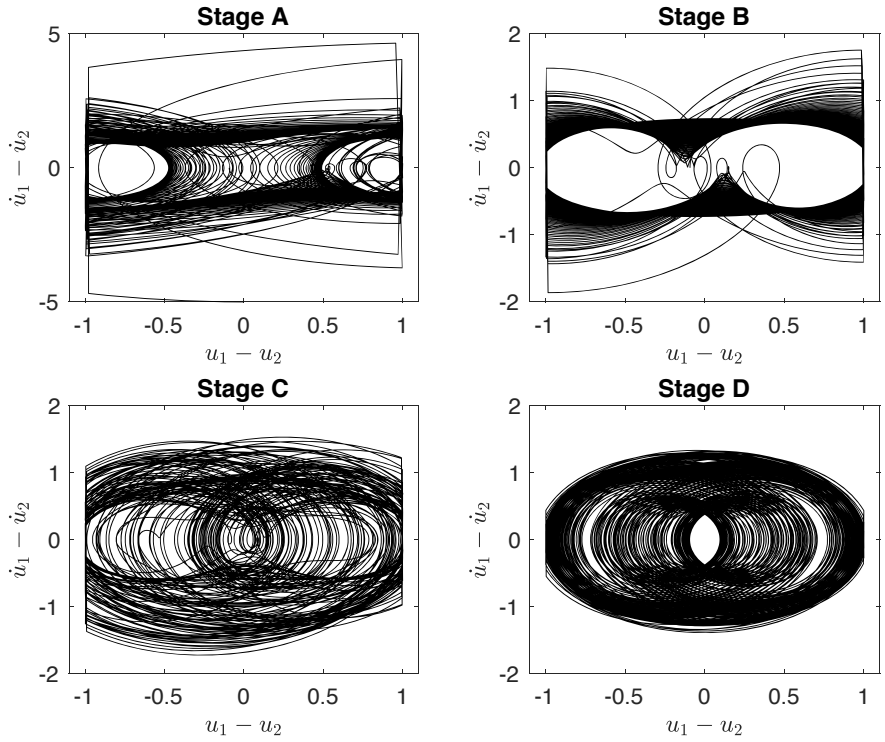

Figure 3.16: Phase portraits of the relative motion between the LO and NES detailing the attractor governing each stage.

the even harmonics corresponds to the loss of even TRCs (e.g. 2:1, 4:1, etc. TRCs), such that the first half of stage A is characterized by even and odd TRCs whereas the latter half is characterized by only odd TRCs; this loss explains the observed difference in dissipation rates. We address this hypothesis in the next subsection. The latter half of stage A reveals the loss of the fifth harmonic and, more interestingly, the darkening of the third harmonic, which corresponds to an increase in the energy concentrated in it. Stage B contains only the first and third harmonics, and the third harmonic appears much lighter than in stage A. The B-C transition sees the reappearance and disappearance of the second and third harmonics, respectively. Thus, we hypothesize that the B-C transition results from the loss of a 3:1 TRC that leads into the reappearance of a 2:1 TRC. Stage C is governed by first and second harmonics, and the irregular and chaotic motions are reflected in the WT spectrum by the frequency-smearing seen above the second component. Finally, stage D is also governed by the first and second harmonics; however, we find that the second harmonic has decreased in frequency and now corresponds to the frequency of the second mode of the underlying linear system. Thus, we hypothesize that the C-D transition results from the loss of a 2:1 TRC, leaving only 1:1 TRCs in the dynamics, and that this loss is responsible for the significant decrease in dissipation observed in stage D.

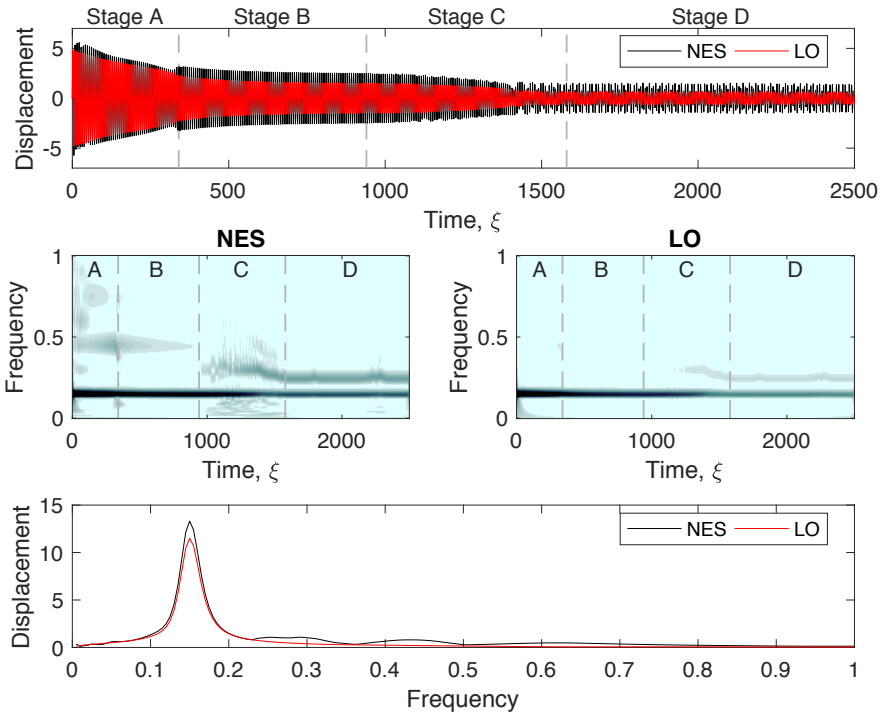

Figure 3.17: Displacement time series, corresponding WT spectra and MWT spectra for the NES and LO. Note that, the WT spectra have been scaled such that the darkest and lightest shades correspond to amplitudes of 5 and 0, respectively.

Based on the previous observations, we plot the number of impacts and energy dissipated per fundamental period in Figs. 3.18(a) and 3.18(b), respectively. Stage A is marked by some variance in the number of impacts, which corresponds to the large dissipation observed in the first half of the stage. Once the dynamics settles on four impacts per period, the energy dissipated per period decreases noticeably. We note that a maximum of only two impacts per period is achievable with the first harmonic, and higher harmonics are necessary to achieve more impacts per period. The decrease is interesting because the number of impacts remains constant, which implies that the impacts become less energetic with increasing time. Although four impacts per period persist throughout the majority of stage A, the end is characterized by a significant increase in energy dissipated per period. Thus, the VIs must become significantly more energetic with increasing time towards the end of stage A. This result is perplexing since we expect the VIs to become less energetic with increasing time (since the system has less overall energy). The A-B transition results in a loss of half of the VIs per period, which results in an immediate reduction in the energy dissipation rate. Although stage B maintains a constant two VIs per period, the energy dissipated in this stage does not remain constant and decays to near-zero amplitude.

In stage C, the number of impacts per period frequently varies between one and two impacts, which

corresponds to the variation observed in the energy dissipated per period and reflects the irregular and chaotic nature of the dynamics during this stage. The C-D transition sees the maximum number of VIs per period decrease from two to one. Finally, stage D is characterized by great sparsity in the number of VIs occurring per period, with at most one VI occurring in any one period. This is reflected in the fact that nearly no energy is dissipated in stage D. The differences in energy dissipated and number of impacts per period observed in each stage are undoubtedly related to the TRCs that occur in each stage.

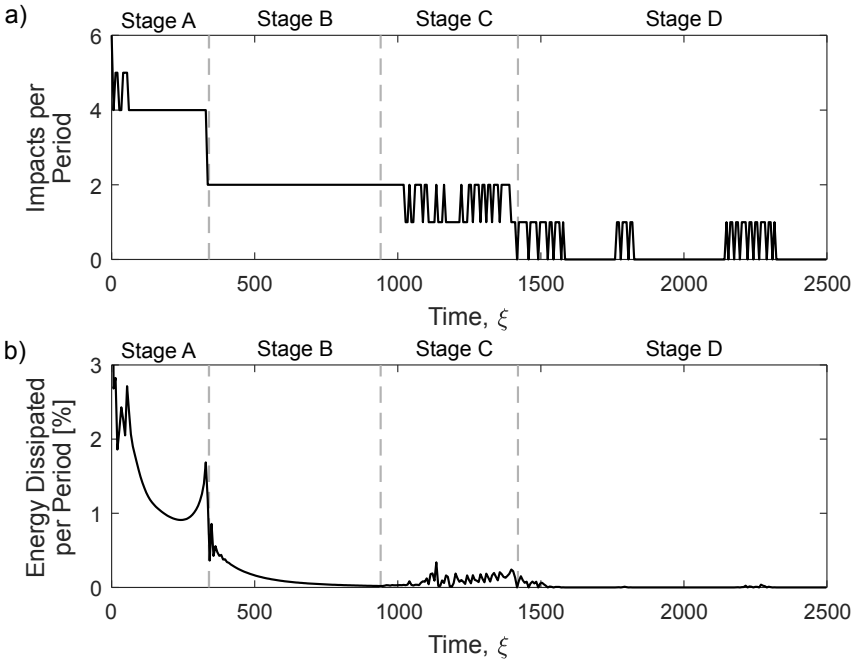

Figure 3.18: Number of impacts and percentage energy dissipated per period of the first harmonic.

3.4.3.3 Contribution of Higher Harmonics

In this subsection, we study the contribution of the higher harmonics to the response and proceed by applying WBEMD to the displacement responses of the NES and LO depicted in Fig. 3.17. Even though only two components are visible in the WT of the LO response (Fig. 3.17), we extract six IMFs at the same characteristic frequencies for both the LO and NES and present the time series and WT spectra of the IMFs in Figs. 3.19(a) and 3.19(b). We reverse the ordering of the IMFs to improve the clarity of the discussion, such that the first IMF corresponds to the first harmonic in the original response. We note that the amplitudes of the LO-IMFs are much smaller than those of the NES-IMFs. In fact, the amplitudes of the second through fourth IMFs extracted from the response of the NES are almost five times as great as those of the corresponding IMFs from the response of the LO. The amplitude difference in the NES-IMFs

compared to the LO-IMFs indicates that most of the energy in the higher harmonics is concentrated in the NES.

Moreover, we find that the amplitude of the first IMF is two orders of magnitude larger than that of the second IMF for both the NES and LO, and is comparable to the magnitude of the exact responses depicted in Fig. 3.17. Lee et al. [2009a] found similar results and claimed that their smooth IMFs closely approximated the exact responses. Thus, they concluded that only the smooth IMFs were physically representative of the exact responses of the LO and the NES. Indeed, when one compares the first IMFs directly with their respective exact responses, as in Fig. 3.20(a), one might conclude that the first IMF accurately captures the exact response. However, if this is true, then we should be able to reconstruct the relative displacement between the LO and NES by computing the difference of the two IMFs. We define the nth difference IMF as

$$d_n(\xi) = c_n^{NES}(\xi) - c_n^{LO}(\xi), \tag{3.23}$$

and present the comparison of the relative displacement with the lowest three difference IMFs in Fig. 3.20(b). The relative displacement is not well approximated by the first difference IMF, and substantial portions of the response are missing, which correspond to periods of large amplitude in the higher harmonics.

Several minima of the amplitude of $d_1(\xi)$ are observed in the plot, which correspond to the maxima visible in the second and third difference IMFs depicted in Figs. 3.21(b) and 3.21(c), respectively. The A-B transition marks to the first minimum amplitude of $d_1(\xi)$ and corresponds to the global maximum of the amplitude of $d_3(\xi)$ which is followed by a significant decrease in amplitude. Recall that an increase and decrease in the displacement and velocity responses of the NES, respectively, were observed at the A-B transition, and these changes correspond exactly with the changes in the amplitude of the first and third harmonics. Additionally, we found that the number of impacts per period decreased from four in stage A to only two in stage C. This implies that the constructive interference of the first and third harmonics is maximized in stage A, and that the A-B transition results in a phase shift in one of the harmonics such that their destructive interference is maximized in stage A.

To investigate further, we present zoomed-in views around the A-B transition of the comparisons of the relative displacement and the first and third difference IMFs in Fig. 3.21. The first plot, Fig. 3.21(a), presents a comparison of the relative displacement and the sum of the first and third difference IMFs. This plot reveals that the overall pattern of VIs is captured by the summation of the two harmonics. Figure 3.21(b) depicts the relative displacement and the third difference IMF and reveals that in stage A four peaks within one cycle correspond to impacts (constructive interference), whereas two correspond to zero relative displacement (destructive interference). In stage B, we observe the exact opposite, with only two peaks

corresponding to impacts, but no corresponding phase shift is observed around the A-B transition. Thus, we turn to the comparison of the relative displacement and the first difference IMF shown in Fig. 3.21(c). Stage A reveals that the peaks correspond to zero relative displacements, whereas in stage C every peak corresponds to an impact. More importantly, we find that a phase shift occurs between $\xi = 330$ and $\xi = 350$ with the most pronounced shift occurring around $\xi = 345$. The effect of the phase shift is most visible in the comparison of the first and third difference IMFs presented in Fig. 3.21(d). This plot reveals that stages A and B correspond to periods where the first and third harmonics are in phase (maximized constructive interference) and out of phase (maximized destructive interference), respectively. In the portion of stage A presented in Fig. 3.21, the amplitudes of the first and third difference IMFs are 0.49 and 0.51, respectively. This means that although the first harmonic of the absolute displacements has amplitude two magnitudes larger than the third harmonic, its contribution to the VIs in stage A is, at most, equivalent to that of the third harmonic. For the portion of stage B presented in Fig. 3.21, the amplitudes of the first and third difference IMFs are 0.61 and 0.20, respectively. Thus, the amplitude of the third harmonic is effectively one-third of that of the first harmonic, and the largest contribution to the VIs comes from the first harmonic.

We note that similar analysis can be performed for the other transitions using the appropriate difference IMFs, such that the contribution of each harmonic can be qualitatively assessed. The results of this reveal that the higher harmonics play a vital role in the patterns of the VIs and, thus, influence the ability of the NES to dissipate energy. Furthermore, the results suggest that higher-order TRCs do occur in the dynamics; however, the results do not demonstrate the existence of these TRCs. Thus, we proceed into the next subsection with the objective of demonstrating some of the higher-order TRCs.

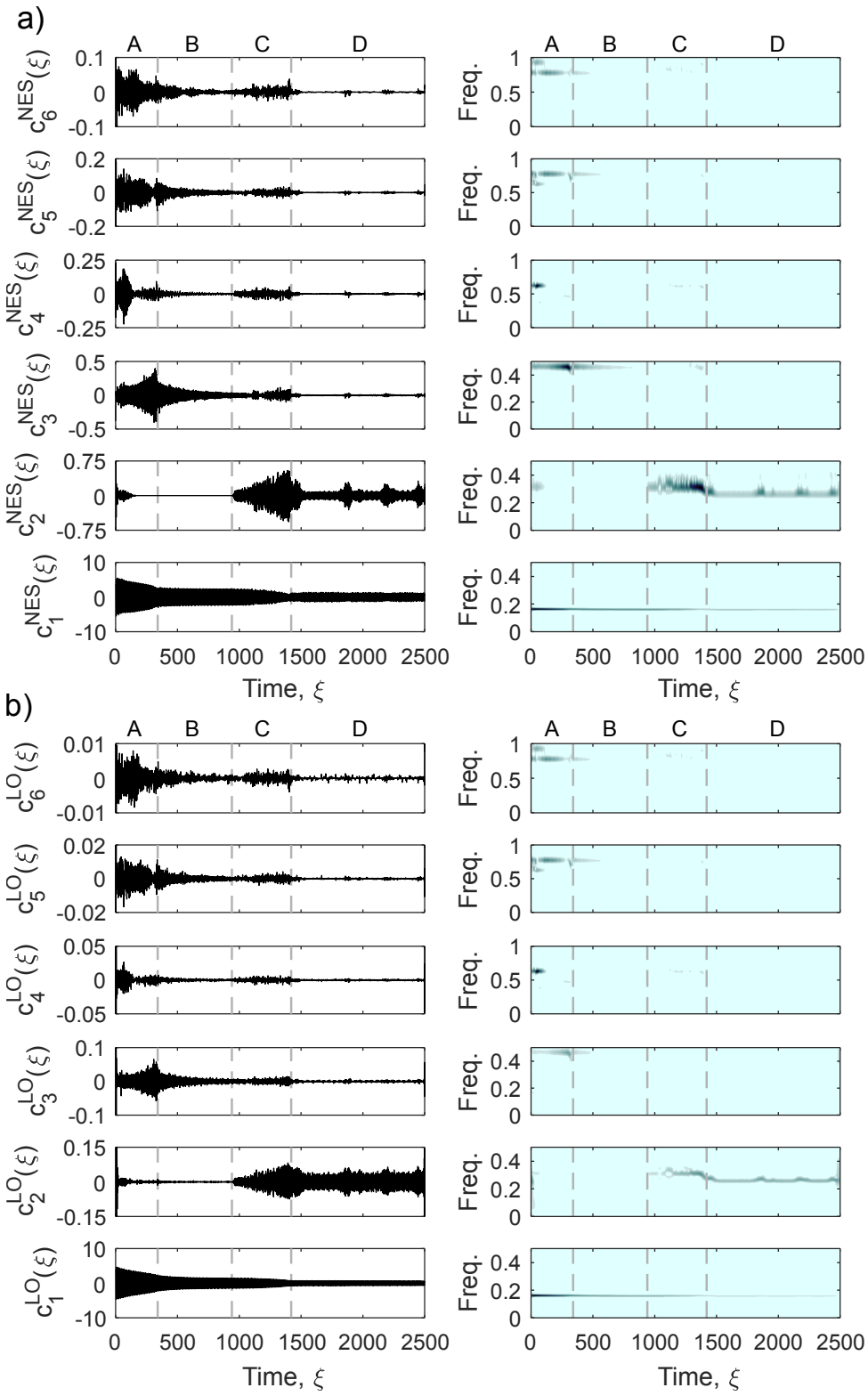

Figure 3.19: Time series, WT spectra, and MWT spectra of the IMFs separated using WBEMD from the absolute displacements of (a) the NES and (b) the LO. The WT spectra have been scaled locally, so that each component is readily visible.

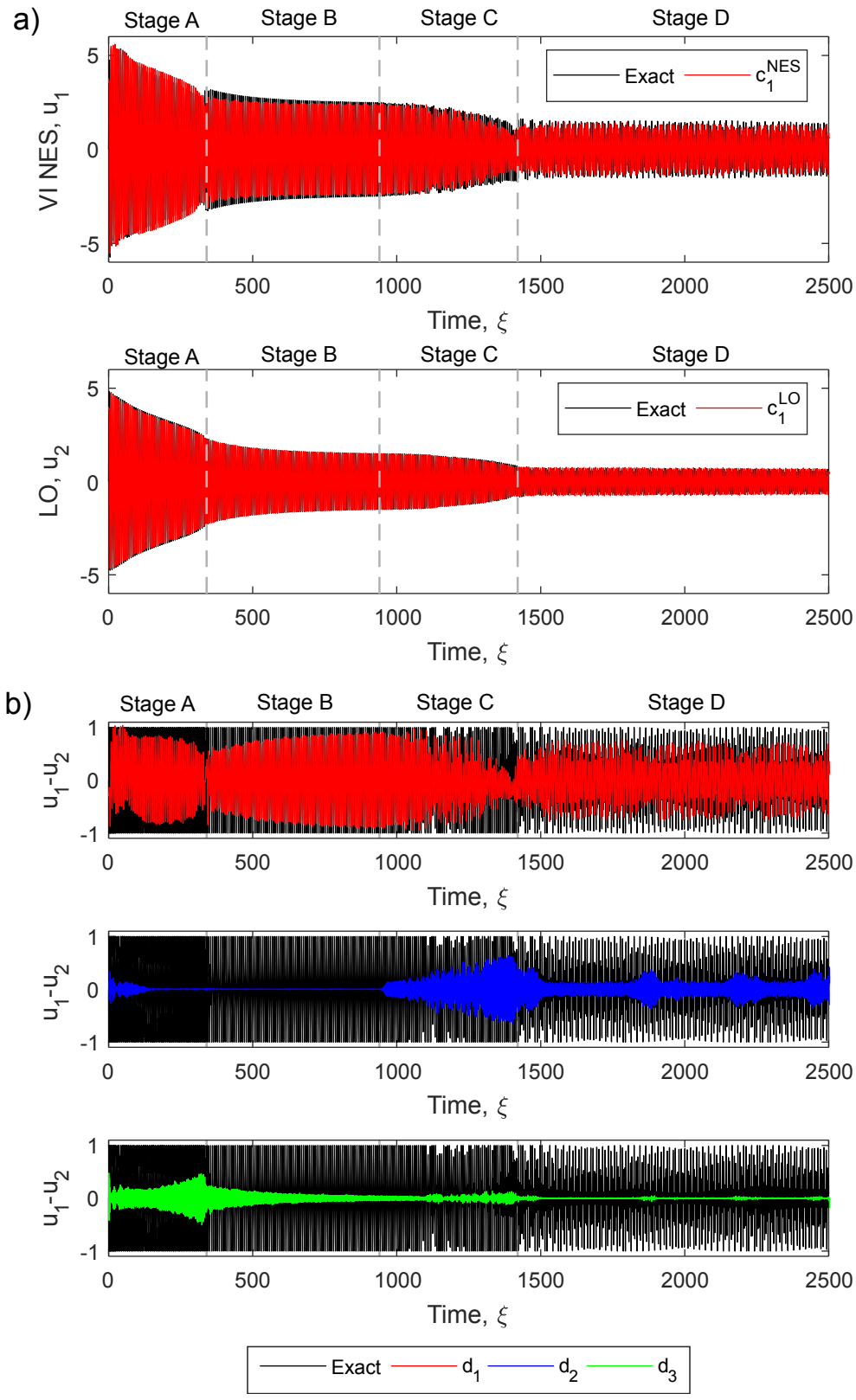

Figure 3.20: Comparison of (a) the exact responses and the first IMF of the NES and LO, and (b) the relative displacement and the lowest three difference IMFs.

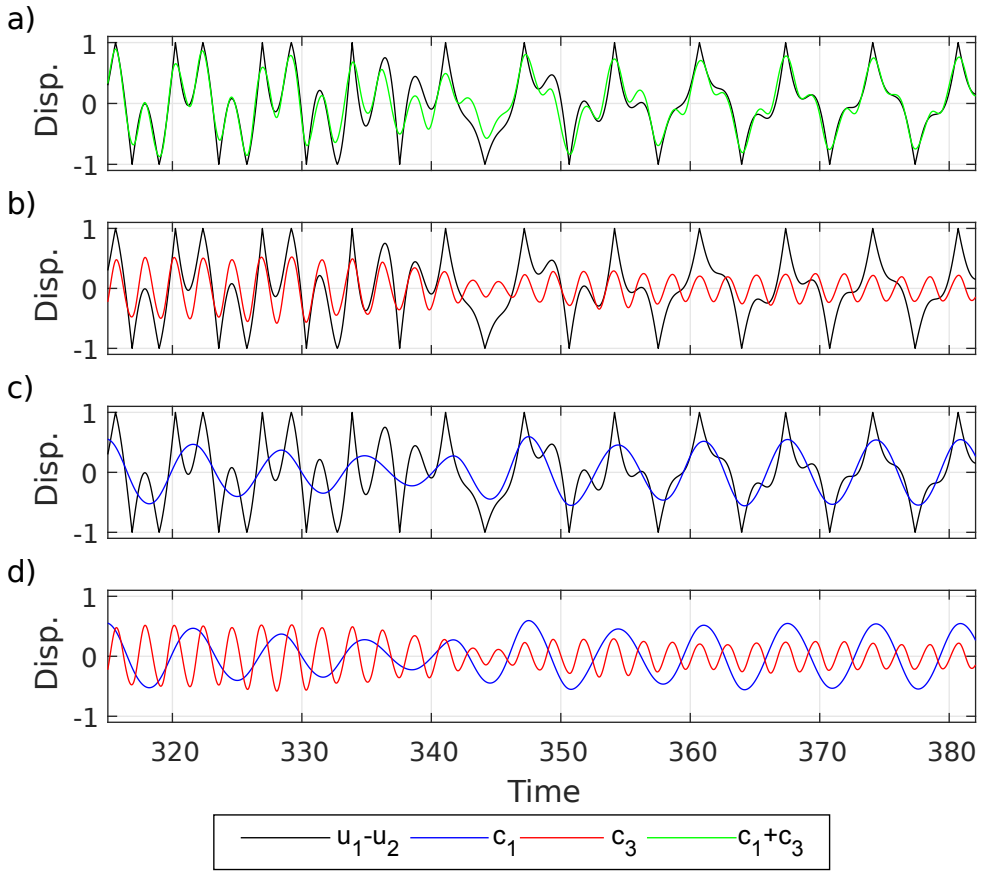

Figure 3.21: Zoomed-in view around the A-B transition of the comparison of (a) the relative displacement and the sum of the first and third difference IMFs; (b) the relative displacement and third difference IMF; (c) the relative displacement and the first difference IMF; and (d) the first and third difference IMFs.

3.4.3.4 Higher-order Internal Resonances

Mathematically, a TRC in the dynamics is associated with non-time-like behavior (non-monotonic behavior) of a certain slow phase of the problem, which leads to the failure of the averaging theorem with respect to that slow phase . To study the phases of the IMFs for the NES and LO, we create the analytic signals

$$\hat{\psi}_i^{NES} = c_i^{NES}(\xi) + j\text{HT}\left\{c_i^{NES}(\xi)\right\} = \hat{A}_i^{NES}(\xi)\exp\left\{j\hat{\theta}_i^{NES}(\xi)\right\}, \tag{3.24}$$

$$\hat{\psi}_i^{LO} = c_i^{LO}(\xi) + j\text{HT}\left\{c_i^{LO}(\xi)\right\} = \hat{A}_i^{LO}(\xi)\exp\left\{j\hat{\theta}_i^{LO}(\xi)\right\}, \tag{3.25}$$

where $\hat{A}_i^{NES}(\xi)$ and $\hat{A}_i^{LO}(\xi)$ are instantaneous amplitudes of the ith IMF for the NES and LO, respectively, $\hat{\theta}_i^{NES}(\xi)$ and $\hat{\theta}_i^{LO}(\xi)$ are the instantaneous phases of the ith IMF for the NES and LO, respectively, and $j = \sqrt{1}$. Then the instantaneous phase of each IMF is computed as

$$\hat{\theta}_i^{NES}(\xi) = \arctan\left(\frac{\text{HT}\left\{c_i^{NES}(\xi)\right\}}{c_i^{NES}(\xi)}\right), \tag{3.26}$$

$$\hat{\theta}_i^{LO}(\xi) = \arctan\left(\frac{\text{HT}\left\{c_i^{LO}(\xi)\right\}}{c_i^{LO}(\xi)}\right), \tag{3.27}$$

The instantaneous frequency of the IMF can be computed by taking the time derivative of the instantaneous phase. In Vakakis et al. [2008], the slow phase is obtained by subtracting the fast phase, $\omega_i\xi$ from $\hat{\theta}_i(\xi)$; however, due to the inelastic VIs the fast frequency, ω_i, is time-dependent, which complicates the extraction of the slow phase. Instead, we define the phase variable for this system to be

$$\Phi_{ij}^{m:n}(\xi) = m\hat{\theta}_i^{LO}(\xi) - n\hat{\theta}_j^{NES}(\xi), i, j = 1, \ldots, 6, m, n \in \mathbb{Z}, \tag{3.28}$$

where the ratio $m : n$ is rational. It is important to point out that, as defined, the phase variable will capture the slow phase only when the fast phases are related by the ratio such that the fast phases are canceled out. This limitation is acceptable because our objective is to study the TRCs that occur at the ratio $m : n$ and directly involve the slow phases. The phase variable can be used to study the existence of TRCs in the dynamics by studying its corresponding phase trajectory; i.e., plotting $\dot{\Phi}_{ij}^{m:n}(\xi)$ against $\Phi_{ij}^{m:n}(\xi)$. In the phase trajectory, TRCs manifest as non-time-like behavior, or loops, and correspond to times where both the instantaneous phases and frequencies are related by the ratio $m : n$. We note that if one were to look for a 1:1 TRC between the LO and NES when the system is in the linear regime, the resulting phase plot would contain no loops. Instead, this phase trajectory would contain a single point at zero phase and frequency

because the instantaneous phase and frequency would be identical. In the case of a $m:n, m \neq n$ TRC in the linear regime, the resulting phase trajectory would be characterized by fast-varying phase with only time-like behavior; that is, no loops would appear in the trajectory. Thus, a $m:n$ TRC can only occur in the nonlinear regime and only when the phases are related by the ratio $m:n$; this is captured in the phase trajectory by small angle changes and loops. Thus, the phase trajectory, as discussed, proves to be the optimal tool for demonstrating the existence of TRCs using IMFs.

We proceed with our analysis returning to the hypotheses proposed in Section 3.4.3.2 and study the appropriate phase variable for each hypothesis. The first hypothesis is that the decay of the transients results in the loss of even TRCs (which corresponds to the loss of the even harmonics), that the first half of stage A is characterized by even and odd TRCs whereas the latter half is characterized by only odd TRCs, and that these losses correspond to the difference in dissipation rates observed in stage A. Thus, we start by examining the phase variable $\Phi_{12}^{2:1}(\xi)$ which represents the lowest even TRC that can occur in the dynamics, and present it in Fig. 3.22(a). We find that only the first half of stage A and all of stage C are slowly varying (regions i-iv) and that all other stages consist of fast-varying phase. Moreover, the disappearance of the second harmonic in stages A and B is captured by the larger slope observed in those stages compared to the slope observed in stage D. To verify that the slow phase corresponds to a 2:1 TRC, we plot the corresponding phase trajectory, i.e., $\dot{\Phi}_{12}^{2:1}(\xi)$ against $\Phi_{12}^{2:1}(\xi)$, in Fig. 3.19(b) and present a zoomed-in view of region i in Fig. 3.22(c). We find that region i contains numerous loops, which indicates that a 2:1 TRC between the first component of the LO and the second harmonic of the NES occurs in stage A. However, after the transients exit the response, we find no further loops until the dynamics transitions into stage C (region ii). Clearly, the latter half of stage A and all of stage B correspond to periods where no 2:1 TRCs occur and, since the 2:1 TRC is the lowest even TRC that can occur in the dynamics, its exit from the response implies that the other even TRCs also exit. Thus, we conclude that even TRCs found in stage A end after the transients exit the response, confirming the first part of the hypothesis.

To verify the second part of the first hypothesis (that odd TRCs occur throughout stage A), we now consider the phase variable $\Phi_{13}^{3:1}(\xi)$ which allows us to study any 3:1 TRCs that occur in the response, and plot it in Fig. 3.23(a). We find that stage A is characterized by a brief period of fast-varying phase followed by slowly varying phase (region i). More importantly, this slow phase, that is unaltered by the loss of the transients, exists throughout stage A and is interrupted only at the A-B transition. This suggests that the 3:1 TRC lasts throughout stage A, and we turn to the corresponding phase trajectory depicted in Fig. 3.23(b) and the zoomed-in view of region i in Fig. 3.23(c). The phase trajectory reveals that region i does correspond to a 3:1 TRC (as indicated by the loops), and that this TRC is sustained throughout stage

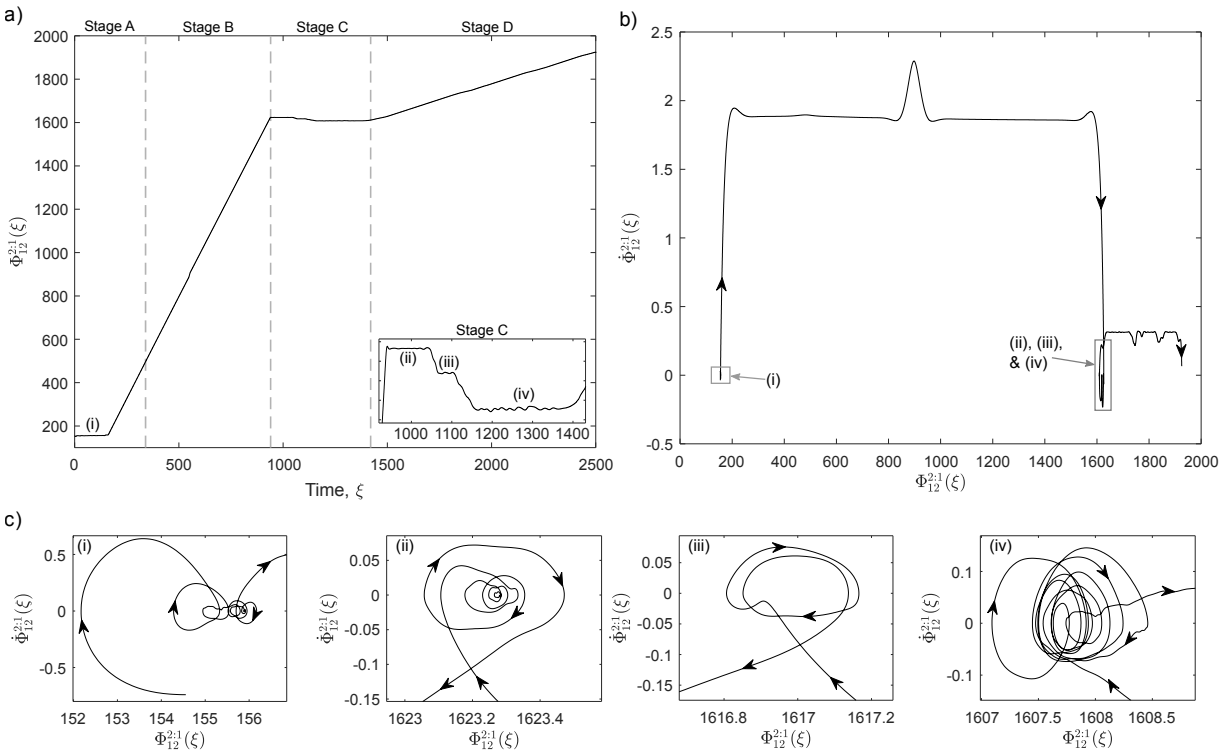

Figure 3.22: (a) Instantaneous phase $\Phi_{12}^{2:1}(\xi)$ with example slow angles indicated by i-iv, (b) phase trajectory depicting the TRCs, and (c) zoomed-in views of i-iv which reveal the presence of multiple 2:1 TRCs.

A. Since this 3:1 TRC is the lowest odd TRC that can occur in the dynamics, it is evident that the odd TRCs do not exit the dynamics with the transients as the even TRCs do. This confirms the first hypothesis proposed in 3.4.3.2 and, moreover, provides an insight into the difference in dissipation rates observed for the two stages.

The second hypothesis presented in Section 3.4.3.2 is that the B-C transition results in the reappearance of the 2:1 TRC and the disappearance of the 3:1 TRC. Looking first at Fig. 3.22, we find that stage C contains several periods of slowly varying phase (regions ii-iv). The phase trajectories, Figs. 3.22(b) and 3.22(c), verify that slow phases in regions ii-iv do correspond to 2:1 TRCs between the first harmonic of the LO and the second harmonic of the NES. The presence of three different 2:1 TRCs is a result of the chaotic and irregular motion observed in stage C, and most likely is the result of bifurcations and branch changes in the dynamics [Lee et al., 2005]. To test the second part of the hypothesis, we turn to Fig. 3.23, which reveals that the slow phase initiated in stage B survives the B-C transition and is interrupted part way through stage C. After the interruption, the dynamics briefly escapes from the 3:1 TRC only to be recaptured by another 3:1 TRC. This cycle is repeated one more time until the third harmonic completely

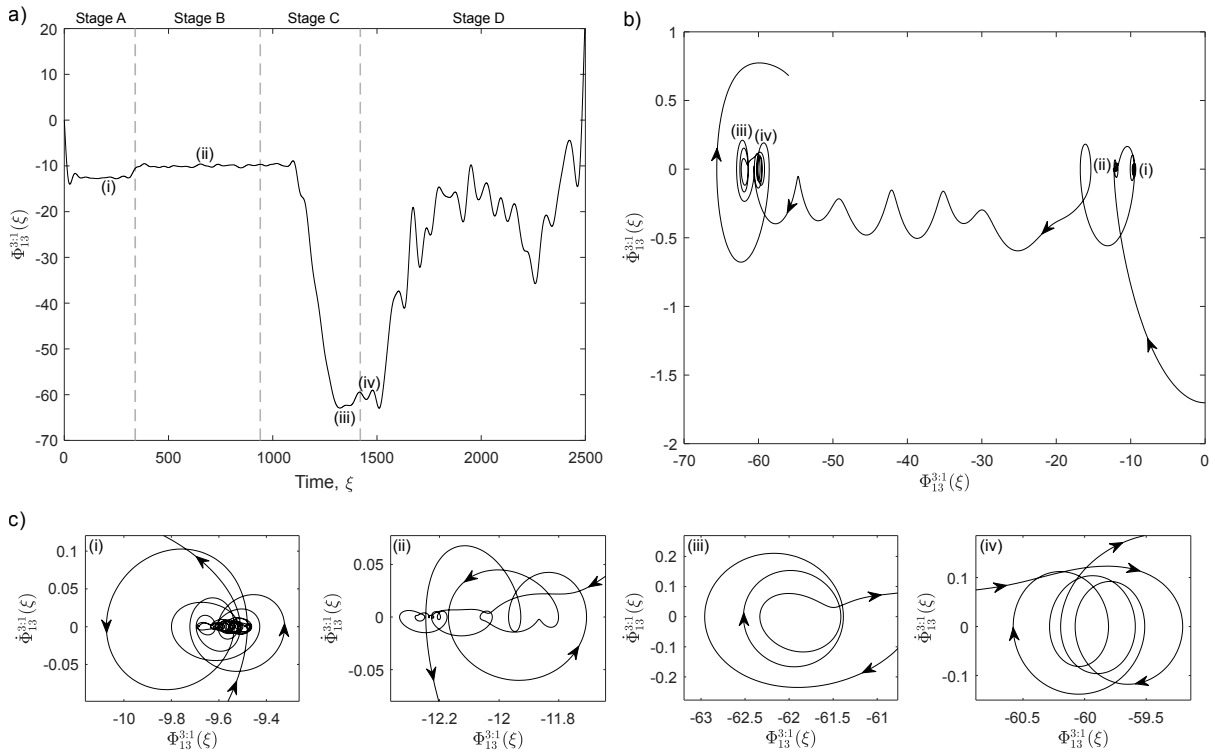

Figure 3.23: (a) Instantaneous phase $\Phi_{13}^{3:1}(\xi)$ with example slow angles indicated by i-iv, (b) phase trajectory depicting the TRCs, and (c) zoomed-in views of i-iv which reveal the presence of multiple 3:1 TRCs.

exits the dynamics in stage D. This result reveals that the B-C transition is the result of the re-emergence of the 2:1 TRC only and is unrelated to any change in the 3:1 TRCs.

Moreover, the phase plots and trajectories reveal that stage D does not contain, for the most part, any higher TRCs, which confirms the first part of the third hypothesis proposed in Section 3.4.3.2. Although Lee et al. [2009a] demonstrated the existence of a 1:1 TRC facilitated by the first harmonic, this is not the only type of 1:1 TRC that can populate the dynamics. Indeed, the NES can absorb energy from the LO through the second harmonic, and we depict the corresponding phase variable in Fig. 3.24(a). We find that stages A, C, and D contain slowly varying phases, which correspond to the periods where the second component participates in the response. More important, the 1:1 TRC remains uninterrupted for the entirety of stages C and D, confirming that stage D contains only 1:1 TRCs. The substantial decrease in dissipation observed in stage D is attributed to the fact that only 1:1 TRCs, which dissipate energy at much slower rates than higher-order TRCs, are present in this stage. Without any other source of dissipation, the system becomes trapped in stage D such that no higher-order TRCs ever appear in the dynamics and the 1:1 TRCs persist.

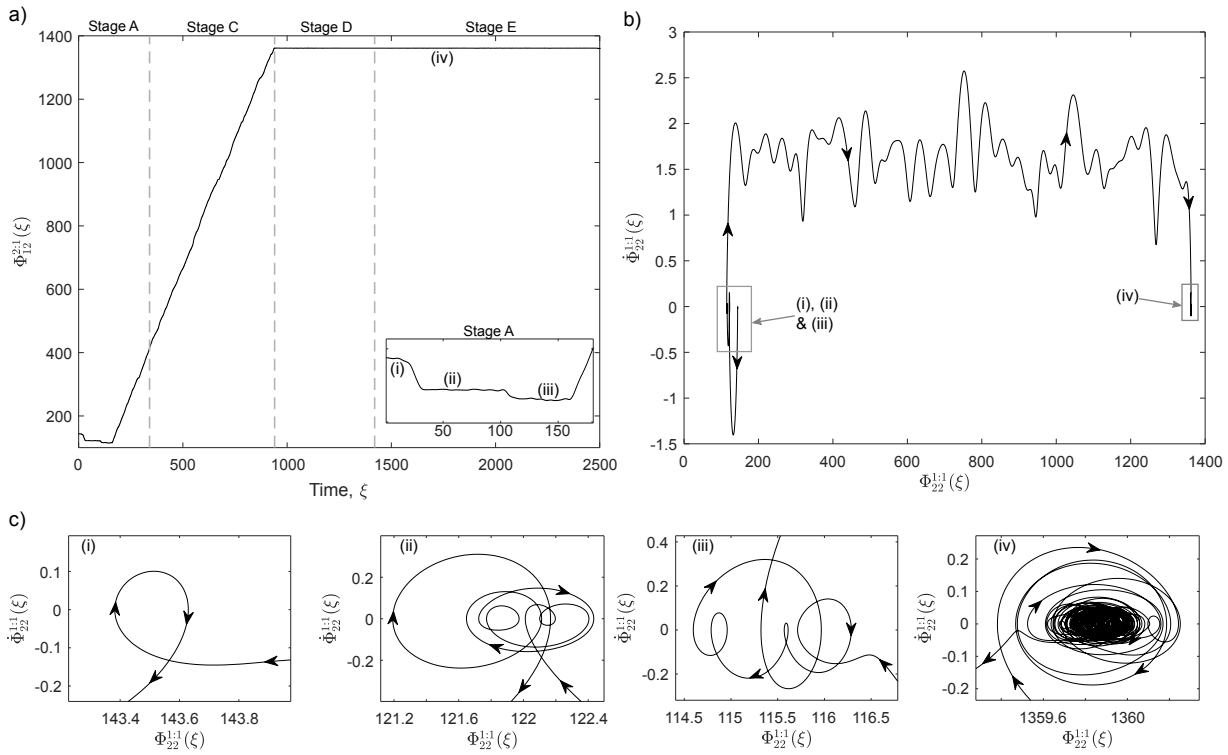

Figure 3.24: (a) Instantaneous phase $\Phi_{22}^{1:1}(\xi)$ with example slow angles indicated by i-iv, (b) phase trajectory depicting the TRCs, and (c) zoomed-in views of i-iv which reveal the presence of multiple 1:1 IRs between the third harmonics in the NES and LO.

3.4.4 Concluding Remarks

We studied the response of a single-degree-of-freedom LO with a VI NES subject to an impulse applied to the LO. Using the displacement and velocity time series of both the LO and NES, we partitioned the dynamics into five separate stages and found that each stage corresponded to different participating harmonics, dissipation rates, and number of VIs per fundamental period. The wavelet-bounded empirical mode decomposition algorithm was employed to decompose the displacement responses into six well-separated IMFs, each representative of a different harmonic contained in the response. From the IMFs, appropriate phase variables were computed and used to demonstrate the existence of higher-order TRCs that facilitate the transfer of energy from the LO to the NES. We found that each stage was governed by different combinations of TRCs and that the presence of higher-order TRCs (e.g., 2:1 TRC) in a stage corresponded to the observed differences in dissipation rates and number of VIs per period.

The results presented in this work study only some of the possible TRCs that can populate the dynamics. Indeed, every higher harmonic observed in the response of the NES during stage A corresponds to an integer multiple of the first harmonic and, thus, each component engages in a higher-order TRC with the

first harmonic. The analysis for studying these TRCs is identical to the analysis for the 1:1, 2:1, and 3:1 TRCs presented in Section 3.4.3.4 so long as the appropriate phase variable is selected. The results demonstrate the strength of the WBEMD approach for studying the strongly nonlinear interactions that occur in systems with VIs, and the resulting IMFs can be used to gain significant insight into the governing physical processes. In addition, the presented results demonstrate the efficacy the wavelet-bounded EMD to analyze the nonlinear interactions of the transient responses of non-smooth coupled oscillators. As such, and to the authors' knowledge, this methodology is unique in the literature, due to its capacity to extract, identify and analyze strongly nonlinear interactions of strongly nonlinear oscillating processes with smooth and non-smooth effects.

3.5 Discussion

In our examples, we used WBEMD to decompose strongly nonlinear signals into well-separated IMFs. These IMFs provided significant insight into the underlying physics governing each system. However, this physical understanding is limited by how strongly the components participate in the dynamics. Specifically, the weaker the participation of a component the more challenging it is to extract that component using WBEMD. By applying WBEMD, we sacrifice the ability to extract every component in order to extract IMFs that are representative of the strong components. With this limitation in mind, the biggest deficiency of WBEMD is that orthogonality is not considered in the algorithm. Instead, the focus of WBEMD is to extract IMFs that are isolated around a component in the MWT domain. Thus, in theory, it is entirely possible for WBEMD to extract IMFs that are well-separated, but not even remotely orthogonal. In our experiments, we found that the index of orthogonality between IMFs extracted using WBEMD are typically comparable to that of the IMFs extracted using EMD or EEMD. However, applying EMD and EEMD resulted in mixed, and therefore physically meaningless, IMFs whereas applying WBEMD resulted in well-separated and meaningful IMFs.

Obtaining meaningful IMFs depends on the choice of bounding function and masking signal, which, in general, depends on the signal being decomposed. In this work, we chose a Gaussian bounding function and sinusoidal masking signal based on a mixture of experience and observation. These choices worked quite well for the signals studied herein; however, we expect for signals with numerous nonstationary components, which individually span large frequency ranges, that the success of a stationary masking signal will become quite limited. For such signals, a nonstationary masking signal must be developed and incorporated into the WBEMD algorithm. Additionally, WBEMD may struggle with decomposing signals which possess components that start off at distinct frequencies and shift to the same frequency. For such components, WBEMD

extracts an IMF that corresponds to the first component before combining with the other component and a second IMF which contains the second component and the combined components. In the current implementation, WBEMD cannot accurately separate intersecting components, such as two intersecting chirps. When applied to such signals, WBEMD extracts IMFs with "V" shapes in the WT domain, similar to the result when applying EMD, as observed by Liang et al. [2005].

In this dissertation, WBEMD was applied to study the NNMs, IRs, and TRCs that govern and occur in the dynamics of two strongly nonlinear mechanical systems. However, there are numerous fields where EMD is already used that would benefit from WBEMD. For example, both EMD and EEMD have been used to study the complex, multi-scale processes that occur in the sun and how these processes affect the Earth. Specifically, Coughlin and Tung [2004] applied EMD to study the 11-year solar cycle and Xiang and Qu [2016] applied EEMD to study the fluctuations in the solar mean magnetic field. In both applications, the IMFs were related to specific processes that occur in the sun and, thus, might benefit from using WBEMD. Pachori and Bajaj [2011, 2012] applied EMD to electroencephalogram (EEG) signals, which measure brain activity levels, and used the IMFs to discriminate normal EEG signals from epileptic seizure EEG signals. By improving the decomposition through using WBEMD, the IMFs may provide better discrimination between non-epileptic and epileptic patients and might help provide a physical understanding of these differences. As a final example, Zhang et al. [2016] and Wang et al. [2016] applied EMD and EEMD, respectively, to short-term wind speed measurements and used the IMFs to create models that reproduced the measured time-series and could be used to predict future wind speeds. The accuracy of these models depends strongly on the IMFs, and thus could be improved by applying WBEMD. Finally, just as EMD has been extended to multivariate analysis [Rehman and Mandic, 2010], we believe that WBEMD can be extended to multivariate analysis with some adaptation to the bounding function and masking signals.

All too often, EMD and EMD-based methods are used to extract IMFs blindly; that is, to extract IMFs without being aware of the frequency content of the original signal. Furthermore, without this knowledge and inspecting the frequency content of the IMFs, it is impossible to distinguish physically meaningful IMFs from the spurious or mixed, and thus physically meaningless, IMFs. Worse yet, important physics can be lost in poorly separated IMFs, and physical interpretation of spurious IMFs can lead to drastic misunderstanding of the physics contained in the signal. In contrast, WBEMD does not act blindly, but targets specific characteristic frequencies (as provided by the analyst) and extracts IMFs that correspond to those components. As such, the issue of spurious IMFs that plague EMD, EEMD, and other EMD-based methods is eliminated. More importantly, WBEMD necessitates that the analyst be aware of the frequency content of the signal in that they must be able to choose specific characteristic frequencies to extract from that

signal. Another key advancement of WBEMD lies in the wavelet-bounding of the extracted component; that is, minimizing the bounding function such that the isolation of the IMF around its characteristic frequency is maximized. The wavelet-bounding procedure is entirely independent of the decomposition method, and EMD can be replaced with nearly any decomposition method, provided that the method results in time-varying components and relies on parameters that can be varied by the optimization algorithm. For example, EMD could be replaced by EEMD, and the overall decomposition will either remain the same or improve, so long as the parameters used to create the white noise and the number of averages is used as free variables in the minimization.

3.6 Concluding Remarks

We applied a closed-loop, optimization-based solution, called wavelet-bounded EMD (WBEMD), to the problem of mode-mixing. This approach optimizes an IMF by isolating it around the corresponding component in the frequency domain. Specifically, the original time signal and IMF are transformed using the MWT, and a bounding function is used to measure the quality of the IMF. The bounding function is defined such that it encompasses the transformed IMF and is centered about the characteristic time scale with maximum amplitude greater or equal to that of the transformed time signal. Since the bounding function depends on the specific IMF extracted, we used the area under the bounding function as a measure of the quality of the IMF in the frequency domain. We found that, as the IMF becomes more isolated around its corresponding component, the area under the bounding function becomes smaller. This observation formed the basis of an optimization routine with the objective of minimizing the bounding-function area and the masking signal parameters serving as free parameters. The result is a powerful and semi-automated algorithm that relies minimally on the analyst and is capable of decomposing strongly nonlinear and nonstationary signals into physically representative IMFs.

Chapter 4

Direct Detection of Strongly Nonlinear Modal Interactions

4.1 Introduction

As mentioned in Section 1.2, Herrera et al. [2017] generalized the results described in [Kurt et al., 2014a] by applying POD to extract proper orthogonal modes (POMs), representative of the participating NNMs, and computing the Rayleigh quotient (RQ) using the POMs as trial vectors. An estimated FEP was created by plotting the resulting RQs as functions of energy, which revealed that the dynamics could be partitioned into three distinct regimes: two linear regimes in the limits of low and high energy, and a strongly nonlinear transition regime connecting the other two. These regimes were different for each NNM since each modal response depends on the system energy, and the duration of the nonlinear transition regime was found to increase with increasing frequency. Moreover, the curves in the RQ-FEP were found to contain non-smooth perturbations (spikes) that appeared to indicate strongly nonlinear modal interactions, i.e., dynamic mixing between NNMs in internal resonance; however, the previous study did not provide conclusive proof to substantiate this claim. As such, the focus of this chapter is to determine the physical meaning of the aforementioned non-smooth effects in the frequency estimates, and, in particular, to demonstrate the correspondence between the spikes on the RQ-FEP and the strongly nonlinear modal interactions that occur due to IRs in the measured time series. After presenting a theoretical analysis with an impulsively forced linear cantilever beam with a local strong stiffness nonlinearity, an experimental study of this system is performed in order to validate the theoretical findings and prove conclusively that the non-smooth effects in the frequency estimates derived by the proposed methods are attributed to nonlinear modal interactions due to the local stiffness nonlinearity of the system considered.

4.2 Computational Study

4.2.1 System Configuration

We apply the proposed approach to the cantilever beam depicted in Fig. 4.1, which has a local, smooth nonlinearity attached near its free end. The beam is made from steel (with modulus of elasticity 200 GPa, and density 7800 kg/m^3), is uniform and homogeneous, and has a length of 1.311 m, a width of 0.0446 m, and a thickness of 0.008 m. An essentially nonlinear (nonlinearizable) spring with a stiffness coefficient of 5×10^8 N/m^3 and a pure cubic force-displacement law (c.f., Fig. 4.2) was attached transversely near the free end of the beam to ground. We assume light, viscous damping and use the viscous damping ratios found in a prior study of the same system [Mane et al., 2011, Kurt et al., 2012, 2014b] for the first ten modes. These viscous damping ratios are provided in Table 4.1, and the ratios for higher modes were assumed to be equal to 0.001. We discretized the beam into 100 Euler-Bernoulli beam elements, where each element consisted of two nodes, each with a translational and rotational degree of freedom (DOF). The beam was subjected to the impulsive-type load depicted in Fig. 4.3 and defined as,

$$F(t) = P \sin\left(\frac{\pi t}{0.0006}\right) \left(H(t) - H(t - 0.0006)\right), \tag{4.1}$$

where $H(t)$ is the Heaviside function. The duration of the applied load was chosen to be comparable to the force provided by a standard modal hammer with a hard, plastic tip. To probe the dynamics over a large energy range, we varied the amplitude, P, from 10 to 10^{12} N. Specifically, we chose 1000 logarithmically spaced points between 10 and 10^{12} N and simulated 1 second of the transient response of the beam for each value of the force amplitude P using ode45 in MATLAB® with a time step of 10^{-5} s. The response was simulated for only 1 second because, due to weak damping, the response of the system remains approximately stationary in this window. The beam parameters, forcing amplitudes and location, and the nonlinearity were chosen based on previous studies done in [Mane et al., 2011, Kurt et al., 2012, 2014b, Herrera et al., 2017].

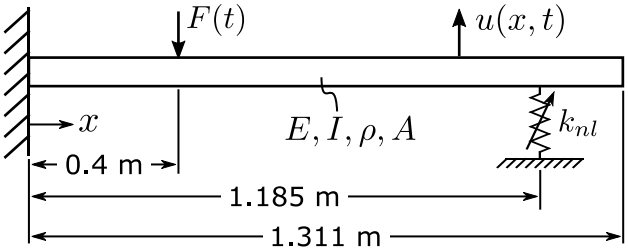

Figure 4.1: Schematic of the cantilever beam with a local attached strongly nonlinear spring used in the computational study.

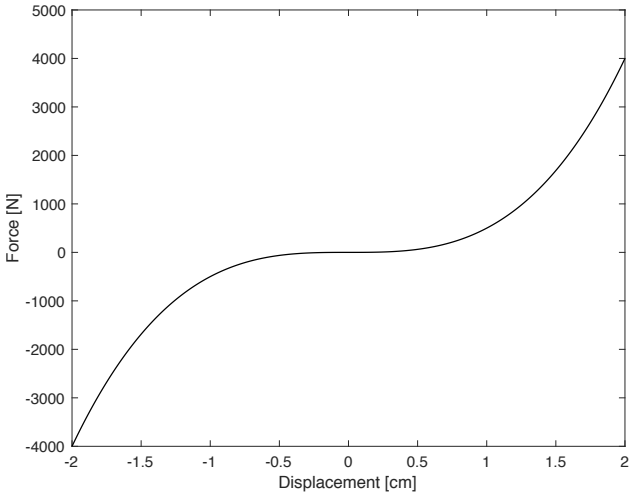

Figure 4.2: Force-displacement law governing the nonlinear spring attached to the free end of the beam.

Table 4.1: Frequencies and viscous damping ratios for the leading 10 modes of the underlying linear beam.

Mode #	**Frequency [Hz]**	**Damping Ratio**
1	3.794	0.0071
2	23.78	0.0011
3	66.60	0.0014
4	130.6	0.0029
5	216.2	0.0068
6	323.9	0.0013
7	454.5	0.0073
8	608.9	0.0018
9	787.3	0.0023
10	978.7	0.0015

In the absence of the local strong stiffness nonlinearity, the cantilever beam possesses linear normal modes of vibration. When the nonlinear stiffness is added the beam possesses nonlinear normal modes (NNMs) of vibration which, in the absence of internal resonances, are synchronous vibrations that may be regarded as nonlinear extensions of the linear vibration modes [Vakakis et al., 1996]. Modal interactions between NNMs can occur when certain internal resonance conditions are met, in which case nonlinear modal interactions and nonlinear energy exchanges between NNMs occur, and mode mixing is realized; in that case, non-synchronous oscillations occur with more than one mode participating in the dynamics. Moreover, the modal characteristics of nonlinear dynamical systems are intrinsically dependent on their energy, which in this study is related to the forcing amplitude.

Accordingly, an interesting feature of the strongly nonlinear cantilever beam considered in this study is

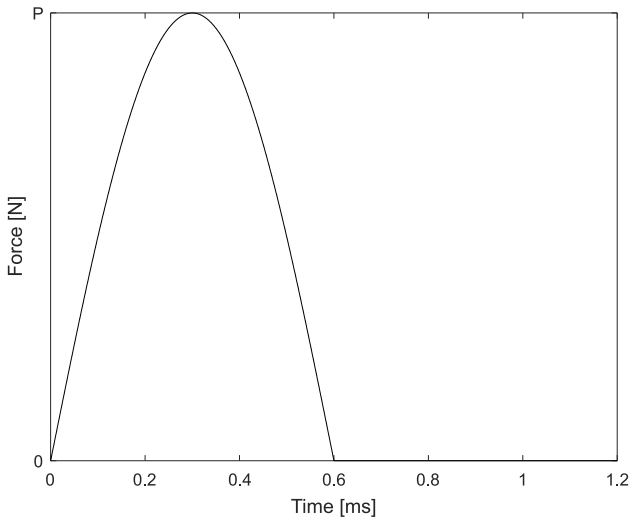

Figure 4.3: Forcing function applied to the beam in the computational study with variable amplitude denoted by P.

that, depending on its instantaneous energy, its dynamics can be categorized into two limiting linear regimes and an intermediate (bridging) strongly nonlinear regime that connects the two limiting linear regimes. Indeed, in the limit of low energy (low forcing amplitude), the local nonlinear restoring force of the spring is negligible, and the system behaves as a linear cantilever beam with no spring attachment; this is the low energy limiting regime of the dynamics. In the limit of high energy, however, the restoring force of the spring is so large that all translational motion is restricted at the attachment point, and the system behaves again as a linear system but, in this case, as a fixed-pinned beam; this represents the high-energy limiting regime of the dynamics. Thus, at these two limits, the modal characteristics are independent of energy, and the beam behaves linearly. The limiting two linear regimes are connected through a strongly nonlinear transition regime, where the modal characteristics depend strongly on the forcing amplitude (i.e., the overall system energy).

By selecting such a large forcing range, we ensure that the dynamics are probed adequately in all three regimes. However, we recognize that the upper limit of the forcing range is not physically realizable in this particular study since it corresponds to unrealistically high forcing amplitudes; however, we show all three regimes to highlight the drastic change in the dynamics that a change in energy precipitates. We note that these three regimes can be realized by other means; e.g., as in a previous study [Herrera et al., 2017]. There, a cantilever beam with a vibro-impact boundary condition was realized through a clearance and the three regimes resulted from varying the clearance from zero (the lower limiting linear regime) to large values (the upper limiting linear regime). At intermediate values of the clearance, the strongly nonlinear bridging regime

was realized corresponding to the occurrence of vibro-impacts.

4.2.2 Detection of Strongly Nonlinear Modal Interactions

Following the completion of each simulation, we apply POD to the translational response at each node and obtain the first 100 POMs. The frequency of each POM is estimated using the discrete Rayleigh quotient and the Guyan-reduced mass and stiffness matrices. Because the POD algorithm sorts the POMs by singular value and not by mode number, we re-sort the POMs based on estimated frequency such that the first POM corresponds to the lowest frequency. The estimated frequencies are plotted as functions of the total energy induced by the forcing function, and form the RQ frequency-energy plot (FEP). In Fig. 4.4, we plot the RQ-FEP for the first four POMs. As mentioned before, in the limits of low and high energy the system behaves linearly, and these two regimes are represented by straight lines in the RQ-FEP since they do not depend on energy. Indeed, at low energies the estimated frequencies of the POMs converge to the horizontal black dashed lines of the plot, whereas at high energies the frequency estimates converge to the horizontal gray dashed lines. The black and gray dashed lines correspond to the leading natural frequencies of the (linear) fixed-free and fixed-pinned beam configurations, respectively. More importantly, a strongly nonlinear transition regime appears to bridge the previous two linear regimes where the estimated frequencies, and therefore the POMs, depend on the instantaneous energy of the system.

Additionally, non-smooth perturbations (in the form of spikes) emanate from the curves and appear to indicate strongly nonlinear interactions between the NNMs. Indeed, when the ratio between the frequencies of two or more NNMs becomes close to a rational number, a subharmonic bifurcation occurs, and the NNMs enter into a regime of internal resonance (IR) where energy is scattered from low to high frequencies [Vakakis et al., 2008]. In the case of IR between two NNMs, nonlinear mode mixing occurs, and the resulting periodic solution is non-synchronous and contains a mix of the NNM with the lower frequency and of the higher NNM. Moreover, with varying energy, mode conversion from one NNM to the other occurs. As such, a first step in evaluating the physical significance of the spikes is to compare the POMs before, on, and after the occurrence of each spike.

To this end, we examine the first two spikes that occur in the RQ-FEP and present a zoomed-in view of them in Fig. 4.5. The first spike is spread out over several points, whereas the second spike occurs over a single point. This is a result of the spacing between forcing values; the second spike can be captured by simulating additional forcing values. However, the fact that the second spike occurs over a relatively small energy range indicates that the dynamics possess a stronger sensitivity to the energy around the second spike than around the first spike. Figure 4.6 presents the first and second POMs corresponding to the six red

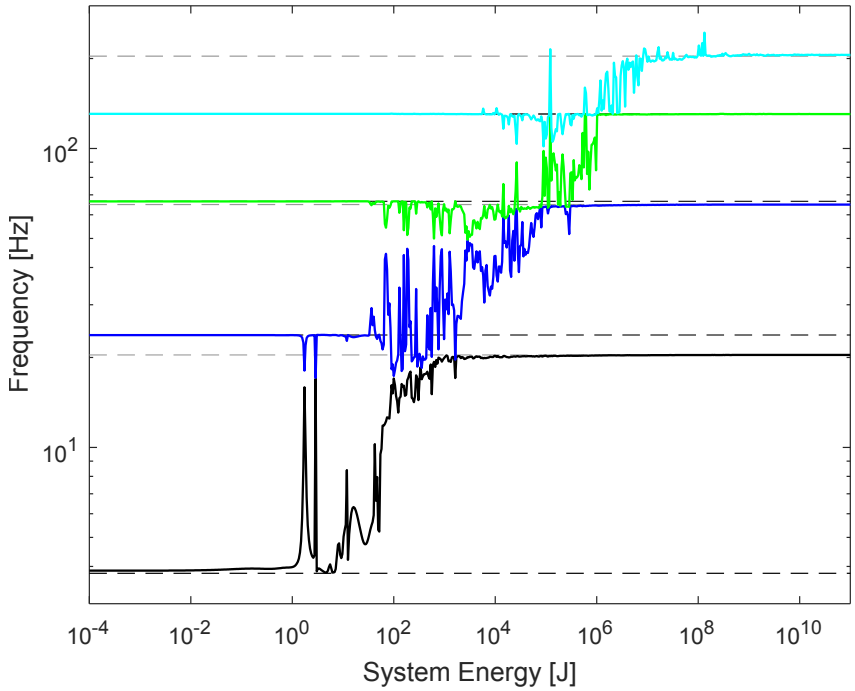

Figure 4.4: Estimated frequency energy plot (FEP) created using the Rayleigh quotient (RQ) and computed POMs for the first four NNMs; the dark and gray dashed lines represent the linear frequencies in the limits of low and high energies, respectively.

dots in Fig. 4.5. We find that the POMs on the spike, plots 4.6(b) and 4.6(e), differ greatly from those off the spike. Off the spike, the POMs correspond to the periodic solutions of their respective non-interacting NNMs in that the first POM has a single anti-node at the free end, whereas the second POM has anti-nodes near its center and at the free end of the beam. In contrast, on the spikes the POMs do not correspond to their non-interacting periodic solutions and, instead, appear as deformed versions of the periodic solution of the second NNM. Since POD relies entirely on the time series data, the fact that the first and second POMs become similar on the spike, but remain distinct off the spike allows us to rule out that the spikes are an artifice created by the RQ. Instead, the POMs indicate that the dynamics fundamentally differs on and off the spikes. Furthermore, the fact that the leading two POMs on the spikes are similar could suggest that the two NNMs enter into an IR where energy is transferred from the first to the second NNM, and nonlinear mode mixing occurs. This either means that the POMs are not representative of their respective NNMs, or that there is, in fact, a difference in the dynamics on and off the spike.

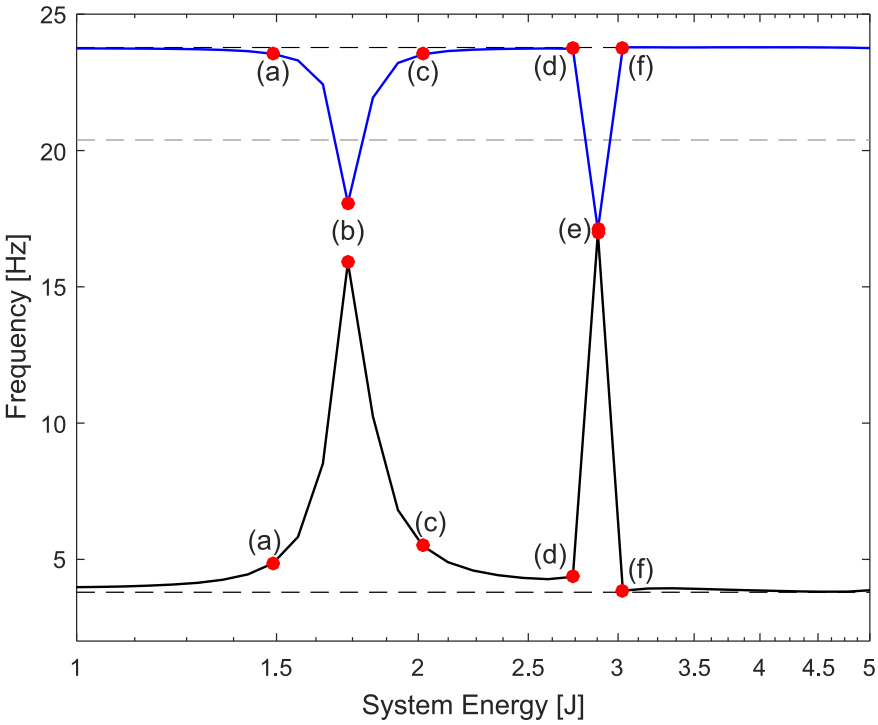

Figure 4.5: Zoomed-in view of the first two modal interactions between NNM 1 and 2. The dark and light gray, dashed lines represent the linear frequencies at low and high energies, respectively. The red dots correspond to the POMs depicted in Fig. 4.6.

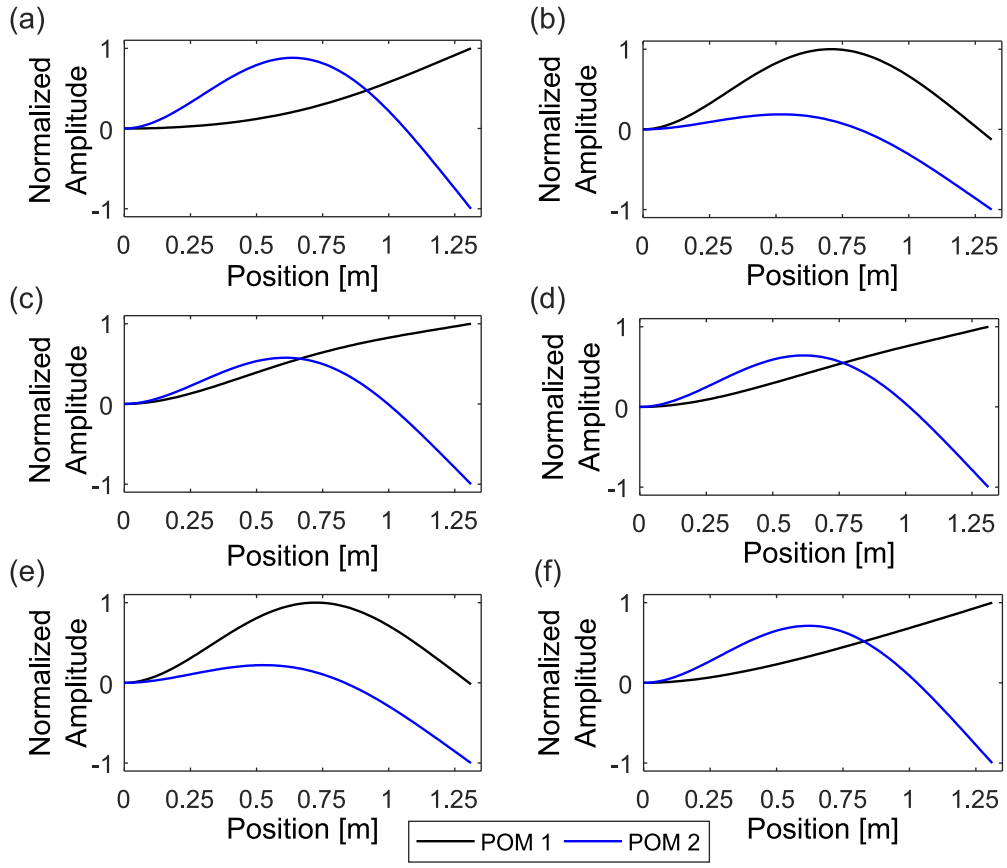

Figure 4.6: Comparison of POMs 1 and 2 corresponding to the six red dots in Fig. 4.5; the plots of (b) and (e) correspond to the spikes of Fig. 4.5 and the occurrence of internal resonance between the leading two NNMs.

4.2.3 Slow-flow Analysis Using WBEMD

Although the comparison of POMs is highly suggestive of the existence of IRs, it does not provide conclusive evidence that IRs actually occur. To show that IRs do occur on the spikes, we take a step back from POD and examine the time series corresponding to each point shown in Fig. 4.5. In Fig. 4.7, we present the time series and corresponding wavelet and Fourier spectra for each of the six points depicted in Fig. 4.5. We find that the displacement response differs for each level of forcing, confirming that the dynamics is amplitude-dependent and that the maximum displacement obtained is approximately 0.02 m, a level that can be realized in experiments. The corresponding wavelet transform spectra confirm that the frequency content remains nearly stationary for the length of each time series. Proceeding, we apply WBEMD and decompose the displacement response into six IMFs, where each IMF is bounded around a single frequency of interest. The time series and wavelet spectra are presented in Fig. 4.8 for each of the six points in Fig. 4.5. The wavelet spectra reveal that the IMFs are well-separated and that each IMF contains only one frequency component. Typically, the IMF with the highest frequency is termed the first IMF since it is the first obtained from EMD. However, for this study, we relabel the IMFs such that the first IMF has the lowest frequency and corresponds to the first NNM. The remaining IMFs are labeled sequentially such that the nth IMF corresponds to the nth NNM. As discussed in [Moore et al., 2018b], when the IMFs are well-separated they are representative of their respective NNMs. More importantly, the IMFs can be used to show the existence of IRs by examining the slow phases of the NNMs.

Mathematically, an IR in the dynamics is associated with the non-time-like (that is, non-monotonically varying, appearing as loops in the phase plots) behavior of a certain slow phase of the problem, which leads to the failure of the averaging theorem with respect to that slow phase [Vakakis et al., 2008]. Specifically, an IR occurs between two IMFs $c_1(t)$ and $c_2(t)$ with phases $\hat{\theta}_1(t)$ and $\hat{\theta}_2(t)$, respectively, when their instantaneous frequencies satisfy the following approximate relationship,

$$m\hat{\theta}_1(t) - n\hat{\theta}_2(t) \approx \text{const} \Rightarrow m\hat{\theta}_1(t) \approx n\hat{\theta}_2(t), t \in [T_1, T_2]\,, \tag{4.2}$$

where the time interval $[T_1, T_2]$ defines the duration of the IR [Vakakis et al., 2008]. For the current system, we compute the instantaneous phase of each IMF using the expression

$$\hat{\theta}_i(t) = \arctan\left(\frac{\text{HT}\left\{c_i(t)\right\}}{c_i(t)}\right), i = 1, 2, \tag{4.3}$$

where $\text{HT}\left\{\cdot\right\}$ refers to the Hilbert transform. In [Vakakis et al., 2008], the slow phase is obtained by

subtracting the fast phase, $\omega_i t$, from $\hat{\theta}_i(t)$; however, due to the damping in the system, the fast frequency, ω_i, is time dependent, which complicates the extraction of the slow phase. Instead, we define the phase variable for this system to be

$$\Phi_{m:1}(t) = m\hat{\theta}_1(t) - \hat{\theta}_2(t), \dot{\Phi}_{m:1}(t) = m\dot{\hat{\theta}}_1(t) - \dot{\hat{\theta}}_2(t), m = 1, \ldots, 6, \tag{4.4}$$

and recognize that the slow phases are only fully separated when the fast phases are related by a $m:1$ ratio. This limitation is acceptable because our objective is to investigate the existence of IRs between the first two NNMs. In general, the number of slow phase combinations that should be studied depends on the ratio between the frequencies of the NNMs. If an $m:1$ IR is suspected, we suggest that the phase trajectories from $(m-2):1$ to $(m+2):1$ be examined to test the original hypothesis and to verify the results. We recommend that the analyst starts with searching for $m:1$ IRs, which are the most common IRs, to explain the spikes in the RQ-FEP; however, if these cannot explain the spikes then the analyst should progress to searching for $m:n$ IRs.

Figure 4.9 presents the phase trajectories up to a ratio of 6:1 from the first two IMFs depicted in Fig. 4.8 for each point in Fig. 4.5. The first set of phase trajectories, Fig. 4.9(a), correspond to the point (a) in Fig. 4.5, which is to the left of the first spike. We find that all six phase plots exhibit time-like behavior, which indicates that no IRs occur at this energy level since there is no slow phase in the transient dynamics. Moreover, the direction of increasing time for the 5:1 and 6:1 trajectories is opposite that of the other trajectories, which means that the frequency ratio of the first two NNMs is somewhere between 4:1 and 5:1. Since the first NNM exhibits a strong dependence on energy at lower energies than that for the second NNM, their frequency ratio will decrease as energy increases until a 4:1 ratio is achieved resulting in a 4:1 IR. As such, if the first spike is physically representative of an IR, it should be a 4:1 IR. We proceed by examining the phase trajectories in Fig. 4.9(b), corresponding to the point (b) on the spike in Fig. 4.5. We find that all trajectories except the 4:1 phase trajectory exhibit time-like behavior. The 4:1 phase trajectory is shown in Fig. 4.10(a) with a zoomed-in view of the non-time-like behavior, which appears as loops around zero phase velocity and over a small phase range. We note that the window in which the 4:1 IR occurs spans almost 0.5 seconds, nearly half of the total simulation duration. The appearance of non-time-like behavior in the 4:1 phase trajectory demonstrates that the time series corresponding to the peak of the first spike contains a 4:1 IR. Given that most of the 4:1 phase trajectory is non-time-like (with only the initial and final portions exhibiting time-like behavior), we conclude that the 4:1 IR is sustained for almost the entire simulation. Since the IR results in an energy transfer from the first NNM to the second, which

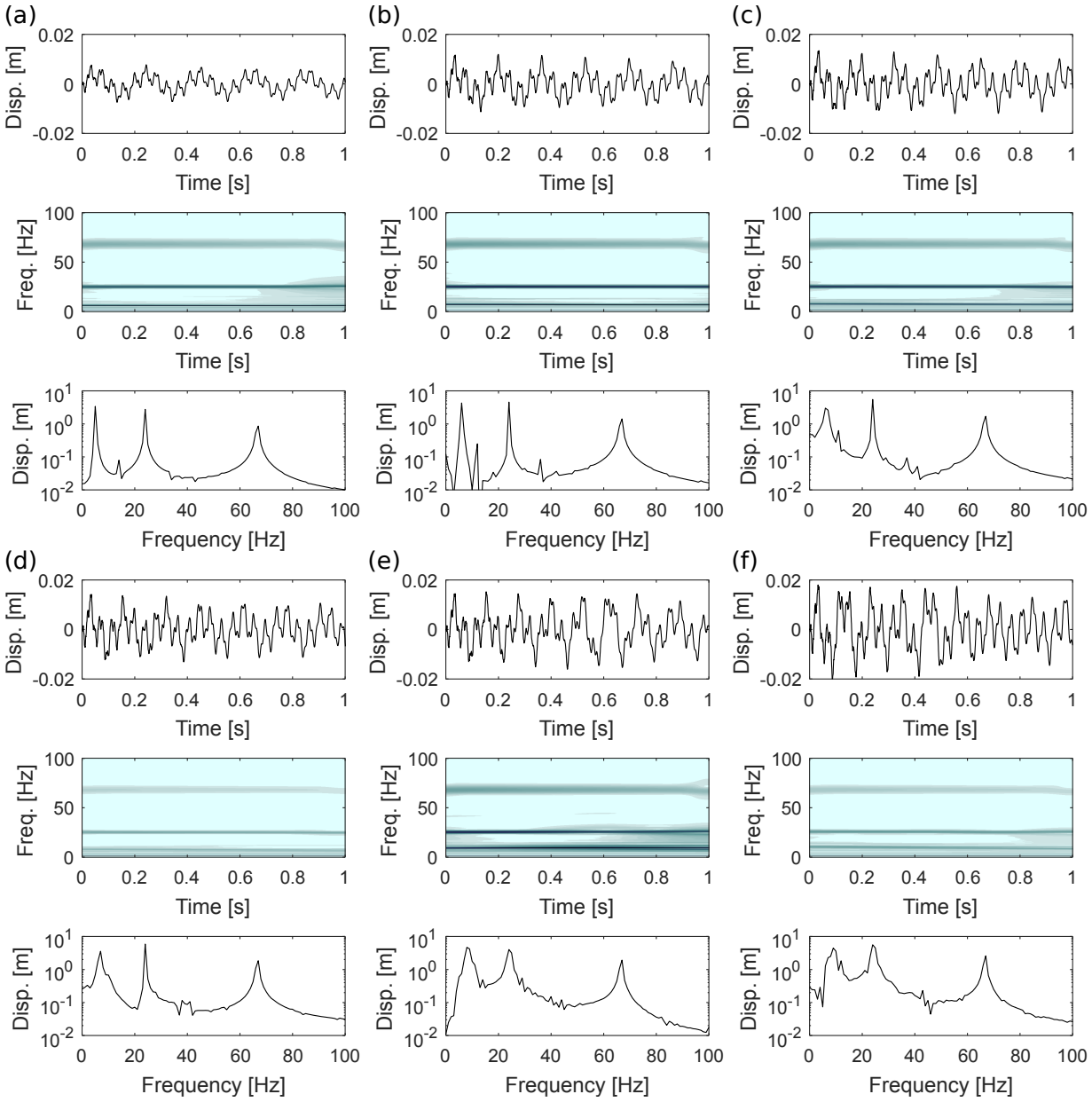

Figure 4.7: Time series, wavelet spectrum, and Fourier spectrum of the displacement response of the free end of the beam corresponding to the six points depicted in Fig. 4.5.

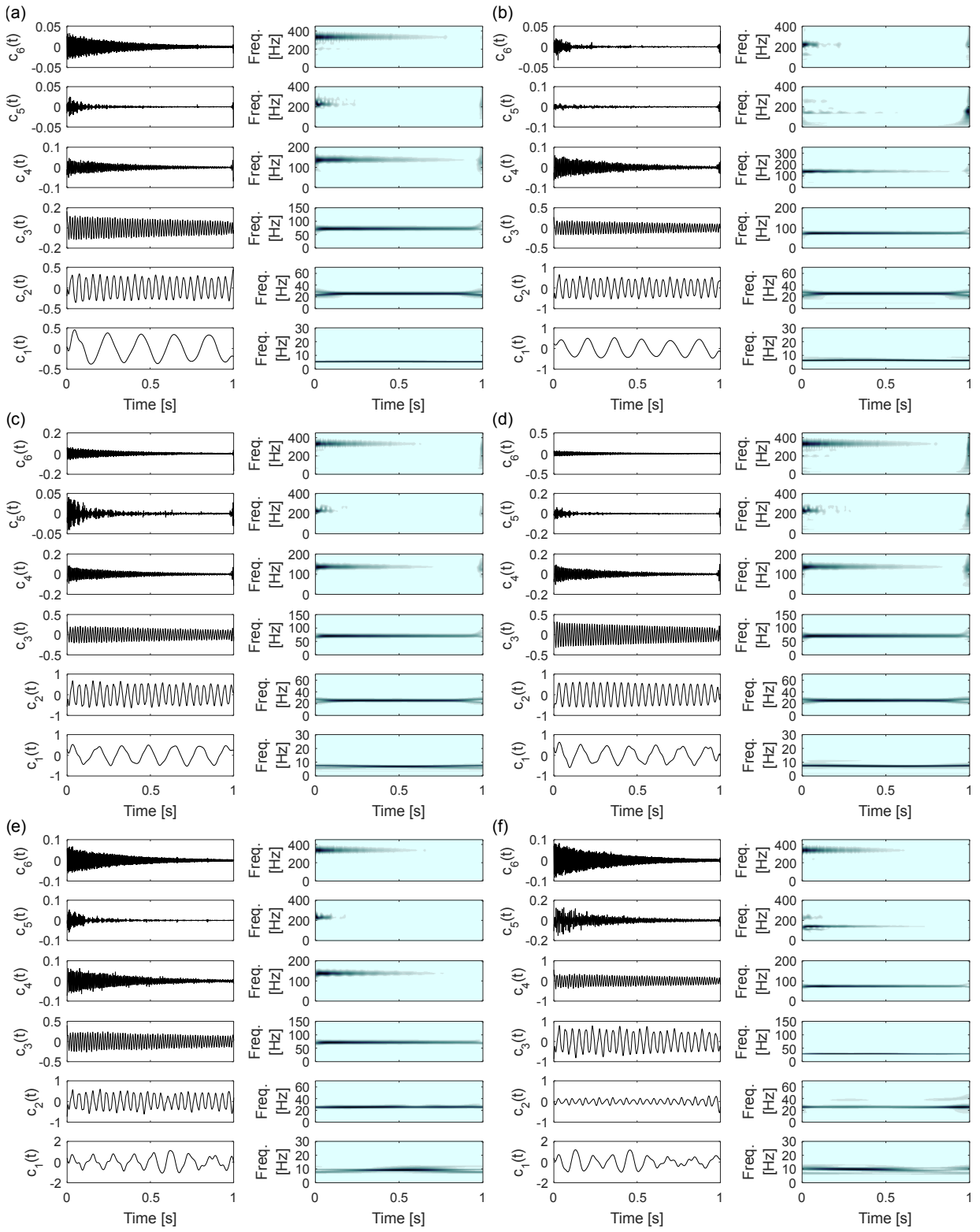

Figure 4.8: Time series and wavelet spectra of the IMFs extracted from the displacement responses shown in Fig. 4.7.

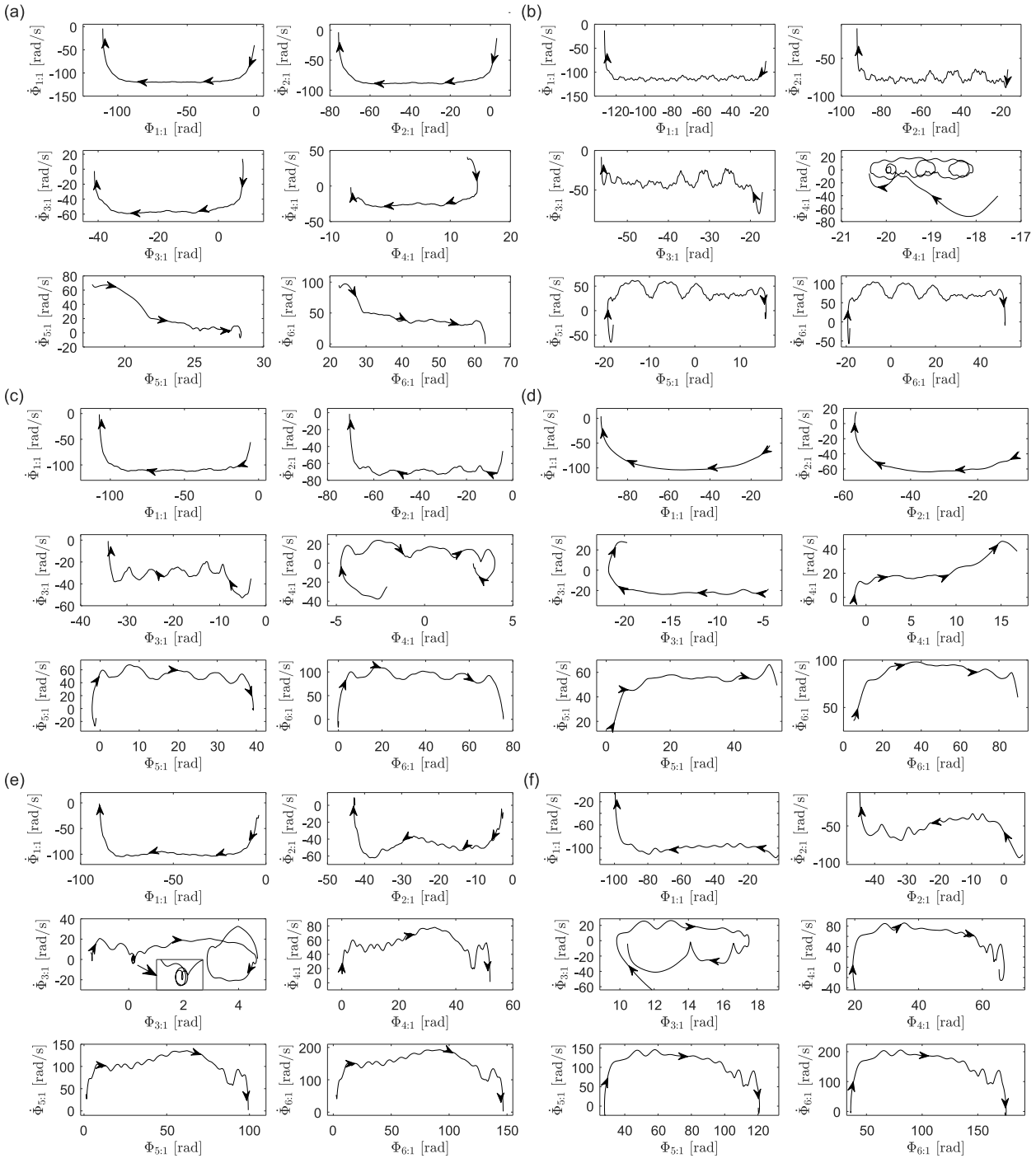

Figure 4.9: Time series, wavelet spectrum, and Fourier spectrum of the displacement response of the free end of the beam corresponding to the six points depicted in Fig. 4.5.

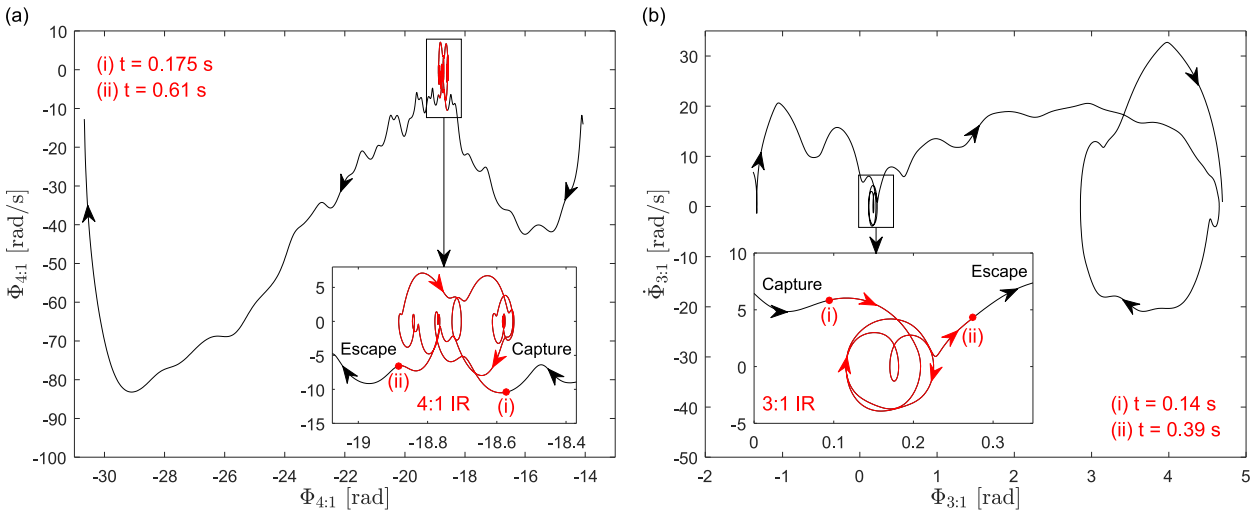

Figure 4.10: Time series, wavelet spectrum, and Fourier spectrum of the displacement response of the free end of the beam corresponding to the six points depicted in Fig. 4.5.

dissipates energy faster, the longer the 4:1 IR is sustained the more energy is dissipated and, consequently, the dynamics must exhibit a weaker dependence on energy around the first spike than at higher energies. Additionally, the direction of increasing time for the 5:1 and 6:1 trajectories is opposite that of the other trajectories, which confirms that the IR frequency ratio is 4:1. Finally, we examine the phase trajectories, depicted in Fig. 4.9(c), of the IMFs corresponding to the point to the right of the first spike, and find that all the phase trajectories exhibit time-like behavior. Just as with the point before the first spike, this shows that the time series contains no IRs. Additionally, the direction of time now changes between the 3:1 and 4:1 trajectories, which indicates that the frequency ratio is between 3:1 and 4:1, such that no IR is possible. These results demonstrate that the first spike in the RQ-FEP is the product of a strongly nonlinear modal interaction that occurs due to a 4:1 IR between the first two NNMs.

Although we have demonstrated that the first spike corresponds to a 4:1 IR, this result does not show that all spikes correspond to IRs. Thus, we now examine the second spike starting with the phase trajectories in Fig. 4.9(d), which corresponds to the point just left of the second spike in Fig. 4.5. Figure 4.9(d) reveals that all phase trajectories exhibit time-like behavior and, thus, the time series contains no IRs. The direction of increasing time changes between ratios of 3:1 and 4:1, indicating that the frequency ratio is still between 3:1 and 4:1, and that the next IR will occur once a 3:1 ratio is achieved. Proceeding, we examine Fig. 4.9(e), which corresponds to the point at the peak of the second spike in Fig. 4.5, and find that the 3:1 phase trajectory exhibits non-time-like behavior whereas all other phase trajectories exhibit time-like behavior. The 3:1 phase trajectory is shown in Fig. 4.10(b) with a zoomed-in view of one of the non-time-

like behaviors, which appears as loops around zero phase velocity and over a small phase range. Two other non-time-like behaviors appear in the plot: a small loop at the far left and the large loop at the right. However, we note that these loops appear near the ends of the signal and could be the result of end-effects that result in errors in the IMFs. The appearance of non-time-like behavior demonstrates that the second spike is the result of a 3:1 IR between the first two NNMs. Moreover, the fact that most of the non-time-like behavior appears in the center of the phase trajectory verifies our previous conclusion from the RQ-FEP that the dynamics possesses a stronger dependence on energy around the second spike than that of the first spike. Finally, inspecting Fig. 4.9(f), which corresponds to the point to the right of the second spike, we find that all the trajectories exhibit time-like behavior and, thus, the dynamics off the spikes does not contain any IRs.

4.3 Experimental Study

To validate the previous methodology, we apply it to the experimentally measured response of the cantilever beam depicted in Fig. 4.12(a). The beam was made from low-carbon steel and had a length of 0.749 m, a width of 0.045 m, and a thickness of 0.008 m. It was connected to two steel wires located 0.7 m from the fixed end. The steel wires were fixed at both ends, and each had a diameter of 0.0012 m and length of 0.0762 m. Using two shaft collars, the wires were mechanically connected to a steel shaft that extended from the beam. The attachment, depicted in Fig. 4.12(b), as well as the length of the beam, were specifically tuned such that the frequency ratio of the first and second NNM at low energy (linear response) was sufficiently close to a 3:1 ratio such that a 3:1 IR was achieved with a low-amplitude excitation.

An impact from a PCB Piezotronics modal impact hammer (model 086C01) was applied to the beam at the position of the attachment, and the acceleration response of the beam was measured at 14 locations along the beam using PCB accelerometers (models U356A11 and Y353B17) all with a nominal sensitivity of 1.02 $\text{mV}/(\text{m}/\text{s}^2)$. The accelerations were measured at a sampling rate of 16,384 Hz for a duration of 2 seconds using VibPilot hardware (m+p International, Hannover, Germany) and m+p analyzer software. After the measurements had been taken, it was found that the 9th accelerometer was saturated in all measurements and was excluded from the analysis. Note that, the 9th accelerometer was not located at a node or anti-node for either the first or the second NNM and, consequently, did not influence the outcome of the experiment or our analysis.

Following the measurements, the accelerations were numerically integrated, and the resulting velocities were passed through a third-order, high-pass Butterworth filter with a cutoff frequency of 18 Hz. The

filtered velocities were then numerically integrated and passed through the same filter, except with a cutoff frequency of 10 Hz. The temporal mean was also subtracted before and after each integration such that the accelerations, velocities, and displacements were zero mean. Subtracting the temporal mean accounts for the small DC offsets due to gravity and small variations in the orientation of the accelerometers. Alternatively, the displacements could have been estimated using a variational approach, such as in [Moreu and Spencer, 2015], or with a Kalman filter [Kalman, 1960]; however, the integration procedure described above was sufficient for this work, and the integrated displacement responses are used in the remainder of our analysis in this section.

(a)

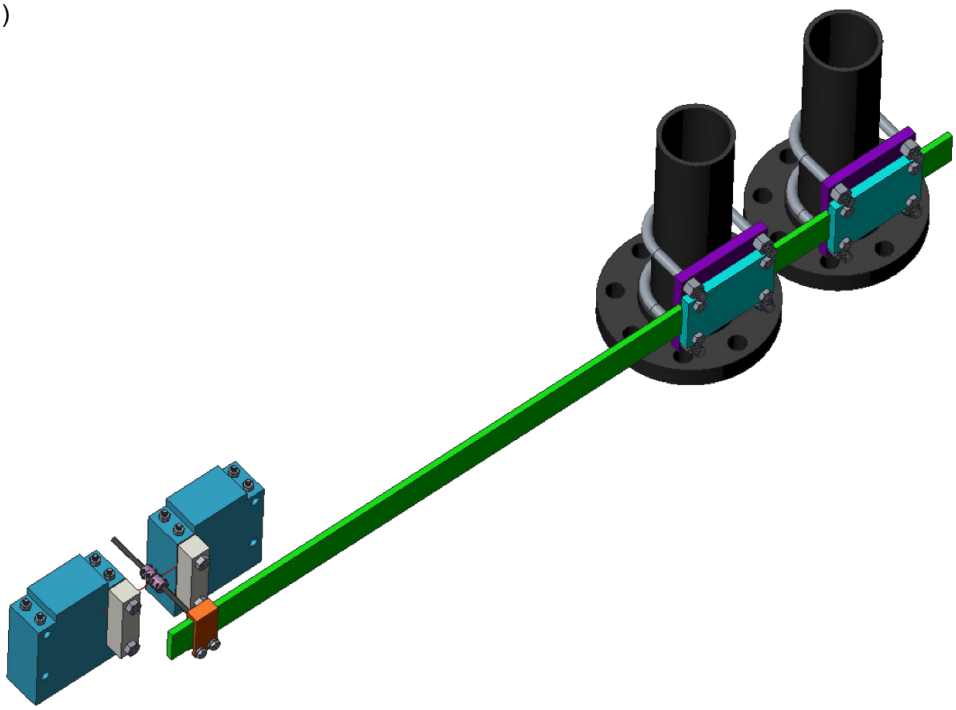

(b)

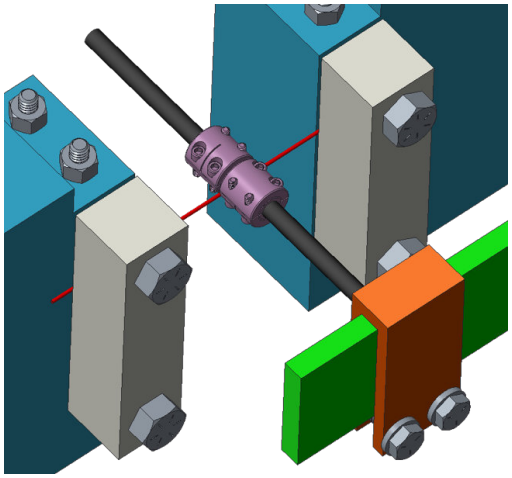

Figure 4.11: (a) CAD model of the beam used in the experiments. (b) Zoomed-in view of the nonlinear attachment CAD model.

(a)

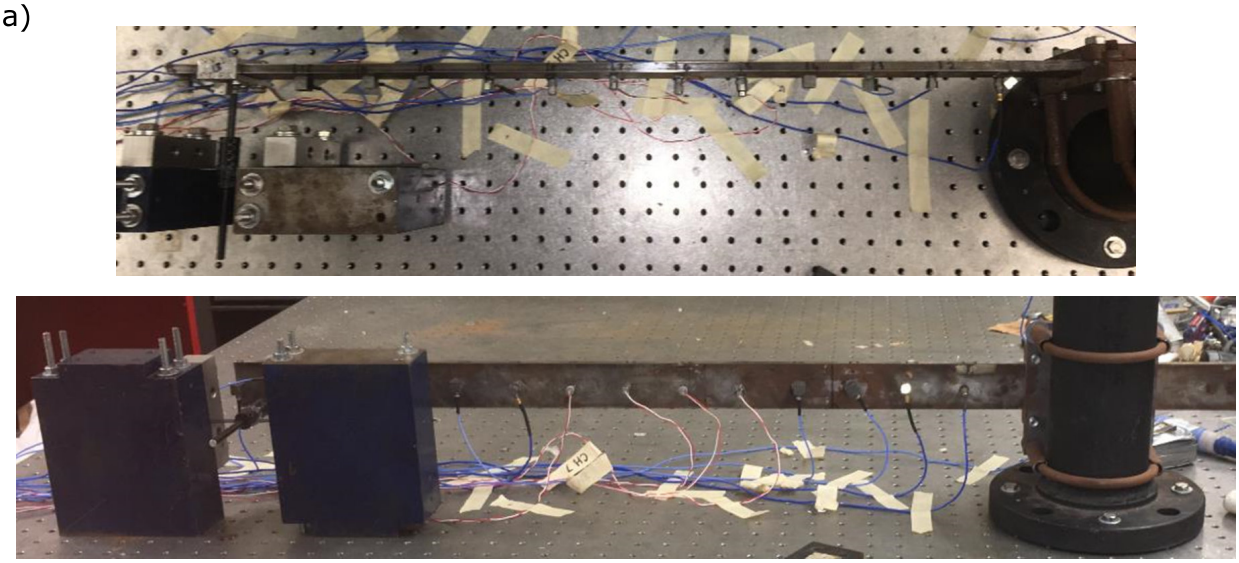

(b)

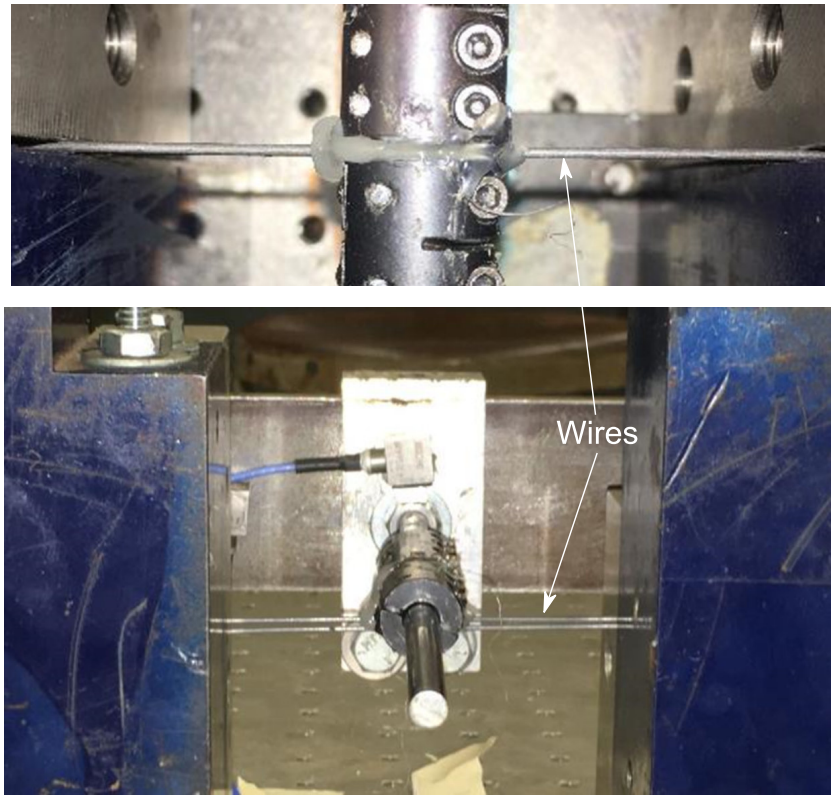

Figure 4.12: (a) Top and front view of beam used in experiments. (b) Top and front view of nonlinear attachment.

4.3.1 Experimental Linear Model Updating

To demonstrate the application of the presented method, we study the displacement response of the beam in Fig. 4.12 to the large amplitude impact depicted in Fig. 4.13(a). The displacement response at the attachment location and the corresponding wavelet and Fourier spectra are depicted in Fig. 4.13(b). Both the wavelet and Fourier spectra reveal the nonstationary nature of the response. From the FFT, the first and second NNMs cover a frequency range of 21.6 to 31.5 Hz and 68.8 to 73 Hz, respectively, whereas the third NNM contains a single peak at 186.6 Hz, which indicates that the system energy is not large enough for the third and higher NNMs to shift in frequency. While the FFT reveals the nonlinear nature of the signal, the wavelet spectrum is a better tool for analyzing the characteristics of the response. Looking at the wavelet spectrum, we observe a hardening nonlinearity as the frequency of the first NNM begins at 31 Hz and decreases to 21.5 Hz as energy dissipates. This is expected as the attachment, in theory, should behave like a spring with a cubic force-displacement relationship, which results in a hardening response. In this experiment, a purely cubic force-displacement relationship was not realized due to the thickness of the wires, and the attachment was not designed to be essentially nonlinear. Instead, the attachment exhibited a sum of linear and nonlinear stiffnesses with an approximately cubic force-displacement relationship.

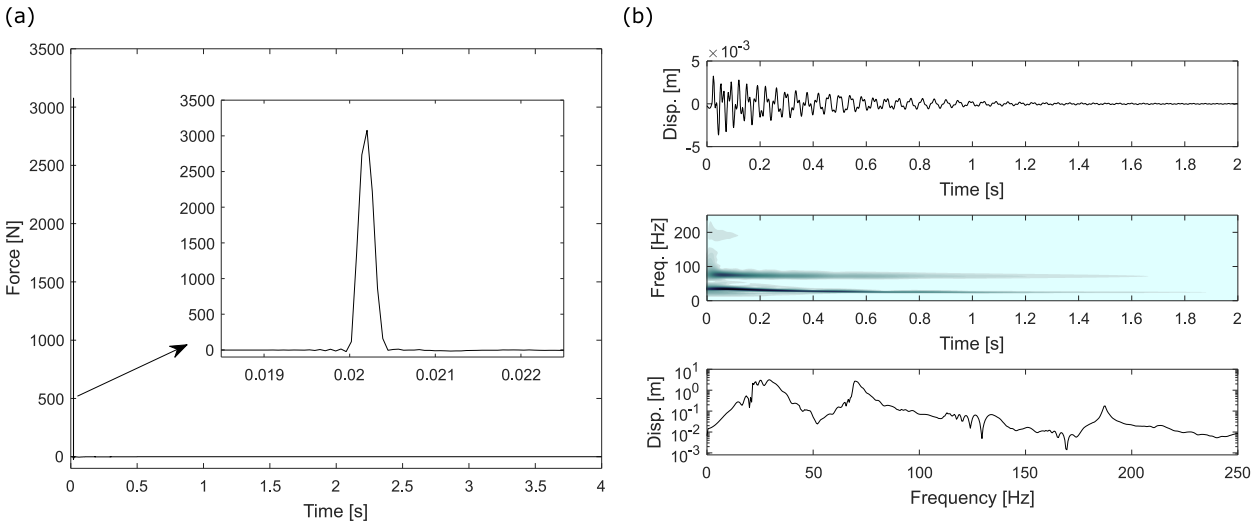

Figure 4.13: (a) High amplitude, impulsive load applied at nonlinearity location, (b) Time series, wavelet transform, and FFT of the displacement at the nonlinearity location (integrated from accelerometer measurements).

Since our method does not require a priori knowledge of the nonlinearity, the nonlinearity was not identified in this work, and the attachment was modeled as a point mass and a discrete linear spring from the beam to ground. The mass of the attachment was measured to be 0.171 kg, and the density of the beam

Table 4.2: Comparison of eigenfrequencies measured experimentally for low-amplitude forcing with those predicted using the FE model.

NNM #	**Experiment [Hz]**	**FE Model [Hz]**	**Percent Error [%]**
1	20.90	20.90	0
2	68.3	68.7	-0.06
3	188.3	194.1	-3.09
4	373.3	387.0	-3.69
5	614.3	645.7	-4.49
6	927.0	967.0	-4.32

was chosen to be 7800 kg/m^3. The elastic modulus of the beam and the linear stiffness of the attachment were identified by matching the first six bending eigenfrequencies for the experimental beam measured at low-amplitude impact with those of a representative FE model created using Euler-Bernoulli beam elements. We used the GlobalSearch function in MATLAB® to perform a global minimization of the error norm

$$\varepsilon_k = \sum_{n-1}^{6} \frac{\left|\omega_n^{Exp} - \omega_n^{FE}\right|}{n\omega_n^{Exp}}, \tag{4.5}$$

where $|\cdot|$ is the absolute value, and the contribution from each NNM is weighted by its modal number. The identified elastic modulus and linear stiffness are 190 GPa and 10854 N/m, respectively, which are considered reasonable for this system. The experimental and FE model eigenfrequencies and the percent error are presented in Table 4.2. Following the identification, the rotational DOFs were condensed out of the FE matrices, as discussed earlier.

4.3.2 Detection of Strongly Nonlinear Modal Interactions

In contrast with the data in Section 4.2.1, the response of the experimental system decays rapidly within the 2-second measurement window. Consequently, the time window must be divided into segments that are sufficiently small to capture the transient nature of the response, but large enough to capture at least one-half cycle of the first NNM. For this study, we used a segment length of 0.0216 s, which resulted in a total of 92 nonoverlapping time segments. Additionally, the first 0.0251 seconds of the measurement were excluded from the analysis, since it contained the response of the beam to the ambient vibration before the impact was applied. For each time segment, we extracted 13 POMs; however, only the two corresponding to the first two NNMs were analyzed. The higher NNMs were neglected because IRs are most likely to occur between the first two NNMs than with higher NNMs due to damping effects. A sixth-order polynomial with no constant, linear, or quadratic terms was fitted to each POM, which reduced the effect of measurement

Table 4.3: Time and energy values corresponding to the nine red dots in Fig. 4.14

Point	**Time [s]**	**Energy [J]**	**Percent of Initial Total Energy [%]**
i	0.0251	1.011	100
ii	0.0467	0.931	92.09
iii	0.1331	0.346	34.22
iv	1.040	0.0035	0.346
v	1.278	0.0013	0.129
vi	1.408	0.0008	0.079
vii	1.538	0.0006	0.059
viii	1.688	0.0003	0.030
ix	1.926	0.0002	0.020

noise. The final POMs were created by evaluating the polynomials at each accelerometer location (except the 9th – we refer to the previous discussion).

Using the POMs, we compute the RQ for the first two NNMs for each time segment and plot them as functions of time and energy in Figs. 4.14(a) and (b), respectively. The times and energy values associated with the nine red dots are provided in Table 4.3. The total energy was estimated by fitting a shape-preserving, piecewise cubic Hermite polynomial to the successive maximums of the kinetic energy, computed using the integrated velocities and FE mass matrix. We find that there are three spikes in the resulting frequency estimates: One at the beginning of the measurement window, one centered around 1.28 s, and one centered about 1.54 s. Interestingly, the first spike occurs over a much shorter duration than the other two spikes, which means that the dynamics is captured into a strongly nonlinear modal interaction, quickly escapes, and does not enter into another interaction for over a second. The fact that this interaction is short-lived indicates that it results in a large and rapid dissipation of energy, which cannot be accounted for by viscous damping alone. From the values in Table 4.3, we find that over 66% of the initial total energy is lost during the first spike, which only lasts for 0.13 s. This rapid dissipation is the result of the IR, during which the first NNM irreversibly transfers energy to the second, which dissipates energy at a much faster rate than the first. It is precisely this energy transfer that ultimately "kills" the interaction since the dissipation results in a rapid decrease in the frequency of every nonstationary NNM and reduces the frequency ratio below the critical threshold for IR. As soon as the frequency ratio drops below that threshold, it abruptly terminates, the dynamics escapes the nonlinear modal interaction, and, if enough energy is dissipated, the dynamics never returns to that IR without additional external excitation. From the wavelet plot, the frequencies of the first and second NNMs during the first spike are 28.6 and 72 Hz, respectively, which results in a frequency ratio of 5:2; Thus, the first spike is the result of a 5:2 IR.

In contrast to the first spike, the second and third spikes persist and appear almost immediately after one another. These spikes are so close together that it suggests the dynamics escapes one IR only to be captured by another. From the wavelet spectrum, the frequencies of the first and second NNMs during these spikes are 23 and 68.8 Hz, respectively. This results in a frequency ratio of 3:1; thus, both spikes are the result of a 3:1 IR. Although the spikes last much longer than the first spike, this does not mean that they dissipate comparably less energy. While the first spike dissipates 66% of the initial total energy, the second and third spikes dissipate only 0.27% and 0.05%, respectively. However, this comparison is deceptive since the energy available at the beginning of the second and third spikes (points iv and vi, respectively) is considerably less than that for the first spike. Instead, we must compare the energies dissipated as percentages of the available total energy at the start of each spike. Computing this metric results in dissipation of the available total energy of 66%, 77%, and 63% for the first, second, and third spikes, respectively. Instead of dissipating less available energy, the second and third spikes dissipate more than twice the available total energy as the first spike. The reason why these interactions survive longer than the first interaction is that the system was tuned to achieve a 3:1 IR for low-amplitude excitations (low energy). Consequently, the change in frequency for a given change of energy around the 3:1 IR is much lower than that around the 5:2 IR and, thus, the threshold for a 3:1 IR to occur is considerably larger.

From 1.7 to 2 seconds, we find several smaller spikes on the curve for the first NNM. While these may appear to be modal interactions, the fact that they occur after the 3:1 spikes, which is the lowest IR that system was designed to achieve and that they have no partner spikes implies that they are not. However, it is plausible for the spikes to be an IR between the first NNM and some higher NNM, but the frequency ratio would need to be 9:1 and 16:1 for an IR to occur between the first and third NNMs and first and fourth NNMs, respectively. While such high IRs are permitted in theory, the presence of damping in practice typically prevents these resonances from occurring. Additionally, the fact that the first POM corresponding to these spikes corresponds to only the first NNM (specifically, the only node is at the fixed boundary) lead us to speculate that they are the result of signal decay and small measurement and numerical errors.

To investigate further, in Fig. 4.15 we depict the POMs corresponding to the nine red dots in Fig. 4.14. Away from the spike (points i, iii, iv, vi, viii, and ix), the POMs are representative of the periodic solutions of their respective NNM; that is, the first POM has a single anti-node at the free end and the second POM has anti-nodes at the free end and near the center of the beam. On the spikes (points ii, v, and vii), the two POMs are similar and resemble the periodic solution of the second NNM in that both have anti-nodes near the center and at the free end. However, neither POM is exactly the periodic solution, but they result in the spike in the RQ plot. These are very similar to the results found for the computational system of the

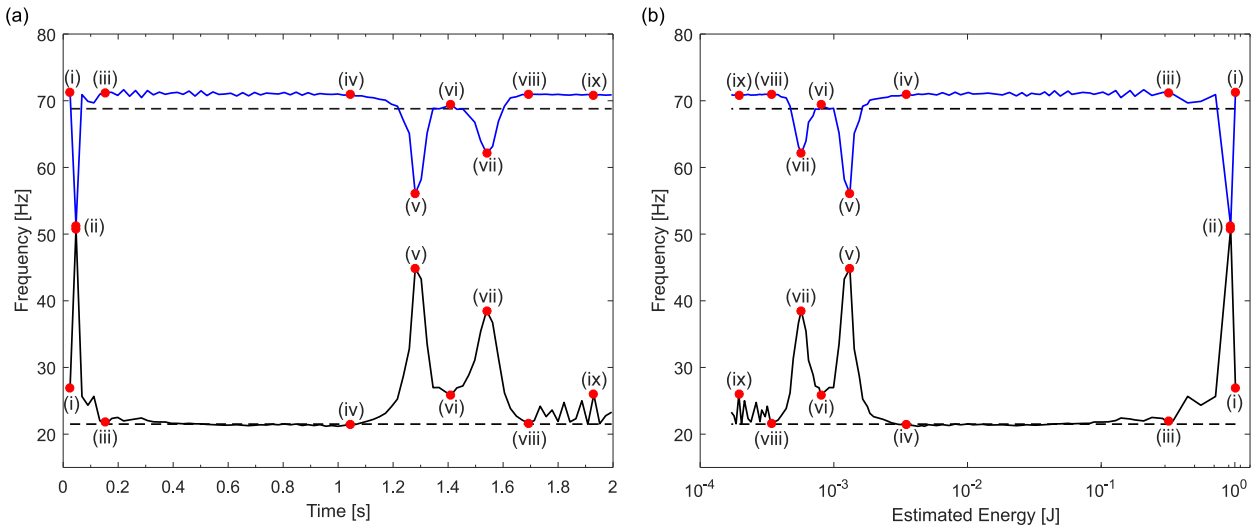

Figure 4.14: Rayleigh-quotient frequency computed using the POMs corresponding to the first two NNMs plotted as a function of (a) time and (b) estimated energy. The black dashed lines represent the linear, experimental frequencies at low energies.

previous section, and demonstrate that the previous theoretical results are representative of physical reality. Additionally, on point ix the first POM does not resemble the periodic solution of the second NNM; thus, the small spike does not represent a modal interaction. Instead, a slight oscillation appears in the first POM, which is caused by small measurement and numerical errors and results in the deviation from the linear, experimental natural frequency.

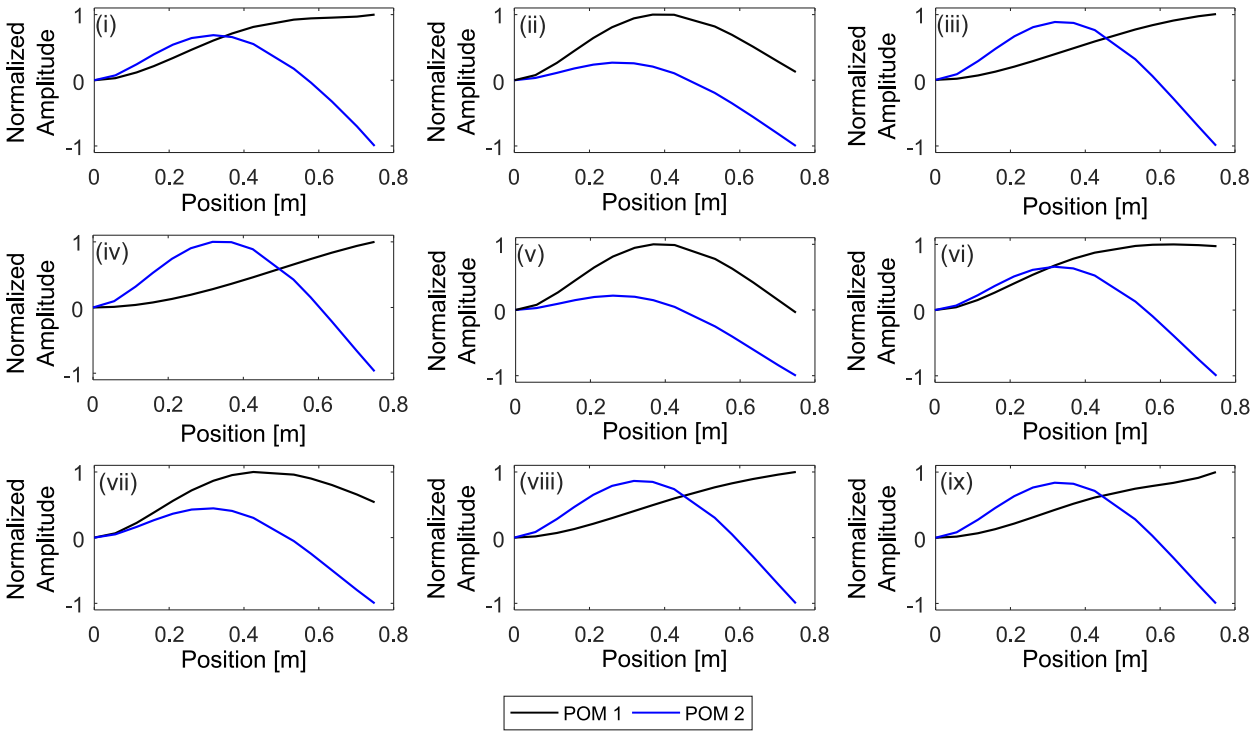

Figure 4.15: Comparison of POMs 1 and 2 corresponding to the nine red dots in Fig. 4.14.

4.3.3 Slow-flow Analysis Using WBEMD

Just as in Section 4.2.3, we demonstrate the existence of IRs by considering the slow phases of the NNMs. To this end, we apply WBEMD to the displacement response in Fig. 4.13(b), extract four IMFs and relabel them sequentially such that the nth IMF corresponds to the nth NNM. The IMFs and their wavelet spectra are depicted in Fig. 4.16(a). We find that the IMFs are well-separated and, thus, representative of their respective NNMs [Moore et al., 2018b]. The instantaneous phases and phase variables are computed using

$$\hat{\theta}_i(t) = \arctan\left(\frac{\mathrm{HT}\left\{c_i(t)\right\}}{c_i(t)}\right), i = 1, 2. \tag{4.6}$$

and

$$\Phi_{m:1}(t) = m\hat{\theta}_1(t) - \hat{\theta}_2(t), \dot{\Phi}_{m:1}(t) = m\dot{\hat{\theta}}_1(t) - \dot{\hat{\theta}}_2(t), m = 1, \ldots, 6, \tag{4.7}$$

respectively, and the phase trajectory is plotted for $m = 1, \ldots, 6$ in Fig. 4.16(b). The phase trajectories reveal that the direction of increasing time points to the left in the 1:1 and 2:1 trajectories, whereas it points to the right in the 3:1 and higher trajectories. Additionally, the 3:1 trajectory contains a cusp near the right end, which indicates a small angle change and non-time-like behavior. The 3:1 trajectory and a zoomed-in

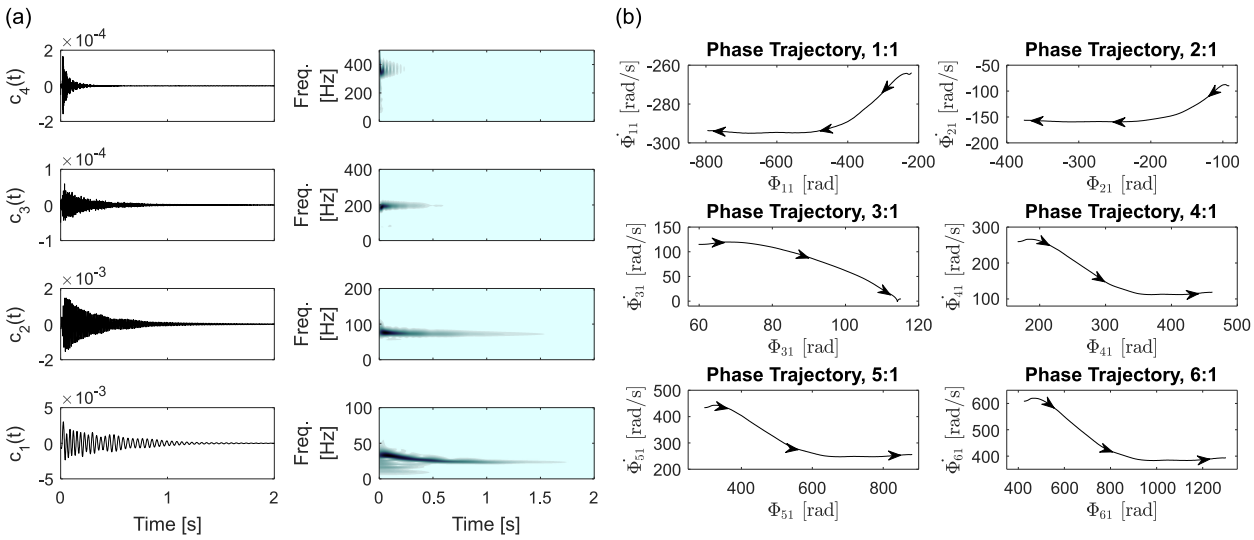

Figure 4.16: (a) IMFs extracted from the displacement response in Fig 4.12(b), (b) corresponding phase trajectories for $\Phi_{m:1}(t) = m\hat{\theta}_1(t) - \hat{\theta}_2(t)$.

view of the cusp is provided in Fig. 4.17, which reveals that the cusp point is made up of two loops and not a cusp at all. These loops are non-time-like, violate the averaging theorem [Vakakis et al., 2008], and indicate that a 3:1 IR occurs between the first and second NNM. While the loops appear near the end of the phase trajectory, which can be influenced by end effects, the fact that 0.3 seconds of the signal remains after the escape of the second loop implies that the loops are not the result of an end effect. By construction, the phase variable is only slow when the 3:1 ratio is satisfied and, thus, is fast until the first capture and results in a large phase variation in the first half of the trajectory. After the escape from the second loop, the phase variable becomes fast again; however, the ratio remains close to 3:1. Moreover, the duration of each loop corresponds to that of each spike, and the presence of two loops indicates that two separate IRs occur, which confirms the physical interpretation of the two latter spikes in Fig. 4.14.

Since we predicted that the first interaction corresponds to a 5:2 IR, we compute the phase variable

$$\Phi_{5:2}(t) = 5\hat{\theta}_1(t) - 2\hat{\theta}_2(t) \tag{4.8}$$

and plot the corresponding phase trajectory and a zoomed-in view of the initial portion in Fig. 4.18. The zoomed-in view reveals a single loop between 0.02 and 0.13 seconds, which corresponds to the duration of the first spike in Fig. 4.14. Since this loop does occur at the beginning of the measurement window, it is possible that the loop is the result of an end effect. However, the fact that the duration of the loop and the points of capture and escape correspond to those of the first spike signifies their correspondence to the

loop and the spike. The presence of the loop, its correspondence with the first spike, and the large energy loss associated with the first spike suggest that the first spike is the result of a 5:2 IR and not a numerical artifact, and confirm that the dynamics never returns to the 5:2 IR after it escapes the first interaction.

These results demonstrate the power of our method for detecting strongly nonlinear modal interactions directly from measured data, which provides significant insight into the nonlinear physics governing the response of dynamical systems with smooth, local nonlinearities. Hence, the method proves to be a valuable tool for gaining a thorough understanding of and interpreting the transient responses of strongly nonlinear dynamical systems, including nonlinear modal interactions caused by IRs.

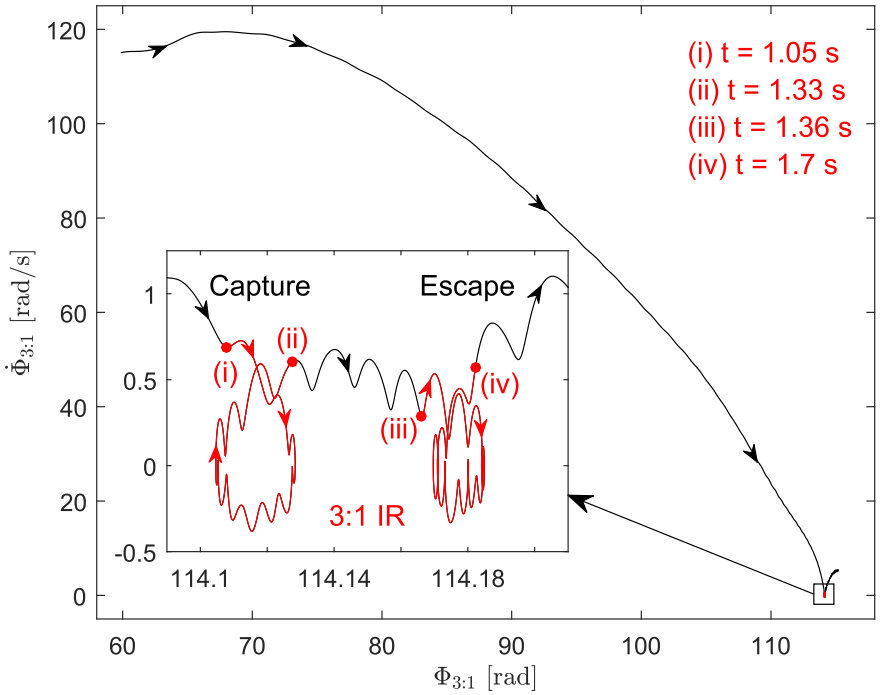

Figure 4.17: Phase trajectory for $\Phi_{3:1}(t) = 3\hat{\theta}_1(t) - \hat{\theta}_2(t)$ which corresponds to the second and third spikes depicted in Fig. 4.14.

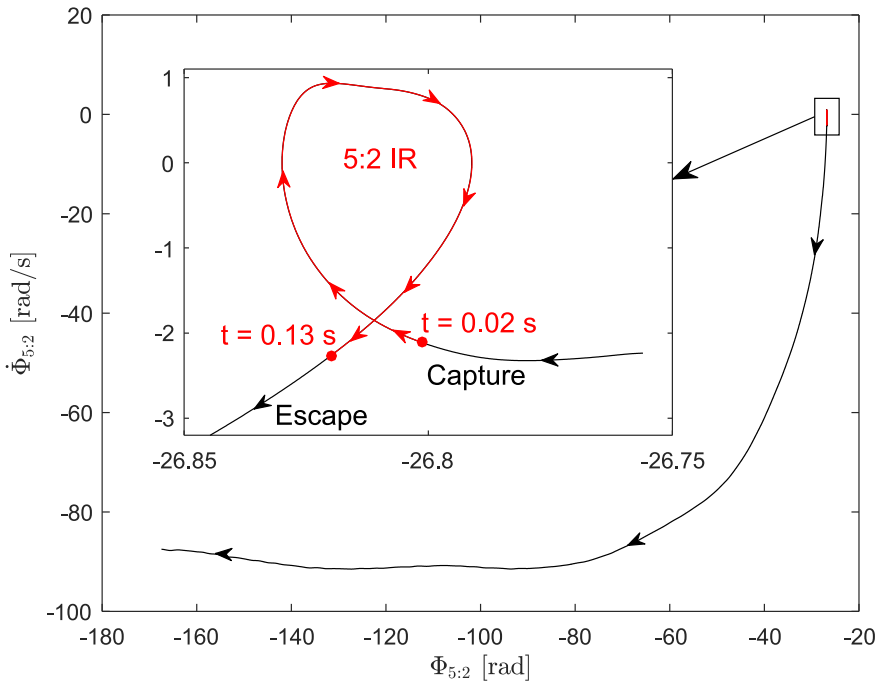

Figure 4.18: Phase trajectory for $\Phi_{5:2}(t) = 5\hat{\theta}_1(t) - 2\hat{\theta}_2(t)$ which corresponds to the first spike depicted in Fig. 4.14.

4.4 Concluding Remarks

We studied the response of two cantilever beams, one computational and the other experimental, each with a smooth, local nonlinearity attached near its free end. The response of the first beam was simulated using the FE method whereas the response of the second beam was measured experimentally. Singular value decomposition was applied to the displacements, obtained directly from the simulation or by integrating and filtering the measured accelerations, and POMs representative of the NNMs of the system were extracted. For the computational system, multiple simulations were performed for different forcing amplitudes, and SVD was applied to each simulation separately. In contrast, the response of the experimental system was divided into segments, and SVD was applied to each segment separately. For both systems, the frequencies of the NNMs were estimated using the discrete RQ with the POMs as trial vectors. The estimated frequencies were plotted as functions of time and energy, which revealed the presence of non-smooth perturbations (spikes), which appeared to indicate strongly nonlinear modal interactions.

The physical significance of the spikes was investigated by first examining the POMs off and on the spikes. The POMs off the spikes were found to correspond to the periodic solutions of the non-interacting NNMs, whereas the POMs on the spikes were found to correspond to the periodic solutions of the NNMs during an IR. Using WBEMD, the displacement responses were decomposed into well-separated IMFs that are

representative of their respective NNMs, and the Hilbert transform was used to compute the instantaneous phases for each component. For each spike, a phase variable was defined, and the corresponding phase trajectories were examined. We found that the spikes coincided with the appearance of non-time-like behavior (loops) in the phase trajectories, which resulted in the failure of the averaging theorem and indicated that the spikes are the result of strongly nonlinear IRs, where energy is irreversibly transferred from one NNM to another.

The results in this work demonstrate that the proposed method can be used to accurately detect the presence of strongly nonlinear interactions directly from post-processing of measured transient response data. Since the method relies on the underlying linear properties of the system, which are readily available from FE models, the method avoids the steep analytical and computational costs associated with traditional methods for identifying IRs. In the case that linear properties are not available, the POMs and time can be used as alternatives to the RQ and estimated energy, since our results demonstrated that "similar" POMs indicate the occurrence of IRs in the response.

Chapter 5

Data-driven Nonlinear System Identification

5.1 Introduction

In theory, the method demonstrated in this chapter applies to any dynamical system that can be naturally described by time-scales and a characteristic, time-varying energy quantity, and possesses an underlying linear structure that permits the formulation of the RQ operator. Thus, the method may be applicable to a broad class of systems in many fields; however, in this work, we focus on mechanical structures with local nonlinear attachments undergoing linear and nonlinear vibrations, where the modal frequencies of the structure and its instantaneous mechanical energy serve as the time-scales and characteristic time-varying quantity, respectively. The proposed method requires that the user possess an updated model of the linear underlying system (FE model in this work) and measured displacement response data at a sufficient number of measurement points coincident with nodes of the FE mesh. The displacement response data may be obtained from acceleration or velocity measurements using numerical integration (as in this work), Kalman filtering [Kalman, 1960], or variational approaches [Moreu and Spencer, 2015]; further assumptions are provided in Section 1.4.

The proposed method is divided into two processes: first, the analyst creates the RQ-FEP using the POMs extracted from the measured displacement responses and uses the the RQ-FEP to characterize and study the nonlinearity and accompanying strongly nonlinear modal interactions. This portion of the proposed method is summarized by the following steps for a given model of the underlying linear system and transient displacement response measured or simulated at n locations:

1. Extract n POMs using SVD from multiple time records, or multiple segments of a single time record.
2. Compute the RQ using the POMs as trial vectors and sort from lowest to highest frequency.
3. Plot the RQs as functions of time or energy.
4. Study the features in the RQ-FEP to detect the presence of nonlinearity and modal interactions in the measured time series data.

The second portion of the proposed method begins with the user plotting the estimated frequencies as functions of the relative displacement between the nonlinear attachment and the structure, to form a RQ frequency-displacement plot (FDP). The objective of exchanging energy or time for relative displacement in the plot is to identify the parameters of the nonlinearity. However, the estimated frequencies are computed for short signals or for windowed segments and not for every time instant. Instead, we define the characteristic displacement for the window defined by the interval $[T_1, T1_2]$ to be

$$\bar{\delta} \equiv \frac{1}{T_2 - T_1} \int_{T_1}^{T_2} |\delta(t)|\, dt, \tag{5.1}$$

where δ is the relative displacement between the attachment and its connection points to the structure, and $|\cdot|$. For discrete signals, the characteristic displacement is defined as,

$$\bar{\delta} \equiv \frac{1}{N} \sum_{n=1}^{N} |\delta_n| \tag{5.2}$$

for N points in the interval $[T_1, T_2]$. This enables us to plot the estimated frequencies as functions of the characteristic displacement.

For an attachment with stiffness nonlinearity, its equation of motion can be written as

$$\ddot{x} + \frac{c}{m}\dot{x} + \left(\omega_n^2 + g(\delta)\right) = 0 \tag{5.3}$$

where $\omega_n^2 \geq 0$. Let $\Omega^2(\delta) = \omega_n^2 + g(\delta)$; then, by simply exchanging δ with $\bar{\delta}$, the displacement-dependent frequency is

$$f(\bar{\delta}) = \frac{1}{2\pi}\sqrt{\omega_n^2 + g(\bar{\delta})} \tag{5.4}$$

At this point, the parameters can be identified by fitting Eq. 5.4 to the frequency-displacement curve estimated using the RQ and characteristic displacement. However, if the frequency of the attachment equals the frequency of the ith NNM, f_i, at some characteristic displacement, $\bar{\delta}_i$, then the number of unknown parameters can be reduced by requiring that $f(\bar{\delta}_i) = f_i$. This process can be repeated until either all NNMs that intersect the frequency of the attachment are exhausted or only one unknown parameter remains. Provided that the frequency of the attachment intersects a sufficient number of NNMs, all parameters can be explicitly determined; however, we recommend that this procedure be applied for the NNMs that possess clear intersection points with the estimated frequency of the attachment (as will be seen in computational and experimental results). This reduces the influence of small measurement and numerical errors that arise in the estimated frequencies.

The primary purpose of the method, at least in the context of this work, is to serve as a data-driven method for detecting the presence of nonlinearity and the accompanying strongly nonlinear modal interactions, and as a means for nonlinear system identification of strongly nonlinear attachments. As such, the method does not substitute for knowledge of the modal characteristics of the structure, and other techniques, such as wavelets and WBEMD [Moore et al., 2018b], are necessary to gain an in-depth understanding of the modal interactions. However, the relative simplicity of the proposed method and its use of time-domain data and linear FE models, which are both readily available, enable its use over a broad range of applications without incurring the steep costs normally associated with traditional methods.

In the next section, the proposed method is applied to the computational and experimental studies of the response of a cantilevered wing with a strongly nonlinear energy sink attached at the wing tip.

5.2 Computational Study

5.2.1 System Configuration

We now apply the proposed approach to the cantilevered wing depicted in Fig. 5.1 which has an NES with smooth nonlinearity coupled to the center of the wing tip. The wing is made from aluminum (with modulus of elasticity 69 GPa, and density $\rho = 2700$ kg/m^3), is uniform and homogeneous, and its dimensions are shown in Fig. 5.1(a). The NES is coupled to the wing-tip center by a combination of a linear spring and a nonlinear spring with stiffnesses of 10 N/m and 3×10^9 N/m^3, respectively. The mass of the NES is 0.25 kg, and an additional mass of 0.35 kg is lumped at the center of the tip of the wing, which represents the mass introduced by the support structure (see the experimental results in the next section). The linear stiffness is included such that the underlying linear natural frequency of the NES is 0.997 Hz, so the NES can interact with the fundamental mode of the wing. We assume light, viscous damping and use the damping ratios found in a prior study of the same system [Hubbard et al., 2010, Hubbard, 2014] for the first six modes. These damping ratios are provided in Table 5.1, and the ratios for higher modes were assumed to be equal to 0.001.

We discretize the wing into 28 quadrilateral shell elements (S4R) using Abaqus®, with each node possessing three translational and three rotational DOFs. Guyan reduction is used to condense out all DOFs except the out-of-plane translational DOFs. The corresponding mesh is presented in Fig. 5.1(b). The wing is subjected to the impulsive load defined as,

$$F(t) = P \sin\left(\frac{\pi t}{0.0006}\right) \left(H(t) - H(t - 0.0006)\right), \tag{5.5}$$

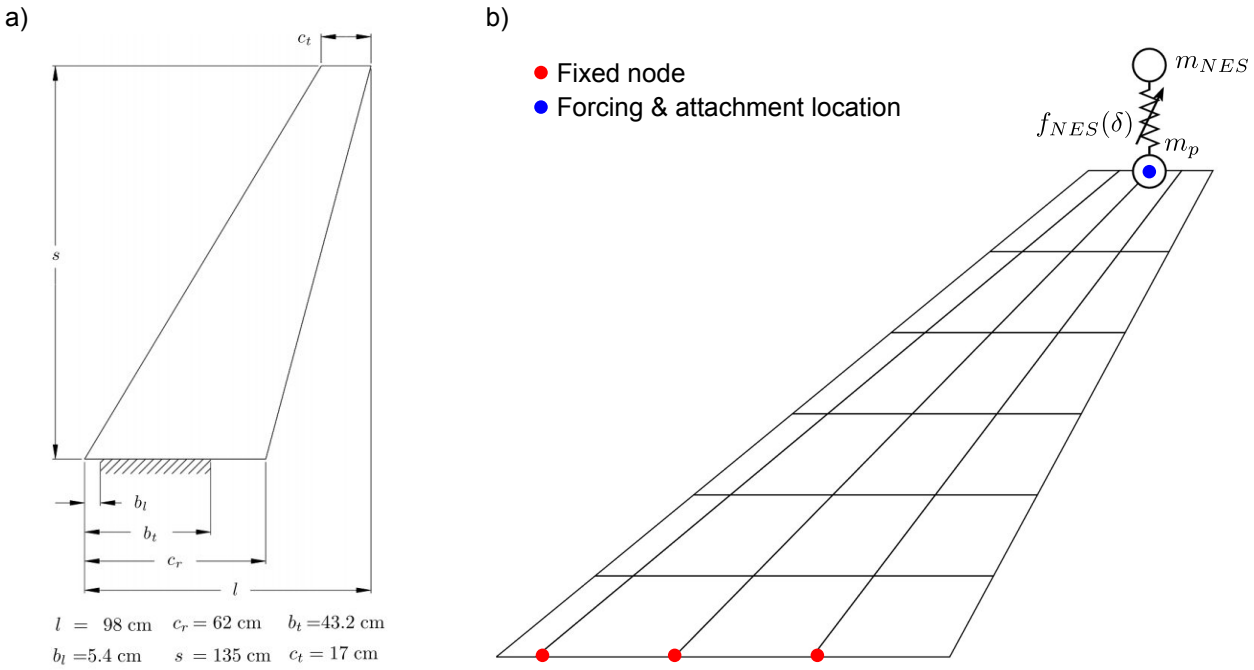

Figure 5.1: (a) Geometry and boundary conditions of the wing and (b) the FE model mesh used to model the wing.

where $H(t)$ is the Heaviside function. The load is applied to the leading edge of the wing tip, and its duration is comparable to the impulse provided by a standard modal hammer with a hard, plastic tip. To probe the dynamics over a large energy range, we vary the amplitude, P, from 10^{-3} to 10^{12} N. Specifically, we choose 2000 logarithmically spaced points between 10^{-3} and 10^{12} N and simulate 1 second of the transient response of the wing for each value of the force amplitude P using ode45 in MATLAB® with a time step of 10^{-5} s. The response was simulated for only 1 second because, due to weak damping, the response of the system is expected to remain approximately stationary in this early window of the transient response.

In the absence of coupling nonlinearity, the wing possesses linear normal modes of vibration. When the

Table 5.1: Natural frequencies and damping ratios for the first six modes of the wing. The abbreviations B and T correspond to bending and torsional modes, respectively.

Mode	**Natural Frequency [Hz]**	**Damping Ratio, ζ_i**
1B	3.030	0.0095
2B	15.73	0.0024
1T	28.14	0.0014
3B	46.86	0.0018
2T	71.91	0.0010
4B	109.7	0.0023

NES is attached, the wing possesses nonlinear normal modes (NNMs) of vibration which, in the absence of IRs, are synchronous vibrations that may be regarded as nonlinear analogs of the linear vibration modes [Vakakis et al., 1996]. When certain internal resonance conditions are met, the NES can modally interact with NNMs with frequencies higher than its own. These modal interactions result in strongly nonlinear and irreversible energy transfer from the interacting NNM to the NES, causing mode mixing and non-synchronous oscillations, and can also result in energy transfers between NNMs. Moreover, the modal characteristics of nonlinear dynamical systems are intrinsically dependent on their energy, which in this study is related to the forcing amplitude. Thus, by selecting such a large forcing range, we ensure that the dynamics are probed adequately. However, we recognize that the upper limit of the forcing range is not physically realizable in this particular study since it corresponds to unrealistically high local stresses. We note that the large energy range can be realized with other means, as demonstrated in a previous study [Herrera et al., 2017] where a cantilever beam with a vibro-impact boundary condition was realized through a clearance.

5.2.2 Detection of Strongly Nonlinear Modal Interactions

Following the completion of each simulation, we apply POD to the translational response at each node and obtain the first 33 POMs. The frequency of each POM is estimated using the discrete Rayleigh quotient and the Guyan-reduced mass and stiffness matrices. Because the POD algorithm sorts the POMs by singular value and not by mode number, we re-sort the POMs using a modified modal assurance criterion (MAC) [Allemang and Brown, 1982], defined as

$$\mathbf{MAC}_{ij} = \frac{|\boldsymbol{\varphi}_i^{\mathsf{T}} \boldsymbol{\psi}_j|^2}{\boldsymbol{\varphi}_i^{\mathsf{T}} \boldsymbol{\varphi}_i \boldsymbol{\psi}_j^{\mathsf{T}} \boldsymbol{\psi}_j}, \tag{5.6}$$

where $\boldsymbol{\varphi}_i$ is the ith linear mode shape computed using the FE matrices and $\boldsymbol{\psi}_j$ is the jth POM for $i, j = 1, \ldots, 33$. From this definition, the MAC is a scalar constant that expresses the degree of linearity between the FE modal vectors and the POMs. Thus, by sorting the POMs based on their MAC values, we ensure that they are sorted corresponding to the mode number. In the case of similar POMs, where two POMs correspond to one FE mode shape, we sort the two POMs by frequency as well as the by the MAC numbers (we will return to this special case shortly).

In Fig. 5.2(a), we plot the RQ-FEP for the first five POMs, which reveals that significantly different behavior occurs for the NNMs of the wing than that of the NES. Similar to the cantilever beam studied in the previous chapter and [Moore et al., 2018a], each of the NNMs of the wing can be partitioned into two limiting linear regimes and an intermediate (bridging) strongly nonlinear regime that connects the two

limiting linear regimes. In contrast, the NNM governing the NES can only be partitioned into a single linear limiting regime and a strongly nonlinear regime. Indeed, in the limit of low energy (low forcing amplitude), the restoring force of the nonlinear coupling is negligible, and the NES behaves as a linear attachment; this is the low energy limiting regime of the dynamics. However, in the limit of high energy, the restoring force is so large that the motion of the NES is restricted such that the NES serves only as added mass on the wing tip; this represents the high-energy limiting regime of the dynamics. Thus, at these two limits, the modal characteristics of the wing are independent of energy, and it behaves linearly. For the wing, the two limiting linear regimes are connected through a strongly nonlinear transition regime where its modal characteristics depend strongly on the forcing amplitude (i.e., the overall system energy). However, since the frequency of the NES approaches infinity in the limit of large energy, its response never converges to a second limiting linear regime; rather, its strongly nonlinear regime persists. Moreover, the RQ-FEP reveals that as soon as the frequency of the NNM governing the NES grows to be larger than the frequency of one of the NNMs governing the wing, that NNM converges to the second limiting linear regime such that the NES serves only as a mass-effect for that NNM.

Since the modal frequencies do not depend on energy in the limiting linear regimes, they are represented by straight lines in the RQ-FEP. Indeed, at low energies the estimated frequencies of the POMs converge to the horizontal black dashed lines of the plot, whereas at high energies the frequency estimates converge to the horizontal gray dashed lines. The black and gray dashed lines correspond to the leading natural frequencies of the (linear) NNMs governing the wing with the NES acting as a linear attachment and added mass, respectively. The first torsional NNM converges to the same frequency in both regimes because the NES is attached near its node and, thus, it is unaffected by the mass-effect introduced by the NES. The strongly nonlinear regime bridges the two linear regimes, and the estimated frequencies, and therefore the POMs, depend on the instantaneous energy of the system. Interestingly, the nonlinear regime of the estimated frequency of the NES can be partitioned into weakly and strongly interacting regimes. The partition occurs at an energy of 2.86×10^{-4} J where the estimated frequency of the NES crosses that of the first bending mode. Above this energy, the variations in the estimated frequency of the NES significantly increase, which implies an increase in strongly nonlinear modal interactions. Moreover, the first bending mode enters its high-energy linear regime and settles to a lower frequency than that of its low-energy linear regime. This confirms that after the frequency of the NES grows to be larger than that of a wing mode, the NES acts only as added mass for that mode.

The non-smooth perturbations (in the form of spikes) that emanate from the curves in the strongly nonlinear regimes indicate strongly nonlinear interactions between the NNMs [Moore et al., 2018a]. The

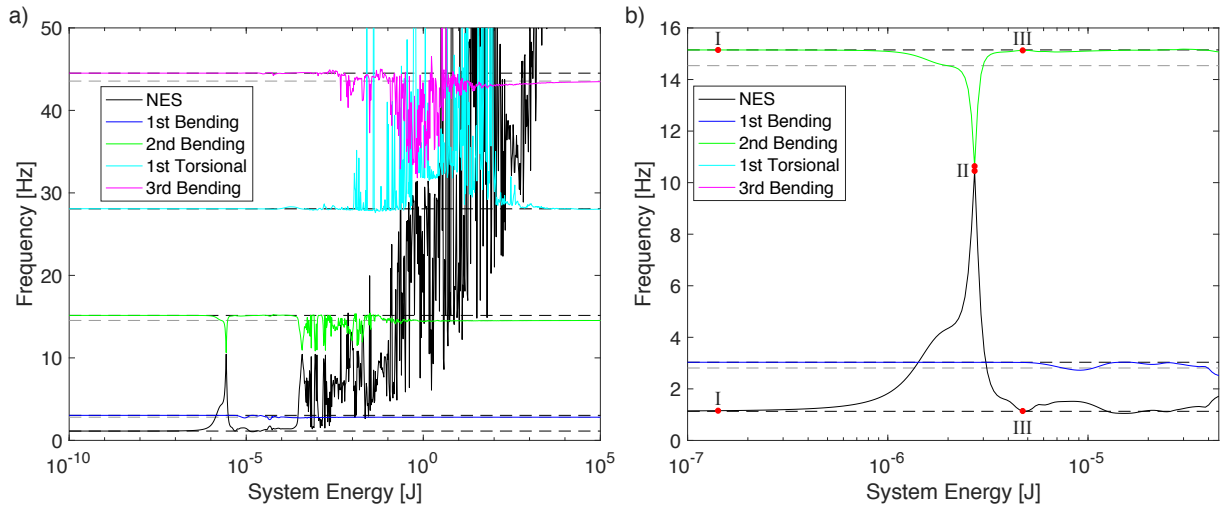

Figure 5.2: (a) The resulting RQ FEP from the computational study. (b) Zoomed-in view of the first spike in the RQ FEP with the red dots indicating cases I, II and III.

interactions are the result of IRs between NNMs where mode mixing occurs, and the resulting periodic solution is non-synchronous with mixed (non-separated time scales); that is, it contains a mix of the lower and higher NNMs participating in the IR and mode conversion from one NNM to the other occurs. This mode mixing and conversion is captured by the POMs in the special case of similar POMs, where two POMs have shapes similar to that of a single NNM [Moore et al., 2018a]. Thus, to determine if the spikes in the RQ FEP correspond to IRs, one must compare the POMs before, on and after the occurrence of each spike. In Fig. 5.2(b), we present a zoomed-in view of the left-most spike visible in the RQ FEP and indicate three cases (labeled as I, II and III) with the red dots, with the corresponding POMs presented in Fig. 5.3. We find that off the spike (cases I and III), the POMs correspond to the underlying linear mode shapes; however, on the spike (case II), the POMs do not correspond to any single linear mode shape but, instead, appear as a combination (or mixing) of the first and third mode shapes. When mode conversion occurs, the orthogonality of the mode shapes (or periodic solutions) is lost; however, the POMs are, by definition, orthogonal, and orthogonality is preserved by the difference of sign in the amplitude of the NES in each POM. Otherwise, the two POMs are entirely identical in shape and amplitude. The correspondence between similar POMs and TRCs was demonstrated in [Moore et al., 2018a] using the WBEMD technique [Moore et al., 2018b] and slow-flow analysis [Vakakis et al., 2008]. We refer the reader to the analysis presented in the previous chapter and in[Moore et al., 2018a] for further details on how to demonstrate that the similar POMs in this work correspond to TRCs.

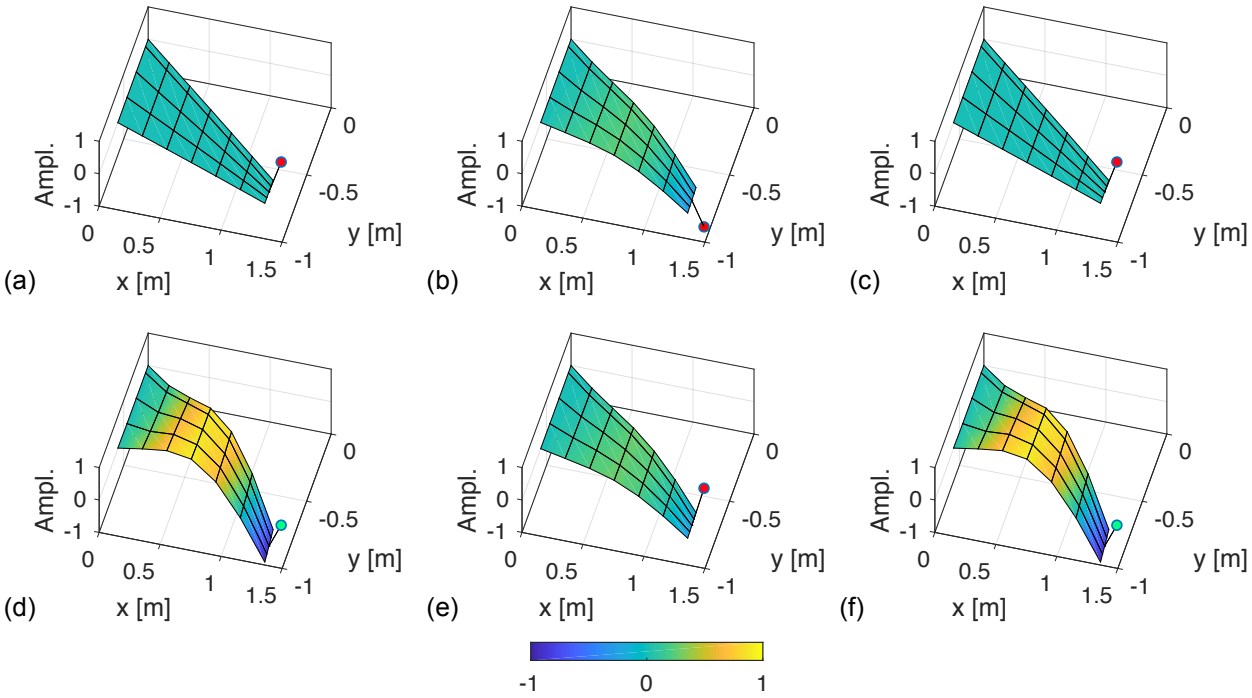

Figure 5.3: (a) Geometry and boundary conditions of the wing and (b) the FE model mesh used to model the wing.

5.2.3 NSI and Model Updating

Following the procedure presented in Section 5.1, we compute the characteristic displacement using Eq. 5.2 and plot the estimated frequencies as functions of characteristic displacement in Fig. 5.4. We refer to this plot as the RQ frequency-displacement plot. Note that the frequency-displacement pairs have been sorted ascendingly based on the displacements. The backbone branch of the Hamiltonian Duffing oscillator, computed using NNMcont [Peeters et al., 2009], corresponding to the grounded NES is overlaid on the plot as the red curve. For the Duffing oscillator, the characteristic displacement is chosen as the peak amplitude of the periodic solution for each frequency. The backbone branch not only matches the trend of the estimated frequency of the NES, but also it intersects the estimated frequency of the first bending mode at the same displacement as the estimated frequency of the NES, which verifies that the characteristic displacement defined by Eq. 5.2 is appropriate for this system.

Assuming that the mass of the attachment is known (it can be measured directly experimentally), the linear stiffness k is identified from the low-energy, linear frequency of the NES, leaving the nonlinear stiffness to be identified. The nonlinearity is modeled in the form $\alpha\,|\delta|^{\beta}\,\delta$ where δ is the relative displacement between

the NES and its attachment points. For this nonlinearity, the equation of motion for the NES is,

$$\ddot{x} + \frac{d}{m}\dot{\delta} + \left(\omega_n^2 + \frac{\alpha}{m}\left|\delta\right|^{\beta}\right)\delta = 0; \tag{5.7}$$

replacing the relative displacement with the characteristic displacement, the displacement-dependent frequency equation becomes

$$f(\bar{\delta}) = \frac{1}{2\pi}\sqrt{\omega_n^2 + \frac{\alpha}{m}\bar{\delta}^{\beta}}. \tag{5.8}$$

Since the estimated frequency of the NES intersects the first bending NNM, we can use this frequency to relate α to β. Using the low-energy frequency of the first NNM, $f_1 = 3.0297$ Hz, the corresponding characteristic displacement is found to be $\bar{\delta}_1 = 0.000196$ m using linear interpolation. Requiring that $f(\bar{\delta}_1) = f_1$, we find that,

$$\alpha = \frac{m}{\bar{\delta}_1^{\beta}}\left(\left(2\pi f_1\right)^2 - \omega_n^2\right), \tag{5.9}$$

and substituting 5.9 into 5.8 results in the expression,

$$f(\bar{\delta}) = \frac{1}{2\pi}\sqrt{\omega_n^2 + \left(\left(2\pi f_1\right)^2 - \omega_n^2\right)\left(\frac{\bar{\delta}}{\bar{\delta}_1}\right)^{\beta}}. \tag{5.10}$$

In the next step, we identify β using the GlobalSearch algorithm in MATLAB®, which performs a global optimization and is insensitive to initial guesses, to maximize the R-squared value between the filtered frequency-displacement curve for the NES created using the RQ and that created using Eq. 5.10. The lower and upper bounds are set such that $\beta \in [0.5, 3.5]$; with an initial guess of $\beta = 1.5$, the optimization converged to $\beta = 2.0391$. Using this value, we find that $\alpha = 2.9343 \times 10^9$ N/m^3.0391 with an R-squared value of 0.9766. Recall that the exact parameters are $\beta_{\text{exact}} = 2$ and $\alpha_{\text{exact}} = 3 \times 10^9$ N/m^3, resulting in absolute errors of 1.96% and 2.19% for the identified β and α, respectively. The frequency-displacement curves predicted using the identified and exact parameters are presented in Fig. 5.5 as the red and green curves, respectively. Additionally, the low-energy frequency of the first bending NNM is depicted in Fig. 5.5 as the blue-dashed line.

The identified model is validated by comparing its response to the that of the exact system for multiple forcing values. Figure 5.6 presents the comparison of the response of the exact system with that of the identified model for impacts of 1, 10, 100 and 1000 N applied to the leading edge of the free end of the wing. For an impact of 1 N, the response is linear, and the identified model reproduces the response of the exact system. For an impact of 10 N, the energy in the system is large enough that the nonlinearity is engaged, but

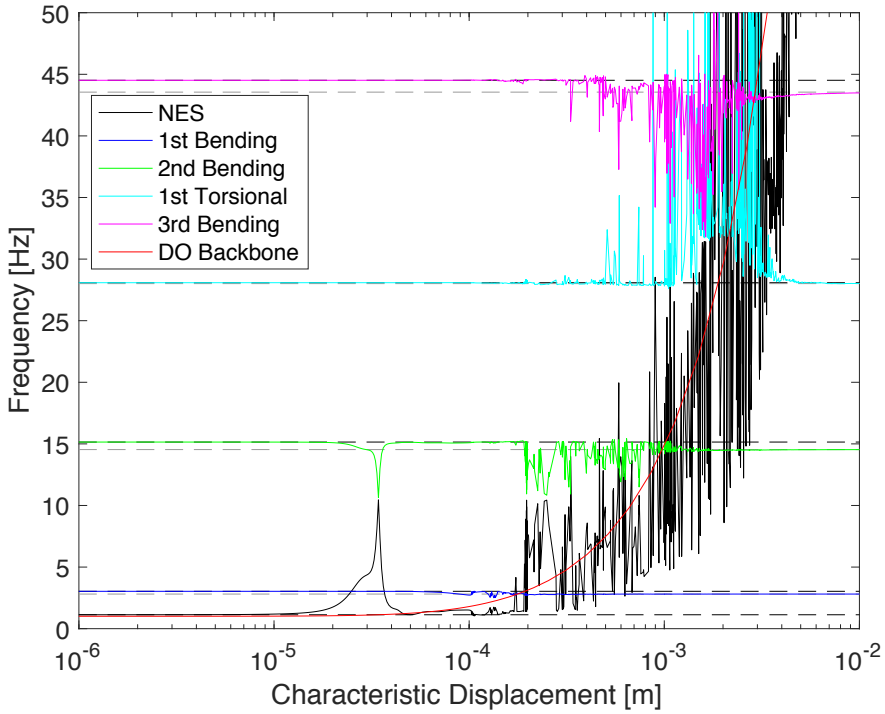

Figure 5.4: The RQ frequency-displacement plot for the first five modes with the unforced, undamped Duffing oscillator backbone branch overlaid.

small enough that only the first two NNMs are affected. The identified model performs worst for this forcing level in terms of the relative displacement; however, the wavelet and FFT reveal that the identified model reproduces the frequency content of the response accurately. For an impact of 100 N, the identified model improves significantly and nearly matches both the amplitude and phase of the exact relative displacement. At this forcing level, there is enough energy in the system that the nonlinearity has engaged the second bending NNM, but not the first torsional NNM. For an impact of 1000 N, the energy is large enough that the nonlinearity engages the first torsional NNM and some other higher NNMs, as well. For this forcing, the identified system accurately reproduces both the amplitude and phase of the relative displacement as well as the frequency content. These results show the strength of the method for identifying local, strong nonlinear attachments in a theoretical study. In the next section, we apply the proposed method to the experimentally measured response of a similar wing with a comparable NES coupled to the leading and trailing edges of the tip of the wing.

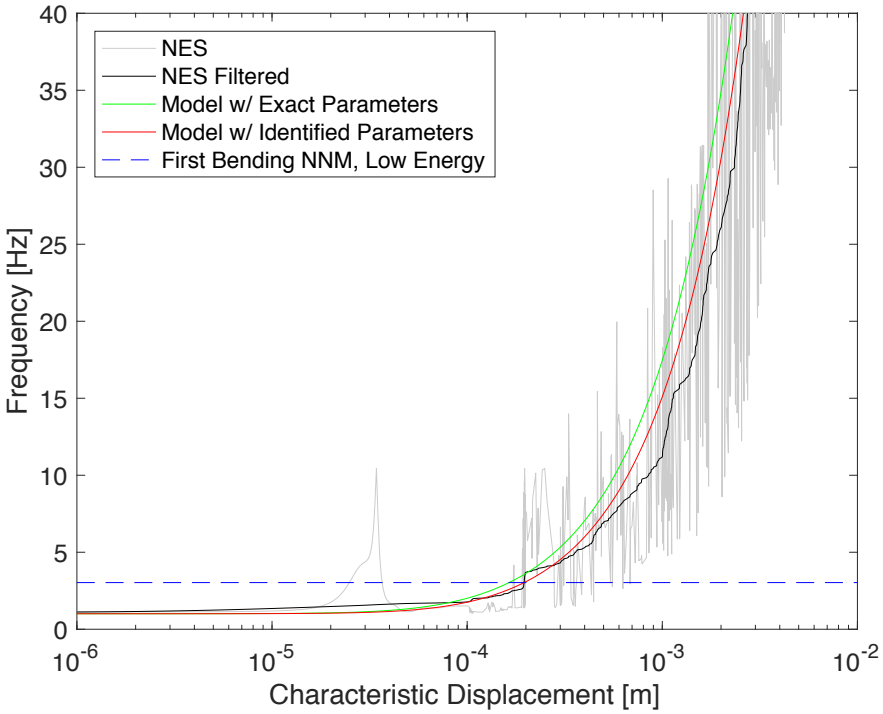

Figure 5.5: The RQ frequency-displacement plot for the unfiltered and filtered estimated frequency of the NES, the model with exact parameters, the model with the identified parameters, and the low-energy frequency of the first bending NNM.

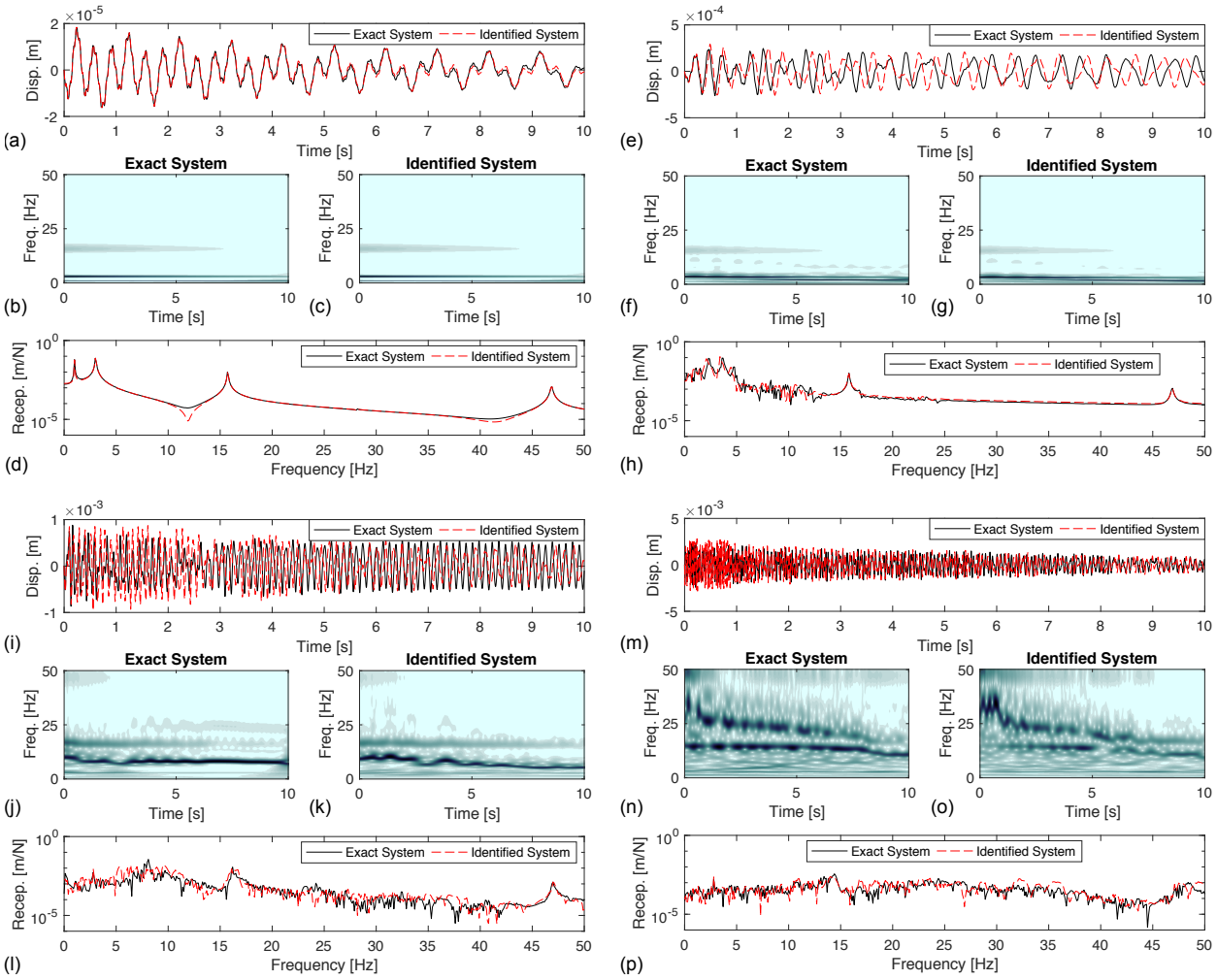

Figure 5.6: Comparison of the relative displacement between the NES and the attachment point computed using the exact and relative systems for impacts of (a) 1 N, (e) 10 N, (i) 100 N and (m) 1000 N. The wavelet spectra for the exact relative displacements are presented in (b), (f), (j) and (n) for each impact case. Similarly, the wavelet spectra for the relative displacement computed using the identified system are presented in (c), (g), (k) and (o). Finally, a comparison of the FRFs of the exact and identified systems are presented in (d), (h), (l) and (p) for each impact case.

5.3 Experimental Study

5.3.1 Design of Winglet-mounted NES

To experimentally verify the computational results, a translational NES was designed, fabricated and attached to the tip of the wing. Figures 5.7(a) and (b) present the schematic and the experimental fixture for the translational NES, respectively. The NES mass is composed of steel, incorporates two solid steel support shafts, and has a total mass of 0.908 kg. The support shafts slide across two rails created from a U-channel made of ultra-high-molecular-weight (UHMW) polyethylene, which has a coefficient of friction comparable to polytetrafluoroethylene (PTFE, Teflon) [Fusaro, 1985, Budinski, 1997, Tong et al., 2006]. The combination of the support shafts and the UHMW U-channel was selected to minimize dissipation due to sliding friction. The essentially nonlinear (nonlinearizable) stiffness was realized geometrically by transversely displacing two steel wires with diameters of 0.00036 m that were clamped inside the anchor blocks and the NES mass using set screws. In addition to the essentially nonlinear stiffness, the wires also introduced a small linear stiffness that resulted from a combination of pretension and bending due to slight misalignment of the NES and anchor blocks. We selected the diameters of the wires such that the linear natural frequency of the NES is less than that of the second NNM, such that a 1:1 TRC can be realized using a standard modal hammer for excitation.

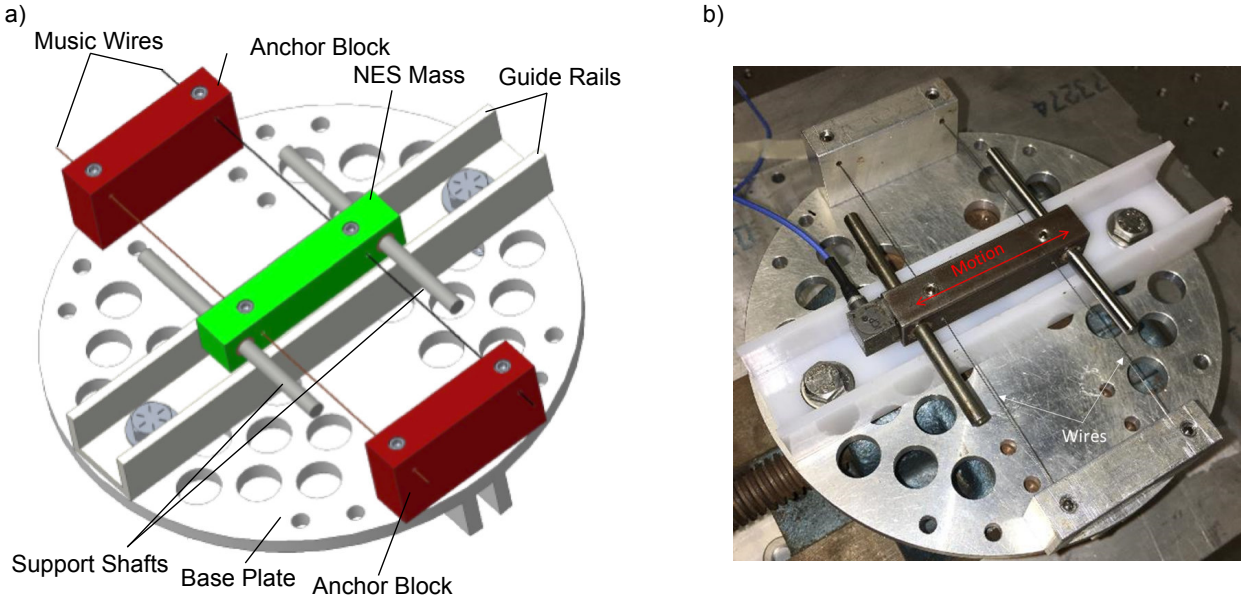

Figure 5.7: (a) Schematic view of the attachment with translational NES and (b) view of the grounded experimental attachment instrumented to measure the translational acceleration of the NES mass.

5.3.2 NSI of Grounded NES

Before attaching the NES to the wing, it was experimentally characterized: Its response to impulsive excitation was measured and used to identify a mathematical model. For these measurements, the base plate was clamped to an optical table, such that only the NES mass was free to translate. An impact from a PCB Piezotronics modal impact hammer (model 086C01) was applied to the NES, and its acceleration response was measured using a PCB accelerometer (model 356A11), with a nominal sensitivity of 1 mV/(m/s^2). The acceleration of the NES was measured at a sampling rate of 32,768 Hz for a duration of 2 seconds using VibPilot hardware (m+p International, Hannover, Germany) and m+p analyzer software. The response was measured for multiple impacts; however, only the response for an impact of 236 N, depicted in Fig. 5.8, was used to perform the identification. The remaining measurements were used to validate the identified model.

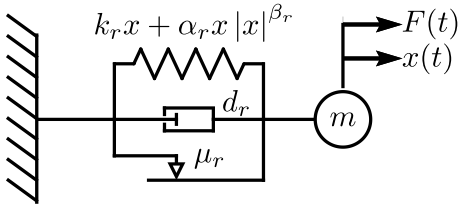

Figure 5.8: Schematic of the model used for the grounded NES.

The NES is modeled according to the schematic presented in Fig. 5.8. The equation of motion is

$$m\ddot{x} + d_r\dot{x} + \mu_r mg\,\mathrm{sgn}(\dot{x}) + \left(k_r + \alpha_r\,|x|_r^{\beta}\right)x = F(t), \tag{5.11}$$

where the nonlinearity is modeled using the same form as in the computational study, and both viscous and Coulomb-friction damping are included. The unknown damping and stiffness parameters are identified using a two-step procedure: First, the restoring force surface (RFS) method [Masri and Caughey, 1979] is used to obtain initial estimates for the parameters; second, the estimates are used as initial guesses in an optimization routine that maximizes the R-squared value between the measured and simulated responses. We describe each of these steps in greater detail below. To construct the RFS, the velocity of the NES was computed by numerically integrating the measured acceleration and high-pass filtering the output using a third-order Butterworth filter with a cutoff frequency of 2 Hz. The displacement of the NES was obtained by applying the same procedure to the velocity response. Figure 5.9(d) presents the RFS corresponding to the response depicted in Fig. 5.9(a). To determine the stiffness contribution to the restoring force, the RFS was plotted as a function of displacement for zero velocity in Fig. 5.9(e). Likewise, the damping contribution was determined by plotting the RFS for zero displacement, and is presented in Fig. 5.9(f). The

stiffness and damping coefficients were estimated by manually fitting the models in Eq. 5.11 to the RFSs presented in Figs. 5.9(e) and (f), respectively, and the resulting models are depicted in red on the plots for comparison. The parameters determined from the estimation are $k_r = 70$ N/m, $\alpha_r = 9 \times 10^8$ N/m$^{3.45}$, $\beta_r = 2.45$, $\mu_r = 0.03$ and $d_r = 0.35$ Ns/m.

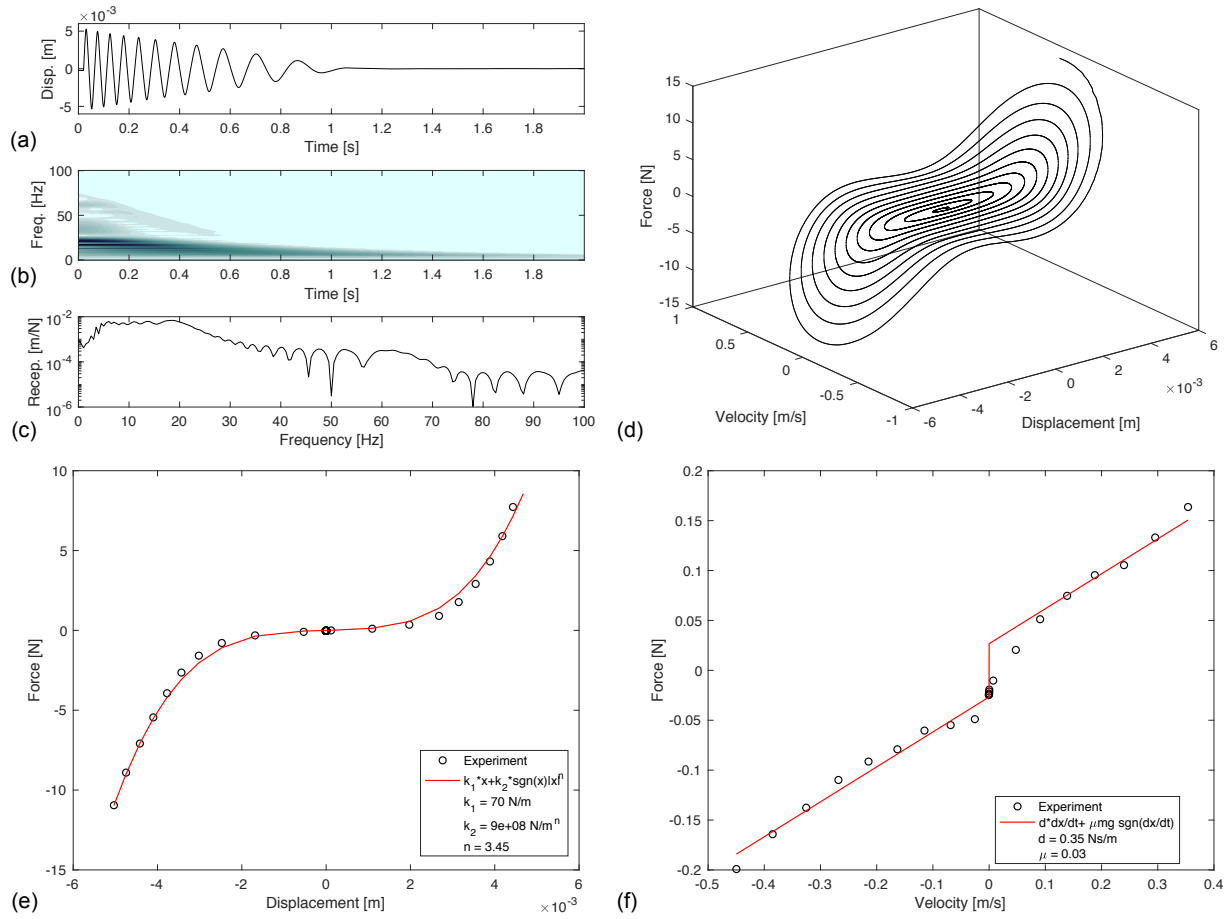

Figure 5.9: (a) The experimentally measured response of the grounded NES used in the RFS method with corresponding (b) wavelet spectrum and (c) FRF. The RFS for (b) non-zero displacement and velocity, (e) zero velocity and (f) zero displacement.

Following the identification using the RFS method, the estimated parameters were used as initial guesses in an optimization routine with an objective function that maximizes the R-squared value between the measured and simulated responses. Additionally, the objective function includes a penalty function that is implemented such that the amplitude of the simulated response for the last 0.5 seconds cannot be less than 75% or greater than 125% of that for the measured response. This penalty function is included to prevent the routine from converging to a solution for which the damping and/or friction coefficients are unrealistically

large. The resulting parameters from the estimation are $k_r = 75$ N/m, $\alpha_r = 9.22 \times 10^8$ N/m$^{3.45}$, $\beta_r = 2.499$, $\mu_r = 0.0320$ and $d_r = 0.35$ Ns/m. We refer to the identified model with these parameters as the RFS model hereafter.

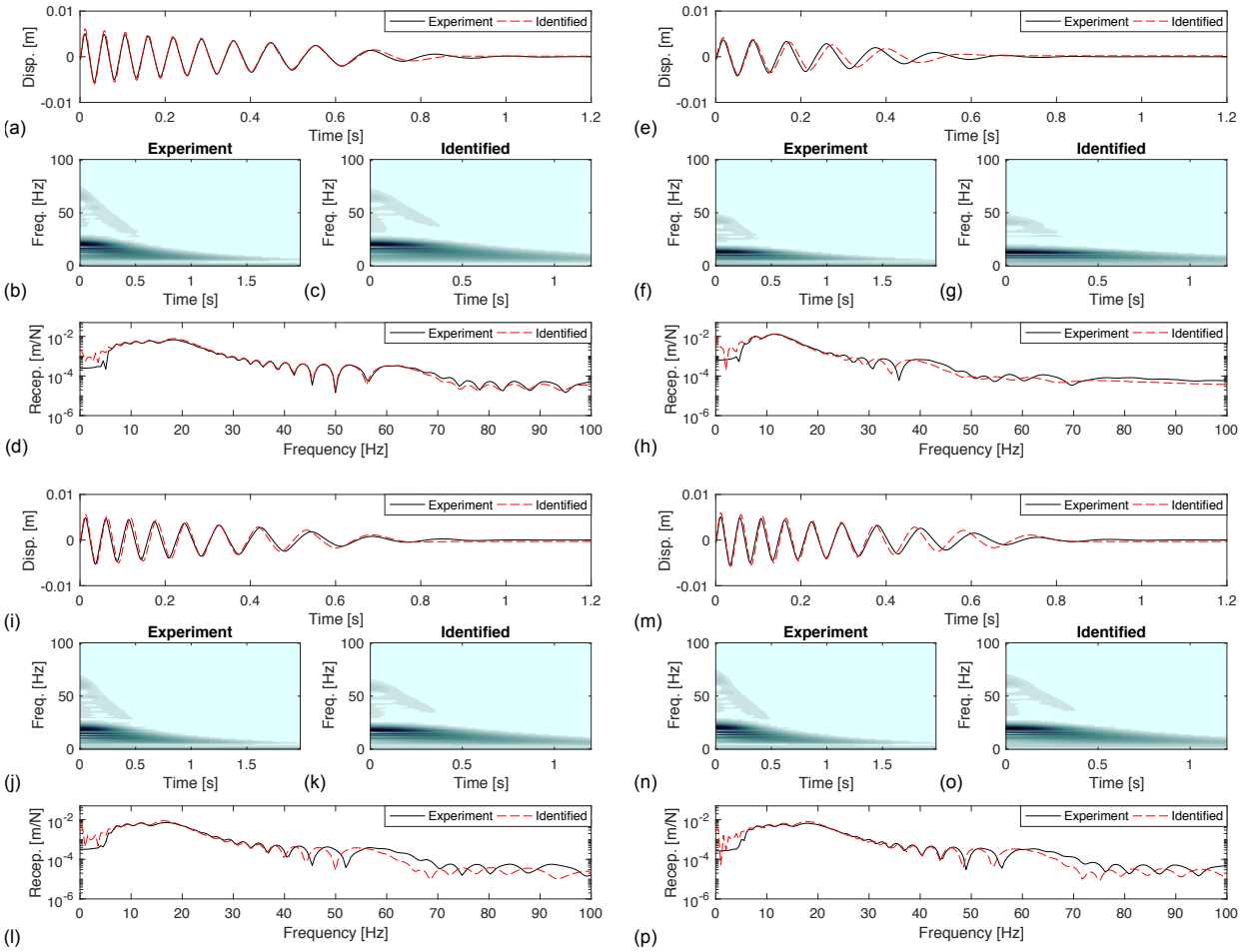

Figure 5.10: Comparison of the displacement of the NES measured experimentally and computed using the identified system for impacts of (a) 236 N, (e) 114.7 N, (i) 189.7 N and (m) 305.5 N. The wavelet spectra for the experimentally measured displacements are presented in (b), (f), (j) and (n) for each impact case. Similarly, the wavelet spectra for the displacement computed using the identified system are presented in (c), (g), (k) and (o). Finally, a comparison of the FRFs of the measured and identified systems are presented in (d), (h), (l) and (p) for each impact case.

Figure 5.10(a) presents the comparison between the measured and simulated responses for an applied impulsive force of 236 N (maximum magnitude), which corresponds to the response used in the identification procedure. Further validation of the model comes from comparing the measured and simulated responses for applied impulses not used in the identification. Accordingly, we present comparisons for impulses of 114.7

N, 189.7 N and 305.5 N in Figs. 5.10(b), (c) and (d), respectively. These results validate the accuracy of the identification procedure for the grounded NES and, as such, the RFS model attached to the wing will serve as a baseline comparison for the model subsequently identified using the proposed NSI procedure, which we refer to as the NSI model. In the next subsection, we present the experimental results with the NES attached to the wing, the identification using the proposed NSI method, and comparisons between the RFS and NSI models.

5.3.3 Linear System Identification and Model Updating of Attached NES

Following the experiments with the grounded NES, the attachment was fixed to the tip of the wing as depicted in Figs. 5.11(a) and (b). An impulsive load from a PCB Piezotronics modal impact hammer (model 086C01) was applied normal to the wing at the leading edge of the tip, and the transverse acceleration responses of the wing were measured at 14 locations along the leading and trailing edges, as well as that of the NES using PCB accelerometers (models U356A11 and Y353B17), all with a nominal sensitivity of 1.02 mV/(m/s^2). The accelerations were measured at a sampling rate of 4096 Hz for a duration of 8 seconds using VibPilot hardware (m+p International, Hannover, Germany) and m+p analyzer software. The same numerical integration scheme used in the prior experiments of the grounded NES were employed to obtain the displacement and velocity responses of the wing and NES.

As with the grounded NES, we use a single measurement case, corresponding to a single impulse, to identify a model for the attachment and employ other measurement cases to validate the identified model. The applied impulse and the corresponding velocity response of the NES are presented in Figs. 5.12(a) and (b), respectively. In addition to the velocity time series response, its corresponding wavelet spectrum and frequency response function (FRF) are presented in Figs. 5.12(c) and (d), respectively. In the wavelet spectrum, lighter and darker shadings correspond to low and high amplitude harmonics, respectively, and indicate the corresponding distribution of the energy of the measured signal in frequency and time. Thus, the wavelet spectrum reveals the broad scattering of energy from low to high frequencies that occurs in the initial 1.75 seconds of the response. This scattering of energy was not present in the response of the grounded NES and is the result of modal interactions between the NES and the second NNM of the wing. Indeed, in the case of the grounded NES, the response is governed by a single NNM, which may possess additional harmonics, but cannot scatter energy across frequencies (or scales) since there are no other NNMs to interact with. This result indicates that the role of the NES and its dynamics differ significantly when grounded and when attached to the wing, and suggests that the model identified for the grounded NES may not be sufficient for reproducing its response when attached to the wing. We will return to these modal

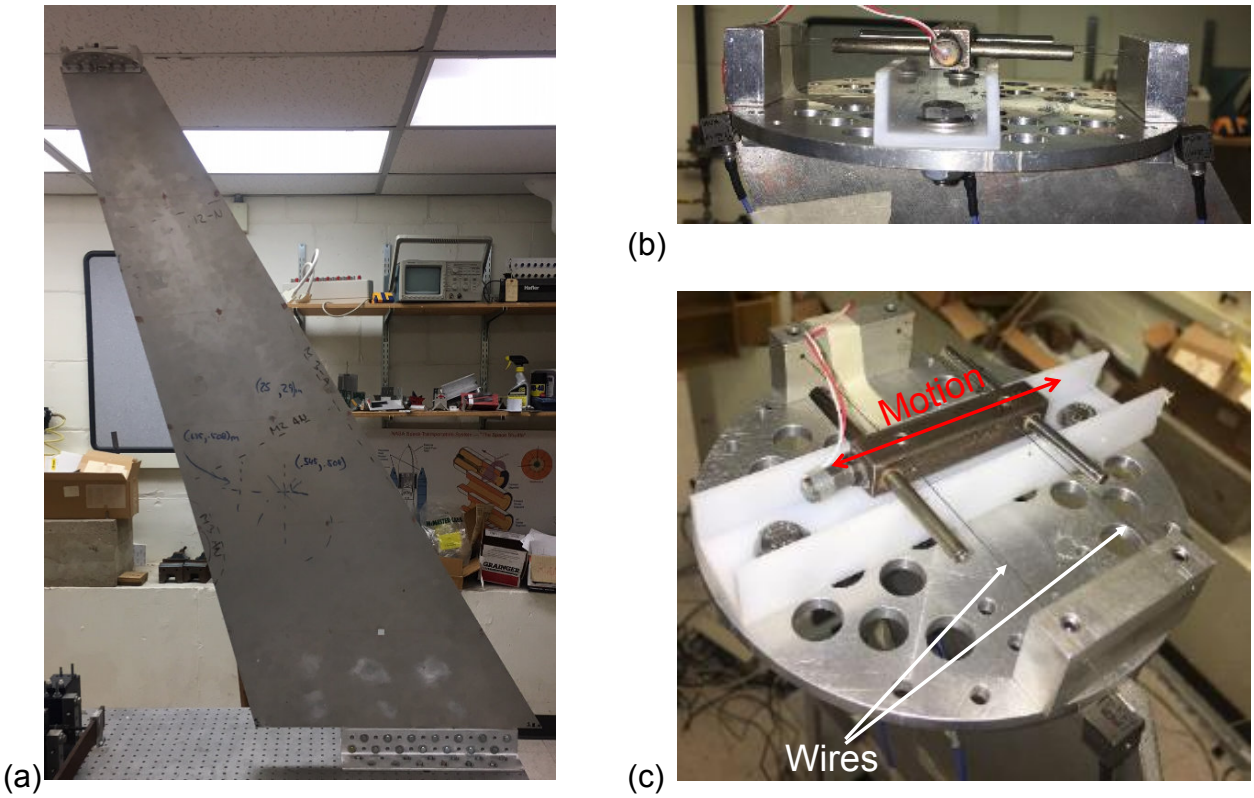

Figure 5.11: (a) Front view of wing used in the experiments. (b) Front view of the nonlinear attachment (the NES). (c) Top view of NES with direction of motion and wires indicated by red and white arrows and text, respectively.

interactions and resulting energy scattering using the RQ-FEP and corresponding POMs after a discussion of the model used for the integrated wing-NES assembly.

The wing is represented by the FE model described in the computational study, except that the thickness of the tip of the wing is increased to 0.016 m and the elastic modulus is set to 68.5 GPa. These changes are incorporated to better match the natural frequencies of the experimental system and are sufficient in this study because the NES interacts only with the second bending NNM of the wing. However, the most likely source of error is in the modeling of the boundary conditions, and these should be examined further to improve the match for higher NNMs. The width of the tip is increased to account for the bolting of the attachment to the wing. The elastic modulus is decreased to reconcile the natural frequencies of the FE model with those of the experimental system. A comparison of the experimental and computational natural frequencies is presented in Table 5.2. The base plate, guide rail, anchor blocks and hardware were modeled as lumped masses at the leading and trailing edges, and half of their combined mass, 0.408 kg, was added to the corresponding DOFs in the mass matrix. The mass of the attachment excluding the NES mass is lumped

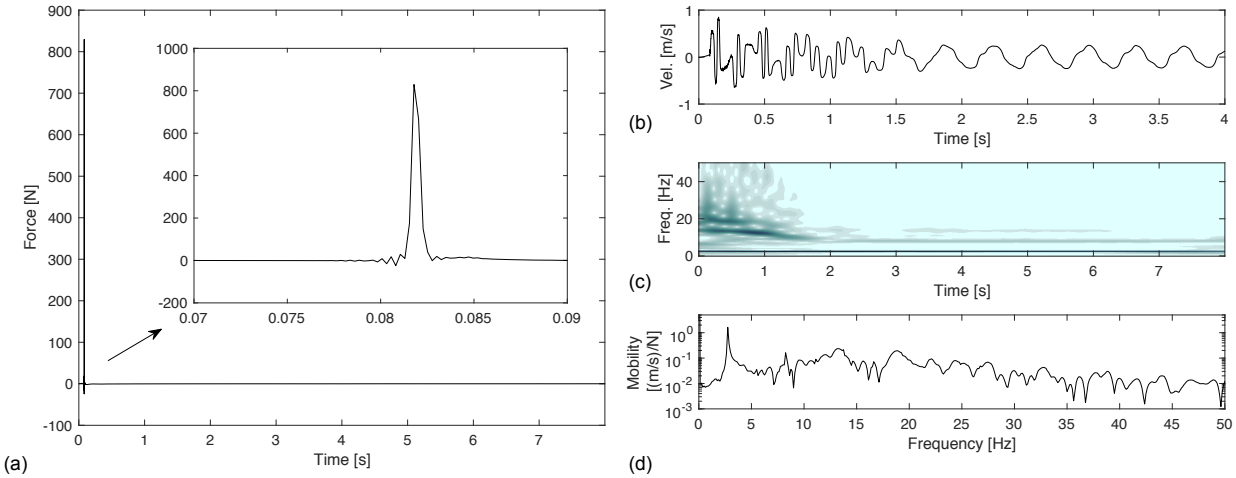

Figure 5.12: (a) High amplitude, impulsive load applied at the nonlinearity location. (b) Velocity response of the NES with corresponding (c) wavelet spectrum and (d) FRF for the impact depicted in (a).

Table 5.2: Comparison of the natural frequencies measured experimentally and predicted using the FE model, the corresponding percent error, and the corresponding damping ratios.

Mode #	**Exp. Freq. [Hz]**	**FE Freq. [Hz]**	**Error [%]**	**Damping Ratio, ζ_i**
1B	2.769	2.795	-0.94	0.0041
NES	8.362	8.362	0	0.060
2B	14.30	15.25	-6.65	0.00258
1T	26.79	27.09	-1.12	0.00247

at the edges to reproduce the reduction in frequency of the torsional NNMs observed in the experiments, which is not reproduced by lumping the mass at the center of the tip. Unlike the RFS method, the proposed NSI method cannot presently be used to identify damping. Thus, the system is modeled using linear modal damping, and the modal damping ratios are identified using response data for an impulse of 10 N at the leading edge of the wing tip with the MFDID toolbox [Kim et al., 2005]. The resulting damping ratios for the first five NNMs are provided in Table 5.2. For simulations, the damping ratios for higher NNMs are set to 0.001. Before incorporating the NES, the FE matrices were reduced using Guyan reduction [Guyan, 1965] into two separate models. The first model retained only the DOFs corresponding to the translational DOFs along the leading and trailing edges. This model corresponds to the experimental setup and is used in the computation of the RQ instantaneous frequencies and for plotting the corresponding POMs. The second model retains all translational DOFs and is used to simulate the response of the wing using the RFS and NSI models.

The NES is modeled as a single-DOF mass coupled to the leading and trailing edges using the same

nonlinear stiffness model employed previously. The NES is coupled to the leading and trailing edges such that it can interact with the torsional NNMs. A schematic of the NES model is presented in Fig. 5.13, and the corresponding equation of motion is given by,

$$m\ddot{x} + d_n\dot{\delta} + \left(k_n + \alpha_n \left|\delta\right|^{\beta}\right)\delta = 0, \delta = x - \tfrac{1}{2}\left(u_{\mathrm{LE}} - u_{\mathrm{TE}}\right), \tag{5.12}$$

where x is the displacement response of the NES and u_{LE} and u_{TE} are the displacement responses of the leading and trailing edges of the wing tip, respectively. In Fig. 5.13, M corresponds to the mass of the attachment excluding the mass of the NES. The measured natural frequency of the NES at low energy is 8.36 Hz. Using the GlobalSearch algorithm in MATLAB®, the linear coupling stiffness is then determined by minimizing the error between the FE natural frequency corresponding to the NES and that of the NES in the experiment. The optimization resulted in a linear coupling stiffness of $k_n = 241.5$ N/mm, which results in a natural frequency of 8.36 Hz when the NES is coupled to the wing. The damping ratio for the NNM corresponding to the motion of the NES is computed using the MFDID toolbox and low-amplitude response data as described previously, and is found to be $\zeta_n = 0.06$ which corresponds to 0.562 Ns/m. Damping due to friction is not included in the NSI model, leaving only the nonlinear stiffness parameters to be identified.

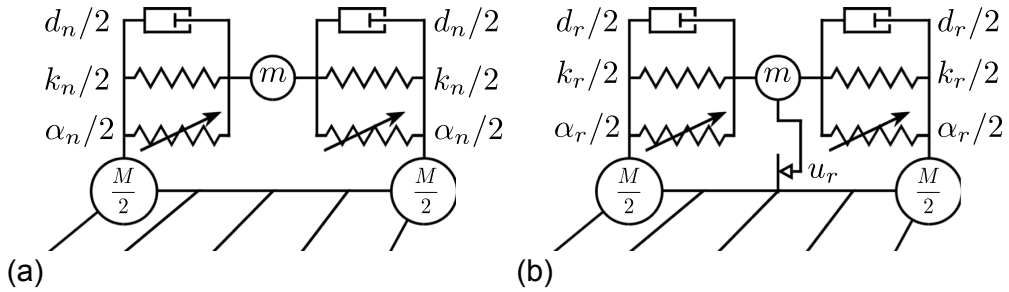

Figure 5.13: Schematics of the (a) NSI model and (b) RFS model used to attach the NES to the wing.

5.3.4 Detection of Strongly Nonlinear Modal Interactions

With the underlying linear FE model updated, we now proceed with the identification of the nonlinear stiffness and begin by computing the representative POMs. Unlike in the computational section where SVD was applied to the entire time series, we instead apply it to windowed segments of the measured response and extract representative POMs for each segment. The signal is divided into 42 non-overlapping segments each with a duration of 0.174 s, which approximately corresponds to one-half of the fundamental period of the wing. Additionally, the first 0.09 s are excluded from the analysis because this portion contains the response

of the system to ambient vibration before the impact and the brief forced response (for reference, the applied load ends at 0.0825 s). The last 0.471 s are also excluded because only the first NNM participates in this portion. Applying SVD results in 15 POMs for each segment; however, only those corresponding to the first four NNMs are analyzed because they contain most of the available energy. A sixth-order, two-dimensional polynomial with no constant or linear terms is fitted to each POM, which reduces the effect of measurement noise. The final POMs are created by evaluating the polynomials at each accelerometer location.

Using the POMs, we compute the RQ for the leading four (i.e., the four lowest-frequency) NNMs for each time segment and plot them as functions of time and energy in Figs. 5.14(a) and (b), respectively. The total energy was estimated by fitting a shape-preserving, piecewise-cubic Hermite polynomial to the successive maximums of the kinetic energy, computed using the integrated velocities and FE mass matrix. In addition to the RQ estimates, the low-energy experimental frequencies for each NNM are plotted as black-dashed lines in Fig. 5.14. While only one spike appears in the resulting frequency estimates, the proximity of the frequencies of the NES and second bending NNMs during the first second in Fig. 5.14(a) suggests that the transient dynamics of the system is engaged in a 1:1 TRC during this period; i.e., the dynamics is transiently captured on a 1:1 resonance manifold [Vakakis et al., 2008]. This leads to strongly nonlinear modal interaction and energy transfer between the NES and the second bending mode of the wing. To study this nonlinear interaction in detail, we highlight eight cases, spaced 1.038 s apart, noted with red dots in Figs. 5.14(a) and (b). In Table 5.3, we provide the corresponding time instants, the instantaneous total system energy, the percent of initial total energy remaining, and the percent of energy dissipated since the previous case. Although only a period of 1.038 seconds elapses between cases I and II, more than 71.74% of the initial total energy is dissipated during that interval. In contrast, only 5.4% of the initial total energy is dissipated between cases II and III, even though the same amount of time elapses between cases II and III as for cases I and II. Such large energy dissipation in a short time cannot be accounted for by linear viscous damping alone, but rather to rapid nonlinear energy transfer from the second bending mode to the NES which appears as effective damping of the wing response. This result further indicates that the system sustains a 1:1 TRC between the second bending NNM and the NES during the first 1.038 seconds and highlights the practical significance of such nonlinear modal interaction on the wing response.

Table 5.3: Time instants and energy values corresponding to the eight cases shown in Fig. 5.14.

Case	Time Instants [s]	System Energy [J]	Percent of Initial Total Energy Remaining [%]	Percent Energy Dissipated Since the previous case [%]
I	0.09	0.363	100	-
II	1.1281	0.103	28.26	71.74
III	2.1661	0.083	22.86	5.40
IV	3.2042	0.071	19.48	3.38
V	4.2422	0.061	16.93	2.55
VI	5.2803	0.053	14.48	2.44
VII	6.3184	0.045	12.47	2.02
VIII	7.3564	0.041	11.27	1.20

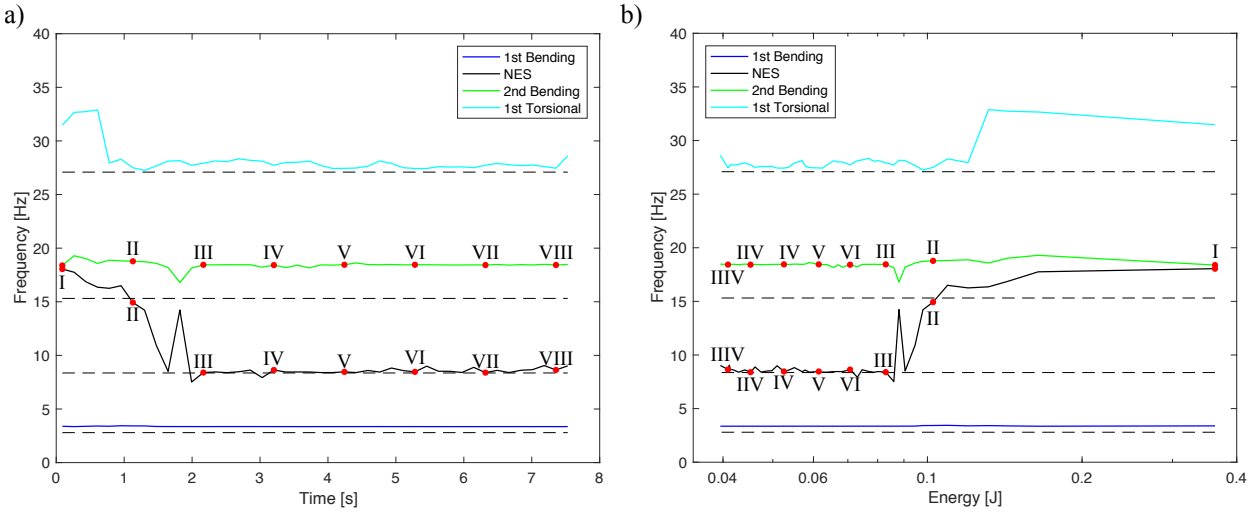

Figure 5.14: RQ frequency computed using the POMs corresponding to the first four NNMs plotted as functions of (a) time and (b) estimated energy. The black-dashed lines represent the experimental frequencies at low energies.

To study further the strongly nonlinear modal interaction between the second bending mode of the wing and the attached NES, in Fig. 5.15 we depict the second and third POMs of the integrated wing-NES assembly for cases I through IV, corresponding to the NES and second bending NNMs, respectively. From these results we note that for cases I and II, the two POMs are similar to each other, possessing two nodal and two anti-nodal lines. The presence of similar POMs verifies that the large energy dissipation observed in the first 1.038 second time interval results from a 1:1 TRC that occurs between the second bending NNM and the NES. Indeed, when the NES engages in 1:1 TRC with the second bending NNM, it passively and irreversibly absorbs energy from the second bending NNM; part of the absorbed energy is dissipated locally

by the NES, whereas the remaining part is scattered to higher frequencies. The end result is that the energy of the system is dissipated much more efficiently and rapidly compared to that dissipated by the inherent modal damping of the second bending NNM of the wing alone. Consequently, the second bending NNM retains very little energy throughout the remainder of the measurement, which reduces the accuracy of the corresponding POM and its corresponding estimated frequency. Hence, the fact that the estimated frequency for the second bending NNM deviates significantly from the experimental low-energy frequency results from the extreme loss of energy that the second bending NNM suffers in the 1.038 s duration of 1:1 TRC.

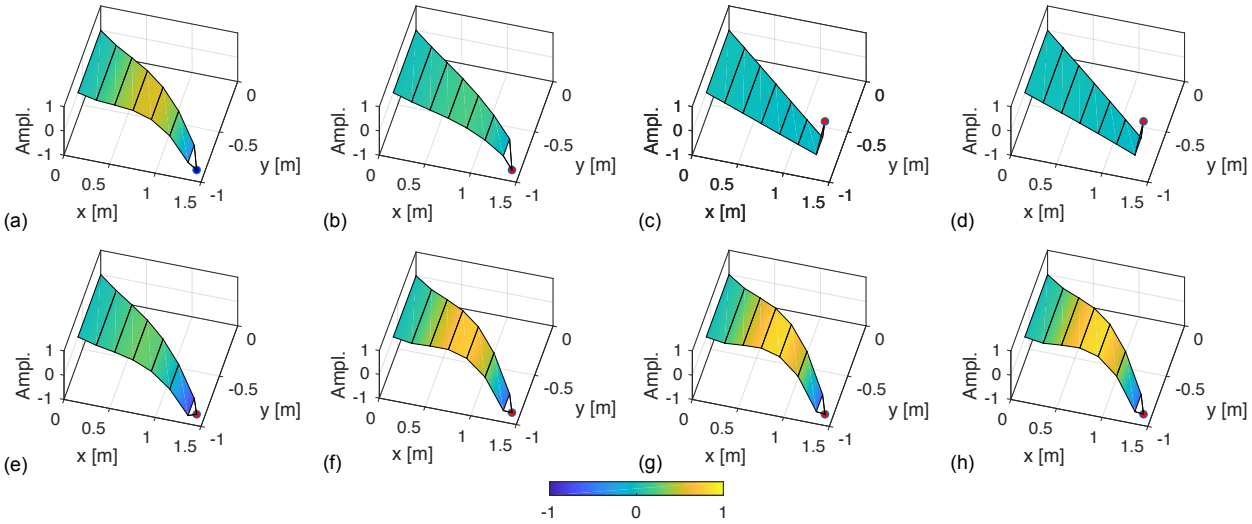

Figure 5.15: The second POM depicted for (a) case I, (b) case II, (c) case III and (d) case (IV) and the third POM depicted for (e) case I, (f) case II, (g) case III and (h) case IV.

The other estimated frequencies sufficiently approximate the frequencies of their respective NNMs, which reflects the fact that these NNMs do not experience TRC or a similar energy loss in the time intervals examined as the second bending NNM. In cases III and IV, the POMs are not similar and, thus, the two NNMs do not engage in a TRC in these cases. Although not presented, the POMs for cases V through VIII are comparable to those of cases III and IV and, similarly, do not undergo any TRCs. The spike that appears between cases II and III results from a higher-order TRC between the second bending NNM and the NES, but this does not persist long enough to dissipate more than a few percent of the initial total energy. The small spikes that appear after case III do not result from TRCs, but rather are the product of small measurement errors and noise that become increasingly influential as the response decays.

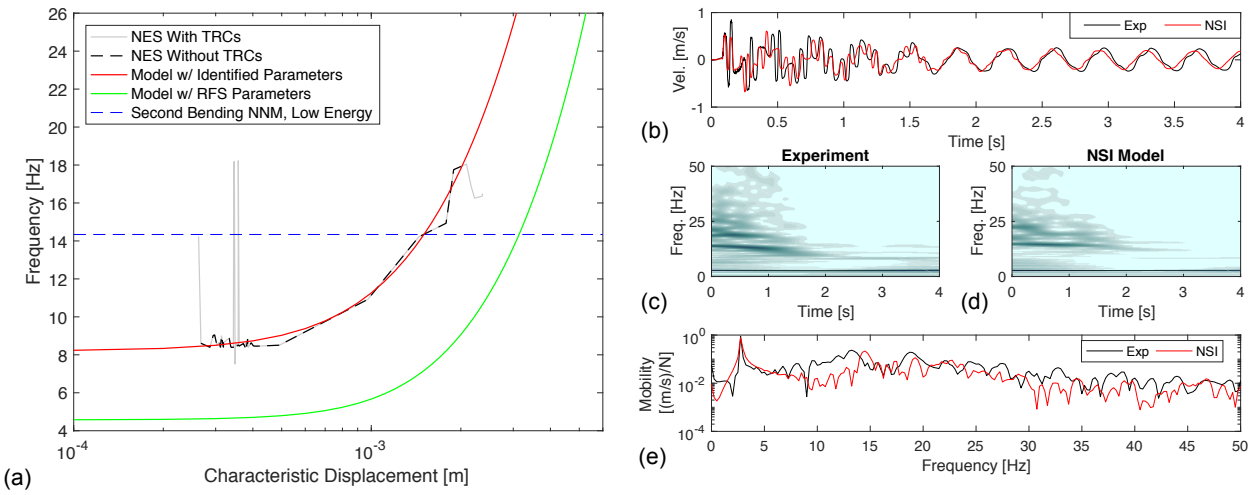

Figure 5.16: (a) Comparison of the RQ frequency-displacement plot for the estimated frequency of the NES and the identified models; (b) Comparison of the velocity response of the NES measured experimentally and computed using the NSI model. The corresponding wavelet spectra for the experimental measurement and simulated response are presented in time series, wavelet spectra and FRFs for the experimental and simulated velocity responses of the NES for the impulse of Fig. 5.12(a).

5.3.5 NSI of Winglet-mounted NES

Proceeding with the previously outlined NSI method, we define the characteristic displacement for this system to be,

$$\bar{\delta} = \frac{1}{T_2 - T_1} \int_{T_1}^{T_2} \left| x - \tfrac{1}{2} \left(u_{\mathrm{LE}} + u_{\mathrm{TE}} \right) \right| dt, \tag{5.13}$$

where $\bar{\delta}$ is computed for each interval used in the computation of the POMs. As such, we compute 42 values for $\bar{\delta}$ that correspond to the 42 non-overlapping windows used in the computation of POMs. Additionally, prior to computing the characteristic displacement, we apply a high-pass, third-order Butterworth filter with a cutoff frequency of 6 Hz to the relative displacement to remove the contribution of the first NNM, which does not engage the nonlinearity (since its frequency is always less than the instantaneous frequency of the NES). In Fig. 5.16(a), we present the resulting RQ frequency-displacement plot for the NES as the gray and dashed black curves, which correspond to the segments of the response during which the NES is and is not engaged in 1:1 TRC with the second bending NNM. Since the gray curve corresponds to periods of mode mixing (i.e., the estimated frequencies result from similar POMs), it cannot be attributed solely to the NNM of the NES and, thus, is excluded from the identification. As such, the identification is performed using only the black curve.

As described previously, we model the nonlinearity as $\alpha_n \left| \delta \right|^{\beta_n} \delta$, which results in the frequency-displacement relationship presented in Eq. 5.8. The characteristic displacement at the point where the NES curve in-

tersects the low-energy frequency of the second bending NNM is found using linear interpolation to be $\bar{\delta}_2 = 0.001503$ m, such that α_n is related to β_n using Eq. 5.9 and leaving β_n to be determined using Eq. 5.10. We identify β_n using the same optimization routine described for the computational study, and for all initial guesses the routine converged to $\beta_n = 2.0714$, resulting in $\alpha_n = 3.4887 \times 10^8$ N/m$^{3.0714}$ with an R-squared value of 0.9800. The frequency-displacement curve predicted using the identified parameters is depicted as the red curve in Fig. 5.16(a).

The identified model is validated by simulating the wing-NES system for multiple impulsive loads and comparing the predicted velocity of the NES with that of the experimental measurements. The velocity of the NES is used for the comparison because the displacement response is dominated by the first bending NNM and provides an unfair comparison as this NNM maintains a constant frequency throughout the response and never interacts with the NES. Figure 5.16(b) presents the simulated response for the impact depicted in Fig. 5.12(a), which corresponds to the measurement case used for the identification. Additionally, the corresponding wavelet spectra and FRFs are provided in Figs. 5.16(c) and (d), respectively. We find that the simulated response reproduces the measured response including the higher harmonics and the interactions between the NES and the second bending NNM as seen in the wavelet spectra. These results confirm that the NSI model accurately reproduces the response for the measurement case used for the identification.

To further validate the NSI model and to compare the proposed NSI method with the RFS method, we consider three additional measurement cases (which were not used for the system identification of the NES); note that the schematic for the RFS model attached to the wing is presented in Fig. 5.13(b). Figures 5.17 and 5.18 depict the comparison of the RFS and NSI models with the experimental response for the impacts of magnitude 264.8, 504.4 and 1158.6 N. For an impact of 264.8 N, the RFS model does not reproduce the high frequency oscillations, which result from the strong nonlinearity, occurring in the first half-second of the response. For the 504.4 N impact, the RFS model captures the high-frequency oscillations for the first half-second of the response but fails to do so for the next half-second. For the impact of 1158.6 N, the RFS model reproduces the nonlinear behavior exhibited in the first two seconds of the response. In contrast, the NSI model reproduces the nonlinear behavior for all three impacts in both the time series and the wavelet spectra.

These results demonstrate the power of our method for identifying models with nonlinear attachments while also detecting strongly nonlinear modal interactions directly from measured data. As such, the method can provide significant insight into the physics of dynamical systems with smooth, local nonlinearities and nonlinear attachments. Hence, the method could prove to be a valuable tool for gaining a thorough understanding of, interpreting and predicting the transient responses of strongly nonlinear dynamical systems.

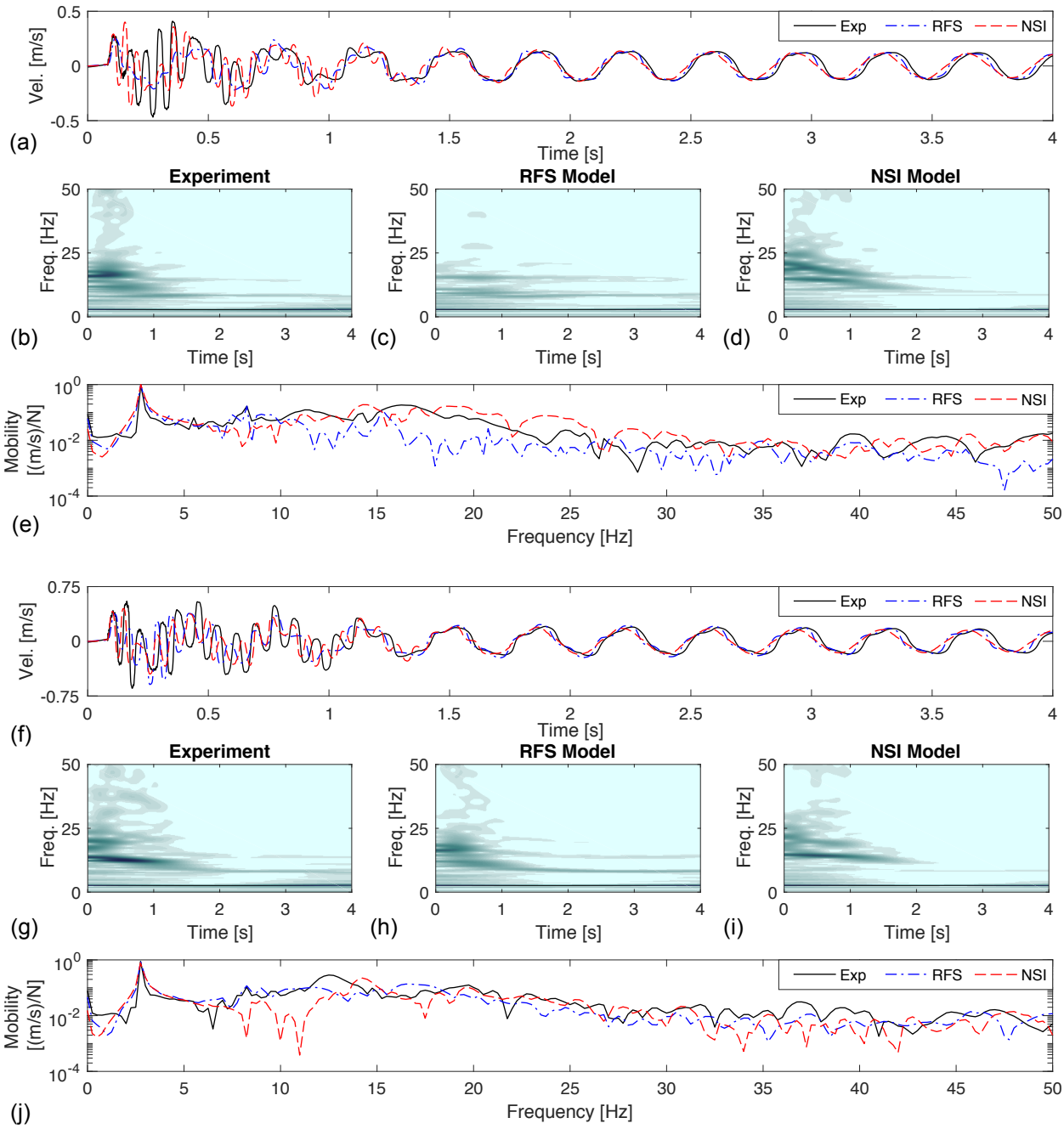

Figure 5.17: Comparison of the velocity of the NES measured experimentally with that computed using the RFS and NSI models for impacts of (a) 264.8 N and (f) 504.8 N. The wavelet spectra for the experimentally measured velocities are presented in (b) and (g) for each impact case. Similarly, the wavelet spectra for the displacement computed using the RFS and NSI models are presented in (c) and (h) and (d) and (i), respectively, for each impact. Finally, a comparison of the FRFs of the measured, RFS and NSI systems are presented in (e) and (j) for each impact case.

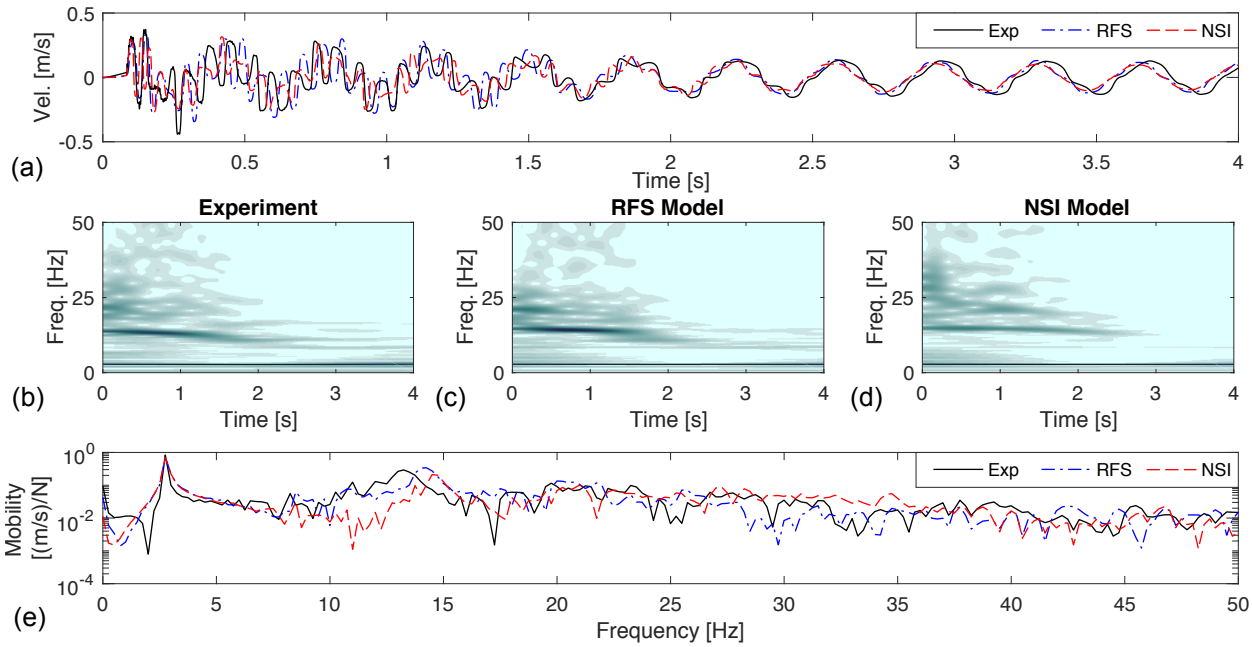

Figure 5.18: (a) Comparison of velocity of the NES measured experimentally and computed using the RFS and NSI models for an impact of 1158.6 N. The wavelet spectra corresponding to the velocity measured experimentally, computed using the RFS model and computed using the NSI model are presented in (b), (c) and (d), respectively. (e) Comparison of the FRFs for the velocity measured experimentally, computed using the RFS model and computed using the NSI model.

5.4 Concluding Remarks

In this chapter, we studied the response of two cantilevered wings, one computationally and the other experimentally, each with a smooth, local nonlinear attachment in the form of an NES attached to the wing tip. The response of the first wing was simulated using the FE model whereas the response of the second wing was measured experimentally. In each case, POD was applied to extract POMs from the displacement responses which were representative of the NNMs governing the system dynamics; these response time series were obtained either from direct simulation or by integrating and filtering the experimentally measured accelerations.

The computational system was studied using multiple simulations corresponding to different forcing amplitudes, and the POMs were extracted from each simulation separately. In contrast, POD was applied to windowed segments of the measured response of the experimental system separately, such that the POMs for each segment were extracted. For both systems, the POMs were used as trial vectors in the discrete RQ to estimate the frequencies of the NNMs. These frequency estimates were plotted as functions of time, energy and displacement, which revealed the presence of non-smooth perturbations (spikes) that indicated strongly nonlinear modal interactions in the form of transient resonance captures.

For both systems, the RQ-FDP for the NES was used to identify the nonlinearity directly from the response data. In the computational study, the form and coefficients of the nonlinearity were known exactly, and the parameters identified using the proposed method agreed with the exact parameters. The errors for the nonlinear coefficient and exponent were 2.19% and 1.96%, respectively. Additionally, the identified model was found to reproduce the relevant transient dynamics when compared to the response of the exact system. In the experimental study, the nonlinearity was identified using the RFS method and the proposed NSI method. The RFS method was applied to the response of the grounded NES and the identified model; the RFS model almost perfectly reproduced the response of the grounded NES measured experimentally. However, when the RFS model was coupled to the FE model of the wing, it failed to reproduce the relevant nonlinear behavior for two out of three loading cases. In contrast, the proposed method was applied to the response of the wing with the NES installed, and the final outcome of the system identification exercise, i.e., the NSI model, proved to accurately reproduce the corresponding transient dynamics for all three loading cases.

The results in this work demonstrate that the proposed method can be used to accurately identify models of strongly nonlinear attachments directly and solely from the post-processing of measured transient response data. Hence the discussed approach is data-driven. Since the method relies on prior identification of the underlying linear properties of the system, which are readily available either from FE models or from experimental modal analysis, the method avoids the steep analytical and computational costs associated with traditional methods for NSI of strongly nonlinear systems.

Chapter 6

Global Dynamic Effects Induced by Local Nonlinear Attachments

6.1 Introduction

This chapter applies the proposed data-driven NSI and model updating methodology to the dynamics of a model airplane (similar to that reported in [Whitican and Copeland, 2016]) with one strongly nonlinear store connected to each wing. The objective of this investigation is to determine and quantify the effect of the stores, which are local attachments, on the global dynamics of the plane through the energy transactions facilitated by the nonlinear store that occur between the NNMs of the plane and the local stores. The rest of this section is divided as follows. First, a linear experimental study of the plane without any stores is performed by experimentally identifying the natural frequencies and corresponding damping ratios of its modes. In the next part, a finite element (FE) model created using Abaqus® is described in detail, and model updating is performed using the linear experimental measurements. This portion also discusses the reduced-order model (ROM) created using Guyan reduction [Guyan, 1965] from the full FE model and compares the resulting natural frequencies and mode shapes of each model. Following that, the design of the nonlinear stores is presented, and ROMs of the store and of the store coupled to the second flexible mode of the plane are used to evaluate the effectiveness of the stores prior to simulation with the reduced FE model. Next, the stores are coupled to the wings of the reduced FE model and the response of the plane is simulated for multiple impulsive excitations in the same way as the cantilevered beam and wing in Sections 4.2 and 5.1, respectively. Using the resulting RQ-FEP and RQ-FDP, the strong nonlinearity is identified, and the updated model is compared to the exact model. The penultimate section presents the nonlinear experimental measurements of the plane with the stores attached. The cases where one or both stores are unlocked (thereby inducing strongly nonlinear effects into the dynamics) are considered separately, and are compared to the cases where they are both locked (so they have only mass-effects and the dynamics is linear). Finally, the effect of the local stores on the global dynamics of the plane is assessed by studying the modal energy transactions that arise.

6.2 Linear Experimental Measurements and System Identification

To facilitate the development of a linear FE model, the free response of the plane without any attachments was measured experimentally prior to any computational studies. In this state, the plane exhibits linear dynamics for all impacts that are achievable using a standard modal hammer (i.e., impact amplitudes from 5 to 3000 N for pulse durations varying from 0.002 to 0.01 s). The plane was constructed using a steel pipe for the fuselage and steel plates for the wings, stabilizers and tail. Steel angle irons were welded directly to the fuselage such that, when connected, the wings and stabilizers sit horizontally and 30° below the wings, respectively. The wings and stabilizer were bolted to the fuselage using 16 (8 per wing) and 6 (3 per stabilizer) 5/16"-18 UNC x 1" bolts with lock washers, respectively. The tail was welded directly to the fuselage and required no bolts. Additionally, two steel U-channels were welded to each wing, which served as mounting rails for the nonlinear stores. The thickness of each component is listed in Table 6.1. The wingspan of the plane is 1.016 m, and the nose-to-tail-tip length is 1.346 m. The fuselage (including angle irons, hardware and tail) and stabilizers had a combined mass of 14.96 kg, and the left and right wings (including mounting rails) had masses of 7.26 kg and 7.32 kg, respectively, resulting in a total mass of 29.54 kg.

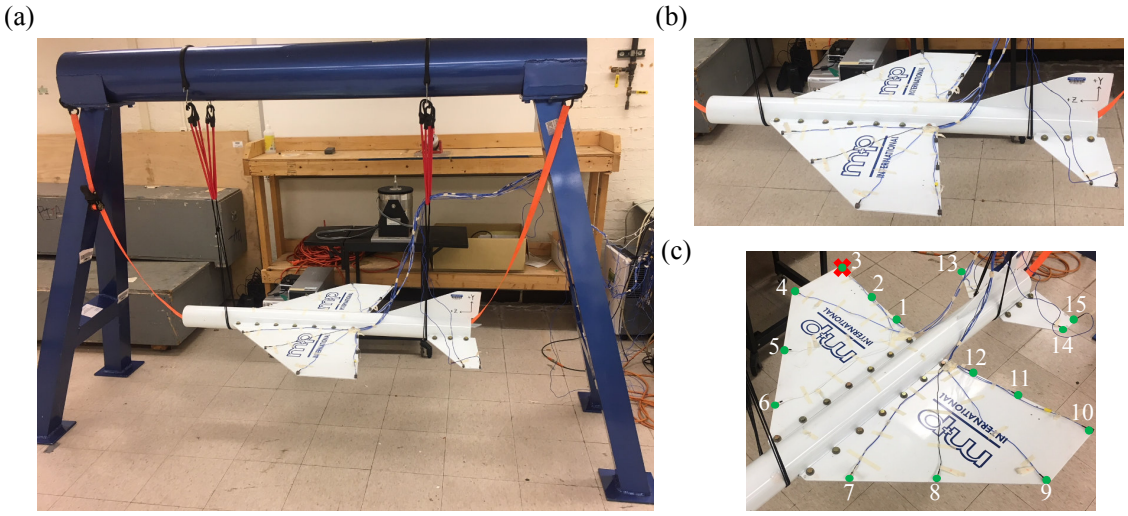

Figure 6.1: (a) Support structure with the suspended plane fully instrumented, (b) zoomed-in view of the suspended plane and (c) the instrumentation scheme used for the experimental measurements with green circles and the red cross indicating accelerometer and impact locations, respectively.

The plane was suspended from the blue support structure depicted in Fig. 6.1(a) using two rubber bungees (these were wrapped around the top of the support structure), six bungees (three in the front

and three in the back) and high-stiffness, nearly inextensible rope. The experimental setup is intended to mimic in-flight conditions where all six rigid-body modes may be activated; however, the suspension system transforms the vertical and pitch rigid-body modes into flexible modes in the sense that the bungees behave as grounding springs (we will continue to refer to these as the vertical and pitch modes). To be clear, these modes remain rigid in terms of the motion of the plane, but no longer possess natural frequencies at 0 Hz. As such, the vertical and pitch modes exhibit in-phase and out-of-phase motion with the plane acting as a rigid-link connected to ground at two points. The suspension system (as previously described) was selected to minimize the frequencies of both the vertical and pitch modes, and the resulting frequencies were each less than 3 Hz. More importantly, the suspension system was placed along the fuselage to minimize its effect on flexible modes of vibration, which are dominated by motion in the wings, stabilizers and tails below 250 Hz. In addition to the suspension system, a ratchet strap was channeled through the fuselage and anchored to the support structure. The ratchet strap (bright orange in Fig. 6.1(a)) was included as a safety precaution in case the bungees failed, and had enough slack to ensure that it did not support the weight of the plane while the suspensions were functioning. The weight of the support structure was sufficient to ensure that it did not move during the measurements, but light enough that it could be repositioned as needed with the plane attached.

The suspended plane was instrumented using 15 PCB accelerometers (models 353B15, 353B18, 356A11, 356B21, 356M41, 352C68, 353B18) all with a nominal sensitivity of 1.02 mV/(m/s^2). A zoomed-in view of the entire plane is presented in Fig. 6.1(b), and the instrumentation scheme is presented in Fig. 6.1(c), where the green, numbered circles and the red cross indicate the locations of the accelerometers and impact, respectively. Note that there were 12 accelerometers on the wings and 3 on the stabilizers. The final channel in the data acquisition system was used to measure the applied impact applied using a PCB modal hammer (model 086C01). This distribution of sensors was selected because the modes within the frequency range of interest (20-150 Hz) were dominated by flexible motion in the wings and stabilizers. The accelerations were measured at a sampling rate of 8192 Hz for a duration of 4 seconds using VibPilot hardware (m+p International, Hannover, Germany) and m+p analyzer software.

An example of the measurements collected in the experimental study of the plane without any stores is presented in Fig. 6.2. Specifically, the acceleration response to the impact depicted in Fig. 6.2(a) of the wing measured at the impact location is provided in Fig. 6.2(b) as well as the corresponding WT spectrum and FRF. The presence of clear resonances and anti-resonances in the FRF and the fact that the dark bands in the WT spectrum do not depend on time are indications that the response is indeed linear for this forcing amplitude. Moreover, the appearance of anti-resonances between every resonance peak confirms that the

Table 6.1: Average thickness of each component.

Component	Thickness [mm]
Fuselage	3.18
Tail	4.55
Wings	4.62
Stabilizers	4.55
Angle Irons	3.20
Mounting Rails	3.20

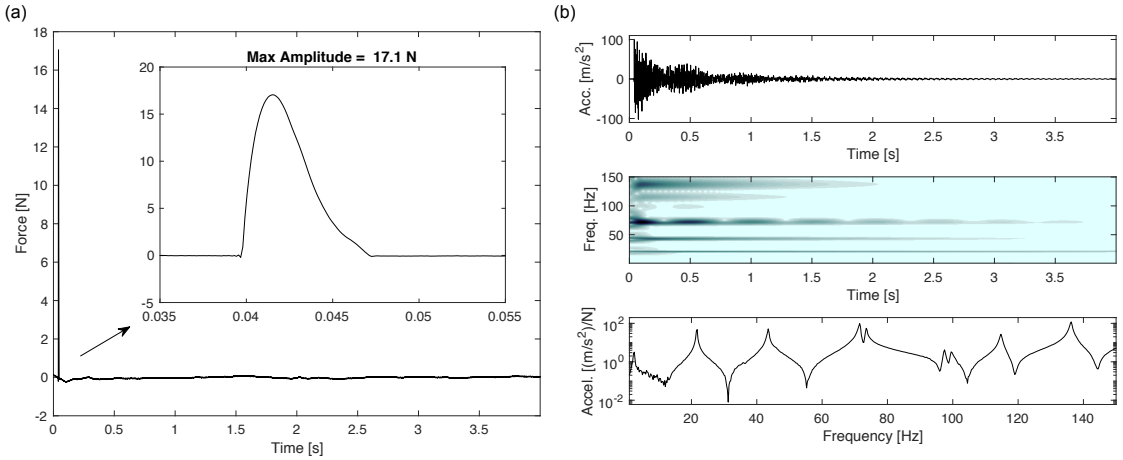

Figure 6.2: (a) Low-amplitude, impulsive load applied to the impact location indicated in Fig. 6.1, (b) Time series, WT spectrum and FRF of the acceleration measured at the impact location.

sensing point is the same as the impact location. The first resonance peak, which appears at 1.75 Hz, corresponds to the vertical mode; the pitch mode is not excited to a large enough amplitude to be visible in either the WT spectrum or the FRF. This suggests that the forcing location is at or near the axis of rotation for the pitch mode, but this was not confirmed in the experiments. Following the vertical mode resonance peak, all other peaks correspond to a flexible mode governing the vibrations of the plane. Note that the third and fourth modes and the fifth and sixth modes are closely spaced, which gives rise to the apparent beating observed in the WT spectrum.

Figure 6.3 presents the FRFs for the sensors placed at (a) the wing tips, (b) the wing midpoints and (c) near the wing roots. These plots confirm that the modal frequencies are spatially independent (which further confirms the linearity of the system); the corresponding frequencies are provided in Table 6.2. The damping ratios for each mode are identified using the FRFs presented in Fig. 6.3 and the MFDID toolbox [Kim et al., 2005], similar to the damping identification performed in Section 5.3.3. The resulting damping ratios for the first eight modes are provided in Table 6.2.

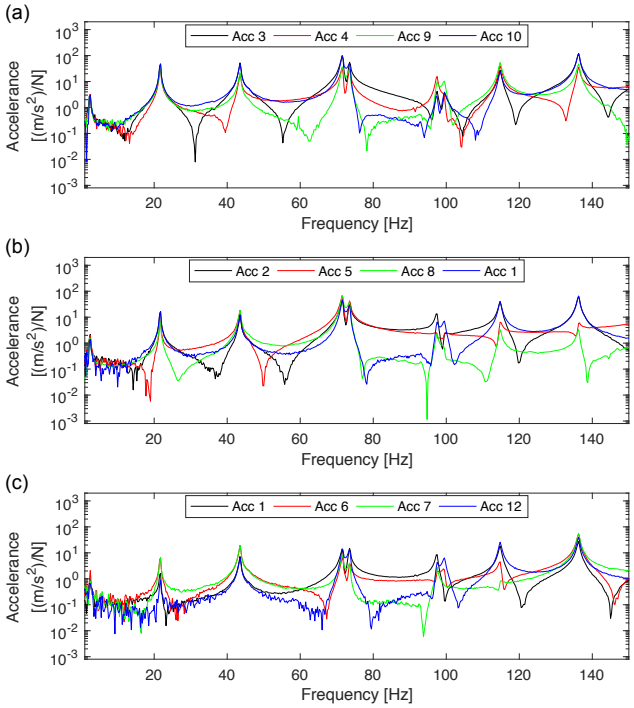

Figure 6.3: Frequency-response functions for the accelerations measured for the impact depicted in Fig. 6.2(a) at (a) the wing tips, (b) wing midpoints, and (c) near the wing root.

Table 6.2: Comparison of the experimental natural frequencies with the natural frequencies and damping ratios identified by the MFDID toolbox.

Mode #	**Experiment**	**MFDID Model**	
	Freq. [Hz]	Freq. [Hz]	Damping Ratio, ζ_i
1	21.67	21.66	0.00291
2	42.63	42.56	0.00619
3	71.14	70.6	0.00364
4	73.73	72.74	0.00354
5	98.14	97.80	0.00278
6	99.88	99.54	0.00330
7	115.0	114.3	0.00271
8	136.5	135.1	0.00219

6.3 Linear Finite Element Modeling and Experimental Model Updating

Following the experimental measurements of the plane with no attachments, a computational model is developed using Abaqus® and the measurements are used to perform linear model updating. The full-order FE model is depicted in Fig 6.4(a), which includes the mounting angle irons and the mounting rails. All components are meshed using S4R elements, which are first-order, quad shell elements, and the structured approach is employed in the mesh creation. The resulting meshes for each component are presented in Fig. 6.5. Note that the mesh for the right wing and stabilizer are identical to that of the left wing and stabilizer, respectively. All components are modeled with a density of 7829 kg/m^3, an elastic modulus of 206.94 GPa and a Poisson's ratio of 0.288, all of which are representative of steel and come from the previous study of a comparable airplane performed by Whitican and Copeland [2016]. The average thickness of each component in the experimental specimen is used for the thicknesses in the modeled components and are listed in Table 6.1. The resulting mass of each wing is 7.30 kg, and the total mass of the other components is 14.94 kg (which are both comparable to the masses of the corresponding experimental components). The total mass of the entire FE model is 29.54 kg, which is equal to the total mass of the experimental plane.

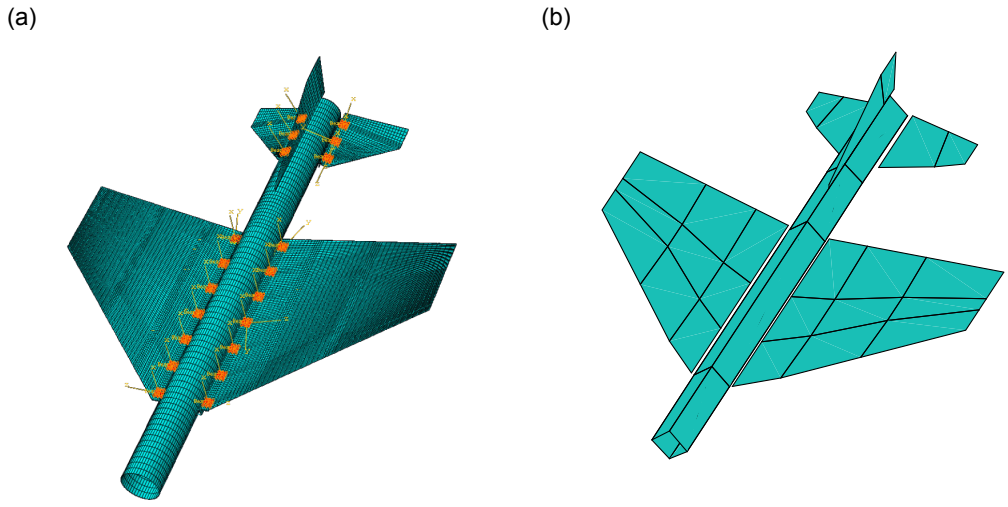

Figure 6.4: (a) Full-order FE model created using Abaqus with 19810 nodes with the bolted connections highlighted in orange. (b) Reduced-order FE model created using Guyan-reduction in Abaqus with 70 nodes.

Since the entire root of the tail is welded to the fuselage in the experimental specimen, the tail is modeled as a direct extension of the fuselage (i.e., the nodes that form the root of the tail are part of the fuselage). All other components are modeled separately and connected to the fuselage through simulated welds or bolts. The angle irons (which are welded to the fuselage in the experiment) are attached to the fuselage using beam

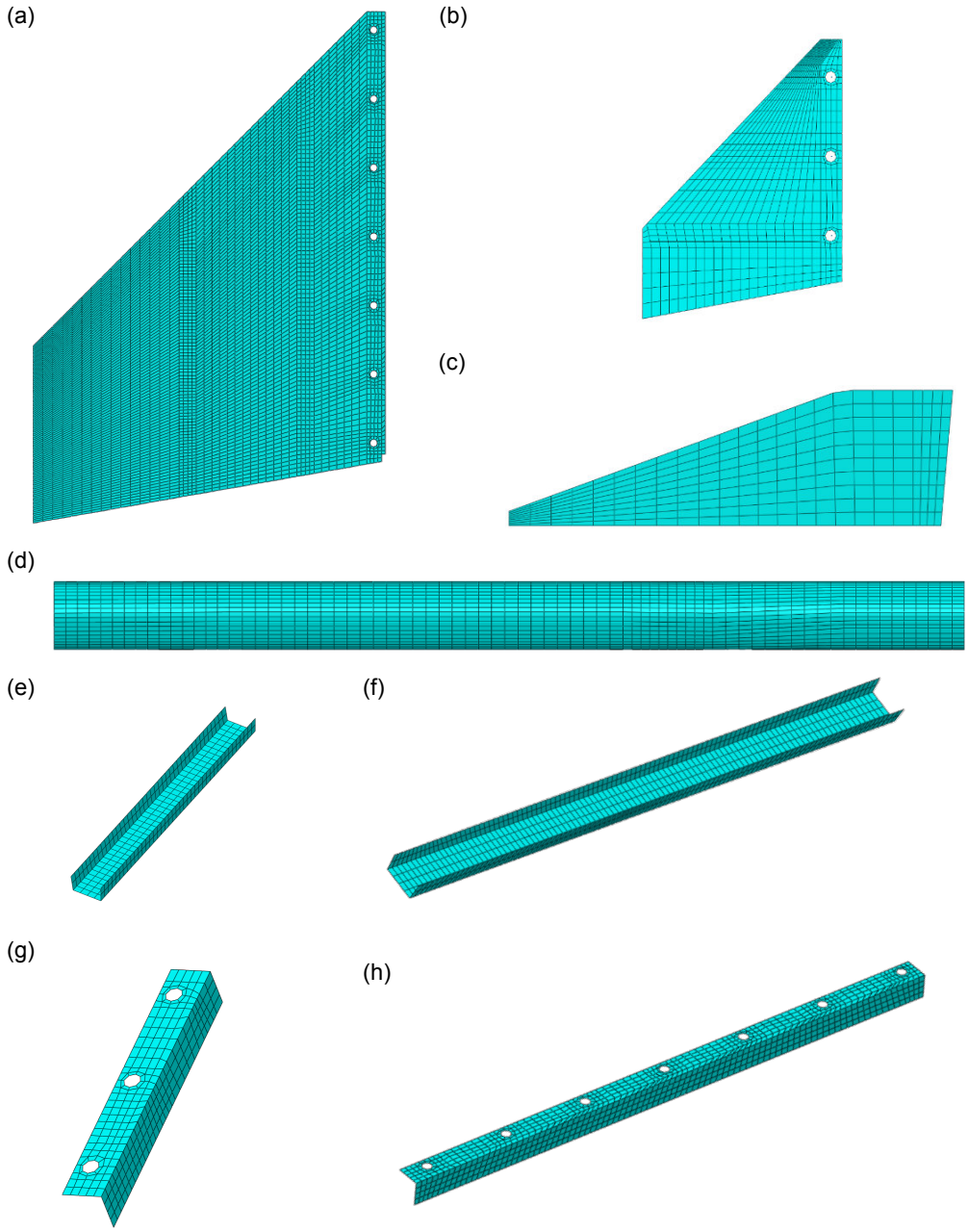

Figure 6.5: FE mesh used in the full-order model of the (a) left wing (right wing has identical mesh), (b) left stabilizer (right stabilizer has identical mesh), (c) tail, (d) fuselage, (e) short angle iron, (f) long angle iron, (g) short mounting rail and (h) long mounting rail.

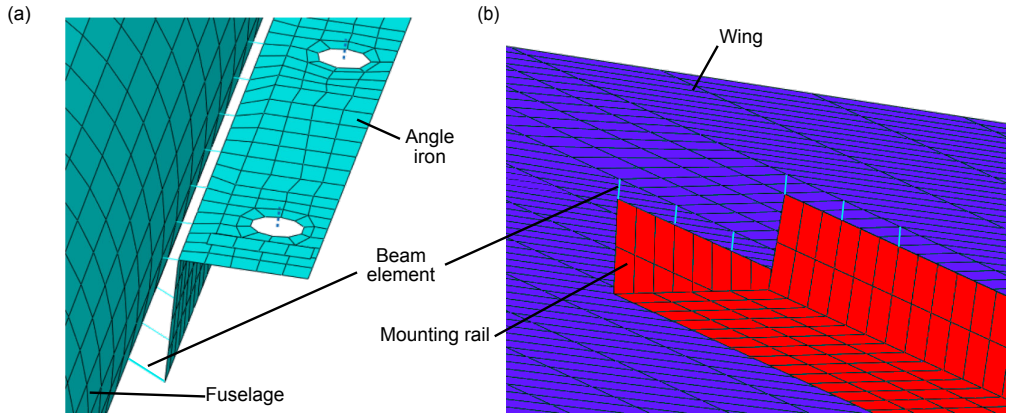

Figure 6.6: Zoomed-in views of the beam elements representing welds between (a) the fuselage and the angle irons used to mount the wings and stabilizers, and (b) the mounting rails and the wings.

elements that represent the welded connections. Similarly, beam elements are used to "weld" the mounting rails to the wings at the locations corresponding to the actual welds in the experimental specimen. Examples of these connections are presented in Fig. 6.6. In total, 166 beam elements are used to model the welds throughout the plane and each beam has a density of 7829 kg/m^3, an elastic modulus of 206.94 GPa and a shear modulus of 80.33 GPa.

The bolts that join the wings and the stabilizers to the corresponding angle irons are modeled as single beam elements that connect the reference points at the centers of the bolt holes. To model the fastening between the bolts, wings and stabilizers, an area around the bolt holes is coupled to the reference points using rigid body elements (i.e, every DOF in that area is rigidly slaved to the corresponding DOFs of the reference point). The height and width of the areas correlate to the relative stiffness of the joint and are adjusted to maximize the match between the predicted and measured modal frequencies. The areas used for the wing joints have a height and width of 32.35 mm and 19.05 mm, respectively, and an example is presented in Fig. 6.7(a). The height and width of the areas used for bolting the stabilizers are 20 mm and 19.05 mm, respectively, and an example is provided in Fig. 6.7(b). This procedure is applied to both the angle irons and the wings and stabilizers. The holes on the mounting rails used to attach the stores are not included in the FE model. A comparison of the modal frequencies of the experiment and the full-order FE model is presented in Table 6.3, and the corresponding mode shapes are depicted in Fig. 6.8.

To facilitate the computational study of the model airplane with nonlinear stores, Guyan reduction is performed using Abaqus® to reduce the full-order model to form the ROM depicted in Fig. 6.4(b). In addition to condensing out many of the translational DOFs, all of the rotational DOFs are also condensed out by the reduction. The rotational DOFs are eliminated because POD requires that all of the data be

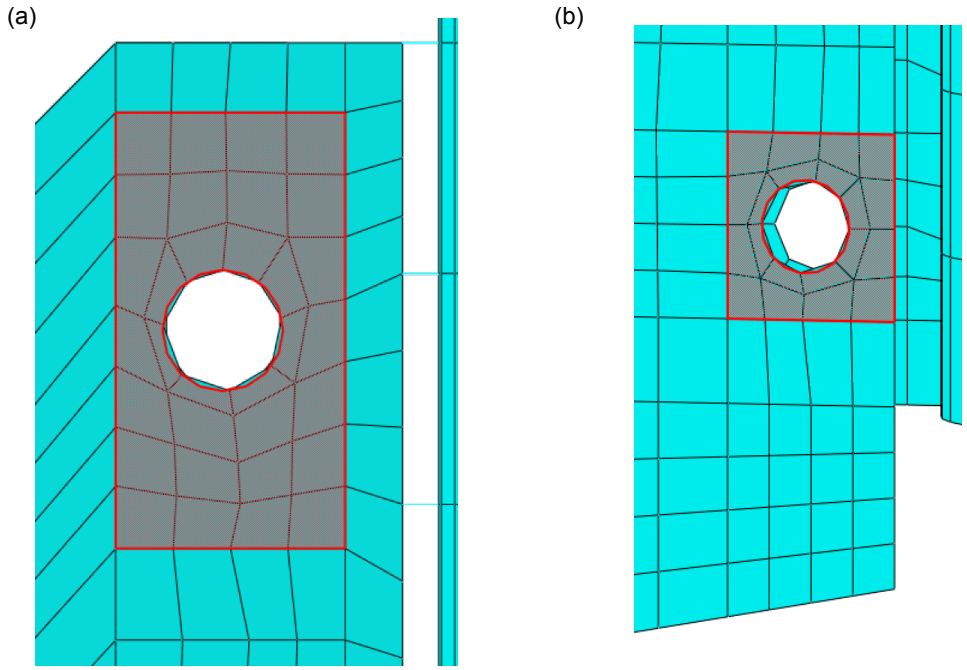

Figure 6.7: Examples the bolt areas rigidly connected to the reference point at the bolt hole center for (a) the wings and (b) the stabilizers

of the same type (i.e., all displacements or all rotations). While one can keep the rotational DOFs in the model and simply exclude them in the application of POD, one would be unable to compute the RQ without further reduction because the POMs would be incompatible with the reduced mass and stiffness matrices (each POM would be an $n \times 1$ vector, whereas the mass and stiffness matrices would be of size $2n \times 2n$). In that case, the analyst would need to further reduce the mass and stiffness matrices to compute the RQ. To avoid this extra reduction and to reduce the simulation times, a single reduction is performed, and the rotational DOFs are condensed out in this reduction. The resulting ROM has 70 nodes each with 3 DOF (totaling to 210 DOFs) whereas the full-order model has 19810 nodes each with 6 DOFs (totaling to 118926 DOFs). Note that all beam elements, angle irons and mounting rails are completely condensed out in the ROM. The nodes in the interior of the wing correspond to the locations of the holes on the mounting rails such that the stores can be connected to the FE model at the same locations as in the experiments.

The resulting modal frequencies of the ROM along with those from the linear experiments and the full-order model are provided in Table 6.3. The percent errors for both the full-order model and ROM are acceptable with average percent error for the full-order model and ROM being -1.52% and -3.28%, respectively. Additionally, the first twelve mode shapes of the ROM are presented in Fig. 6.9, and these show strong agreement with the mode shapes of the full-order model. The ROM will prove valuable in the

Table 6.3: Comparison of the modal frequencies of the experimental system, the full-order FE model and the reduced-order FE model.

Mode #	**Experiment**	**Full-order Model**		**Reduced-Order Model**	
	Freq. [Hz]	Freq. [Hz]	Error [%]	Freq. [Hz]	Error [%]
1	21.67	21.88	-0.97	21.91	-1.11
2	42.63	42.77	-0.36	42.93	-0.71
3	71.14	71.41	-0.38	71.71	-0.80
4	73.38	74.72	-1.83	75.35	-2.68
5	98.14	100.4	-2.30	101.1	-3.02
6	99.88	101.1	-1.22	102.0	-2.12
7	115.0	116.4	-1.22	117.7	-2.35
8	136.5	139.0	-1.83	141.2	-3.44
9	166.1	167.6	-0.90	176.6	-6.32
10	168.5	172.4	-2.31	179.8	-6.71
11	201.1	206.0	-2.44	208.8	-3.83
12	243.5	249.4	-2.42	258.9	-6.32
Avg. Error [%]		-1.52		-3.28	

coming computational and experimental studies of the airplane with nonlinear stores, the design of which is presented in the next section.

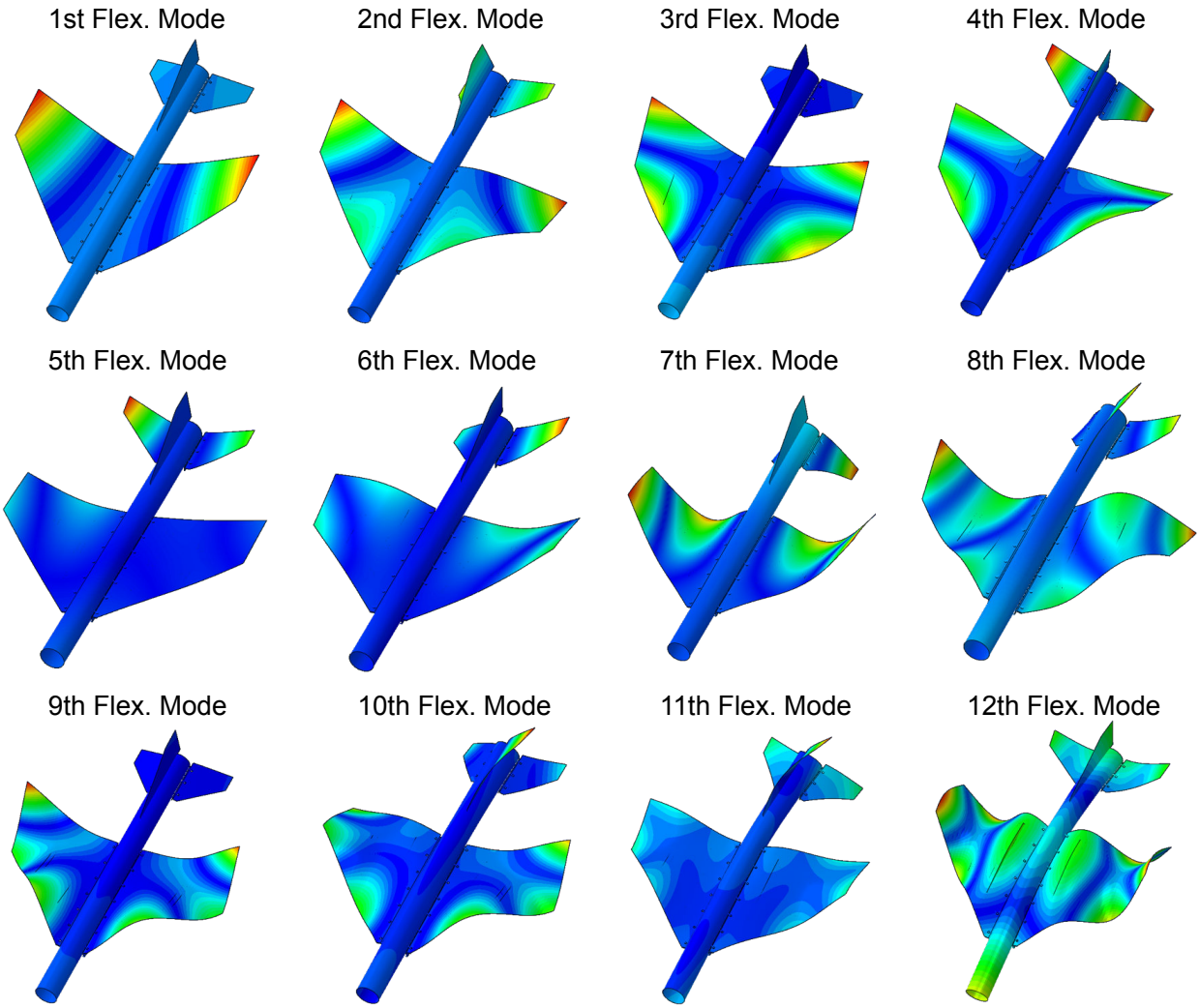

Figure 6.8: The first twelve flexible mode shapes of the plane computed using the full-order Abaqus FE model depicted in Fig. 6.4(a).

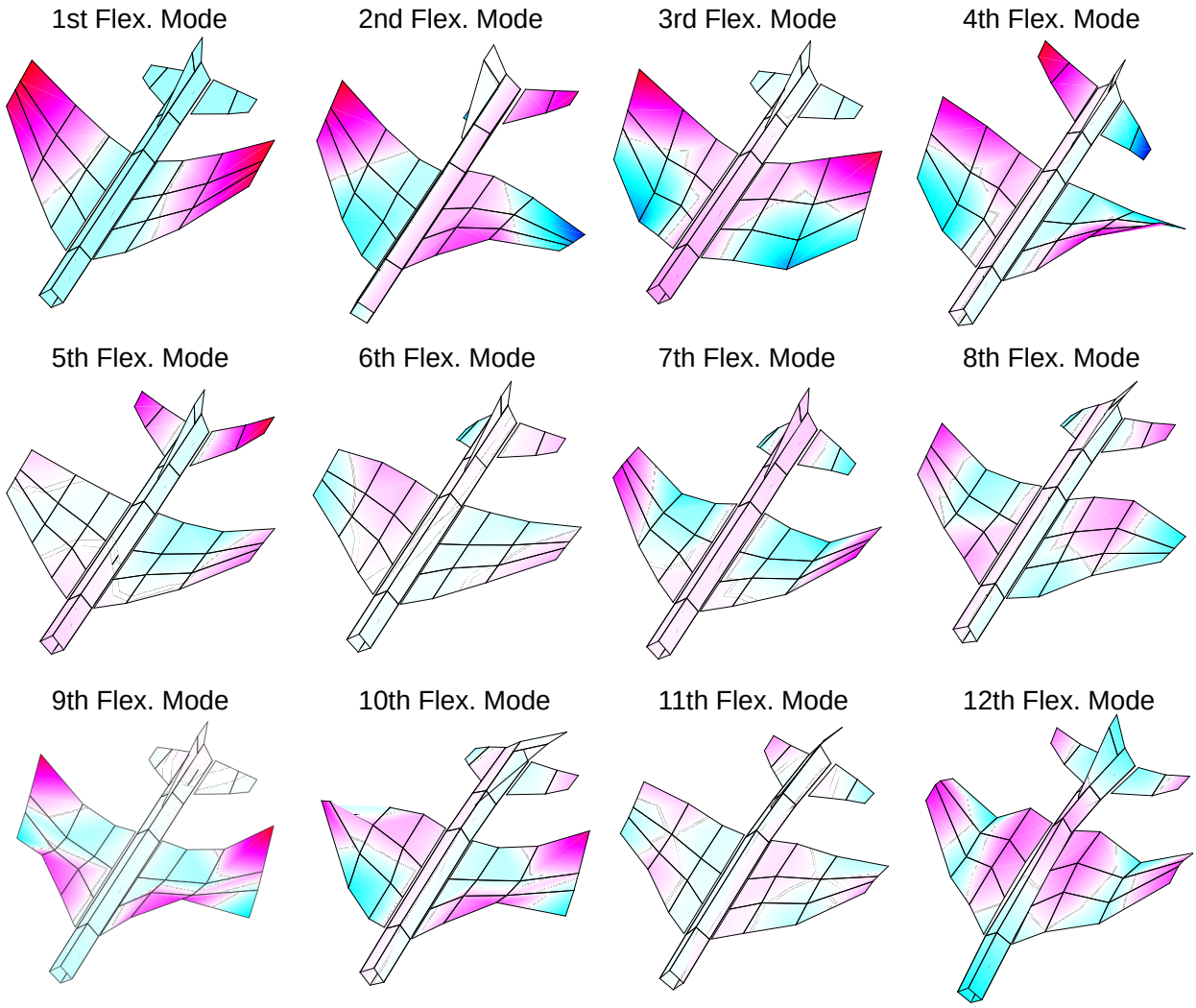

Figure 6.9: The first twelve flexible mode shapes of the plane computed using the reduced-order FE model depicted in Fig. 6.4(b).

6.4 Design of Nonlinear Stores

To minimize the difference between the computational model and the experimental system, the nonlinear stores were designed before any computational studies were performed. The nonlinear stores are designed to behave as rigid links pinned near one end with a nonlinear spring attached to the other end. The nonlinear spring is realized by a thin, steel flexure that undergoes large deformation when the store moves. Two designs are considered for the implementation of the nonlinearity: the first design is based around clamping the flexure to the pylon and the store such that the store behaves as a fixed-guided beam. In addition to strong nonlinearity, this design also introduces a moderate linear stiffness due to bending effects. The second design is based on pinning the flexure to both the pylon and the store such that it behaves like a string. This design minimizes the linear stiffness enabling the nonlinearity to be maximized by increasing the thickness of the flexure. The first and second designs will be referred to as the fixed-fixed and pinned-pinned designs, respectively, in the coming discussion.

The fixed-fixed design is presented in Figure 6.10. Specifically, Fig. 6.10(a) presents CAD images of the plane with one locked and one unlocked store as well as zoomed-in views of each store. The stores are designed to attach to existing bolt holes in the short mounting rails. Figures 6.10(b) and (c) present bottom and isometric views of the unlocked stores, respectively. In these figures, the CAD model of the entire plane except the short mounting rail (the white U-bracket) is hidden. The red components bolt onto the mounting rail and provide the pin joint for the front of the store. The pin joint is implemented using a 1/4" idler rotary shaft, a Teflon bearing and an external retaining ring. The store is constructed with female threads on both sides such that the idler rotary shaft screws directly into it. The Teflon bearings are lightly press-fitted into the mounting bracket and are held in place on the idler rotary shaft using the external retaining ring. The idler rotary shafts, Teflon bearings and retaining rings are colored ivory, yellow and charcoal, respectively. The bright green part at the free end of the store clamps the flexure (dark blue) to the store using three 6-32×3/4" bolts that thread directly into the store. The flexure is clamped to a comparable fixture (bright green) on its other side. This fixture is bolted to the pylon (dark gray) that extends from the mounting rail, where the pylon screws in directly. The orange fixtures that appear in the pictures of the locked stores serve as the locking mechanism that prevents large relative motion across the flexure. These fixtures do not eliminate all motion in the store, but do remove the nonlinearity and shift the frequency of the store outside the range of interest to this study.

The pinned design is depicted in Fig. 6.11 with (a) showing CAD images of the plane with one locked and one unlocked store as well as zoomed-in views of each store with the pinned flexures, and (b) and (c) presenting bottom and isometric views of the store, respectively. The construction of the actual store, pin-

joint fixture and the pylon are the same as in the fixed-fixed design. The bright green parts bolted to the store, and the pylon forms the clevis for the pinned connection. The flexure (dark blue) bolts directly to the shaft (cyan), which inserts into the Teflon bearing (yellow) inside of the clevis. Thus, the flexure is allowed to rotate freely at each of its ends, but its translational displacements are constrained to the motion of the pylon and the store. Just as in the fixed-fixed design, the orange fixtures that appear in the pictures of the locked stores serve as the locking mechanisms that prevent large relative motion across the flexure. Again, whereas this locking mechanism does not eliminate all motion in the store, it does eliminate the nonlinearity of the store, and shifts the frequency of the store outside the range of interest.

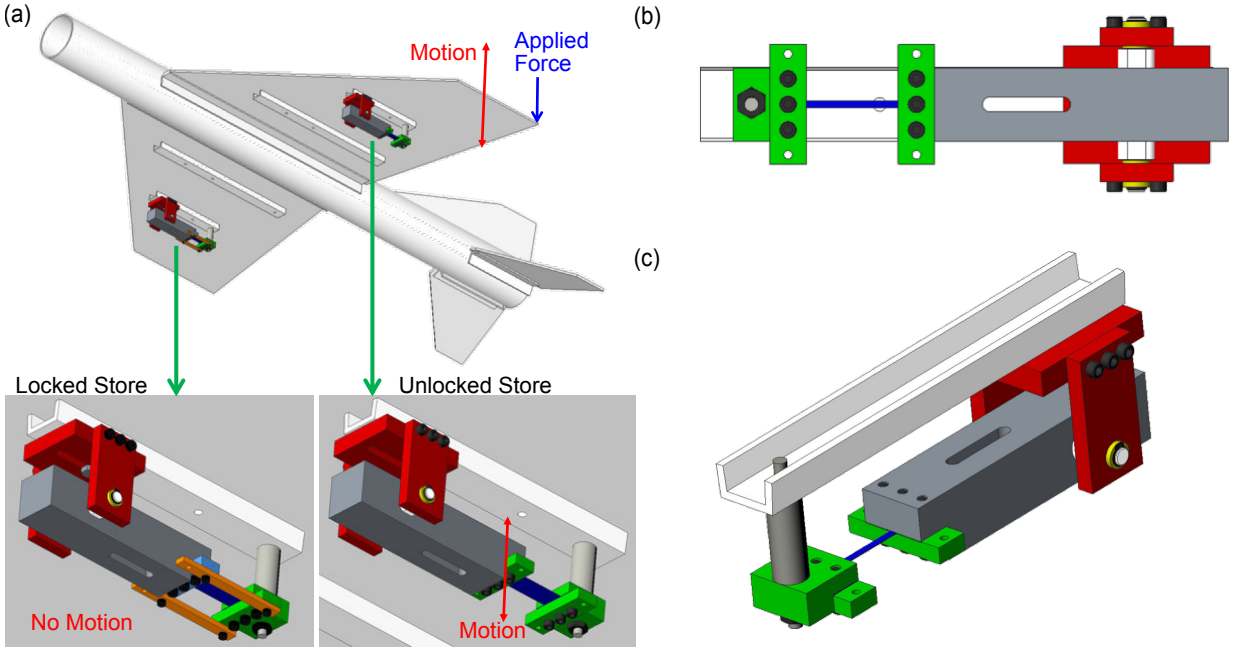

Figure 6.10: Design of the fixed-fixed flexure: (a) CAD views of model airplane with assembled stores attached and zoomed-in views of the locked and unlocked stores. (b) Bottom view of unlocked store. (c) Isometric view of unlocked store.

For these configurations and within the frequency range of interest, the displacements of the store at the pin joint are equivalent to the motion of the wing, whereas the motion of the store at the flexure includes an additional DOF. The pylon rigidly (at least in the frequency range of interest) connects the flexure to the wing such that the motion of the flexure at the pylon side is equivalent to that of the wing. Note that the pylon and bolts do introduce flexibility into the connections, but are stiff enough that any harmonics introduced are well outside the frequency range of interest. Thus, the relative motion across the flexure is the difference between the wing motion at the pylon and the sum of the wing motion at the pin joint and the rotational motion of the store.

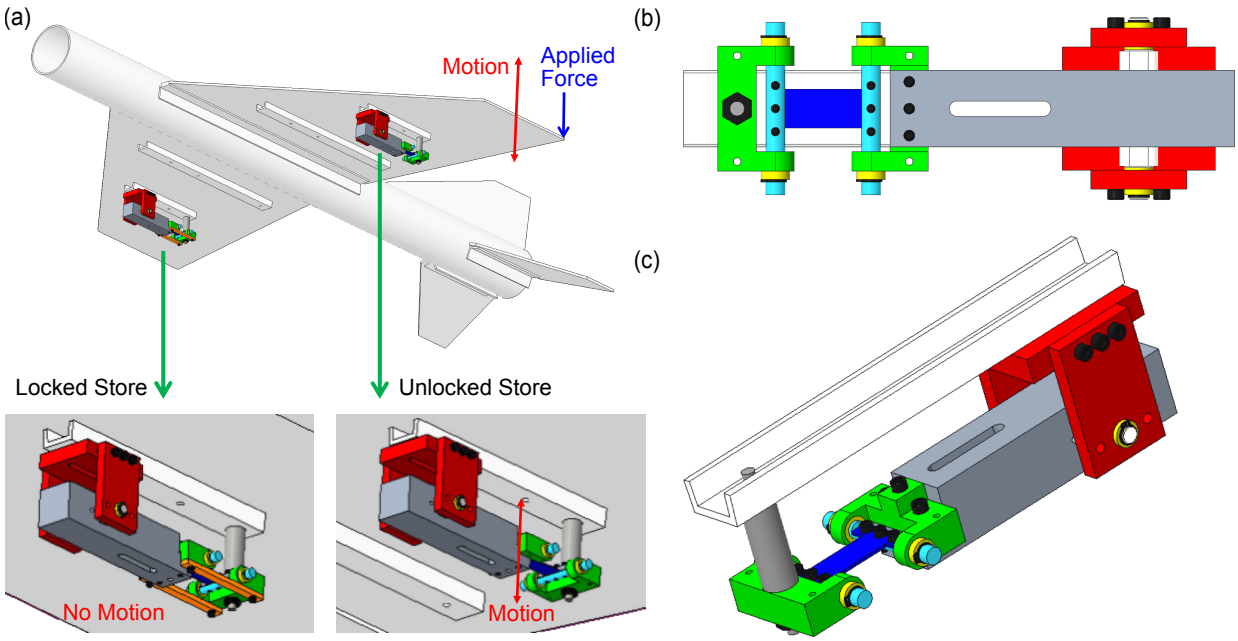

Figure 6.11: Design of the pinned-pinned flexure: (a) CAD views of model airplane with assembled stores attached and zoomed-in views of the locked and unlocked stores. (b) Bottom view of unlocked store. (c) Isometric view of unlocked store.

The entire assembly is designed to be made from 6061 aluminum except for the threaded rods in the pylons, the idler rotary shaft, the retaining rings, the flexures and the hardware, which are intended to be steel. For the fixed-fixed design, the estimated masses of the assembled pylon (excluding the flexures), the pin joint bracket and the store are 0.0610 kg, 0.0907 kg and 0.1939 kg, respectively, resulting in a total mass of 0.3456 kg. For the pinned-pinned design, the estimated masses for of the assembled pylon (excluding the flexures), the pin joint bracket and the store are 0.0730 kg, 0.0907 kg and 0.2059 kg, respectively, resulting in a total mass of 0.3696 kg. Since the pylon assembly and the pin joint bracket do not contribute to the flexible motion in the frequency range of interest, they act only as added mass to the wings such that the mass of each wing in the augmented FE model is 7.4517 kg and 7.4637 kg for the fixed-fixed and pinned-pinned designs, respectively. The mass of the plane excluding the stores is 29.84 kg and 29.87 kg for the fixed-fixed and pinned designs, respectively. As such, the store contains only 2.60-2.76% of the mass of a single wing and only 0.65% the mass of the entire plane (the percentages are the same for both designs).

The flexures are designed to undergo large deformation for relatively small motion in the store, such that the restoring force induced by the flexure deflection is strongly nonlinear (due to geometric effects). This is achieved by designing the flexures to behave as long, slender beams with significantly smaller thickness than that of the store. In the fixed-fixed design, the flexures are designed to have a thickness of 0.254 mm and an

active length of 31.75 mm (the length between the clamps). This value of thickness is chosen to minimize the linear stiffness due to bending, while the length is fixed due to geometry. In the pinned-pinned design, the active length is fixed to 25.4 mm, and both the width and the thickness are adjusted to maximize the nonlinearity. The width of the flexure is left as a design parameter to adjust the linear and nonlinear stiffnesses produced by the deformation. For the fixed-fixed design, the flexure is approximated as a fixed-guided beam as depicted in Fig. 6.12, and the nonlinear restoring force is obtained by performing a static analysis. This model does not account for any pretension introduced by the bolting of the flexure, from misalignment of the components, or from gravity. Any pretension introduced by these effects increases and decreases the linear and nonlinear stiffnesses, respectively, and will be accounted for in the experimental studies. For the pinned-pinned design, the flexure is modeled as a string that undergoes transverse deformation resulting in geometric nonlinear (this is allowable because the pinned connections eliminate the effects of bending). This model results in zero linear stiffness and exactly the same nonlinear stiffness as in the fixed-fixed design. For the latter design, the flexure is treated as fixed-guided beam resulting in a linear stiffness of

$$k_l = \frac{E_f w_f t_f^3}{L_f^3}, \tag{6.1}$$

and a nonlinear stiffness of

$$k_{nl} = \frac{1}{2}\frac{E_f w_f t_f}{L_f^3}, \tag{6.2}$$

where E_f, w_f, t_f and L_f are the elastic modulus, width, thickness and length of the flexure, respectively [Boisseau et al., 2013]. As mentioned previously, the flexure width is used as a design parameter to control the linear and nonlinear stiffnesses. For several widths the corresponding linear and nonlinear stiffnesses of the store are listed in Table 6.4 for the fixed-fixed flexure and Table 6.5 for the pinned-pinned flexure. Note that by changing the width of the flexure, the linearized natural frequency of the store can be altered such that the store may be tuned to interact with a specific mode or set of modes of the plane. For this study, the pinned-pinned store is selected and is designed to interact with the second mode of the plane at low amplitude excitations and, as such, the stiffnesses associated with a width of 12.7 mm in Table 6.5 are used in all computational studies.

Table 6.4: Estimated linear and nonlinear stiffnesses of the fixed-fixed flexure for multiple widths.

Flexure Width [mm]	**Linear Stiffness [N/m]**	**Nonlinear Stiffness [N/m^3]**	**Store Natural Frequency [Hz]**
2.54	273.1	2.117×10^9	11.69
3.81	409.7	3.175×10^9	14.31
5.08	546.2	4.233×10^9	16.53
12.7	1365.5	1.058×10^{10}	26.13

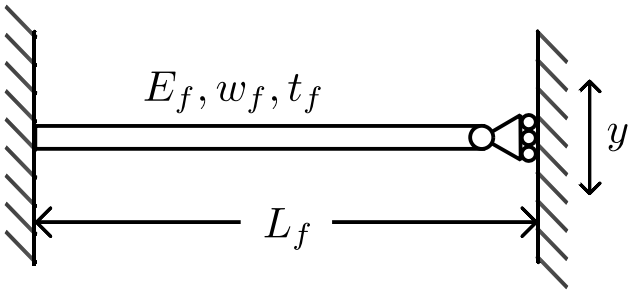

Figure 6.12: Schematic representation of the model used to estimate the linear and nonlinear stiffnesses of the flexures.

Table 6.5: Estimated nonlinear stiffnesses of the pinned-pinned flexure for multiple widths and thicknesses.

Flexure Width [mm]	**Flexure Thickness [mm]**	**Nonlinear Stiffness [N/m^3]**
5.08	0.254	4.23×10^10
5.08	0.635	1.058×10^10
5.08	1.27	2.117×10^10
12.7	0.254	1.058×10^10
12.7	0.635	2.646×10^10
12.7	1.27	1.035×10^{11}

6.5 Reduced-order Modeling of the Nonlinear Store

Prior to performing the computational study using the reduced plane FE model and the nonlinear stores, two reduced-order models (ROMs) are studied; these are depicted in Fig. 6.13. In both models, the store is treated as an inverted pendulum that is pinned at one end with a nonlinear spring connected to the other. As such, the motion of the store is governed by a single DOF which is chosen to be the rotation of the store, given by $\theta(t)$ in the schematics. The nonlinear spring, represented by $G(\theta)$ and $G(\theta, x)$ in the first and second models, respectively, contains both a linear spring and a nonlinear spring with a cubic force-displacement law. As mentioned in the previous section, the flexure is assumed to be the pinned-pinned design with a thickness of 1.27 mm and a width of 12.7 mm, which results in a nonlinear stiffness of 1.035×10^{11} N/m^3. Although the pinned-pinned design predicts a zero linear stiffness, the linear stiffness in the computational model is set to 1365.5 N/m resulting in a store natural frequency of 26.13 Hz (the additional linear stiffness can be realized in the experimental system attaching an additional spring to the store). In the simplified computational model (referred to as the "first model", cf. Fig. 6.13(a)), the nonlinear spring is connected to the ground such that the store is comparable to a Duffing oscillator. In the integrated computational model (referred to as the "second model", cf. Fig. 6.13(b)), the nonlinear spring is attached to a linear oscillator that is representative of the second flexible mode of the plane. The EOM for the first model is

$$I_s\ddot{\theta} + d_c h^2\dot{\theta} + k_l h^2\theta + k_{nl} h^4\theta^3 = 0, \tag{6.3}$$

and the EOMs for the second model are

$$\begin{aligned} M\ddot{x} + d_w\dot{x} + d_c\left(\dot{x} - h\dot{\theta}\right) + k_w x + k_{nl}\left(x - h\theta\right)^3 &= F(t), \\ I_s\ddot{\theta} + d_c h\left(h\dot{\theta} - \dot{x}\right) + k_l h\left(h\theta - x\right) + k_{nl} h\left(h\theta - x\right)^3 &= 0, \end{aligned} \tag{6.4}$$

where the values of the parameters are listed in Table 6.6.

The first model represents the motion of the store when either the store is physically connected to ground or when there is absolutely no motion in the plane. Since the grounded-store model is comparable to a Duffing oscillator, it will not be studied extensively computationally. Instead, it will be used to derive the frequency-displacement relationship for the RQ-based identification in the next section and to identify the grounded store measured experimentally in Section 6.7. The Hamiltonian FEP of the grounded store (computed using NNMcont [Peeters et al., 2009]) is depicted in Fig. 6.14(a) and shows that, in the limit of low energy, the NNM converges to a frequency of 26.03 Hz and does not vary with energy, corresponding to a linear limiting regime. However, no linear regime appears in the limit of large energy. Instead, the nonlinear regime and

Table 6.6: Parameters used for the ROMs depicted in Fig. 6.13.

Parameter	**Value**
I_s	3.47×10^{-4} kg·m^2
M	7.26 kg
h	0.08255 m
k_w	5.20867×10^{5} N/m
k_l	1365.5 N/m
k_{nl}	1.058×10^{10} N/m^3
d_w	24.07 Ns/m
d_c	0.1 Ns/m

its frequency extend to infinity (at which point, the nonlinear restoring force is so strong that all motion in the store is eliminated). The frequency associated with the store increases dramatically at low energy. This results from the relatively large stiffness of the nonlinearity and because all energy is concentrated in the store. When coupled to the plane, the NNM of the store follows a similar trend, but is shifted to higher energies because energy is split between the modes of the plane and the store. This will be explored further in the next section where the NNM of the grounded store will prove valuable in understanding the dynamics of the plane with nonlinear stores. For now, we return to the discussion regarding the highly reduced models.

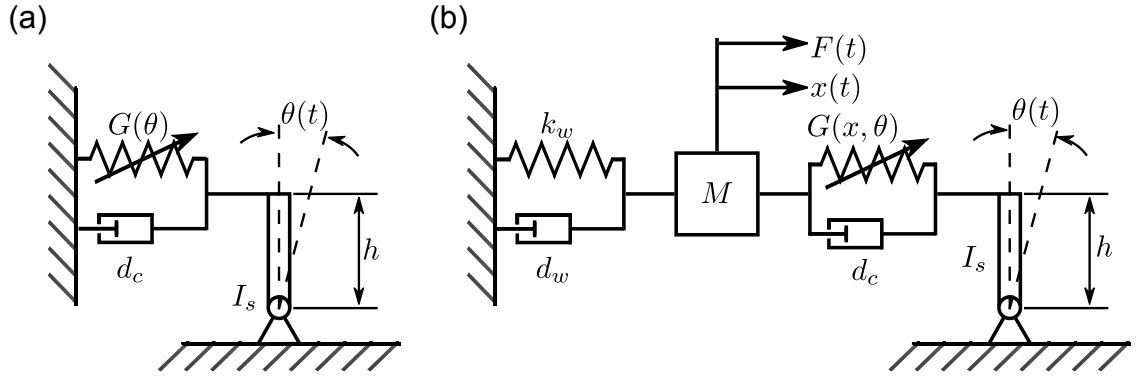

Figure 6.13: (a) Schematic representation of the store coupled to ground (comparable to a Duffing oscillator). (b) Schematic representation of the store coupled to a linear oscillator representative of the second flexible mode of the plane.

The second model, termed the LO-store model, corresponds to interactions between the second mode of the plane and the store. Specifically, the mass and grounding stiffness of the LO are equivalent to the modal mass and stiffness of the second flexible mode of the plane, resulting in a natural frequency of 42.63 Hz (equivalent to that of the second mode of the experimental plane listed in Table 6.2). The grounding damping is computed using the damping ratio reported in Table 6.2 for the second mode of the plane. The

coupling linear and nonlinear damping come from the estimates in the previous section, and the coupling damping is included based on previous experience.

The Hamiltonian FEP (computed using NNMcont [Peeters et al., 2009]) of the LO-store model is presented in Fig. 6.14(b), which reveals the two NNMs that govern this system. In the limit of low energy, the first NNM (the black curve) and the second NNM (the red curve) represent in-phase and out-of-phase linear modes, respectively; however, the amplitude of the LO in the first NNM is four orders of magnitude lower than that of the store (as predicted by NNMcont). Consequently, the first NNM represents the local store mode in the limit of low energy and is comparable to the NNM of the grounded store. In the limit of high energy, the first NNM converges to a linear regime whereas the second NNM does not converge to a linear regime, and its frequency grows to infinity. Interestingly, the high-energy linear regime of the first NNM corresponds to the frequency of the LO with an additional mass equal to the mass of the store. Thus, the author conjectures that in the actual plane, with nonlinear stores, the NNMs of the plane do not experience increases in frequency as the NNMs do in Fig. 6.14(b). Instead, only the frequency of the store increases and once it passes the frequency of an NNM of the plane, that NNM experiences a decrease in frequency. The reasoning behind this is that the store can only interact with NNMs that have frequencies above its own frequency. For an NNM with frequency below that of the store, the store acts only as added mass for that NNM. Thus, if the frequency of the store grows to be larger than that of an NNM, then the effect of the store on that NNM transitions from being that of an absorber to that of added mass, resulting in a decrease in frequency. This result is observed in Section 4.2.2 and will be revisited in the analysis of the next section.

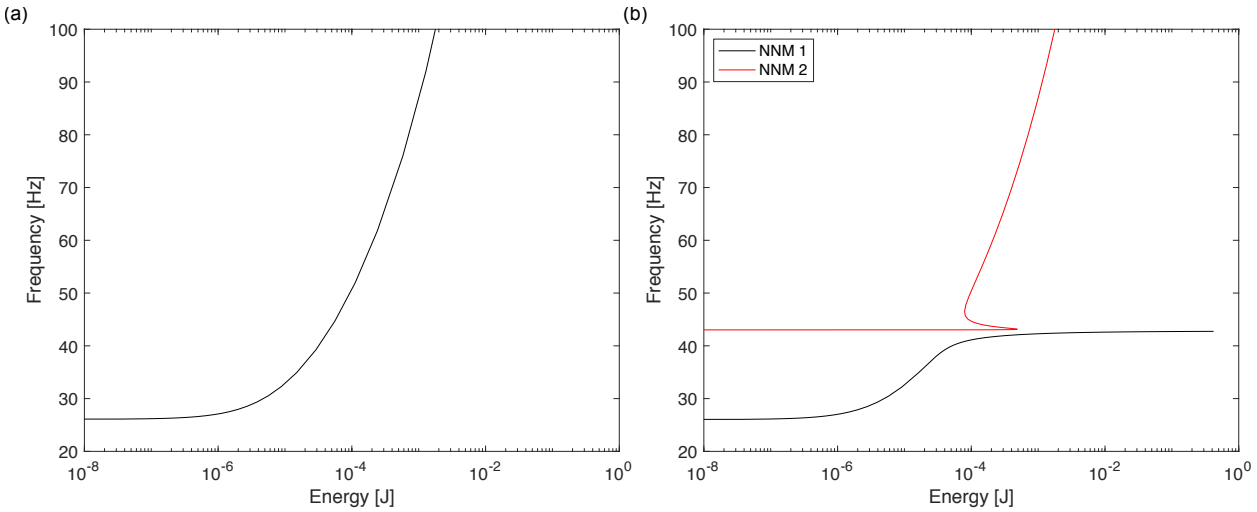

Figure 6.14: Frequency-energy plots depicting the Hamiltonian NNMs governing the (a) the grounded store model (presented in Fig. 6.13(a)) and (b) the LO-Store model (presented in Fig. 6.13(b)).

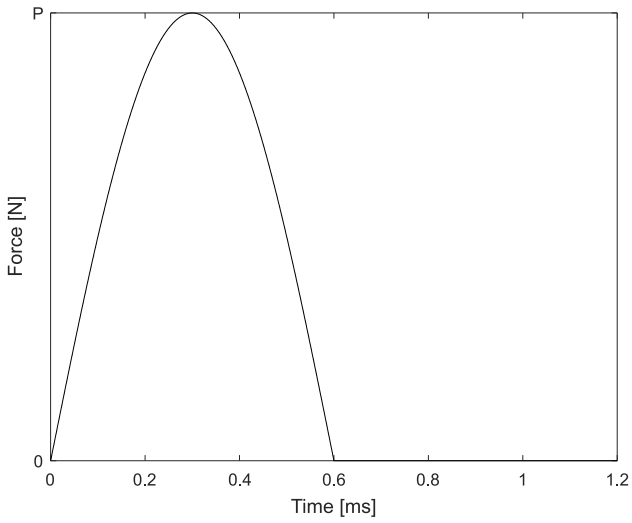

Figure 6.15: Forcing function with variable amplitude denoted by P applied to the linear oscillator in the computational study of the reduced-order model presented in Fig 6.13(b).

To investigate the potential interactions between the stores and the second mode, the response of the system to the impulsive load (with variable amplitude) depicted in Fig. 6.15 is studied. The displacement response ($h\theta$ for the store) and corresponding WT spectra for load amplitudes of 100, 600, 1000, and 3000 N are provided in Fig. 6.16. For an impulsive load of 100 N, the corresponding response in Fig. 6.16(a) indicates that the forcing is too low to engage the nonlinearity such that the system behaves linearly. Note that two components are present in the WT spectrum of the displacement response of the store, whereas only one appears in that of the LO. This confirms that the first NNM at low energies represents a localized motion in the store. Additionally, at this forcing amplitude the displacements of the store and the LO are of comparable magnitudes. Several amplitudes between 100 N and 600 N are also studied; however, these amplitudes do not result in interactions between the store and the second mode, and are not shown or discussed here. Significant interactions only manifest when the amplitude of the applied force imparts enough energy into the store (first NNM) for its frequency to intersect that of the second NNM. When this occurs, as for an amplitude of 600 N, the store enters into a 1:1 TRC with the second NNM. Figure 6.16(b) presents the displacement responses and corresponding WT spectra of the store and LO for an amplitude of 600 N. At this amplitude, the displacement of the store is an order of magnitude larger than that of the LO, and a beating pattern is visible in the responses of both the store and the LO, indicating that the two are engaged in a 1:1 TRC. The WT spectra also contain the beating pattern, but reveal that only the first and second NNMs are significantly involved in the interaction.

Although the 1:1 TRC begins immediately when a 600 N impulsive load is applied to the LO, this behavior

is not preserved with increasing force. Indeed, increasing the applied force imparts more energy into the store resulting in an increased frequency of oscillation. Consequently, the applied load can become large enough (as in the case of 1000 N and 3000 N loads) such that the TRC is delayed in time. Figure 6.16(c) presents the displacements and corresponding WT spectra of the response of the system to a 1000 N impulsive load. A clear beating pattern is present in the displacement response of the store beginning immediately and ending before 2 seconds; however, the corresponding beating does not appear in the displacement response of the LO until after 0.5 seconds has passed. This indicates that the LO and the store do not engage in a 1:1 TRC before 0.5 seconds. Moreover, the WT spectrum of the LO displacement does not indicate the presence of beating until 0.5 seconds into the response. The WT spectrum of the displacement of the store reveals that many sub- and super-harmonics participate in the response, and these can lead to higher order TRCs with higher modes in the actual plane. Finally, Fig. 6.16(d) presents the response of the system to an impulsive load with magnitude of 3000 N. The displacement responses reveal that the store undergoes motion governed by two frequencies, whereas the LO experiences motion governed by a single frequency. No beating is easily observed until almost a full second has passed, indicating that the primary TRC is delayed by nearly a full second. The WT spectrum of the store reveals the participation of numerous harmonics; however, none of these are present in the WT spectrum of the response of the LO. Interestingly, the WT spectrum of the LO in all cases reveals that the response of the LO is governed only by components with frequencies near its linear natural frequency, which provides further evidence that the nonlinearity only alters the NNM that governs the motion of the store.

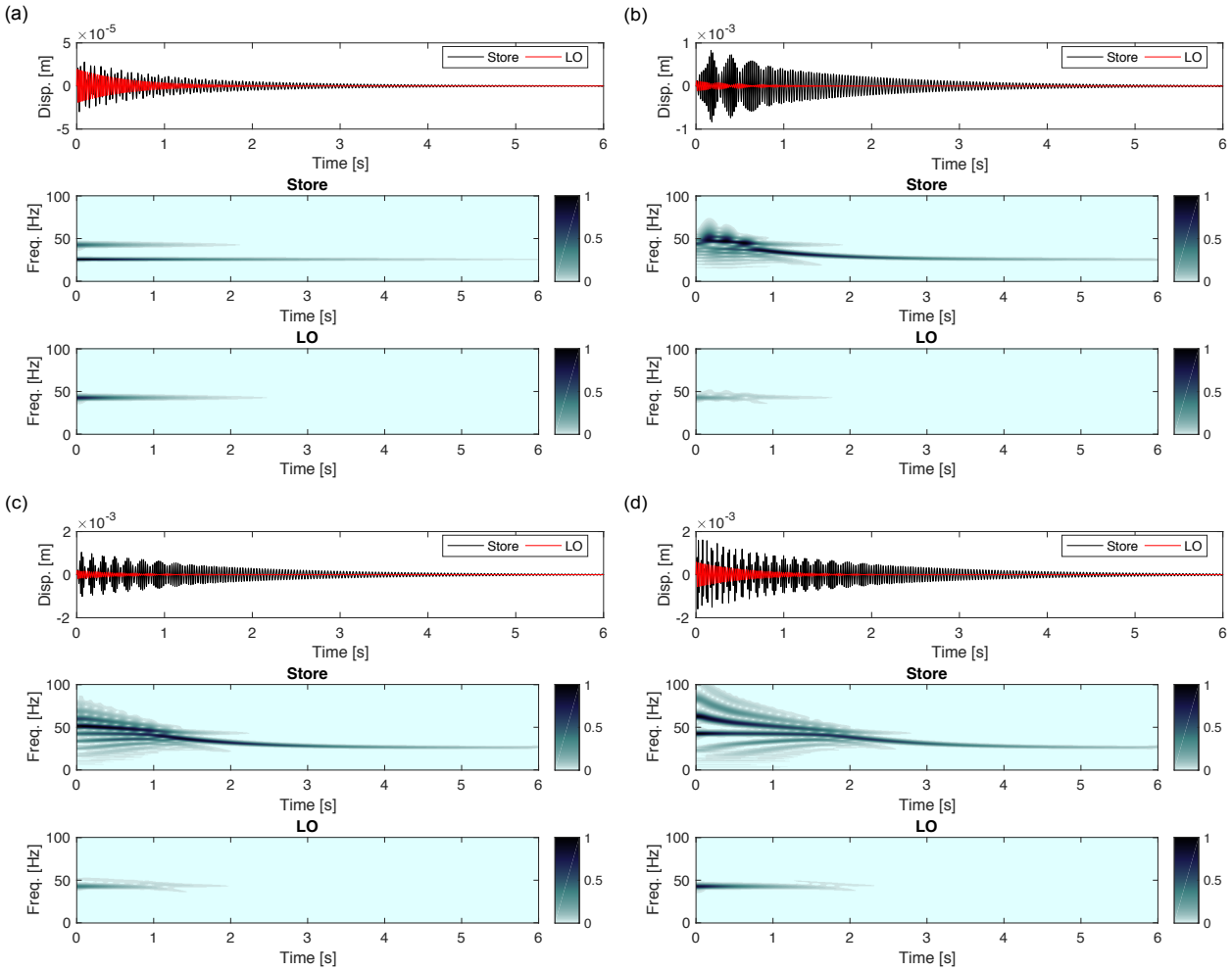

Figure 6.16: Comparison of the responses of the LO and store for impulsive loads applied to the LO of amplitude (a) 100 N, (b) 600 N, (c) 1000 N and (d) 3000 N.

6.6 NSI of Model Airplane with One Active Store: Computational Study

Similar to the previous section, this section seeks to investigate the effects of the nonlinear stores (the local attachments) on the global dynamics of the plane. However, unlike the previous section, the stores are modeled as flexible beams using Timoshenko beam elements. The reason is twofold: first, in modeling the store as a rigid link the total displacement of the store is described as the summation of the displacement of the wing at the pin joint location and the displacement induced by the rotation of the store. The separation of these DOFs hinders the application of POD in that a POM corresponding to the NNM of the store cannot be extracted at low amplitude forcing. The second reason is that in the experimental study any sensor placed on the store will measure the total motion and additional post-processing is required to separate the total

displacement into the two components. The separation is only possible if the response of the wing at the location of the pin joint is measured; however, due to limited sensors and acquisition channels, this location is neglected in the experimental measurements. By modeling the store as a flexible beam using Timoshenko beam elements, the resulting DOFs correspond to the total displacements and are equivalent to the motion that can be measured using traditional sensors.

Each store is modeled using three nodes, each with a translational and rotational DOF, such that the mesh is comprised of two Timoshenko beam elements. The first node is located at the free end where the nonlinear spring attaches, the second node at the location of the pin joint and the third node at the free end near the pin joint. Figure 6.17(a) presents the reduced plane FE model with the left and right stores attached and Fig. 6.17(b) provides a zoomed-in schematic of a store coupled to the wing. The connection between the pin joint and the wing is implemented by coupling the translational DOF at the pin joint to the vertical translational DOF of wing at the attachment point. The coupling is introduced using a linear spring with stiffness of $k_b = 5.4769 \times 10^8$ N/m, which corresponds to the axial stiffness of the pin joint sides. The other end of the store is coupled to the second attachment point using the estimated linear and nonlinear stiffnesses based on the flexure design. The linear coupling is incorporated in the augmented stiffness matrix whereas the nonlinear coupling is treated as an external force. Since POD requires that all data be of the same form (i.e., all displacements), Guyan reduction is applied to condense out the rotational DOFs from the mass and stiffness matrices of the store, leaving only translational DOFs in the augmented FE model. The locked stores are implemented by adding a second linear stiffness to the nonlinear spring with a stiffness of 4.2788×10^5 N/m, which is equivalent to the total bending stiffness of the orange fixtures depicted in Fig. 6.10.

To investigate the effect of the nonlinear stores on the global dynamics of the plane, we study the response of the plane with the left and right stores unlocked and locked, respectively, subject to the impulsive load depicted in Fig. 6.15. The impulsive load is applied at the trailing edge of the left wing tip (c.f. Fig. 6.17(a)) and the response is simulated for 1 second for 3360 logarithmically spaced forcing amplitudes between 10^{-1} N and 10^3 N, which corresponds to the experimentally realizable forcing range. Following each simulation, POD is applied to the simulated response data and the frequencies of the modes are estimated using the POMs as trial vectors in the RQ. The POMs are sorted using the method established in 5.2.2 based on the MAC value. The resulting frequency estimates for three rigid-body modes and eight flexible modes are depicted as functions of the forcing amplitude and total system energy in Figs. 6.18(a) and (b), respectively. The plots reveal that, as designed, the store does not interact with the first flexible mode or any of the rigid-body modes and the frequencies of these modes do not depend on energy whereas the frequencies of all other

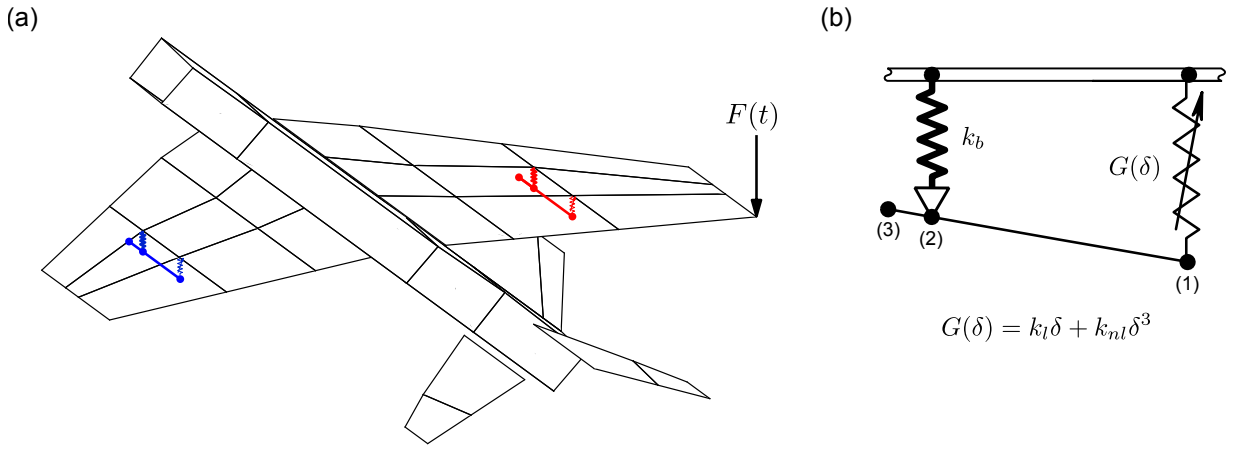

Figure 6.17: (a) The reduced plane FE model with left (red) and right (blue) stores connected to the left and right wings, respectively. (b) Schematic representation of the store FE model with numbered nodes and its coupling to the the plane FE model.

modes do. Consequently, the dynamics of the rigid-body modes and the first flexible mode are restricted to a single linear regime that spans the entire energy domain. In contrast, the dynamics of all other modes can be partitioned into multiple regimes. All other flexible modes of the plane can be partitioned into three regimes just as the modes of the wing in Section 5.2.2: two linear limiting regimes at low and high energy and a nonlinear transition regime that bridges the two linear regimes. The dynamics governing the store can be partitioned into a linear limiting regime at low energy and a nonlinear regime at moderate and high energies. The nonlinear regime of the dynamics of the store persists in the limit of large energy (at least in theory) because the frequency of the store never converges to a finite frequency. Instead, the frequency of the store approaches infinity in the limit of infinite energy, such that the effect of the store on the dynamics of the plane is that of additional mass. As mentioned previously, the store only interacts with modes that possess frequencies greater that of itself. Thus, if the frequency of the store grows to be larger than that of a mode, then it no longer interacts with that mode and instead acts as additional mass resulting in a small decrease in the frequency of the mode. This effect is observed in Fig. 6.18 where the frequency of the second flexible mode (the bright green curve) experiences a decrease in frequency at high energy.

The first two spikes in the estimated frequency of the store (the black curve in Fig. 6.18) correspond to modal interactions between it and the second flexible mode (the corresponding spikes can be seen in the estimated frequency of the second mode by zooming in on the curve). Since the store is designed to interact with the second flexible mode, the appearance of these spikes is not unexpected. What is surprising is that spikes appear in the third and fourth modes and the seventh and eighth modes at comparable forcing amplitudes and system energy. Although these modes are closely spaced in frequency, no spikes appear in

the linear regimes indicating that the modes do not exchange energy. Thus, the appearance of the spikes around a total system energy of 10^{-3} J is the result of strongly nonlinear energy exchanges between the plane modes, which are induced by the strong nonlinearity introduced by the store. Since the frequency of the store is significantly lower than that of the modes, it is possible that the spikes are the result of higher-order TRCs. However, the fact that the spikes that appear in the third flexible modes are mirrored in the fourth and do not align precisely with the spikes seen in the estimated frequency of the store, implies that the store does not participate in the TRC. The same is true for the spikes observed in the estimated frequencies of the seventh and eighth flexible modes. Thus, the spikes serve as a clear indication that the store induces irreparable changes in the global dynamics of the plane even though it is a local attachment with only 2.5% the mass of a single wing. This consequence is easily discovered if one consider that the total displacement of the store at the flexure can be separated into two parts: the motion of the wing at the pin joint (which acts as a base excitation for the store) and the displacement induced by the flexible rotation of the store, such that the total displacement is

$$z(t) = h\theta(t) + y(t), \tag{6.5}$$

where h is the distance from the flexure to the pin joint, $\theta(t)$ is the rotation of the store, and $y(t)$ is the displacement of the wing at the pin joint. Then the relative displacement across the flexure is

$$\delta(t) = h\theta(t) + y(t) - x(t), \tag{6.6}$$

where $x(t)$ is the displacement of the wing at the pylon. Dropping function notation, the restoring force resulting from the flexure is

$$G(\theta, y, x) = k_l \left(h\theta + y - x\right) + k_{nl} \left(h\theta + y - x\right)^3. \tag{6.7}$$

Thus, one finds that each store introduces nonlinear coupling between two DOFs of the plane in addition to the coupling between the store and wing at the pylon location. Such coupling does not occur in the case of the NES attached to the wing studied in the Section 5.1.

Beyond a total system energy of 3×10^{-3} J, the frequency of the store grows to be larger than that of the second flexible mode and the two no longer enter into any TRCs. However, the second flexible mode does not immediately enter into its high-energy, linear limiting regime. Instead, several spikes appear around 10^{-2} J in the estimated frequency of the second flexible mode in Fig. 6.18, and are the result of IRs between the second and third flexible modes. The appearance of these spikes is in contrast to the results discussed

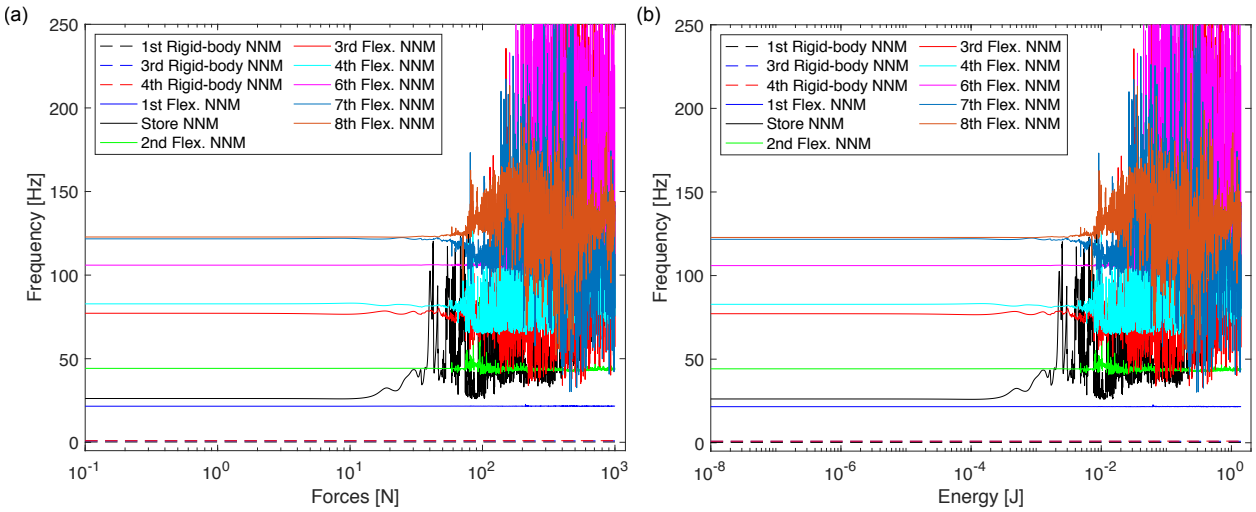

Figure 6.18: The RQ-estimated frequencies of three rigid-body modes and eight flexible modes plotted as functions of (a) forcing amplitude and (b) total mechanical energy.

in Section 5.1 where it was found that after the frequency of the NES increased beyond that of the second NNM, the second NNM ceased interacting with all other NNMs and entered its high-energy, linear limiting regime. Instead, the second mode of the plane continues to interact with other plane modes for the rest of the energies considered in Fig. 6.18. More importantly, after the store crosses the second flexible mode, the dynamics of the plane undergoes a drastic transition in that the RQ-FEP becomes densely filled with spikes. While one might think the appearance of so many spikes is the result of noise, they are actually an indication that the dynamics has become highly chaotic, resulting in many IRs and TRCs. Thus, we find that even though the store is a light local attachment, the strong nonlinearity introduces global repercussions in the dynamics of the plane.

To understand the dynamics of the store and to identify the nonlinearity, we consider the RQ-FEP of the store NNM and compare it to the NNMs predicted for the ROMs introduced in Section 6.5 in Fig. 6.19(a). In this figure, we find that the NNMs of the two ROMs correlate to each other, but do not agree with the prediction of the RQ-FEP. The reason is that in the computation of the FEPs of the ROMs, each NNM receives all of the system energy whereas each mode in the FE simulations receives only a fraction of the total system energy. Furthermore, since the ROMs possess significantly less DOFs than the FE model, the nonlinearity receives considerably more energy in the ROMs than in the FE simulations. Since more energy is induced in the nonlinearity in the ROMs than in the FE simulations, the effects of the nonlinearity are activated at much lower system energies and the resulting comparison in Fig. 6.19(a) is unfair and misleading. To create a fair comparison, we consider the procedure described in Section 5.1 and define a characteristic displacement for each model. Since the FEPs of the ROMs are computed using the periodic solutions at

each energy value, the characteristic displacements are computed directly from the periodic solutions. For the grounded-store model and the LO-Store model, the characteristic displacements are defined as

$$\bar{\delta}_{GS} \equiv |h\theta(0)|\,, \tag{6.8}$$

and

$$\bar{\delta}_{LOS} \equiv |h\theta(0) - x(0)|\,, \tag{6.9}$$

respectively. The notation $|\cdot|$ indicates the absolute value. The initial displacements of each periodic solution are used to define the corresponding characteristic displacements because these are equivalent to the maximum amplitudes that each displacement DOF achieves throughout the undamped response. Since the precise periodic solutions are not used in the computation of the RQ-FEP, the characteristic displacement of the FE is defined to be

$$\bar{\delta}_{FE} \equiv \int_0^1 |u_s(t) - u_p(t)|\, dt, \tag{6.10}$$

where $u_s(t)$ is the displacement of the store at the flexure and $u_p(t)$ is the displacement of the wing at the pylon location.

Provided that the nonlinearity of the store is identified, one could compute a characteristic energy using the relative displacements and this measure could be used to create a fair comparison in the frequency-energy domain. However, the benefit of using characteristic displacements is that these can be computed directly from experimental measurements without identifying the store nonlinear explicitly. The frequency-displacement pairs of the FE model are sorted such that the characteristic displacements increase monotonically. Since the periodic solutions are sorted by increasing amplitude automatically, no reordering is necessary for the ROMs. The resulting RQ frequency-displacement plot (RQ-FDP) is presented in Fig. 6.19(b) and the match between the three models confirms that the use of characteristic displacements results in a fair comparison. Interestingly, the "tongue" that appears in the second NNM of the LO-store ROM in Fig. 6.19(a) does not appear in the corresponding RQ-FDP. This results from the natural ordering of the periodic solutions and indicates that the "tongue" does not correspond to an IR. Moreover, the match between all three models confirms that the RQ-FDP is a physically meaningful representation of the data and, since it is based on displacements, can be used to directly identify the nonlinearity.

Assuming that the mass of the store is known (it can be directly measured experimentally) and its mass-moment of inertia calculated, the linear stiffness k_l is identified from the low-energy, linear frequency of the store NNM, leaving the nonlinear stiffness to be identified. The curves in the RQ-FEP and RQ-FDP indicate

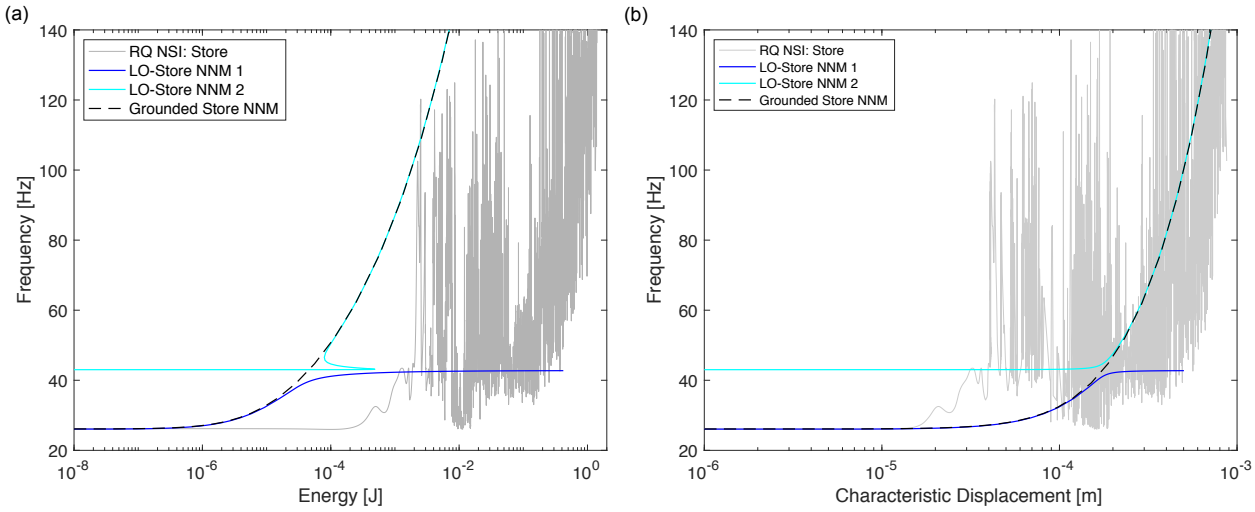

Figure 6.19: (a) Comparison of the FEPs computed using the ROMs with the RQ-FEP from the FE model simulations. (b) Comparison of the NNMs of the ROMs and the RQ estimated frequencies of the modes from the FE model simulations plotted as functions of characteristic displacement.

that the nonlinearity is a hardening-type and can be modeled in the form $\alpha |\delta|^{\beta} \delta$ where δ is the relative displacement between the store and the pylon. Accordingly, the EOM of the store can be expressed as

$$\ddot{\theta} + \frac{dh}{I}\dot{\delta} + \left(\omega_n^2 + \frac{\alpha h^2}{I}|\delta|^{\beta}\right)\delta = 0 \tag{6.11}$$

and, replacing the relative displacement with the characteristic displacement, the displacement-dependent frequency equation is:

$$f(\bar{\delta}) = \frac{1}{2\pi}\sqrt{\omega_n^2 + \frac{\alpha h}{I}\bar{\delta}^{\beta}}. \tag{6.12}$$

Although the estimated frequency of the store intersects the second flexible mode, it does so many times and a single intersection point cannot be determined and Eq. 6.12 cannot be simplified as in Section 5.2.3.

In the next step, α and β are identified using the GlobalSearch algorithm in MATLAB®, which performs a global optimization and is insensitive to initial guesses, to maximize the R-squared value between the filtered frequency-displacement curve for the NES created using the RQ and that created using Eq. 6.12. The lower and upper bounds were set such that $\alpha \in \left[10^9, 10^{12}\right]$ and $\beta \in [0.5, 3.5]$; with an initial guess of $\alpha = 1 \times 10^{10}$ and $\beta = 1.5$, the optimization converged to $\alpha = 9.94 \times 10^{10}$ and $\beta = 2.048$. Recall that the exact parameters are $\beta_{\text{exact}} = 2$ and $\alpha_{\text{exact}} = 3 \times 10^9$ N/m^3, resulting in absolute errors of 3.96% and -2.40% for the identified α and β respectively. The frequency-displacement curves predicted using the identified and exact parameters are presented in Fig. 6.20(a) as the green and red curves, respectively.

The identified model is validated by comparing its response to the that of the exact system for multiple

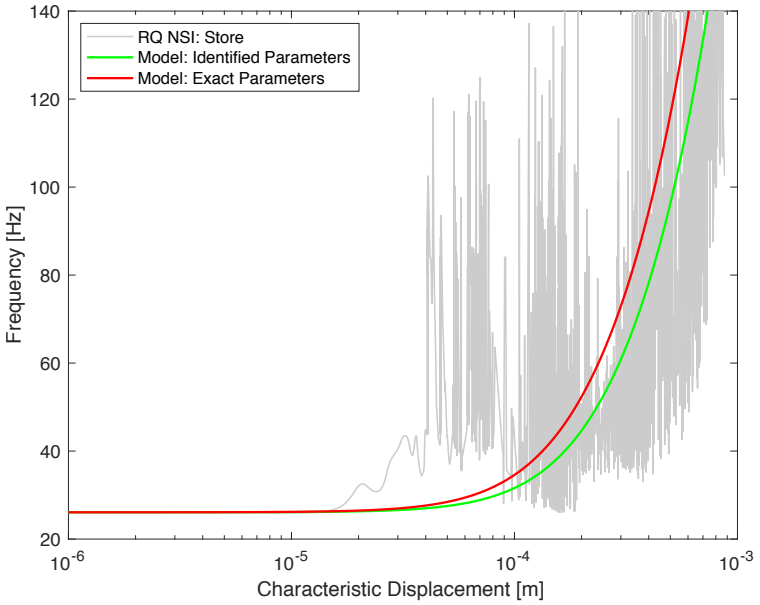

Figure 6.20: The RQ-FDP for the estimated frequency of the store, the model with exact parameters and the model with the identified parameters.

forcing values. Figure 6.21 presents the comparison of the velocity response of the store for the exact system with that of the identified model for impacts of 1, 10, 100 and 1000 N applied to the position indicated in Fig. 6.17. For an impact of 1 N, the response is linear, and the identified model reproduces the response of the exact system. For an impact of 10 N, the energy in the system is large enough that the nonlinearity is barely engaged, and the identified model reproduces the exact response. For an impact of 100 N, the identified model performs the worst in terms of the raw velocity response, but the WT spectra indicate an acceptable agreement. For an impact of 1000 N, the energy is large enough that the frequency of the store is nearly out of the frequency range of interest. Consequently, the store is unable to interact with any of the lower flexible modes considered previously. However, both the velocity response and WT spectra indicate a strong agreement between the identified and exact models. These results confirm that the identified and updated model can accurately reproduce the response of the exact system, verifying the accuracy and strength of the proposed data-driven NSI methodology.

The remainder of this chapter is dedicated to the experimental study of the global dynamical effects on the plane response that the local strongly nonlinear stores induce, but the proposed data-driven NSI methodology will not be applied because the experiments are limited by the number of sensors and channels available. However, if one were to instrument the experimental system with enough sensors and a large enough data-acquisition system, the proposed methodology could be applied to the experimental system and the nonlinear stores identified directly from the data.

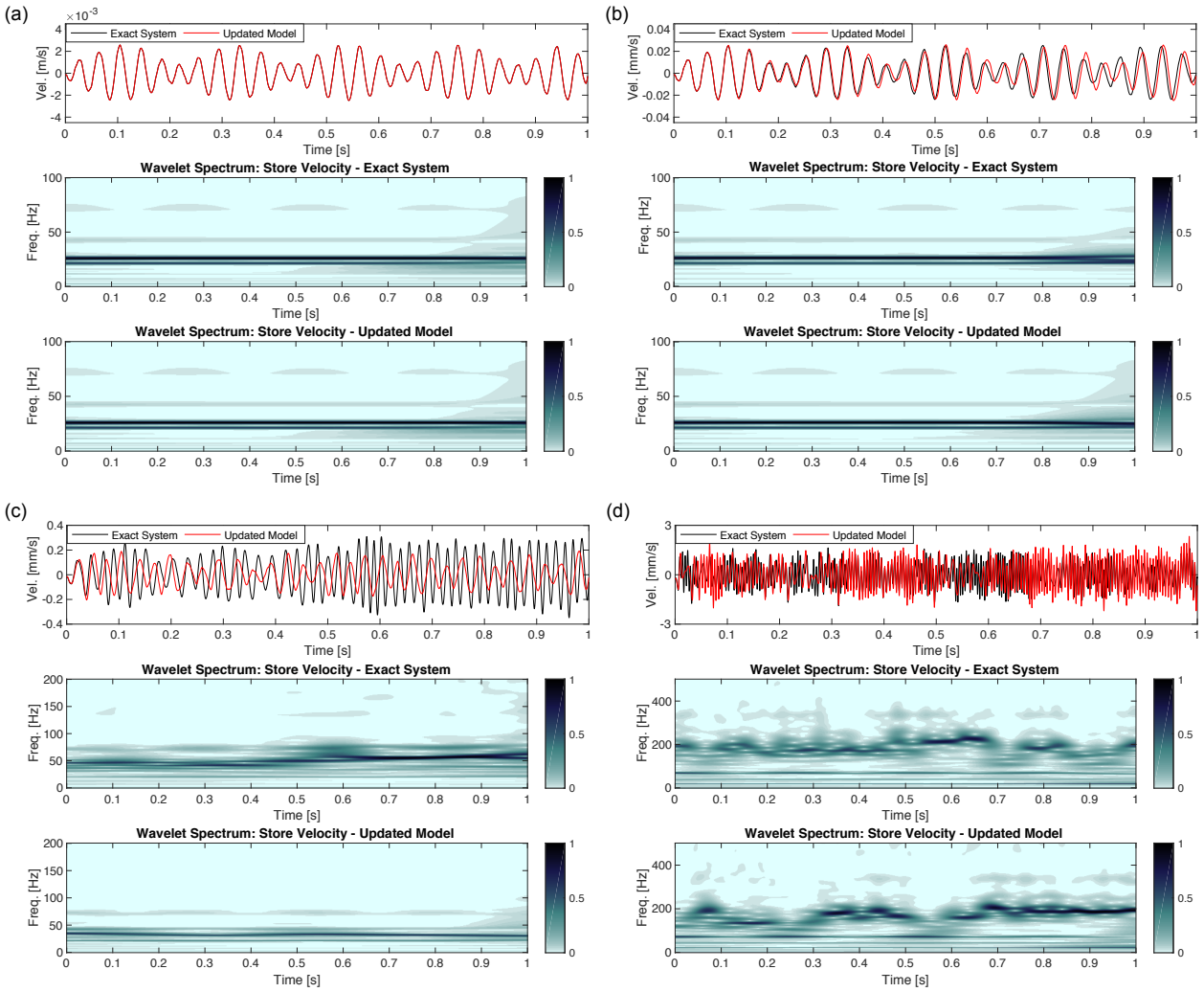

Figure 6.21: Comparison of the velocity response of the store simulated using the exact nonlinearity and the identified nonlinearity for impulsive loads of amplitude (a) 1 N, (b) 10 N, (c) 100 N and (d) 1000 N.

6.7 NSI and Model Updating of Grounded Store

Both the fixed-fixed and pinned-pinned designs were constructed and tested in both grounded and attached configurations. Unfortunately, the pinned-pinned design introduced significant dissipation due to friction in the flexure bearings, and this design was abandoned early in the testing regime. Thus, the remainder of the chapter focuses on the experimental measurements and the dynamics of the store with the fixed-fixed flexure. Furthermore, during the experimental testing of the plane, it was determined that the threaded holes on the mounting rails were either on or too close to the nodal line of the second flexible mode, such that the store was unable to interact with the second flexible mode regardless of the excitation. To address this issue, the flexure was redesigned such that the frequency of the store was less than that of the first flexible mode; thus allowing the store to interact with the first flexible mode. The redesign was accomplished by reducing the width and thickness of the flexure to 2.54 mm and 0.254 mm, respectively. The remainder of this section considers the experimental measurements and NSI of the grounded store with the redesigned, fixed-fixed flexure.

Figure 6.22(a) depicts the assembled store in a grounded configuration and the fixed-fixed flexure. A zoomed-in view of the flexure assembly is provided in 6.22(b). The assembled pylon (excluding the flexure) has a mass of 0.0663 kg, the pin joint bracket has a mass of 0.1170 kg and the mass of the store (including the idler rotary shaft and clamping fixture) is 0.1885 kg, resulting in a total mass of 0.3718 kg added to each wing. The resulting moment of inertia of the store is 3.37×10^{-4} kg·m^2. The adjusted mass of the left and right wings (wing plus pylon assembly plus pin joint bracket) are 7.4433 kg and 7.5033 kg, respectively, and the total mass of the plane excluding the stores is 30.28 kg. As such, the mass ratios of the left and right stores to the left and right wings are 2.51% and 2.53%, respectively, and the mass ratio of the store to the total plane mass is 0.62%.

(a) (b)

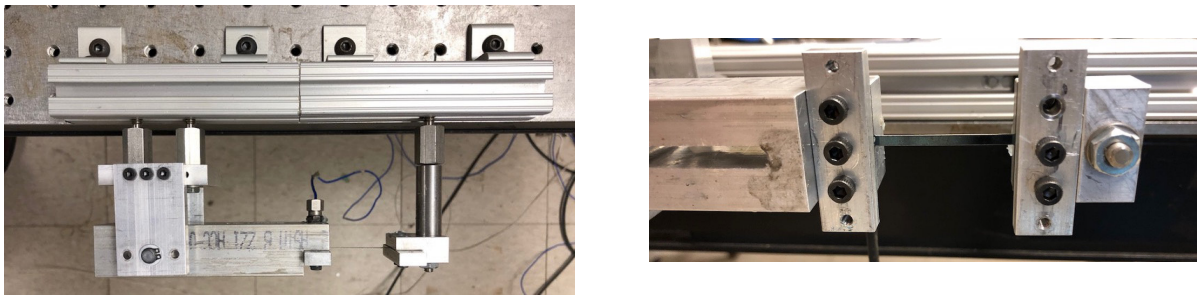

Figure 6.22: (a) The grounded store used in the nonlinear experimental measurements with the fixed-fixed flexure design. (b) Zoomed-in view of the fixed-fixed flexure as attached to the grounded store and grounded pylon.

Before attaching the store to the plane, the response of the grounded store was measured experimentally and used to characterize a mathematical model. Specifically, an impact from a PCB Piezotronics modal impact hammer (model 086C01) was applied to the grounded store near the flexure, and the acceleration response of the store was measured using a PCB accelerometer (model 353B15), with a nominal sensitivity of 1.02 mV/(m/s^2). The acceleration of the store was measured at a sampling rate of 64 kHz for a duration of 16.384 seconds using PSV-400 hardware (Polytec, Waldbronn, Germany) and Polytec vibration measurement software. The velocity response time series of the store for multiple impacts are presented in Fig. 6.23 along with the corresponding WT spectra. Although the response time series were measured for multiple impacts, only the response for an impact of 387.7 N is used for the identification. The remaining measurements are used to validate the identified model.

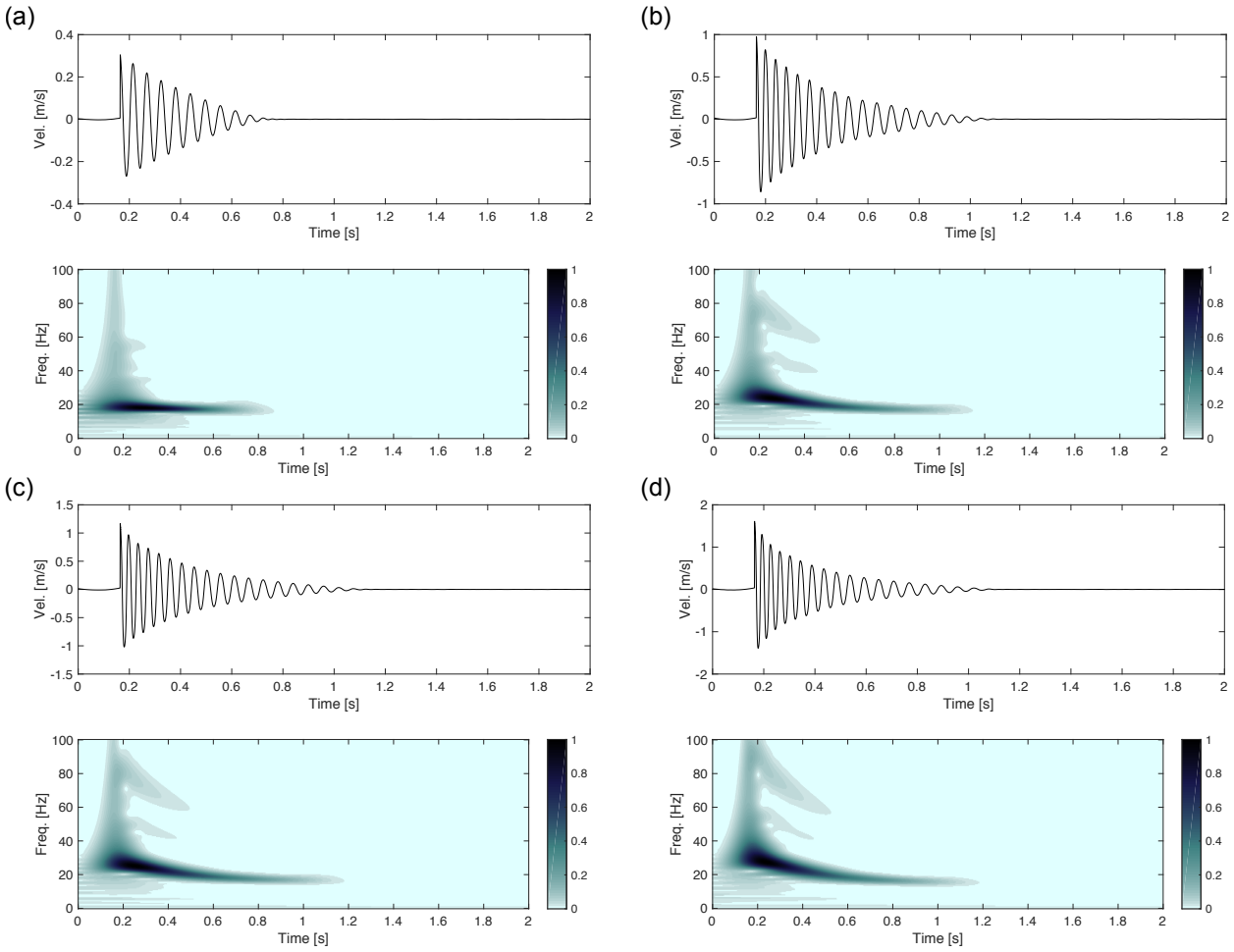

Figure 6.23: Velocity response and corresponding WT spectra of the grounded store for impulsive load of amplitude (a) 64.8 N, (b) 220.3 N, (c) 387.7 N and (d) 497.4 N

The store is modeled according to the schematic presented in Fig. 6.13(a) using the EOM

$$I_s\ddot{\theta} + d_g h^2\dot{\theta} + k_g h^2\theta + \alpha_g h^2 \left|h\theta\right|^{\beta_g} \theta = F(t), \tag{6.13}$$

where the nonlinearity is modeled using the same form as in the computational study, and only viscous damping is included. The unknown damping and stiffness parameters are identified using an optimization routine that maximizes the R-squared value between the measured and simulated responses. The initial guesses are identified manually by comparing the experimentally measured and simulated responses. Additionally, the objective function includes a penalty function that is implemented such that the amplitude of the simulated response for the last 0.5 seconds cannot be less than 75% or greater than 125% of that for the measured response. This penalty function is included to prevent the routine from converging to a solution for which the damping and/or friction coefficients are unrealistically large. The resulting parameters from the estimation are $k_g = 599.6$ N/m, $\alpha_r = 4.902 \times 10^7$ N/m$^{3.09}$, $\beta_r = 2.090$ and $d_g = 0.361$ Ns/m, resulting in a natural frequency and damping ratio of 17.53 Hz and $\zeta_g = 0.017$, respectively.

Figure 6.24(a) presents the comparison between the measured and simulated responses for an applied impulsive force of 387.7 N (maximum magnitude), which corresponds to the response used in the identification procedure. Further validation of the model comes from comparing the measured and simulated responses for applied impulses not used in the identification. Accordingly, we present comparisons for impulses of 64.8 N, 220.3 N and 497.4 N in Figs. 6.24(b), 6.24(c) and 6.24(d), respectively. These results validate the accuracy of the identification procedure for the grounded store and verify that the store will indeed be able to interact with the first flexible mode of the plane when connected to the wing.

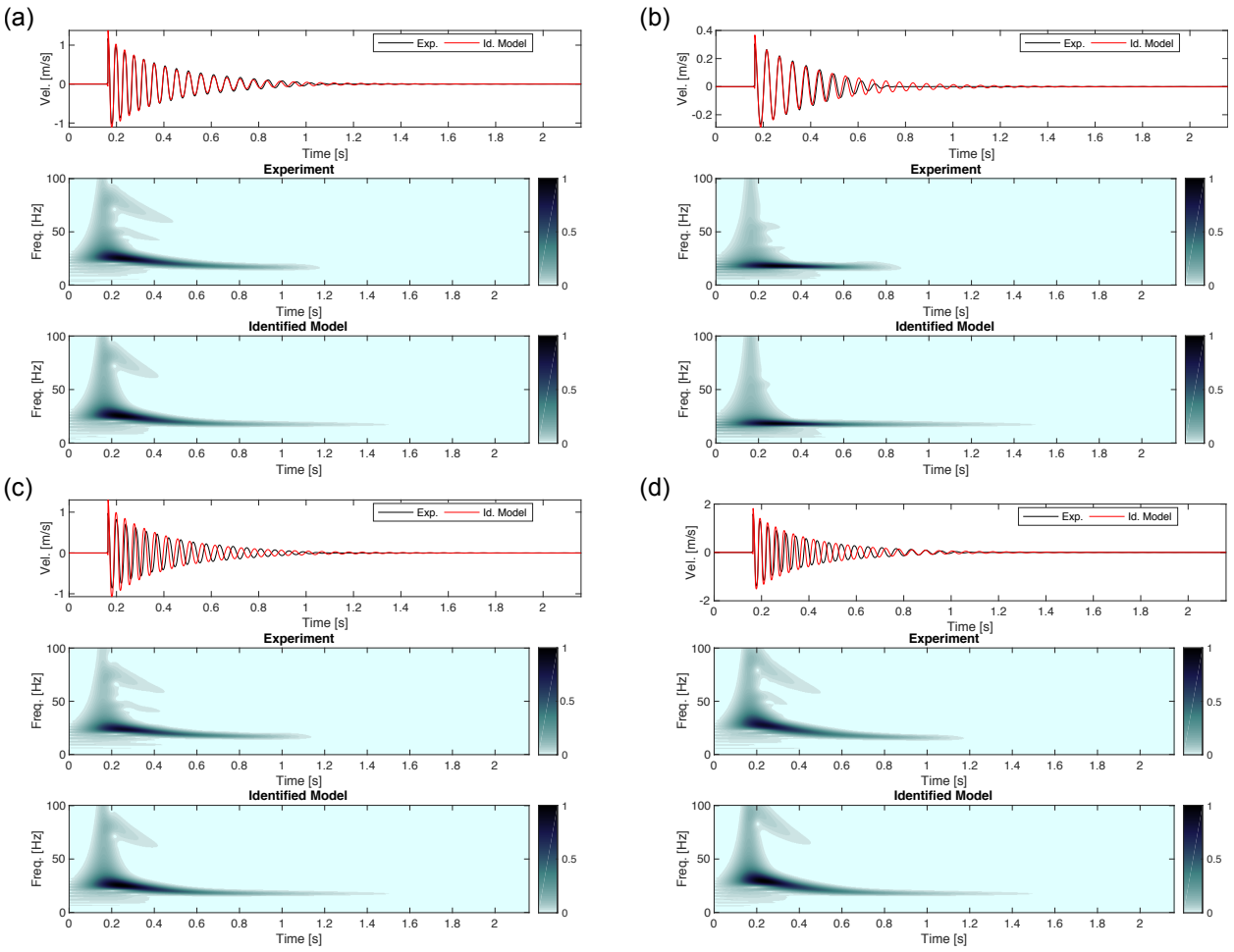

Figure 6.24: Comparison of the velocity response and corresponding WT spectra of the experimentally measured grounded store and the identified model for forcing amplitudes of (a) 387.7 N, (b) 64.8 N, (c) 220.3 N and (d) 497.4 N.

6.8 Nonlinear Experimental Measurements

Following the testing of the grounded stores, the stores were installed on the plane and the system tested in three configurations: locked-locked (L-L), unlocked-locked (U-L) and unlocked-unlocked (U-U), where U-L implies that the left and right stores were unlocked and locked, respectively. Unlike the grounded store testing, gravity did act on the stores and introduced slight curvature in the unlocked flexures at equilibrium. The curvature is visible in Fig. 6.25(a) and results in an asymmetric restoring force, which in turn allows for both softening and hardening behavior [Mojahed, 2018] and introduces many harmonics into the response. The curvature is controlled by the positioning of the pin joint along the longitudinal axis of the plane. The curvature can be eliminated by moving the pin joint towards the front of the plane, which introduces pretension into the flexure. This procedure counterbalances gravity but introduces additional linear stiffness

into the flexure, pushing the linear natural frequency of the store above that of the first flexible mode. Conversely, the curvature can be intensified by placing the pin joint closer to the rear of the plane. Doing so forces the flexure to buckle and introduces bi-stability into the dynamics. However, this also significantly increases the linear stiffness and prevents the stores from interacting with the first flexible mode. Thus, the linear stiffness was minimized by adjusting the position of the pin joint until the frequency of the store was less than that of the first flexible mode.

To verify that the low-energy, linear frequency of the stores was less than that of the first flexible mode, a series of local measurements were performed by directly exciting the store using a PCB modal hammer (model 086C01) with a white plastic tip. The responses of the store and the pylon were measured at the flexure using a PCB accelerometer (model 353B15). The local measurements were performed using P400-V hardware (Polytec, Waldbronn, Germany) and the response was recorded for 16 seconds at a sampling rate of 32 kHz. The location of the accelerometer on the actual store can be seen in Fig. 6.25(a), and the equivalent location on the FE model is provided in Fig. 6.25(b). By directly exciting the store, the energy introduced to the plane is minimized though not entirely eliminated. Nevertheless, as can be seen in Fig. 6.26, this excitation method enables the estimation of the linear natural frequency of the store and a local model of the nonlinearity (not presented here). The velocity response time series of the left and right stores along with the corresponding WT spectra are presented for low- and high-amplitude forcing in Figs. 6.26(a) and (b), respectively. Note that the velocity responses of the pylons (not shown here) are three orders of magnitude less compared to the stores in all of the measurements made, which confirms that the majority of the energy is localized in the stores. The time series show that the stores possess comparable dynamics and verify the repeatability of the assembly process. Moreover, the appearance of exponential decay in the measured time series implies that the dissipation is dominated by viscous damping rather than friction

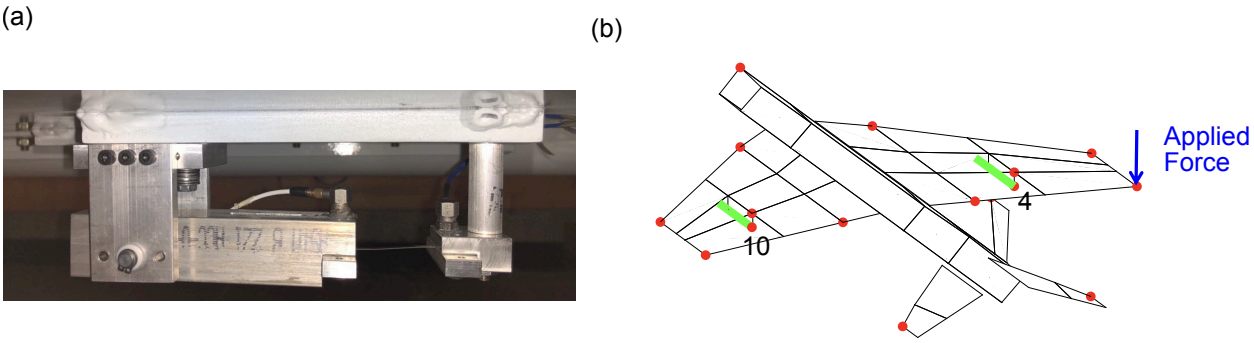

Figure 6.25: (a) The left store attached to the plane in an unlocked and instrumented state. (b) The FE mesh with the stores connected and the measurement locations and forcing position indicated by the red, numbered circles and the blue arrow, respectively.

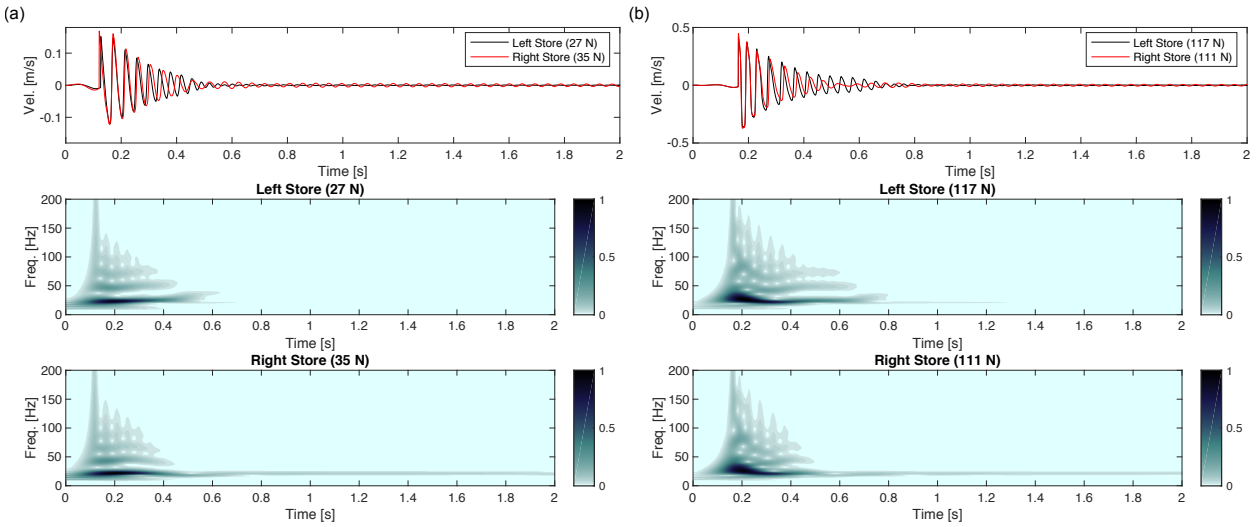

Figure 6.26: Velocity response of each store for local excitation with (a) low amplitude and (b) high amplitude.

effects. The WT spectra reveal significant complexity in the governing harmonics of the response, which go through multiple phases of softening and hardening. Such complexity arises from the asymmetric restoring force due to the curvature in the flexure and gravity. The natural frequencies of the left and right stores are identified from the WT spectra and FFTs (not presented in this work), and are found to be 19.3 Hz and 18.6 Hz, respectively (both of which are less than the first flexible mode). Note that the local testing of the left store was in the U-L configuration whereas the local testing of the right store was done in the U-U state. No local testing was done in the L-L configuration as the stores only contribute additional mass to the dynamics within the frequency range of interest.

For each configuration, the response of the plane was measured using 14 PCB accelerometers, whereas the responses of the stores were measured using one accelerometer on each of them. A total of 16 accelerometers were installed on the system, each with a nominal sensitivity of 1.02 mV/(m/s^2). Figures 6.27(a) and (b) present the experimentally instrumented plane and the corresponding measurement locations on the reduced FE model. Note that the accelerometer at the excitation location (red point 1 in Fig. 6.27(b)) was placed on the underside of the plane to allow for an impact by the same modal hammer as in the local testing (the sign of this accelerometer was flipped during the post-processing to account for this placement). The acceleration response of the system to impulsive loads applied at the location indicated in Fig. 6.27(b) was measured using VibPilot hardware (m+p International, Hannover, Germany) and m+p analyzer software for 8 seconds at a sampling rate of 2048 Hz. The applied force was measured using P400-V hardware for 8 seconds at a sampling rate of 32 kHz. The accelerations and forcing were measured using different systems

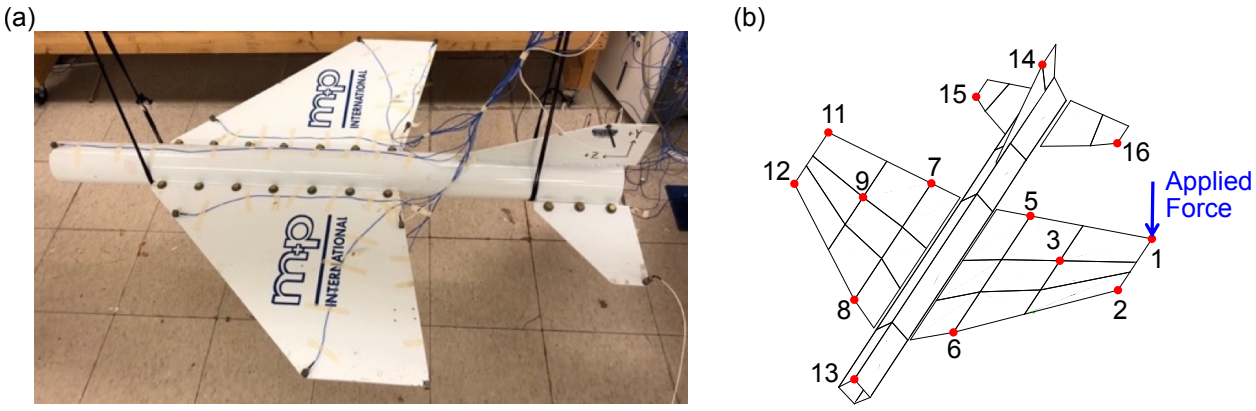

Figure 6.27: (a) The instrumented plane with the stores attached beneath the wings. (b) The reduced FE mesh with the measurement locations and the forcing position indicated by the numbered, red circles and the blue arrow, respectively.

because the m+p hardware was limited to 16 acquisition channels and these were used to maximize the sensor density on the plane. The forcing was recorded at a much higher sampling rate to ensure that it was captured entirely and could be used in an FE simulation if needed.

The response was measured in each configuration for multiple, but comparable, forcing amplitudes such that the dynamics of each configuration was probed in comparable regimes of energy. In this dissertation, the dynamics is studied for three regimes of forcing: 180 N, 300 N and 450 N. Following the measurements, the raw accelerations were integrated numerically and the results high-pass filtered to obtain the velocity responses, which were also integrated and the result high-pass filtered to give the displacement responses. A fifth-order Butterworth filter with a cutoff frequency of 10 Hz was used to remove any rigid-body motion and erroneous low-frequency content introduced by the integration procedure. The displacement response and corresponding WT spectra of the left wing at the impact location for the 180 N and 300 N regimes are presented in Figs. 6.28(a) and (c), respectively. A similar plot for the 450 N regime is provided in Fig. 6.29(a). The red-dashed lines that appear in the WT spectra correspond to the linear natural frequencies of the plane taken from the L-L configuration. The time series corresponding to the 180 N regime (Fig. 6.28(a)) indicate that the U-L (blue) and U-U (red) configurations decay at much faster rates than the L-L response, an interesting result that should be solely attributed to the effects on the plane dynamics of the nonlinear stores. Furthermore, in both the 300 N and 450 N cases, the responses of the plane with unlocked stores decay significantly faster than that of the plane with locked stores.

The WT spectra reveal that, with both stores locked, the first flexible mode participates for longer than 8 seconds regardless of the applied force. With only the left store unlocked, it lasts for only 4.04, 2.76 and 5.21 seconds (50.5%, 34.5% and 65.1% of the L-L time) for forcing at 190, 338 and 452 N, respectively.

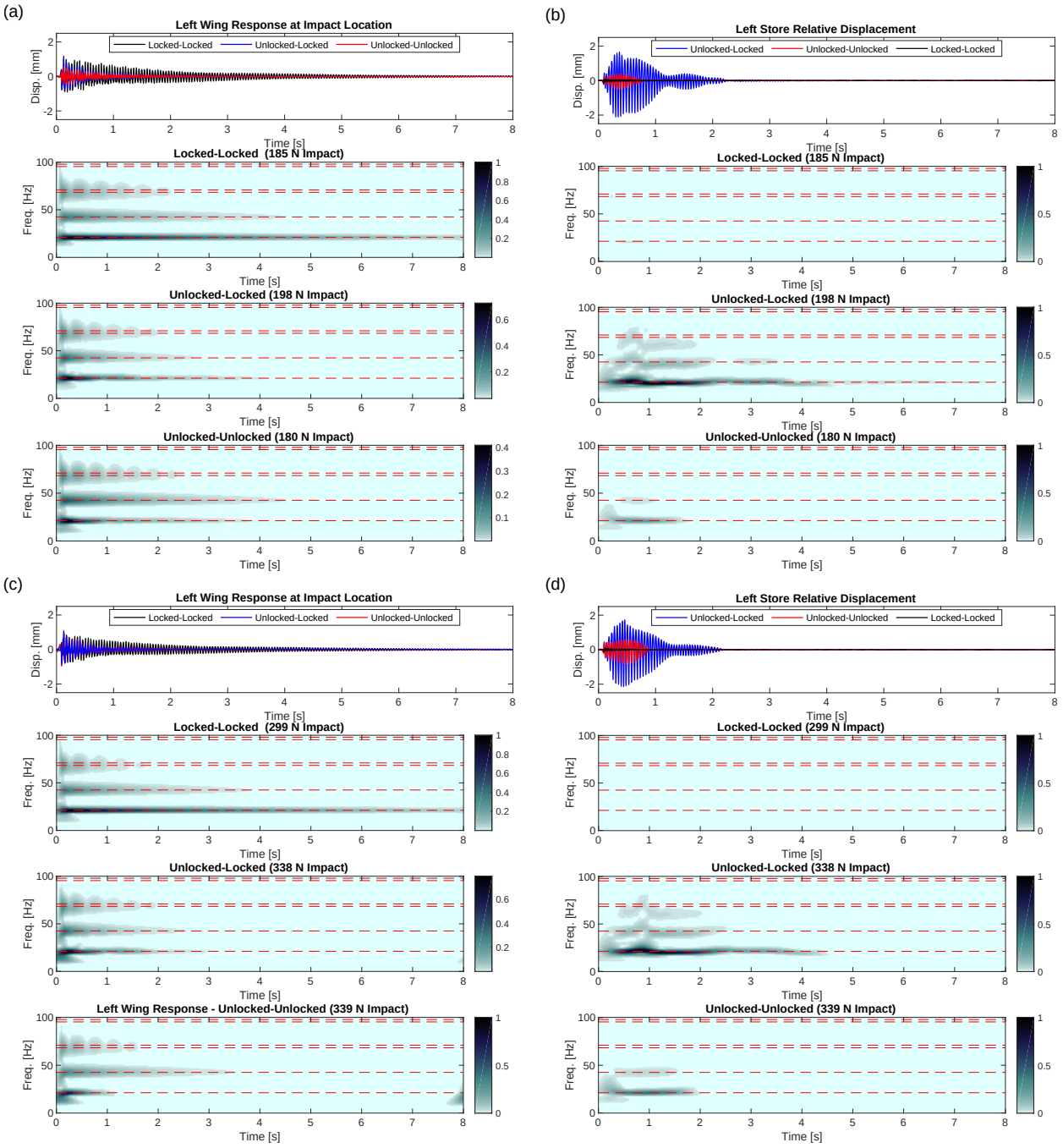

Figure 6.28: Experimentally measured response and corresponding WT spectra of the left wing for impulsive loads of approximately (a) 180 N and (c) 300 N. Experimentally measured relative displacement between the left store and pylon and corresponding WT spectra for impulsive loads of approximately (b) 180 N and (d) 300 N.

With both stores unlocked, it persists for only 3.47, 1.20 and 2.31 seconds (43.4%, 15% and 28.9% of the time with both stores locked) at forcing amplitudes of 180, 339 and 420 N, respectively. All other modes exist for comparable durations in each forcing regime except for the second mode, which persists for less time when the left store is unlocked than in the other two configurations. In fact, with only the left store unlocked, the second mode participates for only 78.9%, 60.6% and 51.8% of the time that it does in the L-L configuration, which indicates that, when only one store is unlocked, the second bending mode of the wing engages in a 2:1 TRC with the store. These results lead to a significant hypothesis: When both stores are unlocked, they each engage in a 1:1 TRC with the first flexible mode and, since this mode corresponds to in-phase motion of the two wings, the dynamical effects of the two stores interfere constructive and drastically amplify their effectiveness at draining energy from the first mode. Similarly, each store engages the second mode in a 2:1 TRC; however, because the second mode corresponds to out-of-phase motion of the wings, the dynamical effects of the two unlocked stores interfere destructively and, ultimately, prevent any energy transfers from the second mode. Another potential explanation is that, instead of absorbing energy from the second mode, the stores actually pump energy from the first mode into it. However, if this were the case then the second mode would last longer with both stores unlocked than it does with both stores locked. The fact that the second mode persists for comparable times in both cases refutes this explanation. Moreover, since the interaction between the stores and the second mode in the U-L case is parasitic, the interaction (if one occurred) between them in the U-U case would also be parasitic.

To verify this conjecture, we turn to the relative displacement between the store and the pylon, and the corresponding WT spectra presented for forcing regimes of 180 N, 300 N and 450 N in Figs. 6.28(b), 6.28(d) and 6.29(b), respectively. The time series reveal that the relative displacement is larger when only one store is unlocked, which implies that the lone store absorbs substantially more energy from the first and second modes than the two stores do when both are unlocked. Note that the relative displacement of the L-L case is an order of magnitude lower than the other two cases, but is non-zero because the store is connected to two points on the plane that do not have equal displacements. The WT spectra of the U-L cases depict three main harmonics that dominate the relative displacement. Of these three harmonics, the first and second align with the natural frequencies of the first and second modes, giving rise to the 1:1 and 2:1 TRCs discussed previously. The WT spectra of the U-U configurations show that two harmonics dominate the responses of the 180 N and 300 N cases with a third harmonic joining in the 450 N case. Again the first two harmonics align with the first and second modes such that, in theory, the stores should engage in both TRCs. However, since, from the previous analysis, the second mode does not lose energy to the stores, this suggests that the effects of the stores are amplified and canceled with respect to the first and second modes

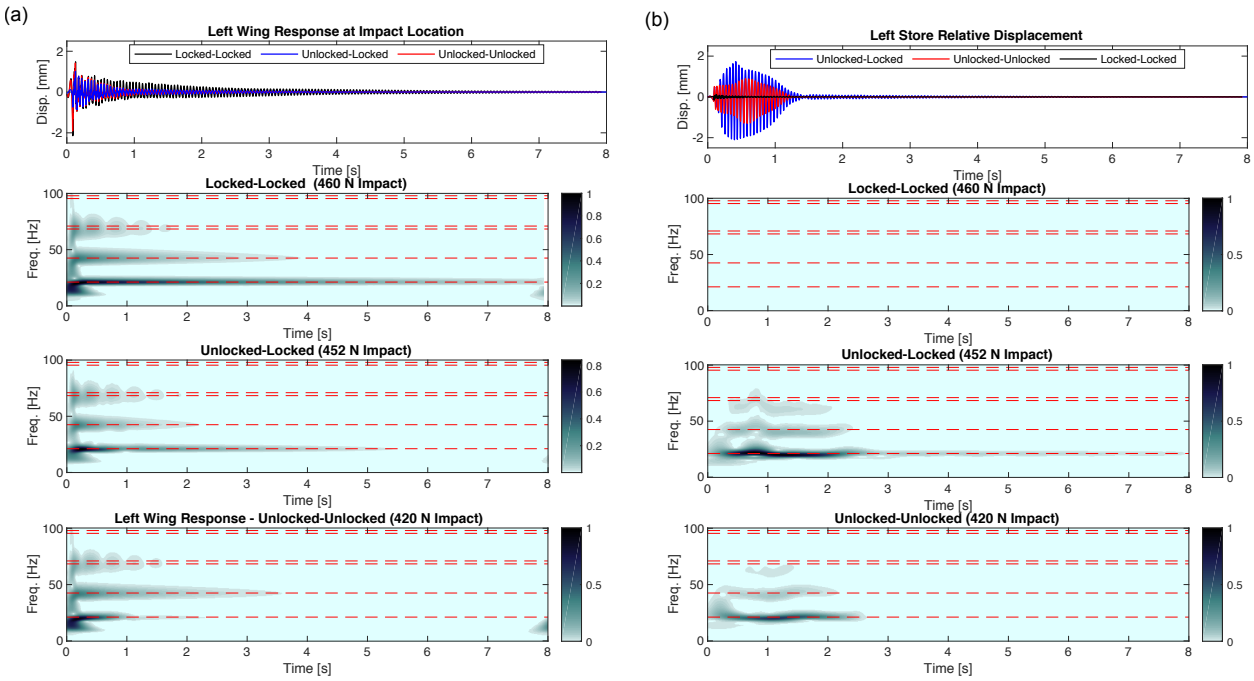

Figure 6.29: (a) Experimentally measured response and corresponding WT spectra of the left wing for impulsive loads of approximately 450 N. (b) Experimentally measured relative displacement between the left store and pylon and corresponding WT spectra for impulsive loads of approximately 450 N.

when both are unlocked.

Further validation of this hypothesis necessitates a deeper investigation of the nonlinear dissipative effects of the stores. We begin with an examination of the total energies for each configuration and forcing case. To ensure a fair comparison, and to isolate the effects of the unlocked stores, we compute the total energies using the FE model with both stores locked and exclude the measured responses of the stores from the computation. These responses are excluded because the locked stores are much stiffer than the unlocked stores and, thus, including them in the computation results in a significant overestimation of the total energies. Since the existing reduced FE model is incompatible with the measured data (i.e., the reduced FE model consists of 216 DOFs whereas only 14 DOFs are measured on the plane), a second Guyan reduction is employed to condense out all DOFs except those corresponding to the measurement locations on the plane, which allows the direct estimation of the kinetic and potential energies of the system using the measured velocities and displacements. We refer to this model as the experimental model and use M_e and K_e to represent the corresponding mass and stiffness matrices, respectively. Mathematically, the total mechanical energy is

$$E(t) = \frac{1}{2}\dot{y}_e^\intercal M_e \dot{y}_e + \frac{1}{2} y_e^\intercal K_e y_e, \tag{6.14}$$

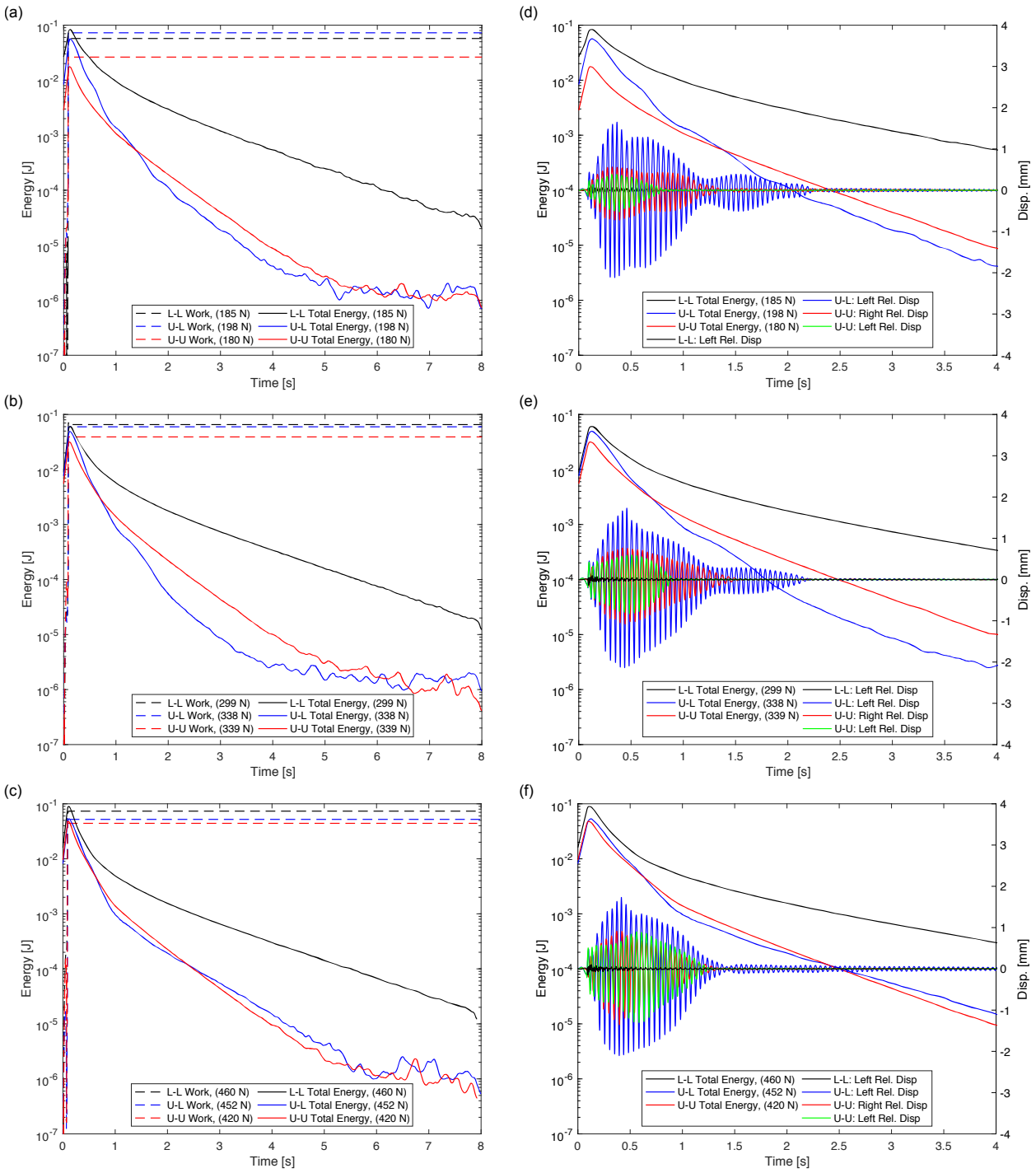

Figure 6.30: Comparisons of the work done and total energies for impacts of approximately (a) 180 N, (b) 300 N and (c) 450 N, and a comparison of the total energies and relative displacements between the stores and pylons for forcing cases of (d) 180 N, (e) 300 N and (c) 450 N.

where $\dot{y}_e$ and y_e are the vectors containing the experimentally measured velocities and displacements, respectively. Additionally, the instantaneous energies are low-pass filtered using a first-order Butterworth filter with a cutoff frequency of 3 Hz. The low-pass filtering is applied to remove oscillations in the total energies that arise from small inaccuracies in the FE model (both those existing prior to and introduced by the second Guyan reduction) and minor measurement errors. The estimated total energies are validated by comparing them to the total work done by the applied force, which is computed as

$$W(t) = \int_0^t F_{in}(\tau)\dot{y}_{e,1}(\tau)\,\mathrm{d}\tau, \tag{6.15}$$

where $F_{in}(\tau)$ is the experimentally measured input force and $\dot{y}_{e,1}(\tau)$ is the measured velocity of the plane at the location of the impact (measurement point 1 in Fig. 6.27).

Figures 6.30(a), (b) and (c) present comparisons of the experimental work (dashed lines) and total energies (solid lines) of each configuration for forcing regimes of 180 N, 300 and 450 N, respectively. We find that the work done by the applied force is comparable to the maximum total energy in every case, which validates the use of the experimental model for computing the energies. Note that the responses of the system in the U-L and U-U configurations are dominated by noise in the final 3-4 seconds, resulting in the oscillations observed in the total energies. Considering Fig. 6.30(a), we find that the U-L configuration decays faster than the other two cases and reaches the noise floor first. This trend is also observed in the other two forcing regimes. This result is unsurprising as the system is expected to dissipate energy at a much faster rate with one store unlocked than with both stores locked; however, the fact that one store is more efficient at dissipating energy than two stores is unexpected, but serves to reinforce the hypothesis proposed earlier. That is, one store is more efficient because it is able to simultaneously absorb energy from both the first and second modes, whereas when both stores are unlocked they only interact with the first mode. In Fig 6.30(c), we find that the U-L and U-U configurations exhibit similar overall dissipation trends, but contain local differences in dissipation rates. In fact, both cases begin with a period of significant, non-viscous decay and abruptly switch to viscous decay that gradually dissipates the remaining energy. To understand the mechanisms underlying the changes in the dissipation rates, we compare the relative displacements between the stores and the pylons with the total energies in Figs. 6.30(d), (e) and (f) for forcing cases of 180 N, 300 N and 450 N, respectively. These figures reveal that the periods of significant dissipation correspond to large relative displacements, which implies that they are the result of intense energy interactions between modes of the plane and the stores.

Having explored the effects of the stores on the total energies, we turn our attention towards understand-

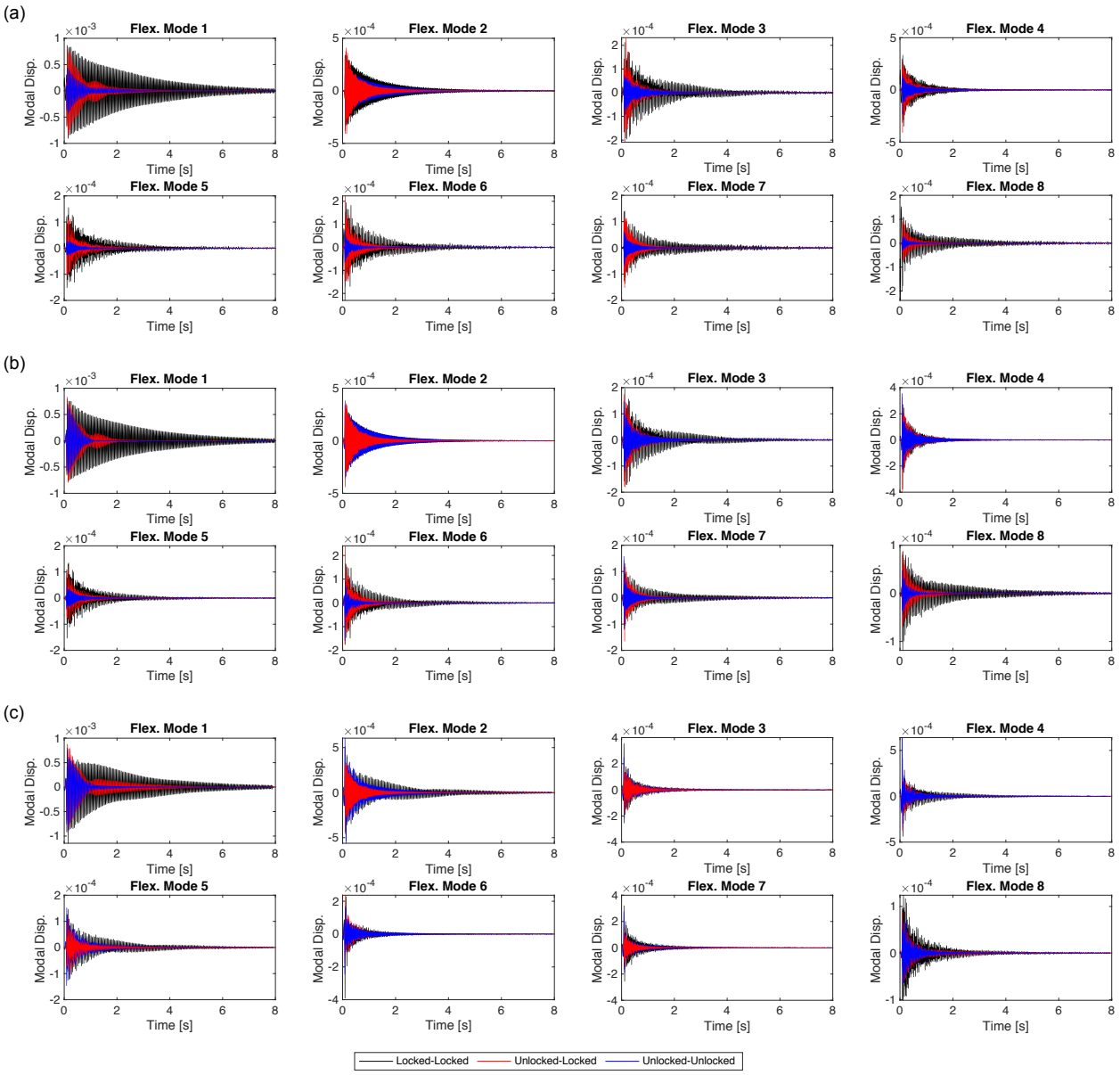

Figure 6.31: Modal displacements of the first eight flexible modes of the plane in all three configurations for forcing regimes of (a) 180 N, (b) 300 N and (c) 450 N.

ing the effect of the stores on each mode. To this end, we project the measured response onto the modal coordinates of the experimental model by computing

$$\eta_e = \Phi_e^\intercal M_e y_e, \tag{6.16}$$

where η_e is the vector of modal displacements and Φ_e is the mass-orthonormalized modal matrix of the experimental model. The modal velocities, $\dot{\eta}_e$, are computed by substituting in $\dot{y}_e$ for y_e in the above relation. The resulting modal displacements are provided for the first eight modes of the plane for the three forcing regimes in Fig. 6.31. In this figure, we find that the response of the first mode is the largest and persists the longest out of all modes when both stores are locked. In contrast, when either the left or both stores are unlocked, the first mode decays rapidly in the first second and, in the case of both stores being unlocked, it does not appear in the response afterwards. In the case where only the left store is unlocked, a beat appears in the response of the first mode after the initial period of large dissipation, after which it is eliminated from the response. The decay trends observed correspond to the durations of the modes noted earlier and demonstrate the effectiveness of the stores at draining energy from the first mode. Looking at the second mode, we find that it experiences the largest rate of decay when only the left store is unlocked. More importantly, when both stores are unlocked, it decays at the same rate as in the L-L configuration regardless of the applied force indicating that the stores have no dissipative effect on it.

While these results support the proposed hypothesis, an even greater understanding of the effects of the stores can be gained by studying the energies associated with each mode. Thus, we compute the energy of each mode as

$$E_i(t) = \frac{1}{2}\dot{\eta}_{e,i}^2 + \frac{1}{2}\omega_i^2\eta_{e,i}^2, i = 1, \ldots, 14, \tag{6.17}$$

where ω_i is the natural frequency (with units of rad/s) of the ith mode. In Fig. 6.32, we present the resulting modal energies of the first eight flexible modes of the plane in each configuration for the each forcing regime. This figure reveals that the unlocked stores introduce significant dissipation into every mode except the second and fourth. We find that, when both stores are unlocked, the second mode decays at exactly the same rate as it does when both stores are locked regardless of the forcing amplitude. Thus, the modal energies demonstrate that, indeed, when both stores are unlocked, their individual effects on the second mode cancel each other out. Interestingly, the stores have no effect on the fourth mode regardless of whether they are locked or unlocked. While interesting at first glance, a quick review of the mode shapes in Fig. 6.9 reveals that the locations of the pin joints on the wings correspond to nodal lines of the fourth mode. Thus, due to the positioning of the pin joint, the stores are unable to interact with the fourth mode

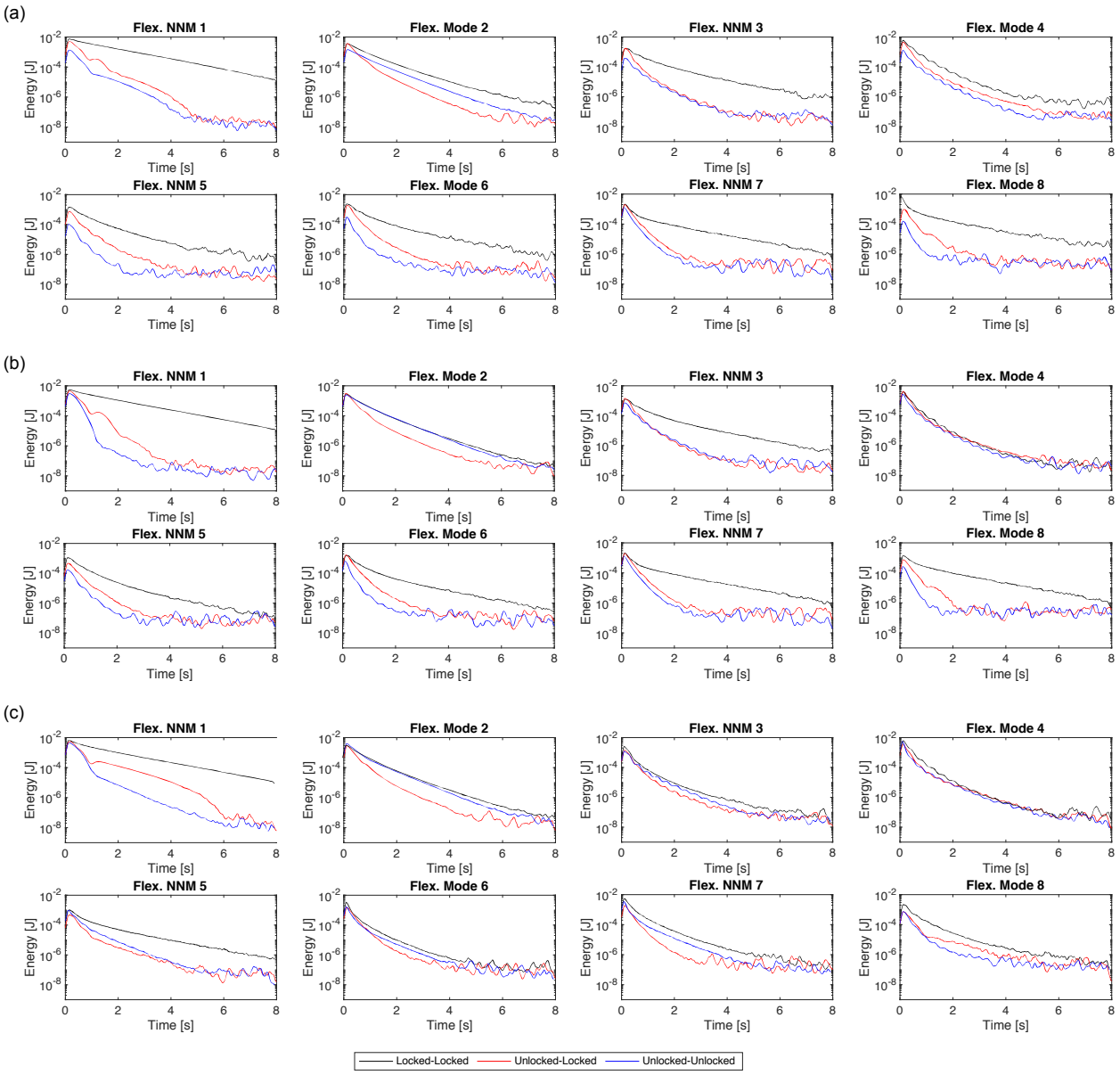

Figure 6.32: Modal energies of the first eight flexible modes of the plane in all three configurations for a forcing regimes of (a) 180 N, (b) 300 N and (c) 450 N.

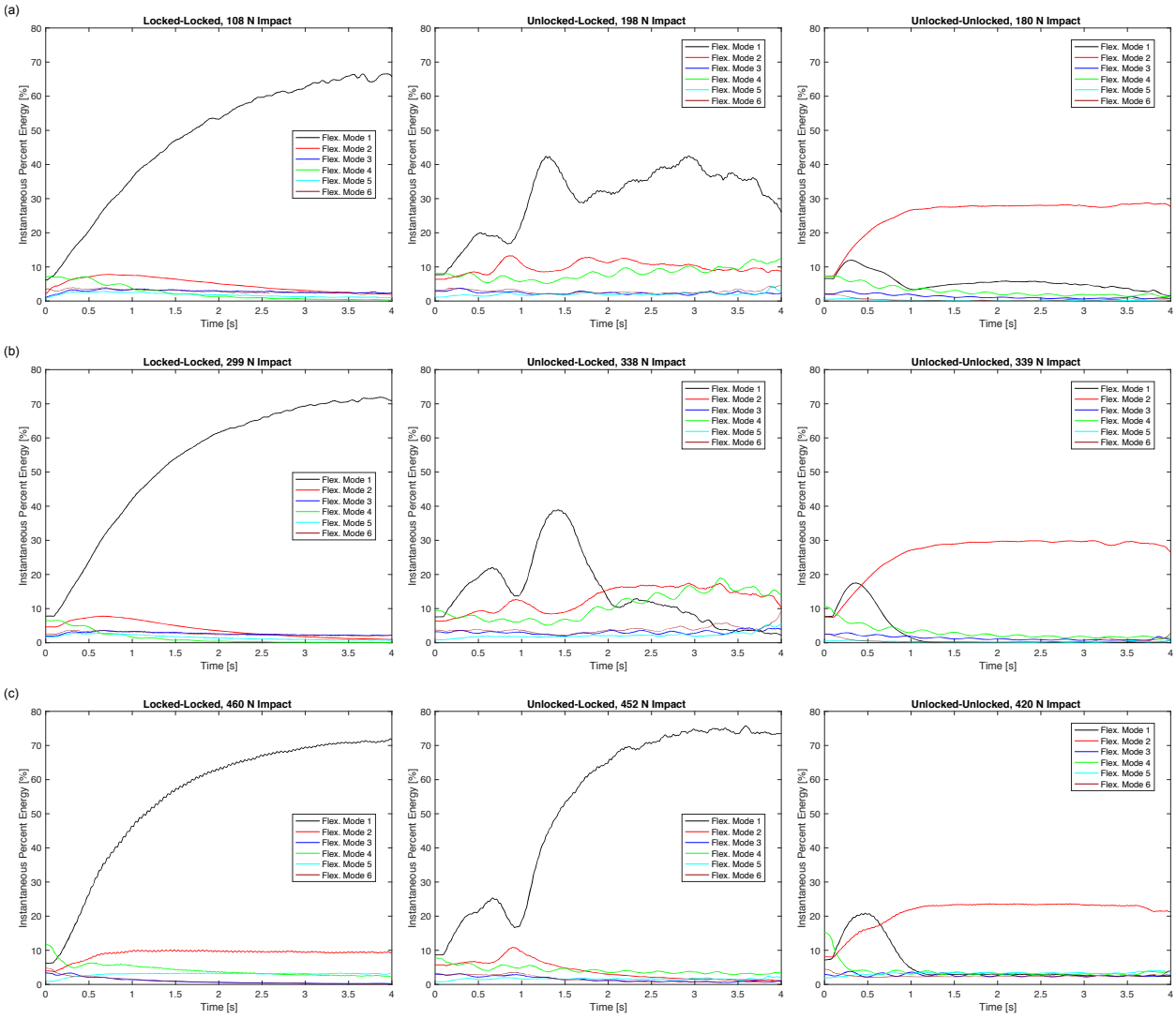

Figure 6.33: Modal energies of the first eight flexible modes of the plane in all three configurations for forcing regimes of (a) 180 N, (b) 300 N and (c) 450 N.

regardless of their configuration. Besides these two modes, the modal energies demonstrate that the stores are capable of absorbing energy from multiple modes simultaneously and, thus, introduce dramatic changes into the global dynamics of the plane even though they are local attachments.

Further understanding of the global repercussions induced by the stores can be gained by studying the interactions between the modes of the plane. To gain insight into these modal interactions, we normalize the modal energies by the total energy at each time instant and compare the resulting energy percentages for each configuration for forcing amplitudes of 180 N, 300 N and 450 N in Figs. 6.33(a), (b) and (c), respectively. These plots reveal the distribution of the remaining total energy in each mode at each time instant. Note that only the first four seconds are presented as after this time the modes become dominated

by noise and do not accurately represent the distribution of remaining total energy. Looking first at the L-L configuration, we find that for all forcing cases the energy begins with an even distribution across the modes. However, as time increases and the response decays, the percentage of energy in the first mode rises steadily until more than 70% of the remaining total energy is concentrated in it. Since the dynamics of the plane are linear when both stores are locked, no energy exchanges can occur between the modes or the stores. Consequently, the first mode dissipates energy at the slowest rate and, thus, it grows to dominate the remaining total energy as all other modes decay faster and exit the response sooner. It follows that, in the absence of energy transfers between modes of the plane and for impulsive excitation, the mode with the slowest decay rate will always grow to dominate the distribution of the remaining total energy. Considering now the U-L case, we find that the remaining total energy does not concentrate in any single mode for all forcing cases. Although the first mode grows to dominate the remaining total energy for the 180 N case, it does not rise steadily and achieves only half the amplitude that it does in the L-L configuration. Moreover, a significant portion of energy remains concentrated in the second and third modes. Note that this does not necessarily mean that the energy in the second mode increases due to transfers from the first mode, but it does imply that the first mode decays at a faster rate than in the L-L configuration. However, a clear beat pattern appears between the first and second modes beginning just after 0.5 seconds and lasting until just before 2.5 seconds. The observed beating pattern corresponds to the beating found in the relative displacements in Figs. 6.28(b) and 6.30(d) and, thus, any energy exchanges between the first and second mode are facilitated by the nonlinear stores. A similar beating pattern appears in the 300 N case, which also matches the beating found in the corresponding relative displacement plots. Unlike the 180 N case, the first mode does not dominate the remaining total energy after 2 seconds. Instead, the second and third modes contain the largest percentage of energy at the end of the response. This indicates that the rate of dissipation in the first mode is larger than that of the second and third modes, which agrees with the previous analysis of the time series. Looking at the 450 N case, a single beat is observed just before 1 second, after which the first mode grows at a comparable rate and trend as in the L-L case. This suggests that the store absorbs only part of the energy in the first mode and, after the interaction ceases, the first mode behaves linearly and dissipates energy at the same rate as in the L-L configuration. Finally, looking at the U-U configuration, we find that in all three forcing cases the second mode exhibits the highest concentration of remaining total energy and that the first mode is eliminated from the response after 1 second. This implies that the rate of decay of the first mode is significantly larger than that of the second mode and further confirms the main hypothesis proposed in this section.

6.9 Concluding Remarks

This chapter investigated the effects of local, lightweight, nonlinear attachments on the global dynamics of a model airplane. First, linear experimental results were used to create a representative FE model of the plane. Based on the natural frequency of the linear normal modes of the plane, a nonlinear store was designed and two ROMS were studied to ensure that the stores would interact with the second flexible mode. Following the study of the ROMs, a FE model was developed for the stores and coupled to the FE model of the plane. This model was used to simulate the response of the system for multiple impulsive loads, and the proposed methodology was employed to investigate the global effects in the dynamics induced by the local stores. Specifically, the resulting RQ-FEP revealed that, in addition to interactions between the modes of the plane and the NNM of the store, the modes of the plane can directly interact with each other due to the nonlinear action(s) of the store(s). Furthermore, after the frequency of the store exceeded that of the second mode, numerous spikes coalesced in the RQ-FEP indicating the existences of chaotic, multi-scale energy transfers in the dynamics. The final portion of the computational study concerned the application of the proposed NSI method, which successfully identified a representative model of the nonlinearity. Moreover, the resulting updated computational model accurately reproduced the simulated response of the exact system.

Following the computational study, two identical stores were constructed and three experimental investigations were performed. The first experimental study focused on evaluating and identifying the nonlinearity of the stores prior to installing them on the wings of the plane, with the primary objective of determining whether or not the stores would interact with the first mode of the plane. To accomplish this, the stores were tested in a grounded state where the pin joint and the pylons were bolted to an optical table. In this configuration, the motion of the stores was restricted to rotation about the pin joint, and they were not subjected to gravity. The response of the stores were measured for four different impulsive loads, and a mathematical model for the nonlinearity was identified and validated using these measurements. The mathematical model provided valuable insight into the nonlinear stores and confirmed that they will interact with the first mode of the plane. After testing the grounded stores, the stores were installed on the wings with the flexures locked. In this configuration, termed locked-locked (L-L), the stores did not introduce new dynamics into the response of the plane within the frequency range of interest of this study. Instead, the stores acted only as added mass with the effect of lowering the natural frequencies of the modes of the plane. As such, the plane behaved linearly in the L-L state and no energy transfers due to nonlinear interactions were possible. In addition to the L-L configuration, the dynamics of the plane was also studied when only the left store was unlocked, termed the unlocked-locked (U-L) state, and also when both stores were unlocked, called the unlocked-unlocked (U-U) setup. Unlike in the grounded store experiments, the installed stores

were subjected to gravity which introduced slight curvature into the flexures. Prior to testing the plane with unlocked stores, a series of local measurements were made by exciting each unlocked store directly using a modal hammer. The local measurements revealed that the responses of the stores contained many harmonics that went through phases of both hardening and softening. The appearance of many harmonics and both softening and hardening behavior were attributed to the initial curvature in the flexure, which also resulted in a non-zero equilibrium point. Moreover, the local responses confirmed that the stores as installed would interact with the first flexible mode of the plane. We note that the local tests allowed for the identification of a mathematical model of the nonlinearity using a similar approach to that used in the grounded store experiments. Such a model could be used to study the effects of the local stores on the global dynamics of the plane by examining the nonlinear restoring force induced by the flexures. However, this identification was not performed in this dissertation, and it remains the topic of future research.

Instead, the global effects of the local stores were investigated using the measured response of the plane in the three configurations for three forcing regimes. In these experiments, an impulsive load was applied to the left wing where the trailing edge meets the wing tip, and the response of the plane and stores was measured for 8 seconds. In the L-L setup, the first mode of the plane was found to last longer than the measurement time regardless of the forcing amplitude, whereas it was found to persist for significantly less time in the U-L and U-U configurations. Interestingly, the second mode was found to participate for less time when only the left store was unlocked than when both stores were locked or unlocked (it persisted for the same time in these configurations), indicating that when only one store is unlocked it absorbs energy from both the first and second modes. These observations led to the hypothesis that, when both stores are unlocked, they each interact with the first mode and, because this mode corresponds to in-phase motion in the wings, their individual effects interfere constructively, amplifying the rate at which energy drains form the first mode. Similarly, each store also interacts with the second mode; however, because this mode corresponds to the out-of-phase motion in the wings, the dynamical effects of the stores interfere destructively, effectively cancel and prevent any energy transfers out of the second mode from occurring.

The investigation of this hypothesis began with an examination of the harmonics exhibited by the relative displacement between the stores and the corresponding pylons. The wavelet transform spectra revealed that, in both the U-L and U-U configurations, the relative displacements possessed three harmonics and that two of these aligned with the first and second modes in terms of frequency. Thus, the relative displacements confirmed that the stores could interact with both modes in either of the unlocked configurations. While these results supported the proposed hypothesis, further validation was sought by investigating the nonlinear dissipative effects of the stores. To accomplish this, we developed a computational model of the plane with

the stores in the locked state and used Guyan reduction to condense out all DOFs except the measurement DOFs on the plane; we referred to this model as the "experimental model". Using the experimental model and the measured plane response, the total energies were computed for each forcing regime and were validated using the work done by the applied force. The resulting energy plots revealed that the U-L case dissipates energy at a faster rate than both the L-L and U-L setups, which was contributed to the fact that the left store absorbs energy from both the first and second modes in the U-L configuration. Furthermore, a comparison between the total energies and the relative displacements established that periods of large dissipation corresponded to periods of large relative displacement, indicating that they were the result of intense energy interactions between the modes of the plane and the stores. After investigating the effects of the stores on the total energies, their effect on the individual modes was explored by projecting the measured responses onto the modes of the experimental model. The resulting modal responses revealed that the first mode decays viscously when the stores are locked (as expected), but undergoes extreme, non-viscous decay when the left store or both stores are unlocked. In contrast, the second mode decayed at the same rate when the stores were either both locked or both unlocked, and experienced a larger decay rate when only the left store was locked. The modal responses were then used to compute the corresponding modal energies for the first eight modes of the plane, which were compared for each forcing regime and configuration. Using the modal energies, we found that the energy of each mode decayed at a faster rate in either the U-L or the U-U configurations than in the L-L state, except for the second and the fourth modes. The rate of decay of the fourth mode did not vary regardless of the setup of the stores. The second mode decayed at the same rate when the stores were either both locked or both unlocked, but experienced greater decay when only the left store was unlocked. This observation agreed with the previous results and further confirmed the hypothesis proposed in the section. Finally, the interactions between the modes of the plane induced by the stores were investigated by studying the modal energies normalized by the instantaneous total energies. These plots demonstrated the relative distribution of energy in the modes and revealed the interactions between the first and second modes. The results presented in this analysis provided further evidence for the main hypothesis of the experimental study.

The results of this chapter demonstrate the power of our methodology for analyzing and understanding the effects of local, nonlinear attachments on the global dynamics of their parent structures. As such, the methodology can provide significant insight into the nonlinear physics governing dynamical systems with local attachments possessing smooth nonlinearities. Furthermore, by identifying mathematical models for the modal responses and using these as a basis for computing the response of the systems, the methodology can be employed to form reduced-order models of the nonlinear systems.

Chapter 7

Concluding Remarks and Future Research

7.1 Summary

This dissertation presents a novel, data-driven nonlinear system identification, reduced-order modeling and model updating methodology that circumvents the steep analytical, computational and experimental costs incurred with existing methods. The methodology achieves this through the synergistic implementation of diverse theoretical, computational and experimental techniques, resulting in a procedure that is both broadly applicable and widely accessible. In application, the methodology requires that the analyst possess an updated model (typically a finite element model) of the underlying linear structure and measured transient response data, both of which are generated by practicing vibration engineers in standard product development cycles. Thus, by relying on existing data and models, the methodology bypasses the need for special measurement, excitation or control equipment and software. Through the implementation of the Rayleigh quotient and the proper orthogonal decomposition, two well-known linear computational methods, the methodology escapes the substantial academic investment (which is often the most significant barrier faced by practicing engineers) that existing methodologies necessitate. Even though the methodology employs linear techniques, the results shown in this dissertation demonstrate that significant insight into the physics governing strongly nonlinear, dynamical systems can be gained by applying the proposed methodology. As such, the remainder of this section is dedicated to summarizing the main contributions and results of each chapter of this dissertation.

Chapter 2 reviewed the diverse theoretical and computational techniques necessary for the development of the propose methodology. This included a discussion of nonlinear normal modes (NNMs) and the accompanying frequency-energy plots (FEPs), which proved invaluable throughout the analyses presented in this dissertation. Following the discussion of NNMs, the proper orthogonal decomposition, Rayleigh quotient and Guyan reduction procedures were described in detail. Next, the wavelet and Hilbert transforms and several examples were presented. Section 2.6 introduced the empirical mode decomposition (EMD) and the ensemble EMD, two computational procedures for extracting dominant harmonics from nonlinear and non-

stationary time signals. Next, Section 2.7 provided a firm theoretical foundation for the analysis of internal resonance and resonance capture phenomena through the failure of the averaging theorem. Finally, Section 2.8 introduced the concept of slow-flow dynamics and established the physical correspondence between the theoretical concepts in Sections 2.1 and 2.7 with those developed in Section 2.6.

Chapter 3 concerned the development of the wavelet-bounded EMD (WBEMD), which is a closed-loop, optimization-based solution to the problem of mode mixing inherent in EMD and EEMD. Section 3.2 introduced the maximum wavelet transform (MWT), which enables one to assess the relative distribution of the energy contained in a signal in the frequency domain. The major benefit of the MWT is that it results in a smooth representation in the frequency domain, unlike the fast Fourier transform (FFT), which makes it amenable for use in an optimization routine. Section 3.3 introduced the wavelet-bounding algorithm, which maximizes the isolation of an IMF by minimizing the area under its corresponding bounding function. After the derivation of the WBEMD algorithm, three example applications were investigated. In Section 3.4.1, a synthetic two-component signal was used to demonstrate the efficacy of WBEMD for extracting well-separated IMFs. Using this signal, WBEMD was shown to be superior to EMD and EEMD for decomposing closely-spaced harmonics and the effect of each parameter on the effectiveness of WBEMD was reported. Section 3.4.2 presented the application of EMD, EEMD and WBEMD to the numerically integrated response of a cantilever beam with a strongly nonlinear spring installed at its free end. Neither EMD nor EEMD was able to extract physically meaningful IMFs, whereas WBEMD produced IMFs that were physically representative of the NNMs governing the dynamics of the beam. As such, the IMFs generated using EMD and EEMD were abandoned, whereas those extracted by WBEMD were used to reconstruct the corresponding FEP and to identify the presence of a 3:1 internal resonance (IR) in the response. Finally, WBEMD was applied to each translational degree-of-freedom (DOF) and the resulting IMFs were combined to create a set of spatio-temporal IMFs, which reconstructed the periodic solution of the first NNM. The final application of WBEMD concerned a linear oscillator (LO) coupled with a vibro-impact (VI) nonlinear energy sink (NES). Due to the strongly nonlinear impacts, only WBEMD was applied to the simulated response. The IMFs demonstrated that, although the response of the LO and the NES can be approximated by the first IMF (recall that the ordering of the IMFs was reversed in this study), the relative displacement could not be reconstructed without the higher harmonics. Furthermore, it was found that the higher harmonics play a vital role in the patterns of the VIs and, thus, significantly influence the ability of the NES to dissipate energy. Finally, the IMFs were used to demonstrate the existence of higher-order transient resonance captures (TRCs), which were thought to be the result of numerical errors in a previous study.

Chapter 4 examined the physical underpinnings of the proposed methodology for detecting (even strongly)

nonlinear interactions in the form of internal resonances (IRs) in the measured response caused by nonlinear modal energy exchanges. The proposed methodology was applied to both a computational and an experimental study of a cantilever beam with smooth, stiffness nonlinearity near its free end. In the computational study, the response of the beam to an impulsive excitation was simulated multiple times for varying impulse amplitude. The proposed methodology was applied to each simulation separately, and the frequency of each NNM was estimated using the proper orthogonal modes (POMs) extracted with POD as trial vectors in the Rayleigh quotient (RQ). By varying the forcing amplitude, the dynamics was probed across a wide range of energies, and an estimated FEP, termed the RQ-FEP, was constructed. The RQ-FEP revealed that the dynamics can be partitioned into two linear regimes in the limits of low and high energy, and a nonlinear transition regime that bridges the two linear regimes. Additionally, non-smooth perturbations (spikes) were observed in the RQ-FEP, and these appeared to indicate strongly nonlinear modal interactions. Upon further examination, the spikes were found to correspond to POMs that were similar in shape whereas points off of the spikes resulted from POMs with dissimilar shapes. Finally, WBEMD and slow-flow analysis were employed to verify that the spikes result from strongly nonlinear IRs that appear in the simulated response. Following the computational study, an experimental study was performed on a comparable cantilever beam with strong stiffness nonlinearity near its free end. Unlike the computational study, the measured response rapidly decayed within the 2-second measurement window and the proposed methodology was applied to windowed segments of the response instead of the entire window. The resulting RQ-FEP revealed three spikes: one at the beginning of the response and two towards the end of the signal. Examination of the POMs confirmed that the spikes corresponded to similar POMs, whereas points off of the spikes results from dissimilar POMs. Once again, WBEMD and slow-flow analysis were used to show that the spikes arose from strongly nonlinear modal interactions caused by IRs in the dynamics. The spike at the beginning of the response was found to be the result of a 5:2 IR between the first and second NNMs, whereas the two spikes towards the end of the measurement were produced by two 3:1 IRs between the first and second NNMs. Thus, the experimental results were found to reproduce almost exactly those predicted in the computational study and verified that the spikes and similar POMs do indicate strongly nonlinear modal interactions that result from IRs and TRCs.

Chapter 5 presented the data-driven NSI procedure for characterizing and modeling local nonlinear attachments connected to a base linear structure. The methodology was applied to a computational and an experimental study of a cantilevered airplane wing with a local NES installed at its tip. In the computational study, the NES was coupled to the center of the wing tip, near the nodal lines of the torsional modes, such that the NES interacted with only the bending NNMs. The linear stiffness of the NES was chosen such

that its natural frequency was less than that of the first bending NNM, enabling the NES to interact with all bending NNMs. The response of the wing with the NES installed to an impulsive excitation was simulated for multiple forcing amplitudes, allowing the dynamics to be probed across a wide range of energies. The proposed methodology was applied to each simulation separately, and the frequencies of the NNMs were estimated at each energy level. The resulting RQ-FEP revealed that the dynamics of the wing could be partitioned into three regimes, whereas that of the the NES could only be partitioned into two regimes. The wing dynamics was separated into two linear regimes in the limits of low and high energy, which were connected by a nonlinear transition regime. Interestingly, the dynamics of the NES could only be partitioned into a single linear regime at low energy and a nonlinear regime which extended to infinite energy. Moreover, the high-energy regime for each NNM of the wing was found to activate only after the frequency of the NES surpassed that of the wing NNM. When this occurred, the NES no longer acted as a separate DOF with respect to that NNM and, instead, behaved as added mass, decreasing the frequency of the NNM. Furthermore, numerous spikes appeared in the RQ-FEP; and these corresponded to similar POMS indicating that they were the result of strongly nonlinear TRCs in the simulated response. Following the discussion of the TRCs, a characteristic displacement was defined for the system using the relative displacement between the NES and the wing. The characteristic displacement was used to form the RQ frequency-displacement plot (RQ-FDP), which allowed the backbone of the NES NNM to be realized directly from the equation of motion governing the NES. Thus, the nonlinearity was identified using the frequency-displacement equation obtained from the EOM, and an updated model was shown to accurately reproduce the simulated response. Following the computational study, an experimental study was performed on a comparable wing, with NES coupled to the leading and trailing edges of the wing tip. Prior to installing the NES on the wing, it was tested in a grounded configuration and identified by combining the restoring force surface (RFS) method and a time-series optimization procedure. Following the tests of the grounded NES, the NES was installed on the wing, and the proposed NSI procedure was applied to the the measured response. Unlike the computational study, the frequencies of the NNMs were estimated using the windowed segments of a single measurement. The resulting RQ-FEP revealed a sustained TRC at the beginning of the response followed by a second TRC given by a single spike. An analysis of the energy dissipated in each segment and the POMS confirmed the existence of the TRCs. Next, the characteristic displacement was computed, and the corresponding RQ-FDP was used to identify the nonlinearity. Finally, two updated models were created: one using the RFS parameters and the other using the RQ-FDP method. The resulting RQ-FDP model was found to reproduce the experimental response for multiple forcing levels, whereas the RFS model could only do so for large forcing. Thus, the experimental results verified those predicted computationally and validated the

proposed data-driven NSI methodology.

Chapter 6 studied the effects of local, lightweight, nonlinear attachments on the global dynamics of a model airplane in both a computational and an experiential setting. The proposed NSI methodology was only applied to the computational study due to sensor and channel limitations in the experimental measurements. Prior to performing the computational study, a series of experimental measurements were carried out suing the plane with no attachments. The resulting linear response was used to update a linear finite element model such that good agreement was achieved between the natural frequencies of the model and the experimental specimen. After the linear model updating, the design of the nonlinear stores was discussed and two reduced-order models (ROMs) were examined. The ROMs verified that the nonlinear stores would behave as intended when installed on the plane. The computational study of the plane with nonlinear stores follower the same procedure as the computational studies in Chapters 4 and 5. The resulting RQ-FEP demonstrated that the dynamics of the plane and the nonlinear stores could be partitioned in the same way as that of the wing and NES in Chapter 5, respectively. However, unlike Chapter 5, where the interactions (spikes) predominately occurred between the NES and other modes, the RQ-FEP revealed that numerous interactions between the modes of the plane were possible. Moreover, once the frequency of the nonlinear store surpassed that of the second flexible mode, the dynamics became densely populated with RCS and IRS between the store and the modes and between the plane modes, respectively. This results was explained by the fact that the total displacement of the store is the sum of the displacement of the wing at the pin joint and the additional DOF introduced by the store. Thus, the installation of the store results in the nonlinear coup;ling of two points on the wing of the plane. By defining a similar characteristic displacement as in Chapter 5, the RQ-FDP was created and the proposed NSI method was used to characterize the nonlinearity. The resulting error between the identified and exact parameters was less than 5% and the updated model was found to accurately reproduced the simulations. Following the computational study, two nonlinear stores were constructed and were tested in a grounded configuration. The plane was experimentally tested in three different configurations: both stores locked, left store unlocked and both stores unlocked. The experimental measurements revealed that one unlocked and two unlocked stores exhibit fundamentally different behavior with the latter being significantly more effective at engaging and dissipating the first flexible NNM for all excitation amplitudes studied. Specifically, when one store was unlocked, it was found to absorb energy from both the first and second modes of the plane. However, when both stores were unlocked, they were found to amplify the dissipation of the first mode, but canceled each other out when it came to the second mode. Thus, the experimental results demonstrated that a lightweight, local nonlinear attachment can lead to global repercussions in the dynamics is of lightly damped aircraft.

7.2 Recommendation for Future Research

Although the proposed NSI methodology was shown to result in updated models that accurately reproduce experimental measurements, several improvements and extensions would enhance its applicability and promote its use in fields outside of nonlinear dynamics and vibrations. First, new types of masking signals should be investigated with the hope of better isolating strongly nonstationary harmonics. In this work, the wavelet-bounding procedure was used in tandem with EMD, but the method is entirely independent of the decomposition algorithm. Extensions to form the wavelet-bounded EEMD or the wavelet-bounded variational mode decomposition [Dragomiretskiy and Zosso, 2014] can easily be implemented and, in doing so, the resulting IMFs or VMFs may be more accurate than those extracted using WBEMD. Moreover, if either method is shown to be more efficient than WBEMD then this may pave the way to a version of WBEMD that extracts optimal components in real time. Another extension of WBEMD might be to enable it to extract dominant harmonics from two- or three-dimensional data. Such an extension would see significant application in the biomedical field, where the response of organs cannot be directly measured, but can be imaged using techniques such as magnetic resonance imaging (MRI).

In this dissertation, the proposed methodology was used to characterize the strongly nonlinear resonances in the response of cantilever beams. However, the method was not able to identify the nonlinearity. In fact, the proposed NSI methodology was only demonstrated for local, nonlinear attachments. The method should be extended to handle the identification of distributed nonlinearity, where there is no local attachment. Such an extension would need to consider the transitions each NNM undergoes and to identify a mathematical model for the nonlinearity that reproduces these trends. Preliminary results not included in this dissertation indicated that the NSI methodology may be applied to local attachments with non-smooth nonlinearity and such applications should be investigated further. Another avenue of improvement is the extension of the methodology to handle the identification of nonlinear damping. One idea to achieve this is to apply POD to the velocity response and use the resulting POMs, RQ and a characteristic velocity to create a RQ frequency-velocity plot, which would be used that to identify the damping. Another issue found in a preliminary study indicated that the proposed methodology struggled to separate the NNMs of two attachments; a more in depth study is necessary to resolve this issue. Finally, all of the studies presented in this dissertation considered impulsive excitation; the applicability of the proposed methodology to other types of excitation (sinusoidal, random, gust, etc.) should be investigated.

References

P. S. Addison. *The illustrated wavelet transform handbook introductory theory and applications in science, engineering, medicine and finance*. Taylor & Francis,, New York, 2002.

J. R. Ahlquist, J. M. Carreño, H. Climent, R. de Diego, and J. de Alba. Assessment of nonlinear structural response in a400m gvt. In T. Proulx, editor, *Structural Dynamics, Volume 3*, pages 1147–1155, New York, NY, 2011. Springer New York.

R. Allemang and D. Brown. Correlation Coefficient for Modal Vector Analysis. In *Proceedings of the International Modal Analysis Conference & Exhibit*, pages 110–116, 1982.

R. Allemang and A. Phillips. The unified matrix polynomial approach to understanding modal parameter estimation: An update. In *Proceedings of ISMA International Conference on Noise and Vibration Engineering*, Leuven, Belgium, 2004. Katholieke Universiteit.

R. J. Allemang and D. L. Brown. A unified matrix polynomial approach to modal identification. *Journal of Sound and Vibration*, 211(3):301–322, 1998.

T. Allison, K. Miller, and D. Inman. A deconvolution-based approach to structural dynamics system identification and response prediction. *Journal of Vibration and Acoustics*, 130(3), 2008.

P. Apiwattanalunggarn, S. W. Shaw, and C. Pierre. Component mode synthesis using nonlinear normal modes. *Nonlinear Dynamics*, 41(1):17–46, 2005. doi: 10.1007/s11071-005-2791-2.

V. I. Arnold. *Dynamical Systems III*. Springer Berlin Heidelberg,, Berlin, Heidelberg :, 1988. ISBN 978-3-662-02535-2.

M. Attar, A. Karrech, and K. Regenauer-Lieb. Non-linear modal analysis of structural components subjected to unilateral constraints. *Journal of Sound and Vibration*, 389:380–410, Feb. 2017. doi: 10.1016/j.jsv.2016.11.012.

M. F. A. Azeez and A. Vakakis. Proper orthogonal decomposition (pod) of a class of vibroimpact oscillations. *Journal of Sound and Vibration*, 240(5):859–889, 2001.

Z. Bai. Krylov subspace techniques for reduced-order modeling of large-scale dynamical systems. *Applied Numerical Mathematics*, 43(1):9 – 44, 2002. doi: https://doi.org/10.1016/S0168-9274(02)00116-2. 19th Dundee Biennial Conference on Numerical Analysis.

V. Bajaj and R. B. Pachori. Classification of Seizure and Nonseizure EEG Signals Using Empirical Mode Decomposition. *IEEE Transactions on Information Technology in Biomedicine*, 16(6):1135–1142, Nov. 2012. doi: 10.1109/TITB.2011.2181403.

T. Baldacchino, E. J. Cross, K. Worden, and J. Rowson. Variational bayesian mixture of experts models and sensitivity analysis for nonlinear dynamical systems. *Mechanical Systems and Signal Processing*, 66-67: 178 – 200, 2016.

M. C. C. Bampton and R. R. Craig, Jr. Coupling of substructures for dynamic analyses. *AIAA Journal*, 6 (7):1313–1319, 1968. doi: 10.2514/3.4741.

S. Bellizzi and R. Sampaio. POMs analysis of randomly vibrating systems obtained from Karhunen-Loéve expansion. *Journal of Sound and Vibration*, 297(3–5):774–793, 2006.

W. A. Benfield and R. F. Hruda. Vibration analysis of structures by component mode substitution. *AIAA Journal*, 9(7):1255–1261, 1971. doi: 10.2514/3.49936.

S. Billings. *Nonlinear System Identification: NARMAX Methods in the Time, Frequency, and Spatio-Temporal Domains*. John Wiley & Sons, Ltd., 2013. doi: 10.1002/9781118535561.

S. Boisseau, G. Despesse, and B. A. Seddik. Nonlinear h-shaped springs to improve efficiency of vibration energy harvesters. *Journal of Applied Mechanics*, 80(6):061013–061013–9, 2013.

M. Brake, editor. *The Mechanics of Jointed Structures: Recent Research and Open Challenges for Developing Predictive Models for Structural Dynamics*. Springer International Publishing, 2018. doi: 10.1007/978-3-319-56818-8.

J. A. Brandon. Some insights into the dynamics of defective structures. In *Proceedings of the Institution of Mechanical Engineers, Part C: Journal of Mechanical Engineering Science*, volume 212 (6), pages 441–454, 1998.

J. Brownjohn, P.-Q. Xia, H. Hao, and Y. Xia. Civil structure condition assessment by fe model updating:: methodology and case studies. *Finite Elements in Analysis and Design*, 37(10):761 – 775, 2001. doi: https://doi.org/10.1016/S0168-874X(00)00071-8.

K. G. Budinski. Resistance to particle abrasion of selected plastics. *Wear*, 203-204(Supplement C):302–309, Mar. 1997. doi: 10.1016/S0043-1648(96)07346-2.

G. Canbaloğlu and H. N. Özgüven. Model updating of nonlinear structures from measured frfs. *Mechanical Systems and Signal Processing*, 80:282 – 301, 2016. doi: https://doi.org/10.1016/j.ymssp.2016.05.001.

K. Carney, I. Yunis, K. Smith, and C. Y. Peng. Nonlinear dynamic behavior in the cassini spacecraft modal survey. In *Proceedings of the 15th International Modal Analysis Conference (IMAC)*, Orlando, FL, 01 1997.

A. Casadei and R. Broda. Impact of vehicle weight reduction on fuel economy for various vehicle architectures. Technical report, Ricardo Inc., 2008.

T. K. Caughey and M. E. J. O'Kelly. Classical normal modes in damped linear dynamic systems. *Applied Mechanics*, 32(3):583–588, 1965. doi: 10.1115/1.3627262.

D. Chelidze and W. Zhou. Smooth orthogonal decomposition-based vibration mode identification. *Journal of Sound and Vibration*, 292(3):461–473, 2006.

H. Chen, M. Kurt, Y. S. Lee, D. M. McFarland, L. A. Bergman, and A. F. Vakakis. Experimental system identification of the dynamics of a vibro-impact beam with a view towards structural health monitoring and damage detection. *Mechanical Systems and Signal Processing*, 46(1):91–113, May 2014. doi: 10.1016/j.ymssp.2013.12.014.

S. Clement, S. Bellizzi, B. Cochelin, and G. Ricciardi. Sliding window proper orthogonal decomposition: Application to linear and nonlinear modal identification. *Journal of Sound and Vibration*, 333(21):5312 – 5323, 2014. doi: https://doi.org/10.1016/j.jsv.2014.05.035.

K. T. Coughlin and K. K. Tung. 11-Year solar cycle in the stratosphere extracted by the empirical mode decomposition method. *Advances in Space Research*, 34(2):323–329, 2004. doi: 10.1016/j.asr.2003.02.045.

R. J. Craig. Coupling of substructures for dynamic analyses - An overview. In *41st Structures, Structural Dynamics, and Materials Conference and Exhibit*, Structures, Structural Dynamics, and Materials and Co-located Conferences. American Institute of Aeronautics and Astronautics, Apr. 2000. doi: 10.2514/6.2000-1573.

J. Cusumano and B.-Y. Bai. Period-infinity periodic motions, chaos, and spatial coherence in a 10 degree of freedom impact oscillator. *Chaos, Solitons & Fractals*, 3(5):515 – 535, 1993. doi: https://doi.org/10.1016/0960-0779(93)90003-J.

J. Cusumano, M. Sharkady, and B. Kimble. Experimental measurements of dimensionality and spatial coherence in the dynamics of a flexible-beam impact oscillator. *Philosophical Transactions of the Royal Society of London A: Mathematical, Physical and Engineering Sciences*, 347(1683):421–438, 1994. doi: 10.1098/rsta.1994.0052.

B. Datta. Finite-element model updating, eigenstructure assignment and eigenvalue embedding techniques for vibrating systems. *Mechanical Systems and Signal Processing*, 16(1):83 – 96, 2002. doi: https://doi.org/10.1006/mssp.2001.1443.

R. Deering and J. Kaiser. The use of a masking signal to improve empirical mode decomposition. In *IEEE International Conference on Acoustics, Speech, and Signal Processing (ICASSP '05)*, volume 4, pages 485–488, Mar. 2005. doi: 10.1109/ICASSP.2005.1416051.

A. Derkevorkian, M. Hernandez-Garcia, H.-B. Yun, S. F. Masri, and P. Li. Nonlinear data-driven computational models for response prediction and change detection. *Structural Control and Health Monitoring*, 22(2):273–288, 2014. doi: 10.1002/stc.1673.

T. Detroux, L. Renson, and G. Kerschen. The harmonic balance method for advanced analysis and design of nonlinear mechanical systems. In G. Kerschen, editor, *Nonlinear Dynamics, Volume 2*, pages 19–34. Springer International Publishing, 2014. ISBN 978-3-319-04522-1.

K. Dragomiretskiy and D. Zosso. Variational Mode Decomposition. *IEEE Transactions on Signal Processing*, 62(3):531–544, Feb. 2014. doi: 10.1109/TSP.2013.2288675.

D. A. Ehrhardt, M. S. Allen, T. J. Beberniss, and S. A. Neild. Finite element model calibration of a nonlinear perforated plate. *Journal of Sound and Vibration*, 392:280–294, Mar. 2017. doi: 10.1016/j.jsv.2016.12.037.

D. J. Ewins. *Modal Testing: Theory, Practice, and Application.* Research Studies Press, 2000. ISBN 978-0-86380-218-8.

A. A. M. Fakir. *Theoretical and Experimental Studies of the Nonlinear Dynamics of a Class of Vibroimpact Systems.* Phd, University of Illinois at Urbana-Champaign, 1998.

B. F. Feeny and R. Kappagantu. On the physical interpretation of proper orthogonal modes in vibrations. *Journal of Sound and Vibration*, 211(4):607–616, Apr. 1998. doi: 10.1006/jsvi.1997.1386.

M. Feldman. *Hilbert Transform Applications in Mechanical Vibration.* Hilbert Transform Applications in Mechanical Vibration. John Wiley & Sons, Ltd., 2011. ISBN 978-0-470-97827-6. DOI: 10.1002/9781119991656.

P. Flandrin and G. Rilling. http://perso.ens-lyon.fr/patrick.flandrin/emd.html, Mar. 2007.

P. Flandrin, G. Rilling, and P. Goncalves. Empirical mode decomposition as a filter bank. *IEEE Signal Processing Letters*, 11(2):112–114, Feb. 2004. doi: 10.1109/LSP.2003.821662.

R. W. Freund. Model reduction methods based on Krylov subspaces. *Acta Numerica*, 12:267?319, 2003. doi: 10.1017/S0962492902000120.

M. Friswell and J. Mottershead. *Finite Element Model Updating in Structural Dynamics.* Springer, 1995.

R. L. Fusaro. Friction, wear, transfer, and wear surface morphology of ultrahigh-molecular-weight polyethylene. *A S L E Transactions*, 28(1):1–10, Jan. 1985. doi: 10.1080/05698198508981588.

U. Galvanetto, C. Surace, and A. Tassotti. Structural damage detection based on proper orthogonal decomposition: Experimental verification. *AIAA Journal*, 46(7):1624–1630, 2008.

I. Georgiou. Advanced proper orthogonal decomposition tools: Using reduced order models to identify normal modes of vibration and slow invariant manifolds in the dynamics of planar nonlinear rods. *Nonlinear Dynamics*, 41(1):69–110, Aug 2005.

P. B. Gonçalves, F. M. Silva, and Z. J. D. Prado. Reduced order models for the nonlinear dynamic analysis of shells. *Procedia IUTAM*, 19:118 – 125, 2016. doi: https://doi.org/10.1016/j.piutam.2016.03.016. IUTAM Symposium Analytical Methods in Nonlinear Dynamics.

A. Grossmann and J. Morlet. Decomposition of hardy functions into square integrable wavelets of constant shape. *SIAM Journal on Mathematical Analysis*, 15(4):723–736, 1984.

J. Guckenheimer and P. Holmes. *Nonlinear Oscillations, Dynamical Systems, and Bifurcations of Vector Fields*. Springer, 1983.

S. Gugercin and A. C. Antoulas. A survey of model reduction by balanced truncation and some new results. *International Journal of Control*, 77(8):748–766, 2004. doi: 10.1080/00207170410001713448.

R. J. Guyan. Reduction of stiffness and mass matrices. *AIAA J.*, 3(2):380–380, Feb. 1965. doi: 10.2514/3.2874.

J. K. Hale. *Ordinary Differential Equations*. Wiley: New York, 1969.

G. Haller and S. Ponsioen. Exact model reduction by a slow-fast decomposition of nonlinear mechanical systems. *Nonlinear Dynamics*, 90:617–647, 2017. doi: 10.1007/s11071-017-3685-9.

W. G. Halvorsen and D. L. Brown. Impulse technique for structural frequency response testing. *Sound and Vibration*, pages 8–21, 1977.

F. Hemez and S. Doebling. Review and assessment of model updating for non-linear, transient dynamics. *Mechanical Systems and Signal Processing*, 15(1):45 – 74, 2001. doi: https://doi.org/10.1006/mssp.2000.1351.

C. A. Herrera, D. M. McFarland, L. A. Bergman, and A. F. Vakakis. Methodology for nonlinear quantification of a flexible beam with a local, strong nonlinearity. *Journal of Sound and Vibration*, 388:298–314, Feb. 2017. doi: 10.1016/j.jsv.2016.10.037.

P. Holmes, J. L. Lumley, and G. Berkooz. *Turbulence, coherent structures, dynamical systems, and symmetry*. Cambridge University Press, 1996.

N. Huang, M.-L. Wu, S. Long, S. Shen, W. Qu, P. Gloersen, and K. Fan. A confidence limit for the empirical mode decomposition and Hilbert spectral analysis. *Proceedings of the Royal Society A: Mathematical, Physical and Engineering Sciences*, 459(2037):2317–2345, 2003. doi: 10.1098/rspa.2003.1123.

N. E. Huang, Z. Shen, S. R. Long, M. C. Wu, H. H. Shih, Q. Zheng, N.-C. Yen, C. C. Tung, and H. H. Liu. The empirical mode decomposition and the Hilbert spectrum for nonlinear and non-stationary time series analysis. *Proceedings of the Royal Society of London A: Mathematical, Physical and Engineering Sciences*, 454(1971):903–995, Mar. 1998.

N. E. Huang, Z. Shen, and S. R. Long. A New View of Nonlinear Water Waves: The Hilbert Spectrum1. *Annual Review of Fluid Mechanics*, 31(1):417–457, 1999. doi: 10.1146/annurev.fluid.31.1.417.

S. A. Hubbard. *Stability enhancement of a transonic wing using a passive nonlinear energy sink*. Ph.D. Thesis, University of Illinois at Urbana-Champaign, 2014.

S. A. Hubbard, D. M. McFarland, L. A. Bergman, and A. F. Vakakis. Targeted energy transfer between a model flexible wing and nonlinear energy sink. *Journal of Aircraft*, 47(6):1918–1931, Nov. 2010. doi: 10.2514/1.C001012.

W. C. Hurty. Dynamic analysis of structural systems using component modes. *AIAA Journal*, 3(4):678–685, 1965. doi: 10.2514/3.2947.

S. Ibrahim. Random decrement techniques for modal identification of structures. *Journal of Spacecraft and Rockets*, 14(11):696–700, 1977.

S. Ibrahim and E. Mikulcik. A method for the direct identification of vibration parameters from the free response. *Shock and Vibration Bulletin*, 47(4):183–198, 1977.

S. R. Ibrahim. *A Time Domain Vibration Test Technique*. Ph.D. thesis, University of Calgary, 1973.

S. R. Ibrahim. *Fundamentals of Time Domain Modal Identification*, pages 241–250. Springer Netherlands, Dordrecht, 1999. ISBN 978-94-011-4503-9.

S. Jain and P. Tiso. Simulation-free hyper-reduction for geometrically nonlinear structural dynamics: A quadratic manifold lifting approach. *Journal of Computational and Nonlinear Dynamics*, 2018.

B. Jaishi and W.-X. Ren. Structural finite element model updating using ambient vibration test results. *Journal of Structural Engineering*, 131(4):617–628, 2005. doi: 10.1061/(ASCE)0733-9445(2005)131:4(617).

J. Juang and R. Pappa. An eigensystem realization algorithm for modal parameter identification and model reduction. *AIAA Journal of Guidance, Control, and Dynamics*, 8(4):620—627, 1985.

T. Kalaycıoğlu and H. N. Özgüven. Nonlinear structural modification and nonlinear coupling. *Mechanical Systems and Signal Processing*, 46(2):289 – 306, 2014. doi: https://doi.org/10.1016/j.ymssp.2014.01.016.

R. E. Kalman. A new approach to linear filtering and prediction problems. *Journal of Basic Engineering*, 82(1):35–45, Mar. 1960. doi: 10.1115/1.3662552.

I. Karayannis, A. Vakakis, and F. Georgiades. Vibro-impact attachments as shock absorbers. *Proceedings of the Institution of Mechanical Engineers, Part C: Journal of Mechanical Engineering Science*, 222(10): 1899–1908, 2008.

K. Karhunen. *On Linear Methods in Probability and Statistics*. Phd, University of Helsinki, 1947.

G. Kerschen and J. C. Golinval. A model updating strategy of non-linear vibrating structures. *International Journal for Numerical Methods in Engineering*, 60(13):2147–2164, 2004. doi: 10.1002/nme.1040.

G. Kerschen, J.-C. Golinval, A. Vakakis, and L. Bergman. The method of proper orthogonal decomposition for dynamical characterization and order reduction of mechanical systems: An overview. *Nonlinear Dynamics*, 41(1-3):147–169, 2005. doi: 10.1007/s11071-005-2803-2.

G. Kerschen, K. Worden, A. F. Vakakis, and J.-C. Golinval. Past, present and future of nonlinear system identification in structural dynamics. *Mechanical Systems and Signal Processing*, 20(3):505–592, Apr. 2006. doi: 10.1016/j.ymssp.2005.04.008.

G. Kerschen, D. McFarland, J. Kowtko, Y. Lee, L. Bergman, and A. Vakakis. Experimental demonstration of transient resonance capture in a system of two coupled oscillators with essential stiffness nonlinearity. *Journal of Sound and Vibration*, 299(4–5):822–838, 2007. doi: 10.1016/j.jsv.2006.07.029.

G. Kerschen, O. Gendelman, A. F. Vakakis, L. A. Bergman, and D. M. McFarland. Impulsive periodic and quasi-periodic orbits of coupled oscillators with essential stiffness nonlinearity. *Communications in Nonlinear Science and Numerical Simulation*, 13(5):959–978, July 2008. doi: 10.1016/j.cnsns.2006.08.001.

G. Kerschen, M. Peeters, J.-C. Golinval, and A. Vakakis. Nonlinear normal modes, Part I: A useful framework for the structural dynamicist. *Mechanical Systems and Signal Processing*, 23:170–194, 2009. doi: 10.1016/j.ymssp.2008.04.002.

S. B. Kim, B. F. Spencer, and C.-B. Yun. Frequency domain identification of multi-input, multi-output systems considering physical relationships between measured variables. *Journal of Engineering Mechanics*, 131(5):461–472, May 2005. doi: 10.1061/(ASCE)0733-9399(2005)131:5(461).

M. Kisa, J. Brandon, and M. Topcu. Free vibration analysis of cracked beams by a combination of finite elements and component mode synthesis methods. *Computers & Structures*, 67(4):215 – 223, 1998. doi: https://doi.org/10.1016/S0045-7949(98)00056-X.

D. D. Klerk, D. J. Rixen, and S. N. Voormeeren. General framework for dynamic substructuring: History, review and classification of techniques. *AIAA Journal*, 46(5):1169–1181, 2008. doi: 10.2514/1.33274.

A. Korpel. Gabor: frequency, time, and memory. *Applied Optics*, 21(20):3624–3632, 1982.

D. Kosambi. Statistics in function space. *J. Indian Math. Soc.*, 7(1):76–88, 1943.

N. M. Krylov and N. N. Bogoliubov. *New Methods of Nonlinear Mechanics in their Application to the Investigation of the Operation of Electronic Generators*. I. United Scientific and Technical Press: Moscow, 1934.

P. Krysl, S. Lall, and J. E. Marsden. Dimensional model reduction in non-linear finite element dynamics of solids and structures. *International Journal for Numerical Methods in Engineering*, 51(4):479–504, 2001. doi: 10.1002/nme.167.

S. G. Kryzhevich. The symmetrization method and limit cycles of vibro-impact systems. *Vestnik St. Petersburg University: Mathematics*, 40(2):114–117, June 2007. doi: 10.3103/S1063454107020057.

M. Kurt, H. Chen, Y. Lee, D. McFarland, L. Bergman, and A. Vakakis. Nonlinear system identification of the dynamics of a vibro-impact beam: Numerical results. *Archive of Applied Mechanics*, 82(10-11): 1461–1479, 2012. doi: 10.1007/s00419-012-0678-5.

M. Kurt, M. Eriten, D. M. McFarland, L. A. Bergman, and A. F. Vakakis. Frequency-energy plots of steady-state solutions for forced and damped systems, and vibration isolation by nonlinear mode localization. *Communications in Nonlinear Science and Numerical Simulation*, 19(8):2905–2917, Aug. 2014a. doi: 10.1016/j.cnsns.2013.12.018.

M. Kurt, M. Eriten, D. M. McFarland, L. A. Bergman, and A. F. Vakakis. Strongly nonlinear beats in the dynamics of an elastic system with a strong local stiffness nonlinearity: Analysis and identification. *Journal of Sound and Vibration*, 333(7):2054–2072, Mar. 2014b. doi: 10.1016/j.jsv.2013.11.021.

M. Kurt, K. J. Moore, M. Eriten, D. M. McFarland, L. A. Bergman, and A. F. Vakakis. Nonlinear model updating applied to the IMAC XXXII Round Robin benchmark system. *Mechanical Systems and Signal Processing*, 88:111–122, May 2017. doi: 10.1016/j.ymssp.2016.10.016.

S. L. Lacy and D. S. Bernstein. Subspace identification for non-linear systems with measured-input non-linearities. *International Journal of Control*, 78(12):906–926, 2005. doi: 10.1080/00207170500214095.

Y. Lee, G. Kerschen, A. Vakakis, P. Panagopoulos, L. Bergman, and D. McFarland. Complicated dynamics of a linear oscillator with a light, essentially nonlinear attachment. *Physica D: Nonlinear Phenomena*, 204 (1-2):41–69, 2005. doi: 10.1016/j.physd.2005.03.014.

Y. Lee, F. Nucera, A. Vakakis, D. McFarland, and L. Bergman. Periodic orbits, damped transitions and targeted energy transfers in oscillators with vibro-impact attachments. *Physica D: Nonlinear Phenomena*, 238(18):1868–1896, 2009a. doi: 10.1016/j.physd.2009.06.013.

Y. S. Lee, S. Tsakirtzis, A. F. Vakakis, L. A. Bergman, and D. M. McFarland. Physics-Based Foundation for Empirical Mode Decomposition. *AIAA Journal*, 47(12):2938–2963, 2009b. doi: 10.2514/1.43207.

I. J. Leontaritis and S. A. Billings. Input-output parametric models for non-linear systems part i: deterministic non-linear systems. *International Journal of Control*, 41(2):303–328, 1985. doi: 10.1080/0020718508961129.

J. Leuridan, D. L. Brown, and R. J. Allemang. Time domain parameter identification methods for linear modal analysis: A unifying approach. *ASME Paper Number 85-DET-90*, 1985.

P. Lévy and M. Loéve. *Processus stochastiques et mouvement brownien*. Gauthier-Villars, Paris, 1948.

L. Li and S. Billings. Analysis of nonlinear oscillators using Volterra series in the frequency domain. *Journal of Sound and Vibration*, 330(2):337–355, 2011.

H. Liang, S. Bressler, E. Buffalo, R. Desimone, and P. Fries. Empirical mode decomposition of field potentials from macaque V4 in visual spatial attention. *Biological Cybernetics*, 92(6):380–392, 2005. doi: 10.1007/s00422-005-0566-y.

Y. Liang, D. Feng, and J. Cooper. Identification of restoring forces in non-linear vibration systems using fuzzy adaptive neural networks. *Journal of Sound and Vibration*, 242(1):47 – 58, 2001. doi: https://doi.org/10.1006/jsvi.2000.3348.

M. Link, R. Rohrmann, and S. Pietrzko. Experience with automated procedures for adjusting the finite element model of a complex highway bridge to experimental modal data. In *Proceedings-SPIE The International Society For Optical Engineering*, pages 218–225. SPIE International Society For Optical, 1996.

L. Ljung. *System Identification: Theory for the User*. Prentice Hall, Englewood Cliffs, New Jersey, 1987.

S. Lyashevskiy and Y. Chen. Identification of nonlinear system parameters using describing function approach. In *American Control Conference 1997. Proceedings of the 1997*, volume 3, pages 1944–1945, New Orleans, LA, 1997.

S. Lyashevskiy, L. Abel, and Y. Chen. On the application of the lyapunov and harmonic balance methods for identification of nonlinear systems. In *Decision and Control, 1995., Proceedings of the 34th IEEE Conference on*, volume 3, pages 1944–1945, New Orleans, LA, 1995.

X. Ma, M. Azeez, and A. Vakakis. Non-linear normal modes and non-parametric system identification of non-linear oscillators. *Mechanical Systems and Signal Processing*, 14(1):37 – 48, 2000. doi: https://doi.org/10.1006/mssp.1999.1267.

M. Mane, M. Kurt, Y. S. Lee, D. M. McFarland, L. A. Bergman, and A. F. Vakakis. Nonlinear system identification of vibro-impact dynamics. *Proceedings of the 7th Euromech Nonlinear Dynamics Conference*, 2011.

A. I. Manevich and L. I. Manevitch. *The Mechanics of Nonlinear Systems with Internal Resonances*. Imperial College Press, London : Singapore ; Hackensack, NJ:, 2005.

S. Mariani and A. Ghisi. Unscented kalman filtering for nonlinear structural dynamics. *Nonlinear Dynamics*, 49(1–2):131–150, 2007.

S. F. Masri and T. K. Caughey. A Nonparametric Identification Technique for Nonlinear Dynamic Problems. *Journal of Applied Mechanics*, 46(2):433–447, June 1979. doi: 10.1115/1.3424568.

S. F. Masri, A. W. Smyth, A. G. Chassiakos, T. K. Caughey, and N. F. Hunter. Application of neural networks for detection of changes in nonlinear systems. *Journal of Engineering Mechanics*, 126(7):666–676, 2000.

L. Meirovitch. *Elements of Vibration Analysis*. McGraw-Hill, New York, 1986.

L. Meirovitch. *Fundamentals of Vibrations*. Waveland Press, Inc., Long Grove, Illinois, 2010.

M. Mohammadali and H. Ahmadian. Efficient model order reduction of structural dynamic systems with local nonlinearities under periodic motion. *Shock and Vibration*, 2014:152145, 2014. doi: https://doi.org/10.1155/2014/152145.

A. Mojahed. personal communication, 2018.

K. J. Moore, M. Kurt, M. Eriten, M. D. Michael, L. A. Bergman, and A. F. Vakakis. Direct detection of nonlinear modal interactions from time series measurements. *Mechanical Systems and Signal Processing*, in press, 2018a. doi: https://doi.org/10.1016/j.ymssp.2017.09.010.

K. J. Moore, M. Kurt, M. Eriten, D. M. McFarland, L. A. Bergman, and A. F. Vakakis. Wavelet-bounded empirical mode decomposition for measured time series analysis. *Mechanical Systems and Signal Processing*, 99:14 – 29, 2018b. doi: https://doi.org/10.1016/j.ymssp.2017.06.005.

K. J. Moore, M. Kurt, M. Eriten, D. M. McFarland, L. A. Bergman, and A. F. Vakakis. Wavelet-bounded empirical mode decomposition for vibro-impact analysis. *Nonlinear Dynamics*, (submitted), 2018c.

F. Moreu and B. F. Spencer. Framework for Consequence-based Management and Safety of Railroad Bridge Infrastructure Using Wireless Smart Sensors (WSS). text, Newmark Structural Engineering Laboratory. University of Illinois at Urbana-Champaign., June 2015.

J. Mottershead and M. Friswell. Model updating in structural dynamics: A survey. *Journal of Sound and Vibration*, 167(2):347 – 375, 1993. doi: https://doi.org/10.1006/jsvi.1993.1340.

J. E. Mottershead, M. Link, and M. I. Friswell. The sensitivity method in finite element model updating: A tutorial. *Mechanical Systems and Signal Processing*, 25(7):2275 – 2296, 2011. ISSN 0888-3270. doi: https://doi.org/10.1016/j.ymssp.2010.10.012. URL `http://www.sciencedirect.com/science/article/pii/S0888327010003316`.

C. Nataraj and H. D. Nelson. Periodic solutions in rotor dynamic systems with nonlinear supports: A general approach. *Journal of Vibration, Acoustics, Stress, and Reliability in Design*, 111(2):187–193, 1989.

J. Noël and G. Kerschen. Frequency-domain subspace identification for nonlinear mechanical systems. *Mechanical Systems and Signal Processing*, 40(2):701 – 717, 2013.

J. P. Noël and G. Kerschen. Nonlinear system identification in structural dynamics: 10 more years of progress. *Mechanical Systems and Signal Processing*, 83:2–35, Jan. 2017. doi: 10.1016/j.ymssp.2016.07.020.

F. Nucera, A. F. Vakakis, D. M. McFarland, L. A. Bergman, and G. Kerschen. Targeted energy transfers in vibro-impact oscillators for seismic mitigation. *Nonlinear Dynamics*, 50(3):651–677, Jan. 2007.

A. Obukhov. Statistical description of continuous fields. *Tr. Geophys. Int. Akad. Nauk SSSR*, 24(151):3–42, 1954.

R. B. Pachori and V. Bajaj. Analysis of normal and epileptic seizure EEG signals using empirical mode decomposition. *Computer Methods and Programs in Biomedicine*, 104(3):373–381, Dec. 2011. doi: 10.1016/j.cmpb.2011.03.009.

M. Peeters, R. Viguié, G. Sérandour, G. Kerschen, and J.-C. Golinval. Nonlinear normal modes, Part II: Toward a practical computation using numerical continuation techniques. *Mechanical Systems and Signal Processing*, 23:195–216, 2009. doi: 10.1016/j.ymssp.2008.04.003.

B. Pokale and S. Gupta. Damage estimation in vibrating beams from time domain experimental measurements. *Archive of Applied Mechanics*, 84(12):1715–1737, Dec 2014. doi: 10.1007/s00419-014-0878-2.

V. Pugachev. General theory of the correlations of random functions. *Izv. Akad. Nauk USSR*, 17:1401–1402, 1953.

D. Quinn. Capture, nonlinear normal modes, and energy transfer through non-stationary resonances. In *Second International Conference on Nonlinear Normal Modes and Localization in Vibrating Systems*, Samos, Greece, 2006.

D. Quinn, R. Rand, and J. Bridge. The dynamics of resonance capture. *Nonlinear Dynamics*, 8:1–20, 1995.

K. A. Ramsey. Effective measurements for structural dynamics testing: Part I. *Sound and Vibration*, 9(11): 1–12, 1975.

K. A. Ramsey. Effective measurements for structural dynamics testing: Part II. *Sound and Vibration*, 10 (4):1–12, 1976.

N. Rehman and D. P. Mandic. Multivariate empirical mode decomposition. *Proceedings of the Royal Society of London A: Mathematical, Physical and Engineering Sciences*, 466(2117):1291–1302, May 2010. doi: 10.1098/rspa.2009.0502.

G. Rilling, P. Flandrin, P. Goncalves, and others. On empirical mode decomposition and its algorithms. In *IEEE-EURASIP workshop on nonlinear signal and image processing*, volume 3, pages 8–11. NSIP-03, Grado (I), 2003.

T. Ritto, F. Buezas, and R. Sampaio. A new measure of efficiency for model reduction: Application to a vibroimpact system. *Journal of Sound and Vibration*, 330(9):1977 – 1984, 2011. doi: https://doi.org/10.1016/j.jsv.2010.11.004.

R. Rosenberg. Normal modes of nonlinear dual-mode systems. *Journal of Applied Mechanics*, 27:263–268, 1960.

R. Rosenberg. The normal modes of nonlinear n-degree-of-freedom systems. *Journal of Applied Mechanics*, 29:7–14, 1962.

R. Rosenberg. On nonlinear vibrations of systems with many degrees of freedom. *Advances in Applied Mechanics*, 9:155–242, 1966.

J. Rutzmoser and D. Rixen. A lean and efficient snapshot generation technique for the hyper-reduction of nonlinear structural dynamics. *Computer Methods in Applied Mechanics and Engineering*, 325:330 – 349, 2017. doi: https://doi.org/10.1016/j.cma.2017.06.009.

A. Saito and B. I. Epureanu. Bilinear modal representations for reduced-order modeling of localized piecewise-linear oscillators. *Journal of Sound and Vibration*, 330(14):3442 – 3457, 2011. doi: https://doi.org/10.1016/j.jsv.2011.02.018.

P. Sakion. Part 2: The sound and vibration market for investors ? summary. Technical report, Elephant Tech, 2014.

J. A. Sanders, F. Verhulst, and J. Murdock. *Averaging Methods in Nonlinear Dynamical Systems*. Springer, 2007.

D. J. Segalman. Model reduction of systems with localized nonlinearities. *Journal of Computational and Nonlinear Dynamics*, 2(3):249–266, 2007.

N. Senroy and S. Suryanarayanan. Two Techniques to Enhance Empirical Mode Decomposition for Power Quality Applications. In *IEEE Power Engineering Society General Meeting*, pages 1–6, June 2007. doi: 10.1109/PES.2007.386016.

N. Senroy, S. Suryanarayanan, and P. Ribeiro. An Improved Hilbert-Huang Method for Analysis of Time-Varying Waveforms in Power Quality. *IEEE Transactions on Power Systems*, 22(4):1843–1850, Nov. 2007. doi: 10.1109/TPWRS.2007.907542.

R. C. Sharpley and V. Vatchev. Analysis of the Intrinsic Mode Functions. *Constructive Approximation*, 24 (1):17–47, Aug. 2005. doi: 10.1007/s00365-005-0603-z.

J. M. M. Silva. *Modal Analysis and Testing*. Springer Netherlands, Dordrecht, 1999. ISBN 978-94-011-4503-9.

L. Sirovich. Turbulence and the dynamics of coherent structures, part i: Coherent structures. *Quarterly of Applied Mathematics*, 45:561–571, 1987.

T. Söderström and P. Stoica, editors. *System Identification*. Prentice-Hall, Inc., Upper Saddle River, NJ, USA, 1988. ISBN 0-138-81236-5.

A. Teughels, J. Maeck, and G. D. Roeck. Damage assessment by fe model updating using damage functions. *Computers & Structures*, 80(25):1869 – 1879, 2002. doi: https://doi.org/10.1016/S0045-7949(02)00217-1.

M. Thothadri and F. C. Moon. Nonlinear system identification of systems with periodic limit-cycle response. *Nonlinear Dynamics*, 39(1):63–77, Jan 2005. doi: 10.1007/s11071-005-1914-0.

M. Thothadri, R. A. Casas, F. C. Moon, R. D'Andrea, and C. R. Johnson. Nonlinear system identification of multi-degree-of-freedom systems. *Nonlinear Dynamics*, 32(3):307–322, 2003.

D. Tiboaca, P. L. Green, R. J. Barthorpe, and K. Worden. Bayesian system identification of dynamical systems using reversible jump markov chain monte carlo. In R. Allemang, editor, *Topics in Modal Analysis II, Volume 8*, pages 277–284. Springer International Publishing, 2014.

J. Tong, Y. Ma, R. D. Arnell, and L. Ren. Free abrasive wear behavior of UHMWPE composites filled with wollastonite fibers. *Composites Part A: Applied Science and Manufacturing*, 37(1):38–45, Jan. 2006. doi: 10.1016/j.compositesa.2005.05.023.

A. Vakakis, D. McFarland, L. Bergman, L. Manevitch, and O. Gendelman. Isolated resonance captures and resonance capture cascades leading to single- or multi-mode passive energy pumping in damped coupled oscillators. *Journal of Vibration and Acoustics*, 126(2):235–244, 2004. doi: 10.1115/1.1687397.

A. Vakakis, O. Gendelman, L. Bergman, D. McFarland, G. Kerschen, and Y. Lee. *Nonlinear targeted energy transfer in mechanical and structural systems I*, volume 156 of *Solid Mech. Its Appl.* Springer Netherlands, 2008. doi: 10.1007/978-1-4020-9130-8.

A. F. Vakakis, L. I. Manevitch, Y. V. Mikhlin, V. N. Pilipchuk, and A. Zevin. *Normal Modes and Localization of Nonlinear Systems*. Wiley and Sons, New York, 1996. ISBN 978-94-017-2452-4.

A. F. Vakakis, L. A. Bergman, D. M. McFarland, Y. S. Lee, and M. Kurt. Current efforts towards a non-linear system identification methodology of broad applicability. *Proceedings of the Institution of Mechanical Engineers, Part C: Journal of Mechanical Engineering Science*, 225(11):2497–2515, 2011. doi: 10.1177/0954406211417217.

V. Vatchev and R. Sharpley. Decomposition of functions into pairs of intrinsic mode functions. *Proceedings of the Royal Society A: Mathematical, Physical and Engineering Sciences*, 464(2097):2265–2280, 2008.

S. Wang, N. Zhang, L. Wu, and Y. Wang. Wind speed forecasting based on the hybrid ensemble empirical mode decomposition and GA-BP neural network method. *Renewable Energy*, 94:629–636, Aug. 2016. doi: 10.1016/j.renene.2016.03.103.

X. Wang, T. L. Hill, S. A. Neild, A. D. Shaw, H. H. Khodaparast, and M. I. Friswell. Model updating strategy for structures with localised nonlinearities using frequency response measurements. *Mechanical Systems and Signal Processing*, 100:940 – 961, 2018a. doi: https://doi.org/10.1016/j.ymssp.2017.08.004.

X. Wang, H. H. Khodaparast, A. D. Shaw, M. I. Friswell, and G. Zheng. Localisation of local nonlinearities in structural dynamics using spatially incomplete measured data. *Mechanical Systems and Signal Processing*, 99:364–383, Jan. 2018b. doi: 10.1016/j.ymssp.2017.06.021.

J.-H. Weng, C.-H. Loh, and J. Yang. Experimental study of damage detection by data-driven subspace identification and finite-element model updating. *Journal of Structural Engineering*, 135(12):1533–1544, 2009. doi: 10.1061/(ASCE)ST.1943-541X.0000079.

S. Whitican and T. Copeland. Structural testbed design and testing with controlled nonlinearities. *Sound and Vibration*, 50(2):6–10, 2016.

K. Worden and W. Becker. On the identification of hysteretic systems. part II: Bayesian sensitivity analysis and parameter confidence. *Mechanical Systems and Signal Processing*, 29:213 – 227, 2012.

K. Worden and P. Green. A machine learning approach to nonlinear modal analysis. *Mechanical Systems and Signal Processing*, 84:34 – 53, 2017. doi: https://doi.org/10.1016/j.ymssp.2016.04.029. Recent advances in nonlinear system identification.

K. Worden and J. Hensman. Parameter estimation and model selection for a class of hysteretic systems using bayesian inference. *Mechanical Systems and Signal Processing*, 32:153–169, 2012.

K. Worden and G. Manson. On the identification of hysteretic systems. part i: Fitness landscapes and evolutionary identification. *Mechanical Systems and Signal Processing*, 29:201–212, 2012.

K. Worden and G. R. Tomlinson. *Nonlinearity in Structural Dynamics: Detection, Identification and Modelling*. Springer, 2010.

Z. Wu and N. E. Huang. Ensemble empirical mode decomposition: a noise-assisted data analysis method. *Advances in Adaptive Data Analysis*, 01(01):1–41, Jan. 2009. doi: 10.1142/S1793536909000047.

N. Xiang and Z. Qu. Ensemble Empirical Mode Decomposition of the Magnetic Field of the Sun as a Star. *Astronomical Journal*, 151(3), 2016. doi: 10.3847/0004-6256/151/3/76.

B. A. Zárate and J. M. Caicedo. Finite element model updating: Multiple alternatives. *Engineering Structures*, 30(12):3724 – 3730, 2008. doi: https://doi.org/10.1016/j.engstruct.2008.06.012.

C. Zhang, H. Wei, J. Zhao, T. Liu, T. Zhu, and K. Zhang. Short-term wind speed forecasting using empirical mode decomposition and feature selection. *Renewable Energy*, 96, Part A:727–737, Oct. 2016. doi: 10.1016/j.renene.2016.05.023.

A. Zimmerman and J. Lynch. Data driven model updating using wireless sensor networks. In *Proceedings of the 3rd Annual ANCRiSST Workshop*, 2006.

S. Zucca and B. I. Epureanu. Bi-linear reduced-order models of structures with friction intermittent contacts. *Nonlinear Dynamics*, 77(3):1055–1067, 2014. doi: 10.1007/s11071-014-1363-8.